

# The Growth, Processing and Characterisation of II-VI Semiconductor Structures

Ian A. Davidson

Submitted for the degree of Doctor of Philosophy

Heriot-Watt University,  
School of Engineering and Physical Sciences

July 2012

1<sup>st</sup> Supervisor – Dr. Kevin Prior

2<sup>nd</sup> Supervisor – Prof. Richard Warburton/Dr. Brian Gerardot

The copyright in this thesis is owned by the author. Any quotation from the thesis or use of any of the information contained in it must acknowledge this thesis as the source of the quotation or information.

## Abstract

The work contained in this thesis focuses on the growth, processing and characterization of II-VI semiconductors for use in opto-electronic devices. Included are efforts to develop both II-VI based distributed Bragg reflectors (DBRs) utilising ZnMgSSe and ZnSe and the epitaxial lift-off (ELO) process pioneered at Heriot-Watt University (HWU).

The optical properties of a range of different II-VI compounds (inc. ZnSe, MgS, MnS and ZnMgSSe) are measured using a range of techniques including photoluminescence spectroscopy (PL), optical transmission measurement and spectroscopic ellipsometry. From these measurements, a more accurate value for the bowing parameter of ZnCdSe of  $0.37 \pm 0.05 \text{ eV}$  is determined.

The effect of lifting structures using an MgS sacrificial layer is investigated by optical microscopy, optical transmission measurement and PL, to allow any structural changes to be determined. The ELO process is also extended to allow structures grown on InP substrates to be lifted by using a magnesium selenide (MgSe) sacrificial layer.

The  $\mu$ -PL measurements of a series of CdSe QDs grown on ZnMgSSe barriers are also reported and compared to previous work on other barrier materials (ZnSe and MgS). The causes of the jitter (spectral diffusion) seen in these samples is also investigated and discussed.

## Publications and Presentations

### Publications

- [1] RT Moug, C Bradford, F Izdebski, I Davidson, A Curran, KA Prior and RJ Warburton. "Development of an epitaxial lift-off technology for II-VI nanostructures using ZnMgSSe alloys" *Microelectronics Journal* 40 (2009) 530-532
- [2] RT Moug, C Bradford, F Izdebski, I Davidson, A Curran A, RJ Warburton, KA Prior, A Aouni, FM Morales and SI Molinal. "A comparison of ZnMgSSe and MgS wide bandgap semiconductors used as barriers: Growth, structure and luminescence properties". *J. Crystal Growth* 311 (2009) 2099-2101
- [3] IA Davidson, RT Moug, C Bradford C, F Izdebski, and KA Prior. "Determination of the band-gap of MgS and MgS-rich  $\text{Zn}_{1-x}\text{Mg}_x\text{S}_y\text{Se}_{1-y}$  alloys from optical transmission measurements". *Phys. Stat. Sol. (B)* 247 (2010) 1396-1398
- [4] IA Davidson, RT Moug, PA Dalgarno, C Bradford, RJ Warburton and KA Prior. " $\mu$ -PL characterization of CdSe Quantum Dots grown on a  $\text{Zn}_{0.2}\text{Mg}_{0.8}\text{S}_{0.64}\text{Se}_{0.36}$  barrier." *Journal of Physics: Conference Series* 245 (2010) 012085.
- [5] IA Davidson, RT Moug, PA Dalgarno, C Bradford, RJ Warburton and KA Prior. "CdSe Quantum Dots grown on a  $\text{Zn}_{0.2}\text{Mg}_{0.8}\text{S}_{0.64}\text{Se}_{0.36}$  barrier: MBE growth and  $\mu$ -PL characterization". *J. Crystal Growth* 323 (2011) 236-240
- [6] KA Prior, C Bradford, IA Davidson and RT Moug. "Metastable II-VI sulphides: growth, characterization and stability". *J. Crystal Growth* 323 (2011) 114-121
- [7] IA Davidson, RT Moug, EC Vallance, MC Tamargo and KA Prior. "MBE growth and design of II-VI hetero-structures for epitaxial lift-off." *Phys. Stat. Sol. (a)* accepted
- [8] DJ Rogers, F Hosseini Teherani, P Bove, A Ougazzaden, VE Sandana, L Goubert, T Moudakir, A Ahaitouf, S Gautier, IA Davidson, KA Prior, RP McClintock, HJ Drouhin and M Razeghi. "Novel process for direct bonding of GaN onto glass substrates using sacrificial ZnO template layers to chemically lift-off GaN from c-sapphire." *Proc. SPIE* 8263 (2012) 82630R

## **Presentations**

1. R Moug, C Bradford, A Curran, F Izdebski, I Davidson, KA Prior, and RJ Warburton, “Development of an epitaxial lift-off technology for II-VI nanostructures using ZnMgSSe alloys”, presented at the Workshop on Recent Advances on Low Dimensional Structures, Nottingham, April 2008
2. RT Moug, C Bradford, F Izdebski, I Davidson, A Curran, RJ Warburton, KA Prior, A Aouni, FM Morales, SI Molina, A comparison of ZnMgSSe and MgS wide bandgap semiconductors used as barriers: growth, structure and luminescence properties, presented at MBE 2008, Vancouver, Aug 2008
3. I Davidson, RT Moug, F Izdebski, C Bradford, KA Prior, Determination of the band-gap of MgS and MgS-rich ZnMgSSe alloys from optical transmission measurements, presented at 14th International Conference on II-VI Compounds, St Petersburg, August 2009
4. IA Davidson, RT Moug, PA Dalgarno, C Bradford, RJ Warburton and KA Prior,  $\mu$ -PL characterization of CdSe Quantum Dots grown on a  $\text{Zn}_{0.2}\text{Mg}_{0.8}\text{S}_{0.64}\text{Se}_{0.36}$  barrier, presented at QD2010, Nottingham, April 2010
5. IA Davidson, RT Moug, PA Dalgarno, C Bradford, RJ Warburton and KA Prior, CdSe Quantum Dots grown on a  $\text{Zn}_{0.2}\text{Mg}_{0.8}\text{S}_{0.64}\text{Se}_{0.36}$  barrier: MBE growth and  $\mu$ -PL characterization. Presented at MBE 2010, Berlin, September 2010
6. KA Prior, C Bradford, IA Davidson and RT Moug, “Metastable II-VI sulphides: growth, characterization and stability.” Oral presentation at MBE 2010, Berlin, September 2010
7. IA Davidson, RT Moug, EC Vallance, MC Tamargo and KA Prior. “MBE growth and design of II-VI hetero-structures for epitaxial lift-off.” Oral presentation at 15th International Conference on II-VI Compounds, Mayan Riviera, Mexico 2011



## Acknowledgements

There are a number of people who I must acknowledge, as without their help, advice, support and hard work, this thesis would not have been possible. First of all, I'd like to thank my supervisor, Dr. Kevin Prior, for putting up with me for the last few years and supporting my work.

I'd then also like to thank (in no particular order):

All of my co-workers: Christine Bradford, Richard Moug, Frauke Izdebski, Paul Dalgarno and Akhil Rajan, as again much of the work presented in this thesis owes a lot to their hard work and advice.

All the other previous members of the MBE and Nano-Optics groups at Heriot-Watt University (HWU) as samples and data generated by them have been used throughout my work.

All our collaborators at other institutions.

All of the technical staff at HWU, in particular Iain Drummond and the guys in the mechanical workshop, as they have provide significant support and advise during my PhD including fixing many of the things that have been broken...

All of the project students that I have worked with or supervised.

All the other PhD students and academic staff in the school of physics, as their advice and suggestions have often proved vital and save me from wasting lots of time on things that probably would never have worked.

My now long suffering girlfriend, Insa, who has had to listen to more than her fair share of my PhD related complaints.

And last and by no means least, all of my friends and family, who have had to put up with many years of listening to me talking and/or whining about my PhD.

# Declaration Statement

## ACADEMIC REGISTRY Research Thesis Submission



Name:	Ian A. Davidson		
School/PGI:	School of EPS/IPAQS		
Version: <i>(i.e. First, Resubmission, Final)</i>	First	Degree Sought (Award <b>and</b> Subject area)	PhD Physics

### Declaration

In accordance with the appropriate regulations I hereby submit my thesis and I declare that:

- 1) the thesis embodies the results of my own work and has been composed by myself
- 2) where appropriate, I have made acknowledgement of the work of others and have made reference to work carried out in collaboration with other persons
- 3) the thesis is the correct version of the thesis for submission and is the same version as any electronic versions submitted\*.
- 4) my thesis for the award referred to, deposited in the Heriot-Watt University Library, should be made available for loan or photocopying and be available via the Institutional Repository, subject to such conditions as the Librarian may require
- 5) I understand that as a student of the University I am required to abide by the Regulations of the University and to conform to its discipline.

\* *Please note that it is the responsibility of the candidate to ensure that the correct version of the thesis is submitted.*

Signature of Candidate:		Date:	16/08/12
-------------------------	--	-------	----------

### Submission

Submitted By <i>(name in capitals)</i> :	Ian A. Davidson
Signature of Individual Submitting:	
Date Submitted:	16/08/12

### For Completion in the Student Service Centre (SSC)

Received in the SSC by <i>(name in capitals)</i> :			
<b>Method of Submission</b> <i>(Handed in to SSC; posted through internal/external mail):</i>			
<b>E-thesis Submitted</b> (mandatory for final theses)			
Signature:		Date:	

# Table of Contents

Abstract.....	ii
Publications and Presentations.....	iii
Acknowledgements.....	v
Declaration Statement.....	vi
Table of Contents.....	vii
Thesis Outline.....	xi
List of Abbreviations .....	xiii
1. Introduction .....	1
1.1. Molecular Beam Epitaxy (MBE) .....	1
1.1.1. Basic Principles.....	2
1.1.2. MBE Growth System Configuration .....	2
2. Experimental Techniques.....	5
2.1. Standard Growth Technique .....	5
2.1.2. RHEED.....	9
2.2. Characterisation Techniques .....	11
2.2.1. X-ray Diffraction (XRD).....	12
2.2.2. Photo-Luminescence Spectroscopy (PL) .....	14
2.2.3. Transmission/Absorption Measurements .....	18
2.2.4. Reflectometry .....	19
2.2.5. Spectroscopic Ellipsometry.....	19
3. Spin Current Detector .....	22
3.1. Introduction .....	22
3.1.1. Spintronics .....	23
3.1.2. Spin Current Detector .....	25
3.2. Spin Current Detector .....	27
3.2.1. Structure and Growth of SCD1.....	27
3.2.2. PL Characterisation .....	29
3.2.3. XRD Characterisation .....	30
3.3. Spin Current Detector 2 (SCD2) .....	31
3.3.1 Calibration of ZnSe rich Quaternary Alloy for SCD 2.....	31
3.3.2. Structure and Growth of SCD 2.....	34
	vii

3.3.3. PL Characterisation of SCD2 Samples .....	35
3.3.4. XRD Characterisation .....	37
3.4. Problems with SCD Design .....	38
3.5. Conclusions .....	38
4. Epitaxial Lift-Off.....	40
4.1. Introduction .....	41
4.1.1. Overview of the ELO Technique.....	42
4.1.2. II-VI Epitaxial Liftoff .....	44
4.2. Development of the MgS Based ELO Process .....	45
4.2.1. Etch Mechanism.....	47
4.2.2. Cracking.....	48
4.2.3. Deposition onto a New Substrate .....	52
4.2.4. Optical Characterisation of ELO Samples.....	53
4.2.5. Recent Problems with MgS ELO Samples .....	54
4.3 Extension of ELO to an MgSe Sacrificial layer .....	54
4.3.1. Etch Mechanism.....	55
4.3.2 MgSe/ZnCdSe Samples from CUNY.....	56
4.3.3. XRI Measurements.....	57
4.3.4. Structural Calibration of the 2 <sup>nd</sup> Sample Set .....	60
4.3.5. Etching Results .....	61
4.3.6. PL Characterisation .....	63
4.3.7. Surface Characterisation and Cracking .....	64
4.4. MgS and MgSe ELO Failure Modes .....	71
4.5. Conclusions .....	75
5. Development of a Lattice Matched, MgS rich ZnMgS <sub>2</sub> Quaternary Alloy .....	76
5.1. Introduction .....	77
5.2. Initial Work.....	81
5.2.1. Growth .....	82
5.2.2. X-ray Characterisation.....	83
5.2.3. Measurement of the Bandgap of the Alloy.....	89
5.2.4. PL Comparison of ZnSe QWs with QA and MgS Barriers .....	91
5.2.5. Lift-Off Results.....	92
5.3. Second Set of Samples .....	94

5.3.1. Growth .....	95
5.3.2. X-ray Characterisation.....	96
5.3.3. Measurement of the Bandgap of the Alloy.....	101
5.3.4. Determination of the QAs Composition .....	102
5.4. Quaternary Alloy XRI/XRD Modelling Problem.....	106
5.4.1. Re-Analysis of the XRI Samples .....	113
5.5. Third Set of Samples .....	117
5.5.1. Growth .....	118
5.5.2. X-ray Characterisation.....	119
5.6. Conclusions .....	122
6. Optical Characterisation of II-VI compounds and Distributed Bragg Reflector Development .....	124
6.1 Introduction .....	125
6.1.1. Bandgap Measurement and PL Spectroscopy .....	125
6.1.2. Reflectometry .....	127
6.1.3. Refractive Index Measurement and Spectroscopic Ellipsometry .....	128
6.1.4. ZnSe Dispersion.....	129
6.1.5. Distributed Bragg Reflectors .....	134
6.2. ZnCdSe Bowing Parameter.....	135
6.2.1. ZnSe Bandgap.....	136
6.2.2. CdSe Bandgap .....	141
6.2.3. ZnCdSe Bandgap .....	144
6.2.4. ZnCdSe Bowing Parameter.....	148
6.3. Reflectometry .....	149
6.4. Spectroscopic Ellipsometry and Refractive Index Measurement .....	153
6.4.1. Zinc Selenide, ZnSe.....	153
6.4.2. ZnSe Oxide Layer .....	158
6.4.3. Zinc Sulphide, ZnS .....	162
6.4.4. Zinc Sulphur Selenide, ZnSSe .....	164
6.4.5. Magnesium Sulphide, MgS.....	166
6.4.6. Manganese Sulphide, MnS.....	174
6.4.7. Cadmium Selenide, CdSe .....	179
6.4.8. Zinc Cadmium Selenide, ZnCdSe .....	183
6.4.9. Zinc Magnesium Sulphur Selenide, ZnMgSSe .....	185

6.5 Distributed Bragg Reflector (DBR) .....	190
6.5.1. MgS/ZnSe DBR .....	191
6.5.2. QA/ZnSe DBR.....	193
6.6. Conclusions .....	195
6.6.1. ZnSe PL/Bandgap Measurement.....	195
6.6.2. CdSe PL.....	196
6.6.3. ZnCdSe PL and Bowing Parameter .....	196
6.6.4. Reflectometry .....	197
6.6.5. Spectroscopic Ellipsometry .....	197
6.6.6. DBR.....	200
7. $\mu$ -PL Characterisation of CdSe Quantum Dots Grown on an MgS rich ZnMgSSe Barrier .....	201
7.1. Introduction .....	202
7.2. Growth .....	203
7.3. Ensemble PL Characterisation.....	204
7.4. $\mu$ -PL Characterisation.....	208
7.4.1. Comparison of $\mu$ -PL Results with ZnSe/CdSe and MgS/CdSe Samples .....	219
7.5. Jitter/Blinking .....	220
7.6. Conclusions .....	229
8. Final Conclusions and Suggestions for Future Work.....	231
8.1. Chapter 3 – Spin Current Detector .....	231
8.2. Chapter 4 – Epitaxial Lift-Off.....	231
8.3. Chapter 5 – Development of a Lattice Matched, MgS rich QA.....	232
8.4. Chapter 6 – Optical Characterisation of II-VI Compounds and DBR Development .....	233
8.5. Chapter 7 - $\mu$ -PL Characterisation of CdSe Quantum Dots Grown on QA Barrier .....	234
8.6. Suggestions for Future Work .....	235
9. References .....	246

# Thesis Outline

The work contained in this thesis concerns a range of different topics related to the growth, processing and characterisation of II-VI semiconductor structures. It is divided into chapters roughly by topic, but many of the results are used numerous times throughout the whole thesis.

Chapter 1 is a very brief introduction to semiconductor growth with particular emphasis on the work of the MBE group at Heriot-Watt University (HWU). This chapter is quite brief as each experimental chapter has its own introduction due to the range of work undertaken.

Chapter 2 describes the various growth and characterisation techniques used in the remainder of this thesis, with particular emphasis paid to x-ray diffraction and optical characterisation, as these are the techniques used most often.

Chapter 3 details the growth and development of a series of spin current detectors for the Experimental Semiconductor Physics group at Philipps-Universität Marburg, and also includes the preliminary work undertaken to grow very wide quantum well structures for the Optical Spectroscopy Group at Bath University.

Chapter 4 describes the development of an epitaxial lift-off (ELO) process for II-VI semiconductors – the use of a sacrificial layer inserted into a structure to allow the upper layers to be transferred to a new substrate. This chapter is in two parts with the first explaining the continuing development of this technique and the second, its extension to samples with MgSe sacrificial layers.

Chapter 5 describes the work undertaken to develop a ZnMgSSe quaternary alloy (QA) to act as a replacement barrier material for ELO structures. Additional work undertaken to investigate the use of the X-ray interference (XRI) technique to determine the composition of quaternary alloy will also be reported.

Chapter 6 summarises the work undertaken to optically characterise the various compounds grown at HWU. Many of these compounds are either unique to HWU or currently cannot be grown thick enough elsewhere to allow their optical characterisation. This work therefore is the first time some of these measurements have been made. The chapter will also contain the details of designs for DBRs based on the II-VI compounds grown at HWU.

Chapter 7 describes the  $\mu$ -PL characterisation of a series of CdSe quantum dot samples with QA barriers. The results from these samples are compared to those obtained previously from dots with MgS and ZnSe barriers and a discussion of the causes of the energy jitter (spectral diffusion) seen in presented.

Finally all the work will be summarised in chapter 8 and suggestions for future work made.



## List of Abbreviations

AFM	Atomic Force Microscopy
ALE	Atomic Layer Epitaxy
a-Se	Amorphous selenium
a-ZnO	Amorphous zinc oxide
BEMA	Bruggeman Effective Medium Approximation
CCD	Charged Coupled Device
CP	Critical Point
CUNY	City College of New York
DBR	Distributed Bragg Reflector
DMS	Dilute Magnetic Semiconductors
DQW	Double Quantum Well
DUV	Deep Ultra-Violet - light with a wavelength 200-300nm
ELO	Epitaxial Lift-Off
ESP	Experimental Semiconductor Physics group at the Philipps-Universität Marburg
FWHM	Full Width at Half Maximum
GOF	Goodness Of Fit
GR	Growth Rate
HH	Heavy-Hole Exciton
HRXRD	High Resolution X-Ray Diffraction
HWA-xxxx	Sample grown in C-end growth chamber
HWC-xxx	Sample grown in A-end (transition element) growth chamber
HWU	Heriot-Watt University
IR	Infra-Red
LED	Light Emitting Diode
LH	Light-Hole Exciton
LO	Longitudinal
LN2	Liquid Nitrogen
MBE	Molecular Beam Epitaxy
MEE	Migration Enhanced Epitaxy
ML	Mono-Layer
MO	Multiple Oscillator
MOCVD	Metal-Organic Chemical Vapour Deposition
MQW	Multiple Quantum Well

MSE	Mean Squared Error
NA	Numerical Aperture
NIR	Near Infra-Red
OG	ZnSe Over Growth sample
PI	Point Inversion
PL	Photo-Luminescence Spectroscopy
PMT	Photo-Multiplier Tube
PV	Photo-Voltaic
QA	Quaternary (ZnMgSSe) Alloy
QCSE	Quantum Confined Stark Effect
QD	Quantum dot
QUIC	Quantum Interference Control
QW	Quantum Well
RADS	Rocking Curve Analysis by Dynamical Simulation - Bede/JV Semiconductor's HRXRD analysis software
RHEED	Reflected High Energy Electron Diffraction
RS	Rock-Salt crystal structure
SAQD	Self-Assembled Quantum Dots
SCD	Spin Current Detector
SE	Spectroscopic Ellipsometry
SEO	Single-Effective Oscillator
SPAD	Single-Photon Avalanche Diode
TEM	Tunnelling Electron Microscopy
UV	Ultra-Violet
VDW	Van Der Waals
VUV	Vacuum Ultra-Violet - light with a wavelength <200nm
WI-ELO	Weight-Induced Epitaxial Lift-Off process
WL	Wetting Layer
WZ	Wurtzite crystal structure
XRD	X-ray Diffraction
XRI	X-ray Interference Characterisation Technique
ZB	Zinc-Blende crystal structure
μ-PL	Micro Photo-Luminescence spectroscopy - PL with a <1μm spot

# 1. Introduction

Over the last 60 years semiconductors have become one of the most important and widely used technologies in society due to their extensive use in micro- and optoelectronics. For this reason, considerable time and effort has been put into their development and as such many semiconductor materials and technologies are now highly mature.

At Heriot-Watt the MBE group is primarily concerned with the growth and development of II-VI semiconductors. The initial interest in these compounds centred on their possible use in blue LEDs and laser diodes. However with the development of gallium nitride (GaN), research has moved away from this area. Currently the research at HWU is mainly focussed on applications such as single photon sources, magnetic materials for spin applications and the development of structures for the investigation of light-matter interactions.

Although there are a number of ways to epitaxially grow semiconductor crystals, the most common and highly developed are molecular beam epitaxy (MBE) and metal-organic chemical vapour deposition (MOCVD, although other names and abbreviations for the same process are sometimes used). The reason these two processes have become predominant is due to a number of factors arising from their ease of use and cost-effectiveness. At HWU growth is undertaken exclusively by MBE.

## 1.1. Molecular Beam Epitaxy (MBE)

Initially developed in the 1960s [1.1, 1.2] MBE has progressed to become the most commonly used growth process for the development of new materials and one of the two main techniques (along with MOCVD) for the industrial growth of epitaxial semiconductor layers. It has a number of key advantages including *in situ* surface monitoring using RHEED (reflection high energy electron diffraction), the use of elemental source materials and the ability to achieve

extremely low dislocation density, single crystal layers [1.3]. The use of elemental sources is of particular benefit when growing new materials as it dramatically reduces the time taken for low impurity level source materials to become available, making MBE particularly attractive for research applications.

### **1.1.1. Basic Principles**

MBE growth typically uses elemental solid sources, although in some systems liquid or gas phase material can also be handled [1.4]. The growth chamber is pumped down, using a series of vacuum pumps, to a pressure of  $<10^{-8}$  mbar and then the source materials are heated in Knudsen cells causing them to evaporate. At these low pressures the mean free path of the source atoms is much larger than the growth chamber, so material transport is in the molecular flow regime. Each Knudsen cell is covered by a shutter and by controlling which shutters are open and the cells fluxes, it is possible to control the composition of a structure during growth.

The substrate is positioned at the centre of the growth chamber and is rotated throughout growth to ensure a uniform coating. The temperature of the substrate can also be controlled through the use of the electrical heater mounted behind it. The measurement and control of the substrate's temperature is the one major area of concern in MBE, as the need to rotate the sample and heat it makes precise control difficult. Typically a thermocouple is mounted as closely to the heater as possible and then calibrated using a pyrometer mounted outside the vacuum and focussed on the sample.

### **1.1.2. MBE Growth System Configuration**

Figures 1.1 and 1.2 show the layout of the MBE machine at Heriot-Watt. It consists of two VG V80H growth chambers linked together by a preparation chamber and entry lock. This arrangement is used as it allows for the rapid introduction and removal of substrates and grown samples without having to bring the main growth chambers up to atmospheric pressure.

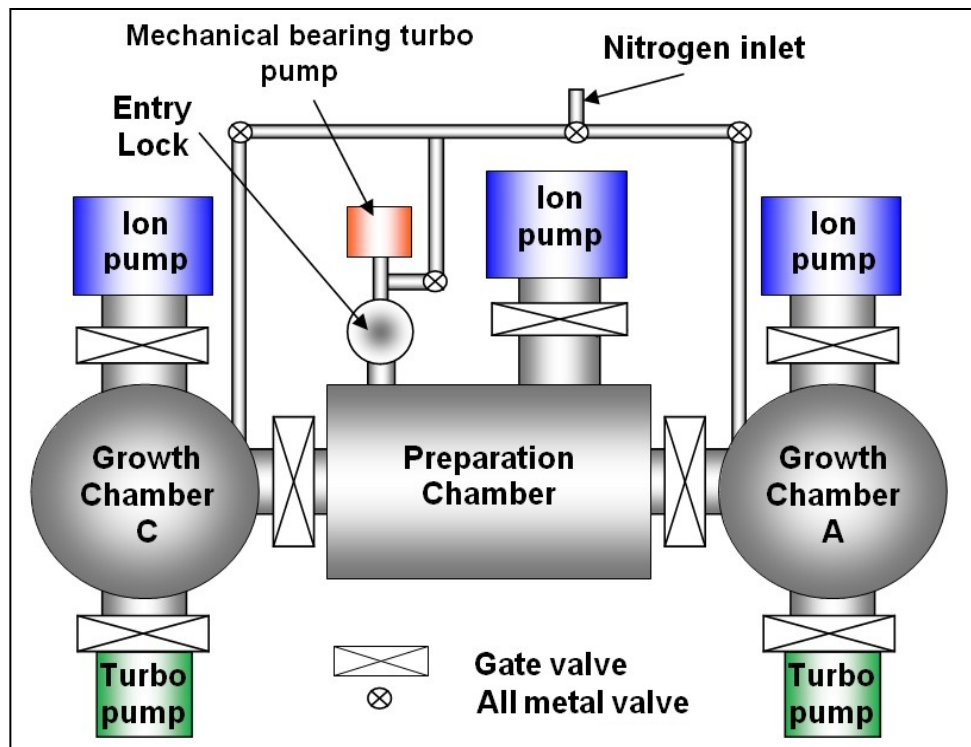


Fig. 1.1 Schematic of the molecular beam epitaxy System at Heriot-Watt.

The A-end of the chamber is used for transition metal work, such as the growth of MnS, whilst the C-end is reserved for other growth work. This is done as the presence of transition elements (principally manganese) in the chamber has been found to dope samples [1.5]. Samples labelled HWC were produced in the C-end and HWA in the A-end.

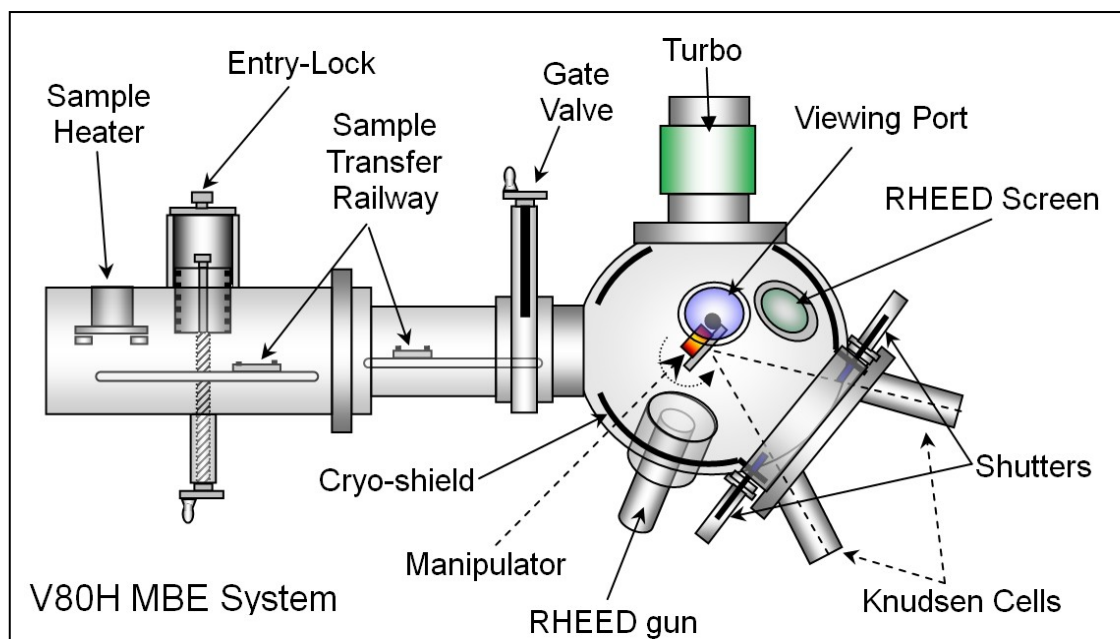


Fig. 1.2. Layout of the VG V80H molecular beam epitaxy system

The C-end has ports for 8 Knudsen cells but currently only 5 are in use, they

contain zinc, cadmium, magnesium, selenium and zinc sulphide. The ZnS cell is a water cooled, high temperature model whilst all the others are standard Knudsen cells. The ZnS cell is also fitted with a liquid nitrogen (LN2) cooled shutter, to reduce the background sulphur pressure in the chamber and reduce the heat load experienced by the substrate when the shutter is open. During growth a LN2 cooled cryo-panel is used to further reduce the chambers pressure.

The C-end is also fitted with a quadrupole mass spectrometer, RHEED system, two ion gauges (one stationary one mounted on the chamber wall and a movable one mounted on the manipulator) and a pyrometer window opposite to the substrate growth position to allow the substrate temperature to be calibrated using a pyrometer. To allow accurate flux measurements to be made the movable ion gauge on the manipulator can be rotated in to the position the substrate would occupy during growth and used prior to growth to measure the flux of all of the cells. The reflected high energy electron diffraction (RHEED) system allows the surface of the substrate/grown sample to be monitored (see section 2.1.1.).

## 2. Experimental Techniques

The experimental work performed at HWU falls into three areas: growth, processing or characterisation. All samples are grown in the MBE system using our standard growth procedure, as described in section 2.1. The majority of the processing work performed at HWU is ELO, which will be explained in detail in chapter 4. A range of characterisation techniques are used throughout this thesis to determine the structure and properties of the samples, as will be explained in section 2.2.

### 2.1. Standard Growth Technique

The majority of the structures grown at HWU are deposited on GaAs wafers, although GaP and InP have been used in the past. Prior to growth the substrate is prepared to ensure an atomically flat surface for growth and to minimise growth chamber contamination. The first stage is a chemical etch to remove contaminants present on the surface and the oxide layer. The etch solution used at HWU is a 2:2:15 solution of  $\text{H}_2\text{O}_2$ ,  $\text{H}_2\text{O}$  and  $\text{H}_2\text{SO}_4$ . High purity reagents and deionised water are used to ensure they are contaminant free. The substrate is etched in the solution at  $80^\circ\text{C}$  for 90s, and then rinsed in deionised water before being dried with oxygen free nitrogen.

The substrate is then mounted to a molybdenum block using indium heated to above  $157^\circ\text{C}$ , its melting point. At this temperature a new oxide layer will form on the substrate, but this new layer is thinner, more uniform and far smoother than the previous one and is also contaminant free [2.1, 2.2].

Subsequently the substrate is placed in the entry lock and pumped down to a pressure  $<10^{-6}$  mbar. It is then transferred to the preparation chamber and heated to  $200^\circ\text{C}$  to remove any water vapour. It is then transferred to the growth chamber and placed on the manipulator (see figure 1.2). Before growth, the thin oxide layer formed during substrate mounting is removed by slowly heating the

substrate while monitoring the surface with RHEED (see section 2.1.1.). As the substrate is heated the oxide layer will slowly evaporate leaving a contaminant free surface.

The GaAs oxide layer consists of a mixture of  $\text{As}_2\text{O}_5$  and  $\text{Ga}_2\text{O}_3$  [2.3, 2.4]. The arsenic pentoxide decomposes to  $\text{As}_2\text{O}_3$  at  $315^\circ\text{C}$ , which then evaporates at  $\sim 460^\circ\text{C}$ . The gallium trioxide has a very low vapour pressure but at  $580^\circ\text{C}$ , small areas of GaAs surface, exposed by the arsenic oxide removal, will produce gallium. This liberated gallium reacts with the gallium trioxide causing it to decompose to  $\text{Ga}_2\text{O}$  which evaporates [2.5].

The thermal removal of the oxide layer has the undesired effect of producing small etch pits due to the evaporation of GaAs [2.6, 2.7]. This is detrimental to growth, as these pits act as nucleation sites for dislocation and stacking faults. However as these pits typically do not pose significant problems for the majority of structures grown, thermal oxide removal still represents the best method of substrate preparation in a II-VI system [2.8, 2.9]. For III-V growth, a buffer layer of GaAs can be grown prior to any structure to ensure an atomically flat surface for the growth, but this is of course not possible in a II-VI system (unless its connected to a III-V growth chamber).

After the oxide has been removed, the substrate is cooled to the growth temperature (typically  $240\text{--}320^\circ\text{C}$ ) with a zinc flux present to ensure that any residual background selenium or sulphur does not react with the GaAs to form gallium selenide or sulphide, as these compounds would disrupt the subsequent II-VI epilayer growth [2.10, 2.11].

Prior to the introduction of the GaAs substrate into the chamber the movable ion gauge will be used to measure the fluxes produced by each cell in turn except for the magnesium – due to its interaction with the ion gauge and any elements coating it. The cell temperatures will then be adjusted to ensure the desired fluxes are being produced.



#### 2.1.1.1. Substrate Temperature Measurement

As the substrate is rotated during growth it is impossible to directly attach a thermocouple. Instead a thermocouple is placed behind the substrate heater (which is in turn mounted directly behind the molybdenum block the substrate is mounted on) and this is used to control the temperature of the substrate during growth. As the thermocouple is not in direct contact with the substrate, there will be an offset between its temperature and the substrates and this is problematic for the controlled growth of samples.

To solve this problem a pair of IR pyrometers are used. These are situated outside the chamber and focussed through a window onto the surface of the sample. The pyrometers are calibrated to measure the temperature of the substrate between the ranges 120-300°C and 350-800°C, with the high temperature pyrometer being used primarily during the GaAs heat clean and the low temp. during growth.

As the pyrometer must be calibrated for the emissivity of the material measured they are only accurate when looking at a GaAs (or other) substrate. The growth of II-VI material on the substrate is not a problem, as they are transparent at the wavelength the pyrometers measure, but the presence of deposited material (such as zinc or cadmium) on the window can be. For this reason typically the temperature measured by the thermocouple is calibrated using the pyrometer periodically, normally just after the pyrometer window has been cleaned, and this calibration is used to determine the actual temperature of the substrate.

#### 2.1.1.2. Magnesium Sulphide Growth

MgS is a very wide band gap ( $\geq 4.8$  eV) II-VI semiconductor with a lattice parameter (5.618Å) closely matched to ZnSe (5.668Å) and GaAs (5.6533Å) when grown in the zinc-blende (ZB) crystal structure and has proved to be an important barrier material for use in II-VI semiconductor structures [2.19, 2.20].

However MgS natural structure is rock-salt (RS) and as such when grown in the ZB phase it is meta-stable and will tend to relax to RS.

Many other research groups have tried to utilise MgS as a barrier material but encounter problems growing it due to the very high overpressures of sulphur required and its tendency to relax to the RS phase. This limits the thickness of MgS possible to a few nanometres, which is insufficient to provide either good electronic confinement or act as a sacrificial layer, as will be explained in chapter 4.

The MBE group at HWU uses a compound ZnS source to provide the sulphur in the growth of MgS and this has allowed layers up to 134nm to be grown [4.23]. The mechanism at work is believed to be that a ~0.5ML thick ZnS layer is constantly being deposited and the zinc in this layer is then replaced by magnesium through an exchange reaction [2.19].

The resultant MgS layers have been shown to contain less than 5% zinc, but the small amount of zinc present has been theorised to be what allows the growth of thick layers to be achieved [2.19]. The ability to grow thick layers of MgS has also allowed the group to measure a number of the material's bulk properties, such as its lattice constant ( $0.5622 \pm 0.0002\text{nm}$ ) and Poisson's ratio (0.425) [2.21].

#### 2.1.1.3. Growth Modes

The layers in each sample grown at HWU are typically produced using one of three growth modes: normal MBE growth, atomic layer epitaxy (ALE) or migration enhanced epitaxy (MEE). MBE is the standard growth mode used for most samples, here the shutters for all the cells necessary for a layer are opened together and then the thickness of the layer determined using a timer.

ALE is a modification of the MBE growth mode where instead of opening all the shutters at the same time, they are instead opened sequentially one at a time so that 0.5ML of each material (metal and non-metal) are deposited. This growth mode works best for binary materials, as it would be necessary to open the pairs of metallic and non-metallic shutters simultaneously for ternary and quaternary alloys, but this should be possible.

MEE is a further development of ALE where a pause is inserted between closing one shutter and opening the next to allow the deposited material to move around the surface so as to reduce the layers roughness.

#### 2.1.1.4. Growth Rate Determination

Where ever possible the growth rates of the materials produced at HWU are determined by growing a thick layer and then using reflectometry (or ellipsometry more recently – see section 2.2.4., 2.2.5. and chapter 6 for details) to determine its thickness and calculate a growth rate. Where this is not possible thin X-ray interference (XRI – see section 2.2.1 and chapter 5 for more details) samples are used as these avoid the difficulties of normalising the intensity of X-ray diffraction (XRD) peak from the layer to determine a thickness (see section 5.4 for further details).

#### 2.1.2. RHEED

RHEED is a very powerful tool for monitoring the surface of any structure being grown. As RHEED can be used throughout the entire growth it produces information about the whole structure. In RHEED a monochromatic beam of electrons diffracts from the surface of the sample at a shallow angle, see fig. 2.1. The shallow angle causes the electrons to penetrate only a few angstroms into the sample. The electrons are then diffracted by the periodic surface structure producing a pattern determined by the surface reconstruction.

As the RHEED beam only interacts with the crystals surface, its interaction can be considered in terms of 2D scattering only. This means that the Laue condition normal to the surface is relaxed and the reciprocal lattice points (the Fourier transform of the crystal lattice planes) become 1D rods. A RHEED pattern will be observed when these rods intersect the Ewald sphere of the electron beam [2.12, 2.13].

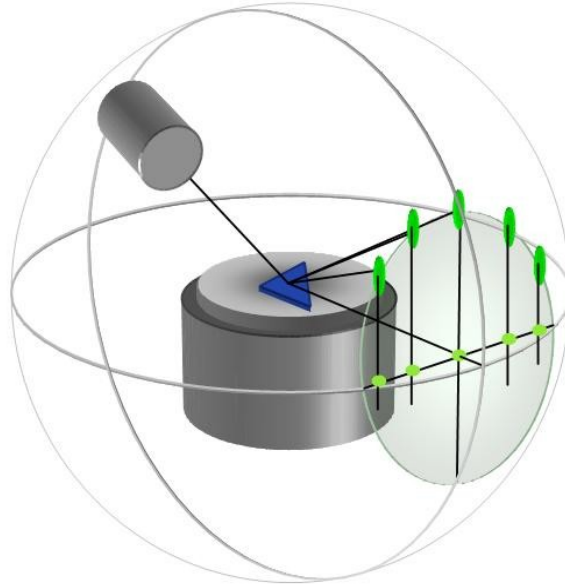


Fig. 2.1. Schematic of the interaction of the RHEED beam with a sample

The oxide layer on the surface of the substrate is amorphous and this results in a series of rings on the RHEED screen. During heat cleaning the RHEED pattern shows an extremely rapid transition from the amorphous pattern to a sharp 4x3 reconstruction along the  $[\bar{1} 1 0]$  crystal axis as expected for GaAs clean-up in a II-VI chamber [2.14]. This indicates that the oxide layer has been removed and the substrate is ready for growth [2.15].

During II-VI growth either a 2x1, c(2x2) or both reconstructions is seen. The c(2x2) is found on a metal (Zn or Cd) rich surface, while a 2x1 reconstruction indicates a non-metal (S or Se) rich surface and the presence of both indicates near stoichiometric growth[2.16-2.18]. If the initially streaky pattern changes to a series of spots, this indicates the growth mode changing from 2D to 3D growth, which can be seen during QD growth.

## 2.2. Characterisation Techniques

Sample characterisation in this thesis mainly involves five techniques: photoluminescence spectroscopy (PL), X-ray diffraction (XRD), spectroscopic ellipsometry (SE), reflectometry and optical transmission/absorption measurements. Results from other techniques (principally AFM or TEM) performed at HWU or other institutions will be used occasionally.

Both XRD and SE are able to determine structural information from the samples. However SE has not been used by the MBE group previously and the results presented in this thesis are the first obtained for samples grown at HWU. As such it will not be used throughout this thesis to characterise samples but instead all the results will be presented in chapter 6. The aim of this chapter is to develop SE so that it can be used as a general characterisation tool, as it will be shown to provide structural information that compliments XRD well.

PL measures the optical emission of a sample and produces a large amount of information about its electronic structure. It can be used to determine both the optical (and by extension structural) quality of a sample and its structure from the energy, FWHM and number of peaks in the emission spectrum [2.22-2.24]. By using high-NA lenses it is also possible to individually address objects as small as single-quantum dots, see chapter 7.

Reflectometry is in theory able to produce similar information to SE but it is not commonly used for this due to the difficulties of interpretation [2.25]. Here it will be used to measure the layer thicknesses, so that growth rates can be determined.

Transmission and absorption measurements can only be made from samples that have been removed from the substrate as GaAs (and other III-V substrates) absorb at the wavelengths of interest for II-VI compounds (~200-800nm) [2.26].

Once a sample has been removed from its substrate by measuring its absorption any optical transitions in the sample can be determined [2.27]. As a result this technique compliments PL well.

### **2.2.1. X-ray Diffraction (XRD)**

X-rays have a much shorter wavelength than light comparable to atomic spacings which allows the structure of samples to be investigated. There are two different x-ray techniques commonly used at HWU. The first technique is double crystal XRD, which determines the thickness and lattice constant of layers ~10-100nm thick. Thicker layers will also produce diffraction peaks, but as these layers are typically relaxed, this makes analysis harder [2.28, 2.29].

The second technique is X-ray interference (XRI) characterisation where a thin layer modulates the XRD peaks from the thicker cladding layers on either side. This allows the properties of the central layer to be determined without growing a layer thick enough to produce its own XRD peak. This technique has been used by the group for over 10 years and has produced a number of interesting results [2.30]. However recently this technique has been found to perform poorly with certain materials as will be discussed in chapters 5.

In theory it should be possible to produce reciprocal space maps using the XRD system at HWU. However as the system was not designed for this they are likely to be extremely poor quality and this combined with the control and modelling software not offering the ability to set-up and analyse these scans and the length of time each normal rocking curve scan takes (typically 8-16 hours) means this is not something that has been attempted.

#### **2.2.1.1. X-ray Theory**

XRD is similar to RHEED, as both techniques produce diffraction patterns from the interaction of the sample with photons or electrons. The major difference

with XRD is that the X-ray photons will interact with the samples to a depth  $>1\mu\text{m}$ , so the analysis must be performed in 3D rather than 2D based either on the kinematic model or the more accurate but computationally intensive dynamical model [2.31, 2.32].

The interaction of the X-ray photons with the atoms in the crystal produces a spherical scattering wave which spreads out from each atom to produce a diffraction pattern. A rocking curve (XRD) plot is produced by measuring the intensity of the diffracted X-rays as a function of the incident angle.

As the layers in a sample have a finite thickness the 3<sup>rd</sup> Laue condition is relaxed causing the diffracted peaks to become broadened as they are no longer points in reciprocal space [2.31]. For structures with two or more layers the broad diffractions peaks will interfere producing a more complex diffraction pattern and as a result dynamical rather kinematic modelling needs to be used, at HWU this is handled by the use of the BEDE RADS software. A full explanation of dynamical X-ray modelling can be found in ref. [2.31].

The RADS simulations are compared with the experimental data using a goodness of fit (GOF) merit figure and information about strain, layer thickness and composition can be determined. The GOF figure is a chi-squared statistic (see equation 1) that ranges from 0-1, where 0 would represent a perfect match.

$$\chi^2 = \sum_{i=j}^k [\log(y_i^{\text{ref}}) - \log(y_i^{\text{comp}})]^2 \quad (1)$$

where,  $y^{\text{ref}}$  is the ordinate of the reference data and  $y^{\text{comp}}$  is the ordinate of the comparison, and  $j$  and  $k$  are the indices of the first and last points defining the overlapping of the two data sets.

#### 2.2.1.2. HWU X-ray system

The HWU X-ray system is shown schematically in figure 2.2 and consists of an

X-ray source, a beam conditioner (to produce a monochromatic and highly collimated beam, not shown in the schematic) and a computer controlled stage on which the sample is mounted. The mount allows the sample to be translated in the x and y direction and rotated in 3 independent azimuths, so that it can be accurately aligned to the incident x-rays at the correct orientation. Typically at HWU only 004 and 115 scans are used, as these are the most intense symmetric and asymmetric reflections for the zinc-blende (ZB) structure [2.32].

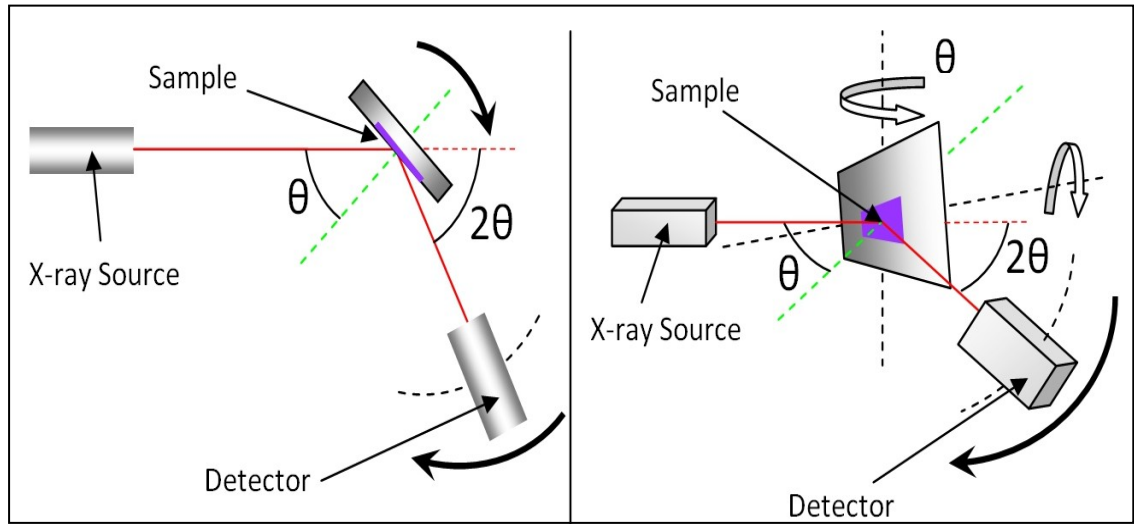


Fig. 2.2 – Schematic of the operation of X-ray set-up. Red lines show beam path and the green line the normal to the sample surface.

### 2.2.2. Photo-Luminescence Spectroscopy (PL)

PL gives the below bandgap luminescence spectrum of a sample which contains information about the structural properties of a sample including the presence of any dislocations or point defects. Samples are excited by an above band gap light source and then the emitted light is spectrally analysed.

PL measurements in this thesis were typically made at 77K where the emission from a defect free II-VI semiconductor is dominated by excitonic emission, the bound state of an e-h pair and therefore at an emission energy lower than the free e-h pair emission. The difference in energy is the exciton binding energy ( $E_B^X$ ) and is typically 10-30meV in a II-VI semiconductor [2.23, 2.33]. Other bound states, such as trions or biexcitons, are also possible [2.34].



Trions are composed of an exciton coupled to either an additional electron or hole and therefore typically have a lower emission energy than the exciton (the difference is again their binding energy,  $E_B^{CX}$ ). However in some materials trions exist in an unstable anti-bound state where their emission is only seen under intense excitation at a higher energy than the exciton [2.30]. Biexcitons are the bound state of two excitons and emit at a lower energy than either the exciton or trion, with the difference from the exciton being their binding energy ( $E_B^{XX}$ ). More complex states, such as charged biexcitons or triexcitons are composed of more than four charge carriers ( $>2e-h$  pairs) and will have at least one carrier occupying the 2p level. This splits their emission into sub-levels and causes them to often exist in anti-binding regimes making them less likely to be observed [2.35].

In the case of a bulk or thick layer samples the PL emission is often dominated by other states where the exciton is bound to impurities in the material, termed donor or acceptor bound excitons, or dislocations. These states have lower energies than the exciton and by observing their intensity and temperature dependence it is possible to determine their origin [2.22, 2.36].

For quantum wells (QW) and quantum dots (QD) the emitted light will be at a wavelength which is a function of both the material and the size of the quantum well or dot. It is therefore possible in conjunction with other measurements (XRD etc.) to determine both the dimensions and composition of QWs and QDs.

#### 2.2.2.1. PL Setup

Several different PL set-ups have been used to make the measurements in this thesis. However the majority of the measurements were made using the one shown schematically in fig. 2.3. The pump source is the 351nm (3.53eV) line of an argon ion ( $Ar^+$ ) laser. This is coupled into a LN2 cryostat containing the sample using a 0.36 NA lens, producing a pump spot  $\sim 975$ nm in diameter and imaging an area 1-2 $\mu$ m in diameter. The same lens is then used to collimate the emitted light into a Spex 1402 0.75m double monochromator attached to a

cooled photomultiplier tube and a lock-in amplifier. This equipment, although over 25 years old and slow, is capable of extremely good signal-to-noise ratios and high resolutions (down to 0.006nm,  $\sim 30\mu\text{eV}$ ).

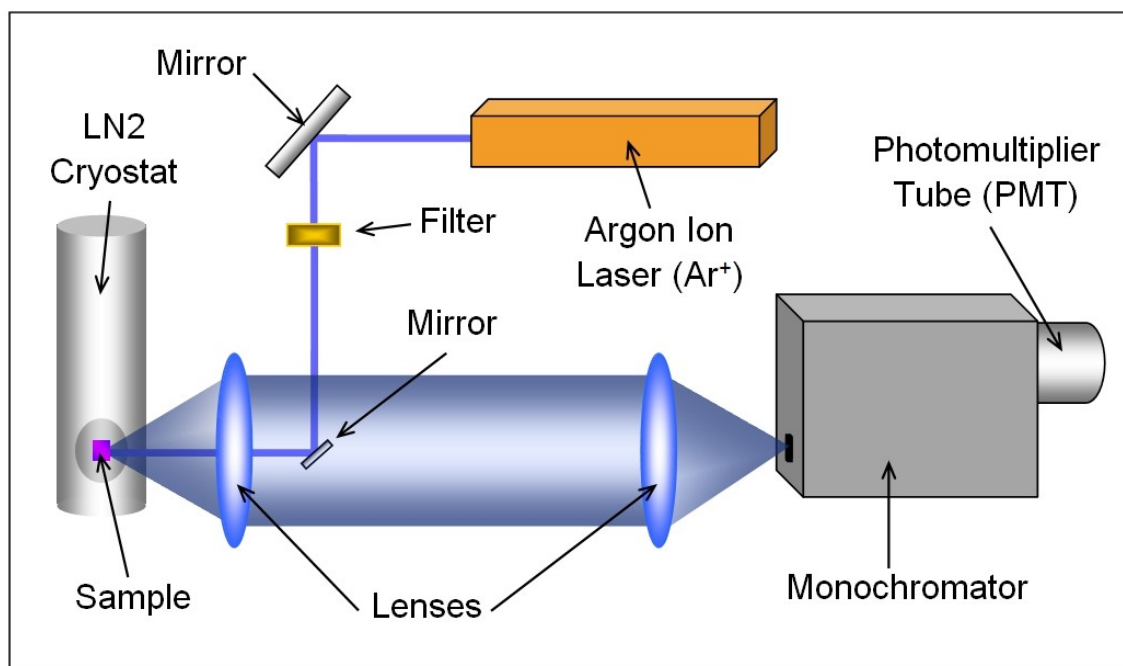


Fig. 2.3 – Optical setup used for photo-luminescence measurements

During this thesis equipment changed as items became unserviceable. Initially the argon ion laser was replaced with a 405nm (3.06eV) laser diode, but eventually the monochromator and PMT also had to be replaced with a 100mm focal length fibre coupled monochromator and CCD detector. This eventual arrangement has a much lower resolution ( $\sim 1.5\text{meV}$  vs.  $30\mu\text{eV}$ ) and lower signal-to-noise ratio, but is capable of taking continuous readings across the entire wavelength range typically measured, 400-800nm.

The majority of the ensemble PL measurements were made with the sample cooled to 77K using the LN2 cryostat. This was done to improve the emission intensity, when compared to room temperature and due to the high cost and handling difficulty of liquid helium. This results in the measured emission energies being different to those reported in most papers (which are typically made at 2-10K) but for the majority of samples this is not a problem as the variation of the bandgap with temperature is well known [2.37, 2.38].

#### 2.2.2.2. $\mu$ -PL Setup

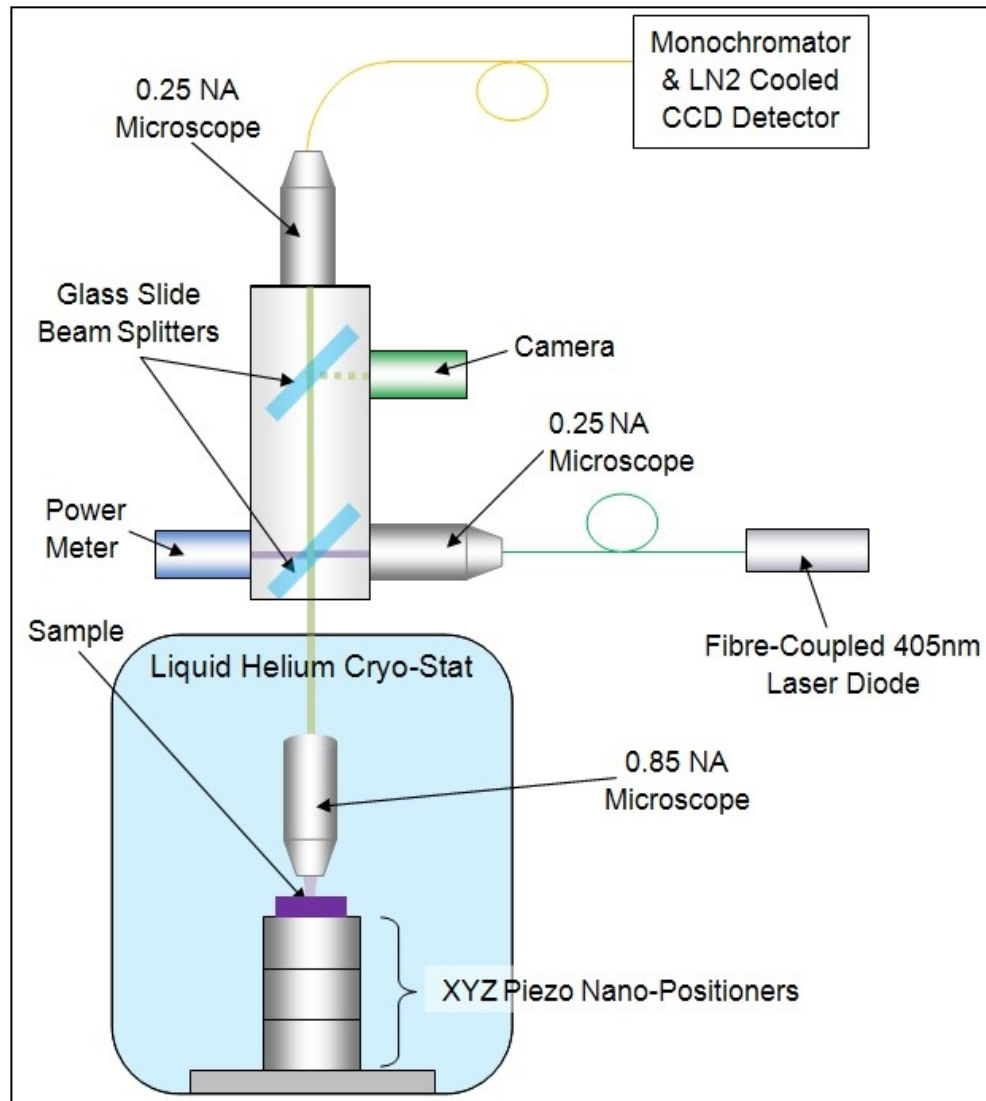


Fig. 2.4. Schematic of the  $\mu$ -photo-luminescence setup

$\mu$ -PL measurements were made using a diffraction limited confocal microscope system with the samples mounted on piezo-electric XYZ nano-positioners in a liquid helium dewar/cryostat, see fig. 2.4. The samples were excited by a 40mW fibre-coupled 405nm (3.06eV) laser diode. Two Brewster angled glass slides were used as beam splitters ensuring that 96% of the emitted light was coupled into the fibre to the monochromator. The monochromator is a Princeton Instrument SP2500 500mm focal length model coupled to a liquid nitrogen cooled CCD detector. This setup has an extremely high signal-to-noise ratio and is capable of a resolution of 0.02nm ( $\sim 90\mu\text{eV}$ ). The XYZ piezo nano-positioners manufactured by Attocube, are capable of moving the sample around under the microscope objective in sub-nm steps, which is necessary if QDs and other nano-structures are to be imaged. During measurements either a 0.85 NA

microscope objective or a 1.3 NA solid immersion and aspheric lens combination was used to focus light onto the sample. These resolve spots ~600 and 400nm diameter respectively [2.39].

### 2.2.3. Transmission/Absorption Measurements

The majority of the transmission measurements presented in this thesis were obtained using a Shimadzu UV-3100 UV/visible/NIR spectrometer, see fig. 2.5. Both a tungsten halide and a deuterium lamp are available and combined with a photomultiplier tube and InGaAs and PbS photodiodes, a spectral range from 190-3200nm (0.39-6.5eV) can be generated and detected. However as the spectrometer is not fitted with either a vacuum or nitrogen purging system, the usable range is limited (by atmospheric absorption) to wavelengths longer than ~240nm (5.7 eV). The emission is split into two beams, with one passing through the sample while the other acts as a reference beam.

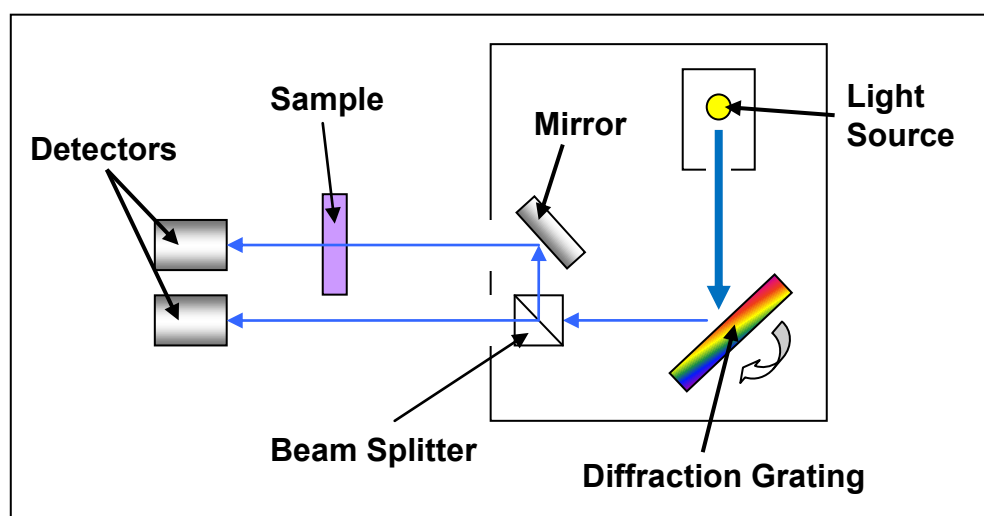


Fig. 2.5 Shimadzu spectrometer in transmission/absorption mode.

Transmission/absorption measurements can be used to measure both the band gap and optical thickness of a sample and from this it is possible to calculate its refractive index using the Kramers-Kronig relation [2.40]. However this method is far less accurate than ellipsometry and was not used in this thesis.

### 2.2.4. Reflectometry

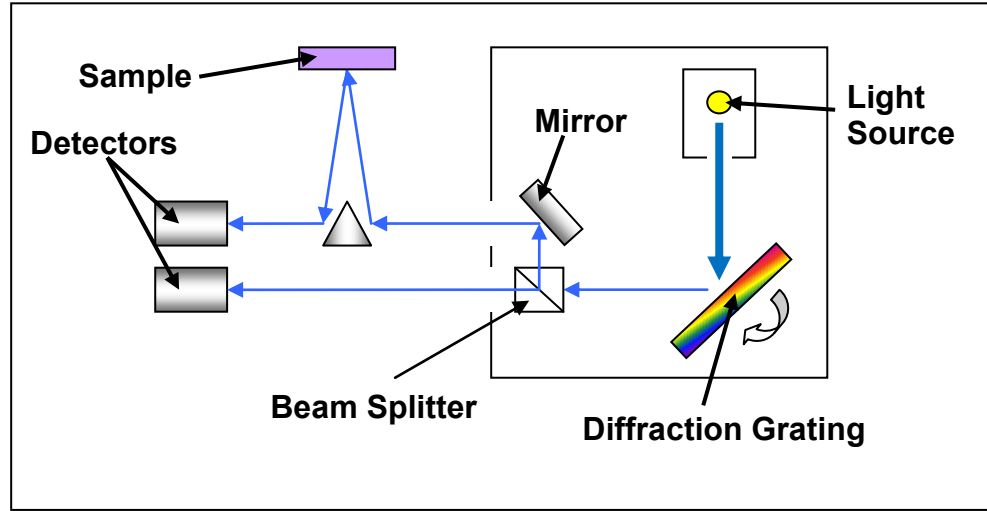


Fig. 2.6 – Schematic of the Shimadzu spectrometer

The Shimadzu UV-3100 spectrometer can also be used in reflection mode, see fig. 2.6. It produces near normal reflections from the sample and by plotting the variation of the reflectivity of the sample versus wavelength for the wavelength region between the bandgaps of the overlayer and the substrate (~450-800nm for ZnSe on GaAs), the optical thickness of the overlayer (the product of its physical thickness and refractive index) can be determined. If the dispersion of the overlayer ( $n(\lambda)$ ) is known, as is the case for ZnSe [2.41-2.45], then it is straightforward to determine the physical thickness ( $d$ ) using equation 2.

$$d = \frac{\lambda_1 \cdot \lambda_2}{2 \cdot (n(\lambda_2) \cdot \lambda_1 - n(\lambda_1) \cdot \lambda_2)} \quad (2)$$

It should also be possible to determine the thicknesses of the various layers in a multi-layer structure by this method. However as there will be a large number of reflections from all of the interfaces between the various layers and many will be weak, finding an accurate and unique solution would require significant data analysis. Therefore the additional information generated by SE makes it a better method for this sort of structure.

### 2.2.5. Spectroscopic Ellipsometry

Spectroscopic ellipsometry (SE) is a non-destructive, optical characterisation

technique for samples. It measures both the intensity and polarization of light incident on a sample and is therefore sensitive to a wide range of different properties: layer and sample thicknesses, composition, crystallinity, surface and interface roughness, refractive index and material uniformity, and others.

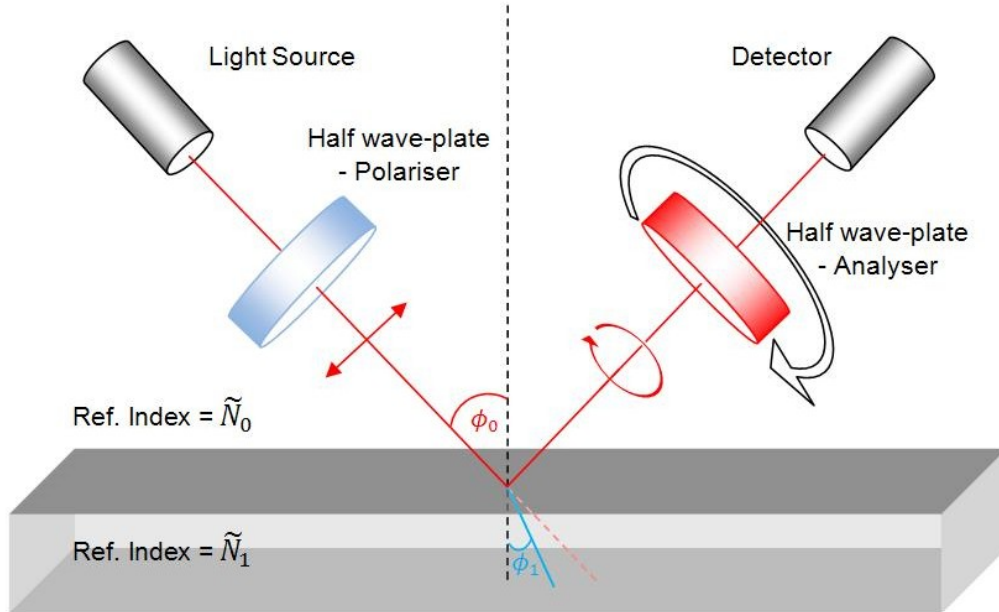


Fig. 2.7. Schematic of a rotating analyser ellipsometer. Red lines show the beam path and the black dashed line the normal to the surface

Figure 2.7 shows the schematic of an ellipsometer. The light source used can either be single wavelength or a broadband source and monochromator. Light from the source is passed through a half wave-plate polariser and then focussed on a sample at a variable angle of incidence, typically around  $70^\circ$ . The incident light is reflected and passes through a second half wave-plate (the analyser) in front of the detector. The polariser and analyser angles are adjusted to locate the maximum and then minimum reflected light intensities.

From the angles of the polariser and analyser the phase shift between the  $p$  and  $s$  polarisations of the incident light,  $\Delta$ , and the magnitude of the ratio of the complex reflection coefficients,  $\psi$ , can be calculated. These are then used to calculate the complex reflectance ratio,  $\rho$ .

$$\rho = \tan \psi \cdot e^{i\Delta} \quad (3)$$

For bulk material this is simply the product of the materials refractive indexes and hence it is possible to calculate the refractive index of the material using

equation 4. Where  $\tilde{N} = n + ik$  and  $\phi$  is the angle of incidence.

$$\tilde{N} = \sin \phi_0 \sqrt{1 + \left( \frac{1-\rho}{1+\rho} \right)^2 \cdot \tan^2 \phi_0} \quad (4)$$

However it is only possible determine  $n$  and  $k$  directly from  $\rho$  for samples that are isotropic, homogeneous and infinitely thick. Even in the case of substrates all of these conditions may not be met, as although they are usually 350-1000nm thick, they typically have a thin (1-5nm) oxide layer, which will have a different optical response to the bulk material.

This inability to directly calculate the optical properties means that it is necessary to model each sample and then optimise any unknown parameters to produce a fit to the measured data. As will be explained later in this thesis, this is complicated for even simple samples and the only way to gain useful data for new compounds whose properties are unknown is to make sure all the properties of the other materials in the structure are known.

Figure 2.8 shows an example of a two layer structure. To model this it is necessary to use Airy functions, which are an extension of the Fresnel equations with the addition of a phase factor,  $\beta$ , to account for the additional interface between the two layers.

$$\beta = \frac{2 \cdot \pi \cdot d_1 \cdot \tilde{N} \cdot \cos \phi_1}{\lambda} \quad (5)$$

This further complicates the calculation of the refractive index of the overlayers and makes direct calculation from  $\rho$  almost impossible. Therefore it is again necessary to model the structure and compare this to the measured data. In cases with more than two layers it is convenient to use a matrix representation of the incident, transmitted and reflected light to account for the multiple reflection and transmission components to be accounted for [2.46, 2.47].

The modelling and analysis in this thesis was undertaken using a number of different computer modelling packages; J. A. Woollams CompleteEASE and

WVASE32, as well as the open-source RegressPRO developed by Francesco Abbate. All of these programs operate in a similar way, the user first inputs a measured ellipsometric spectra and then creates a layer by layer model of the sample, from which the software then calculates the  $\psi$  and  $\Delta$  values for each wavelength and angle of incidence (AOI).

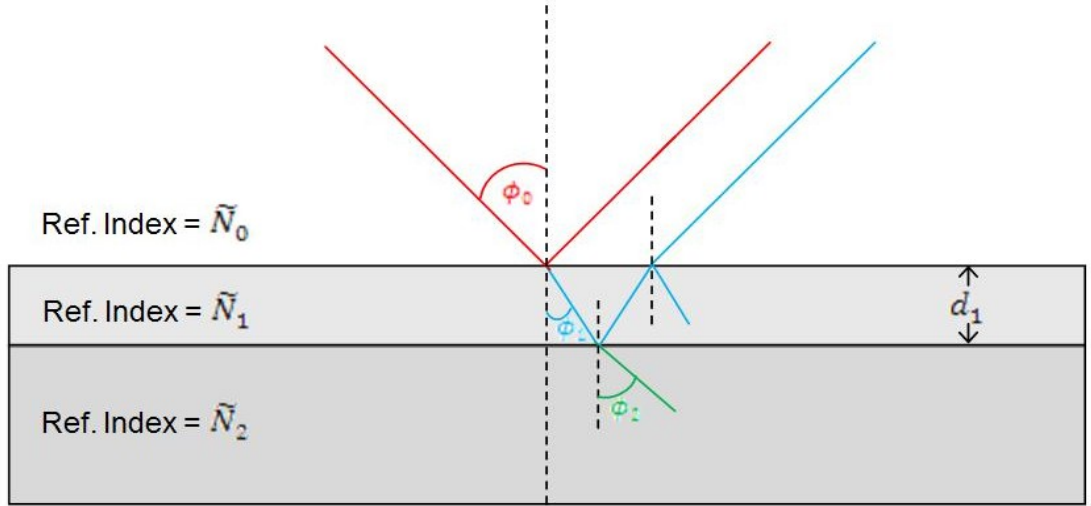


Fig. 2.8. Interaction of a light ray with a multilayer sample. Coloured lines show the incident and reflected light at each interface and the dashed black lines are the normals to interfaces.

The calculated values can then be compared to the measured values and an error value calculated. All of the software packages use the mean-squared error (MSE)/  $\chi^2$  value, as a figure of merit calculated using equation 6.

$$\chi^2 = \frac{1}{N \cdot M - m - 1} \sum_{j=1}^M \sum_{i=1}^N \frac{[\rho_{j,\text{exp}}(\lambda_i) - \rho_{j,\text{calc}}(\lambda_i)]^2}{\sigma_j(\lambda_i)^2} \quad (6)$$

Where  $\rho_{j,\text{exp}}$ ,  $\rho_{j,\text{calc}}$  and  $\sigma_j$  represent the experimental, calculated and error quantities at wavelength,  $\lambda_i$  and data set  $j$ , while  $N$  is the total number of data points,  $m$  is the number of fitted parameters and  $M$  is the number of data sets.

Each software package refines the model to produce a lower MSE in a slightly different way, with RegressPRO offering the greatest flexibility in defining how the model should be refined at the cost of some added complexity. However the result from each package is the same, if properly used the model structure converges on the closest approximation to the actual sample possible.



Multilayer samples have a large number of independent parameters which means the choice of initial model is highly important, as if it differs too much from the actual structure, the optimisation process can find a local minima rather than the true minimum. It is therefore necessary to make sure that the structure is reasonably well understood from other measurements (AFM, X-ray and PL) before its modelled.

The optical constants of the layers in a model can be defined in a number of ways; the simplest is tabulated data representing the values of  $n$  and  $k$  for various energy or wavelength values. The restriction imposed by this is that it is then impossible to vary these values. For well characterised materials this is not a problem, but in the case of the compounds described in this thesis there are often a range of published values.

To allow the values of  $n$  and  $k$  to be varied easily they must be defined as a function. For transparent dielectric materials empirical Cauchy or Sellmeier equations, equations 8 and 9 are typically used [2.48-2.52].

$$n(\lambda) = A + \frac{B}{\lambda^2} + \frac{C}{\lambda^4} + \dots \quad (7)$$

$$n(\lambda) = \sqrt{A + \frac{B \cdot \lambda^2}{\lambda^2 - C} + \frac{D \cdot \lambda^2}{\lambda^2 - E} + \frac{F \cdot \lambda^2}{\lambda^2 - G}} \quad (8)$$

Here A, B, C etc. are empirical constants that have been determined for a particular material and  $\lambda$  is the wavelength (in  $\mu\text{m}$ ). The Cauchy relation, handles absorption by introducing an additional terms such as a Tauc or Cody relation. An example is given in equation 9, where E is the incident photon energy,  $\alpha$  is the extinction coefficient amplitude,  $\beta$  is the exponent factor and  $E_0$  is the bandgap/edge. Other simple mathematical models have been derived to describe the dispersion of other material (Drude, Forouhi and Bloomer [2.53-2.55]), but are less commonly used.

$$k(E) = \alpha \cdot \exp^{-\beta \cdot (E - E_0)} \quad (9)$$

If the incident photon energy is equal to or greater than the band-gap of a

semiconductor, modelling is harder as the electronic transitions introduce their own features (critical points) into the dispersion. An example of this for ZnSe is shown in figure 2.9; the red and blue lines represent the sum of the components and the open and closed circles the measured values.

For the above band-gap region there are again a number of ways to model the dispersion of the semiconductor. However most of them are based around the summation of a series of oscillators, a multiple oscillator (MO) scheme. This has the benefits of allowing physically meaningful parameters to be used and modelling a broad energy range with one expression. MO models typically use harmonic, Gaussian or Lorentzian oscillators [2.43, 2.56, 2.57].

A single effective oscillator (SEO) model, often based around the work of Wemple and DiDomenico [2.58]), can also be used. These model a narrower energy range than a proper MO model, but can model both the below and near band-gap regions of a semiconductor.

The final layer modelling option is to use wavelength-by-wavelength point inversion (PI), resulting in the fitting software calculating the best value at each point without concern for continuity. This PI process will produce very low MSE values but can be more prone to errors due to the lack of continuity.

Layers can also be modelled as a mixture of materials. In this thesis this will be through the use of a Bruggeman effective medium approximation (BEMA) [2.59]. The composition of this mixed layer can be formed by any of the other layer types already discussed, but here is limited to tabulated data for the materials, so as to avoid needlessly complex models.

During the work in this thesis measurements were made using a J.A. Woollam vertical-VASE (Variable Angle Spectroscopic Ellipsometer), a more complex

type of ellipsometer than the one shown in figure 2.7, but whose operation is in principle the same.

### 3. Spin Current Detector

This chapter details the growth and characterisation of a series of samples produced for a collaboration with the Experimental Semiconductor Physics (ESP) group at the Philipps-Universität Marburg to develop a spin current detector (SCD). The samples were all grown and structurally characterised at HWU before being sent to Marburg for further study.

A brief introduction to the field of spintronics will be presented in section 3.1, including its potential uses and impact on the design of future electronic devices. Both spin current generation and detection will be discussed with particular emphasis made to the potential role of II-VI semiconductors.

Section 3.2 contains the details of the growth and characterisation of the first series of SCD samples.

Sections 3.3 will explain the details of the growth and characterisation of both the second series of SCD samples and a series of ZnSe rich ZnMgSSe alloy calibration samples grown for them.

Section 3.4 will describe the problems with the design of the SCD samples and finally section 3.5 will conclude all the work.

#### 3.1. Introduction

Since the production of the first transistor in 1947 [3.1], semiconductors have grown to become an industry worth approximately \$300 billion annually [3.2]. A large part of this huge growth has been the explosion in the use of the electronic equipment that utilises semiconductors and chief amongst these, the personal computer.

At the heart of every computer is a silicon micro-processor and over the last 30 years these have been developed to offer progressively higher and higher performance and reduced power consumption. To achieve this improvement in performance the feature size of the transistors inside the semiconductor chips has continuously been reduced (currently commercial available processors have transistors with a feature size of 22nm) as is encapsulated by the ever-used 'Moore's Law' [3.3]. However this development is rapidly approaching the limits of current silicon technology and it will soon be necessary to start looking to other technologies if it is to continue at the same pace [3.4].

Spintronics is one possible route to allow this development to continue beyond current limits, as it uses the spin of an electron rather than its charge and so should allow further performance improvements without further reduction in feature size [3.5]. However there are still a large number of technical challenges that must be met before this can become a reality. But as a solution to the coming crisis is required, spintronics may prove to be an extremely important field of research.

### **3.1.1. Spintronics**

As well as the interest in using spintronics to improve computer processors and other electronic systems performance, it may also offer a route to develop a range of other interesting technologies including single photon sources and a route to practical quantum computing [3.6-3.9]. II-VI semiconductors are also showing significant promise in this area, primarily due to their long spin decoherence time (which is a necessity if useful spintronic devices are to be realised [3.10, 3.11]) and hence is an area that may become important to the MBE group at HWU.

Spintronics is said to have begun with the discovery of giant magnetoresistance (GMR) effect in 1988 [3.12]. The discovery of GMR had huge effect on the development of hard disk drives resulting in a significant increase in the

data storage densities possible [3.13] and hints at the potential of spintronics to advance other areas of information technology [3.14].

Currently the real area of interest is the development of new materials that either possess both magnetic and semiconductor properties or can be readily integrated with current semiconductor materials [3.15]. One of the main issues affecting this development thus far has been differences in crystal structure and chemical bonding between existing semiconductor materials and those being developed [3.16, 3.17]. An ideal semiconductor material for spin generation or alignment would be lattice matched to a common substrate (GaAs, InP etc.), have a Curie temperature above room temperature and would be able to incorporate both p and n dopants.

Early work, both at HWU and elsewhere, focussed on introducing magnetic atom,  $\text{Mn}^{2+}$  for example, into a semiconductor matrix. These dilute magnetic semiconductors (DMS) showed a lot of promise, as GaMnAs and others were calculated to have Curie temperatures above room temperature, but this was not found to be the case experimentally. However some have been exploited to act as spin aligner with efficiencies of up to 90% [3.18].

The MBE group at Heriot-Watt has previously developed MnS and CrS materials for possible applications in spintronics [3.19-3.22]. However they both proved difficult to work with as they do not comfortably lattice match with any common substrate material – MnS is -1.12% lattice mismatched to GaAs and CrS is mismatched -1.81% to GaP. The intention was to continue the development of these sulphide materials to eventually grow iron sulphide (FeS) on GaP, as it is only -0.57% lattice mismatched. However a range of factors, including the difficulty of working with GaP substrates in a II-VI MBE system have caused this work to be halted at present. Another interesting material that may be of significant interest in the generation of spin currents is chromium selenide, CrSe, as this has been predicted to be half-metallic when grown in the ZB phase and have a lattice constant close to GaAs [3.23].

As well as developing materials to help generate spin currents in semiconductors, it will also be necessary to develop technologies to allow the encoded information to be extracted. One possible route to achieving this would be to grow a ‘spin-LED’ where the spin current is converted to a polarised optical emission[3.24], as It would then simply be a matter of determining the polarisation of the light to extract the information. Another alternative is (as will be described here) the growth of a unique spin current detector structure.

### 3.1.2. Spin Current Detector

The SCD structure converts the spin current into different wavelengths of light depending on their polarisation. This is achieved by the structure having two quantum wells at opposite ends of the absorption region such that when the spin currents separate the up and down spin polarised carriers will end up in different QWs causing the emission of a different wavelength of light depending on the polarisation of the carriers [3.25].

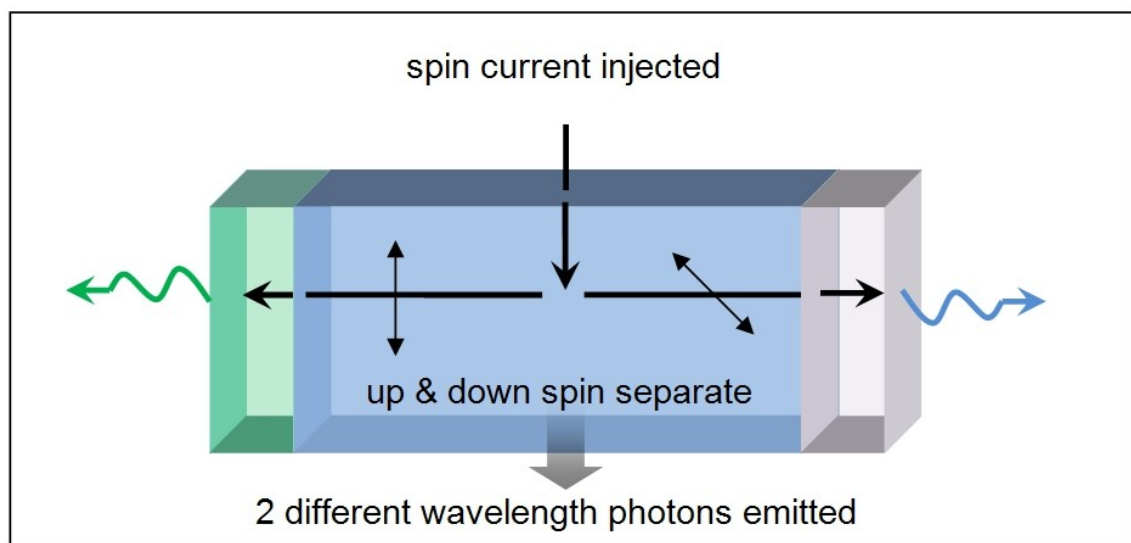


Fig. 3.1. Schematic representation of the spin current detectors operation. The blue region represents the absorption region, the grey and green regions the two quantum wells. The different spin polarised currents are shown separating and moving into the two QWs where they emit different wavelengths of light.

In a practical device the spin current would be generated using either a spin generation or aligning layer, but for the work presented here the current was to be generated optically. However the technology is independent of the technique used to generate the current and hence could be adapted to other structures where spin currents can be generated or manipulated.

To achieve this optical spin current generation the circularly polarised fundamental and 2<sup>nd</sup> harmonic light (at 800nm and 400nm respectively) from a Ti:Sapphire laser is introduced into a ~100nm wide ZnSe absorption region in the middle of the detector (the blue region in fig. 3.1). The two beams are then absorbed through single and two-photon absorption processes and by controlling their intensities, it is possible to generate a current through quantum interference control (QUIC) that can be of the order of several KA/cm<sup>2</sup> [3.25]. The circularly polarised photons generated spin polarised carriers through spin orbit coupling and the optical selection rules, and in combination with QUIC this can produce spin currents that will separate inside the absorption region without an external field being applied [3.25].

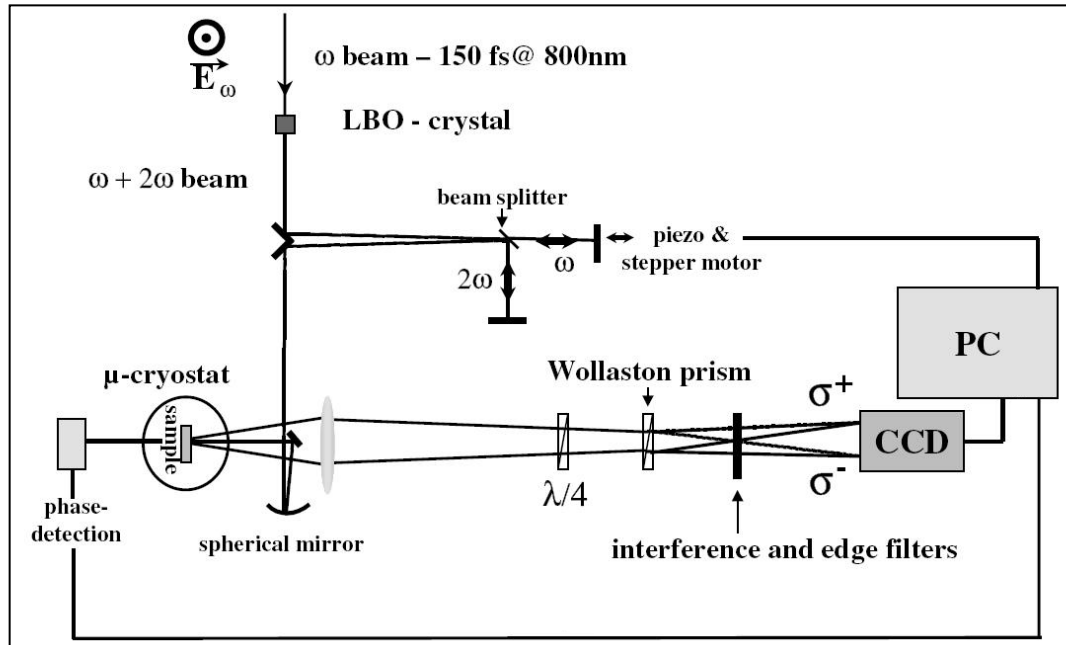


Fig. 3.2. Optical set-up for the generation & detection of spin currents in spin current detector structure [adapted from 3.25]. Description of optical set-up given below

Fig. 3.2 shows the experimental set-up that is used for the optical generation of spin currents. The fundamental (800nm) light from the Ti:Sapphire laser is passed through an LBO frequency doubling crystal (lithium-borate, LBO) converting a proportion of the 800nm light to 400nm. These two beams are then propagated through a beam splitter at near normal incident and then reflected from 2 different mirrors. The mirror that reflects the 800nm light is mounted on a piezo and stepper motor mount that allows its position to be changed, which allows a delay to be added to the 800nm pulses with respect to the 400nm. This allows the relative intensities of the two beams in the sample to be changed.



The two beams are then focused onto a small mirror in line with the sample by a spherical mirror and this then reflects the beam onto the surface of the sample.

The emitted light from the sample is then collected by a large numerical aperture (NA) lens, passed through a quarter waveplate and then a Wollaston prism to spatially separate the wavelengths of emitted light. The two separated beams are then passed through a series of filter and then measured using a pair of CCDs.

## 3.2. Spin Current Detector

Three structures (SCD 1, 2 and 3) were designed for this project and differ only in the choice of internal barrier and well material (see fig. 3.5 and 3.12 for schematics for SCD1 and 2). SCD3 was to have ZnMgSSe barriers and ZnSe QWs, but was never grown due to problems discovered with the SCD1 and 2 samples, as will be discussed later in this chapter.

### 3.2.1. Structure and Growth of SCD1

The structure for SCD 1 is shown in fig. 3.3. The structure is capped with a ZnSSe layer to protect the MgS barriers from oxidation. The whole structure was grown on a standard GaAs substrate with a 50nm ZnSe buffer layer by our standard growth procedure.

The width and cadmium concentration of the two QWs needed to be calibrated to produce emissions at 50 and 100 meV below the ZnSe band gap emission ( $\sim 2.68$  eV @ 300K). These emission energies were selected to ensure that the device would be an efficient emitter and that QW emission was energetically far enough from the ZnSe peak that they do not overlap.

ZnSSe Cap – 5nm
MgS Barrier – 5nm
<b>ZnCdSe Well – 4-5nm</b>
ZnSSe Barrier – 20nm
ZnSe Absorption Region ~ 100nm
ZnSSe Barrier – 20nm
<b>ZnCdSe Well – 10-12nm</b>
MgS Barrier – 5nm
ZnSe Buffer Layer – 30nm
GaAs Substrate

Fig. 3.3. Spin Current Detector 1 structure. The two ZnCdSe QWs are shaded in green and blue.

The internal ZnSSe barriers were designed to be ~100 meV above the ZnSe band gap to provide sufficient confinement for good optical emission while also allowing the carriers generated in the absorption region to pass into the QWs. This requires ~15% sulphur to be incorporated into the barrier. The absorption region was chosen to be ~100 nm wide as this is approaching the critical thickness for ZnSe relaxation due to the strain energy introduced by the ZnSe/GaAs lattice mismatch of 0.26% [3.26].

During growth it was necessary to change the ZnS cell temperature to allow the internal ZnSSe barriers, MgS and ZnSSe Cap layers to be grown with differing sulphur molar fractions. This required three growth interruptions to allow the cell temperature to be changed and stabilise. However in leaving the sample at growth temperature during these interruptions, the surface can become damaged either by material desorbing from the surface or stray atoms absorbing on to it. To try to prevent this a selenium flux was applied throughout the interruption.

To achieve the correct emission energy a series of samples had to be grown. During the growth of all these samples, the RHEED pattern observed was strong and streaky throughout and consistent with smooth, epitaxial growth.

There was also no observable deterioration of the RHEED pattern during the growth interruptions, suggesting that the application of selenium flux was sufficient to protect the surface from damage.

### 3.2.2. PL Characterisation

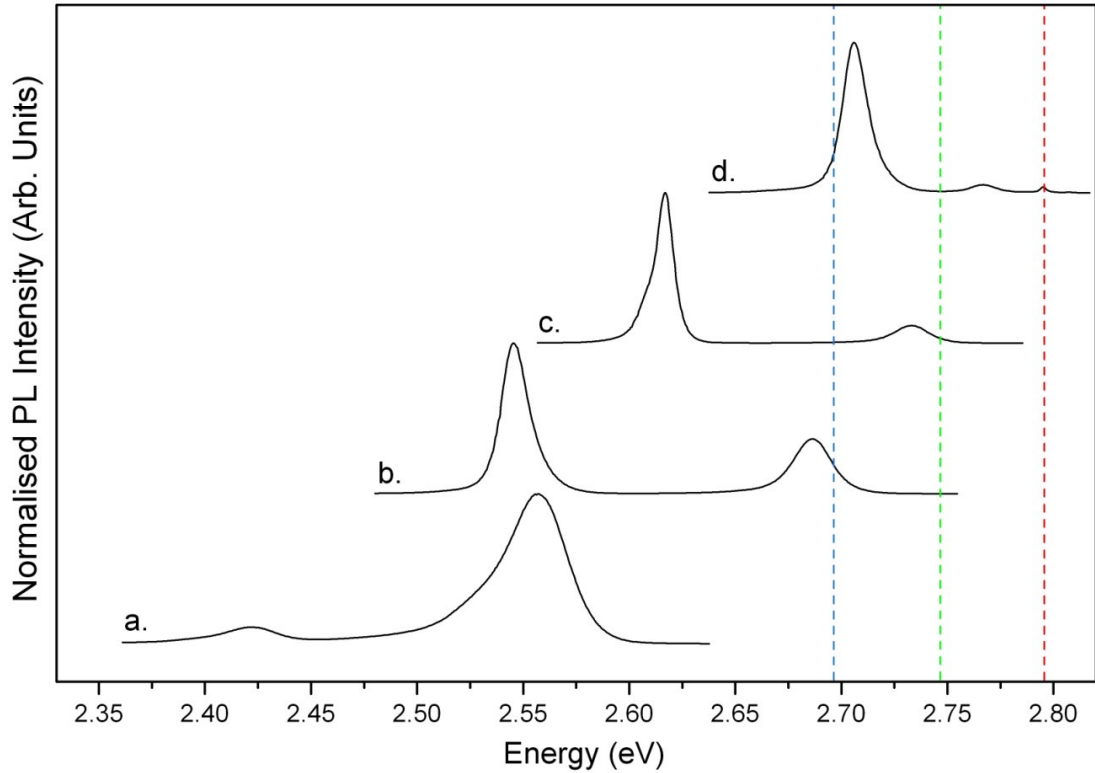


Fig. 3.4. PL Comparison of SCD1 samples – HWC211 (a), 219(b), 221(c) and 222(d). The red line shows the 77K bandgap of ZnSe. The green and blue lines show the intended ZnCdSe QW emission energies, 50 and 100meV below the ZnSe emission respectively.

All the emission from all the SCD1 samples were measured at 77K using the original PL arrangement ( $\text{Ar}^+$  laser and PMT tube) and found to show two (or 3 in the case of HWC222) distinct emission peaks, see fig. 3.4. The peak emission values, FWHM and relative intensities are shown in table 3.1. The emission from all of the samples was bright (compared to the wide QW in section 3.22) due to enhanced confinement provided by the ZnSSe barriers.

The emission from HWC222 was determined to be at 2.707 and 2.767eV, separated from the ZnSe peak at 2.795eV by 88.5 and 28.3meV respectively. Although these are less than the 50and 100meV gaps intended, as both peaks are distinct from the ZnSe peak, they are sufficient the SCD to function.

HWC	Peak 1			Peak 2			Peak 3		
	Energy (eV)	FWHM (meV)	Rel. Int.	Energy (eV)	FWHM (meV)	Rel. Int.	Energy (eV)	FWHM (meV)	Rel. Int.
211	2.421	23.7	0.11	2.556	23.5	1.00	-	-	-
219	2.546	15.9	1.00	2.686	22.1	0.37	-	-	-
221	2.616	10.7	1.00	2.733	19.2	0.12	-	-	-
222	2.707	14.4	1.00	2.767	14.4	0.05	2.795	3.37	0.04

Table 3.1. PL emission characteristics of the SCD1 samples.

### 3.2.3. XRD Characterisation

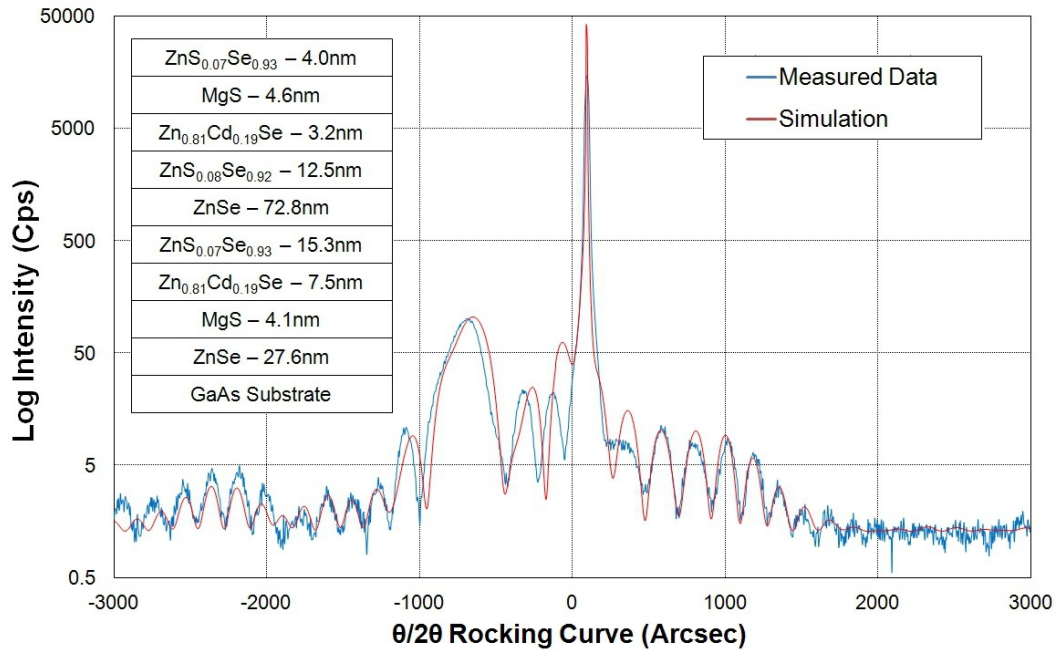


Fig. 3.5. Measured (blue line) and modelled (red line) 004 XRD rocking curve for HWC221, a SCD1 sample. The structure used for the modelling is inset.

Figure 3.5 shows the measured and modelled 004 XRD data for HWC221, which are representative of SCD1 samples grown. The structure used for the modelling is shown inset. The model returned a GOF of 0.164, which is large, but this is due to the complexity of the structure and the large number of peaks rather than a poor fit. The measured spectra are also sharp, consistent with the sample being fully strained. The results of the modelling of HWC211 and 221 are shown in table 3.2.

# HWC	$G_R$ ( $\text{\AA}/s$ )				Composition		GOF
	ZnSe	MgS	ZnCdSe	ZnSSe	$\text{ZnS}_x\text{Se}_{1-x}$	$\text{Zn}_{1-x}\text{Cd}_x\text{Se}$	
211	0.41	0.38	0.56	0.50	0.08	0.23	0.167
221	0.43	0.36	0.58	0.49	0.07	0.19	0.164

Table 3.2. SCD2 sample structural properties.

### 3.3. Spin Current Detector 2 (SCD2)

The height of the internal barrier in the SCD2 structures was raised by 50meV, to 150 meV above the ZnSe bandgap, by the incorporation of magnesium into the ZnSSe layer. The ZnMgSSe quaternary alloy (QA) layer was also intended to provide some strain compensation for the ZnCdSe and ZnSe layers by having a lattice constant larger than GaAs, and hence a positive lattice mismatch, to counter the compressive strain in the ZnCdSe and ZnSe.

To achieve this it was first necessary to calibrate the QA by growing a series of samples (HWC225-228) and then measuring their PL and XRD spectra. PL was possible with these samples as the QA bandgap was around  $\sim 2.90 \pm 0.05 \text{ eV}$ , smaller than the energy of the pump source (3.53eV).

#### 3.3.1 Calibration of ZnSe rich Quaternary Alloy for SCD 2

Figure 3.6 shows the structure used to calibrate the QA composition. The QA layer in the initial sample (HWC225) was grown using the same fluxes as the ZnSSe layer in HWC222 but with the Mg cell at a low temp. The ZnS and Mg fluxes were then changed individually to achieve the desired QA composition. A thick QA layer was chosen to produce both XRD peak and strong PL emission.

ZnMgSSe Layer - 100 - 200nm
ZnSe Buffer 30-40nm
GaAs

Fig. 3.6. Structure of the Low MgS fraction ZnMgSSe calibration samples

### 3.3.1.1. PL Characterisation

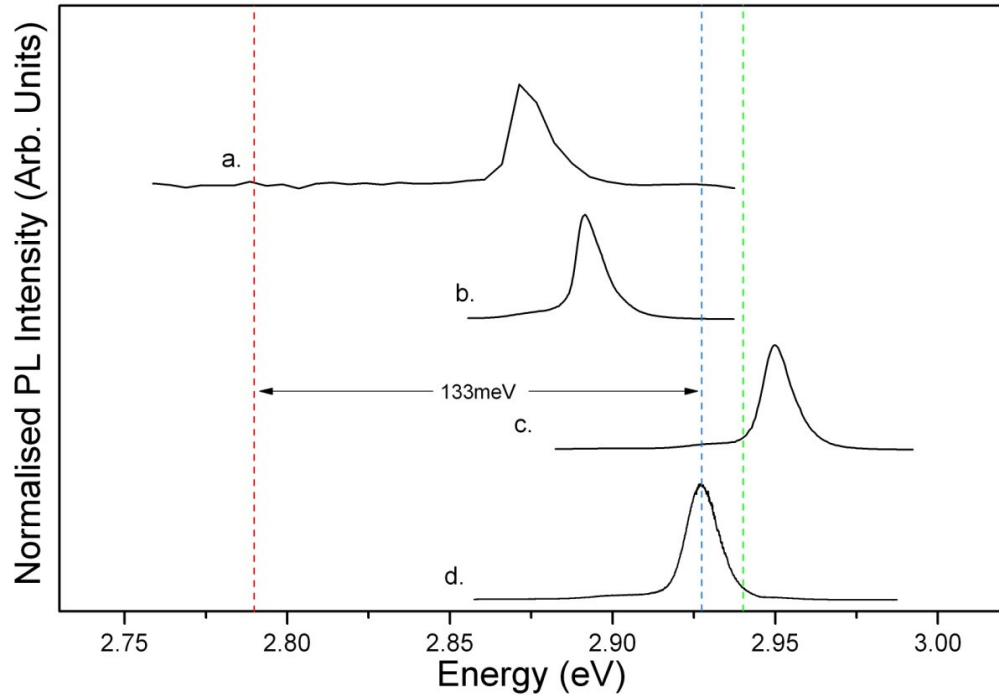


Fig. 3.7. Comparison of the PL results from the four ZnSe rich QA samples – HWC225(a), 226(b), 227 (c) and 228 (d). Red line shows the 77K ZnSe bandgap. The green line the intended QA bandgap and the blue line the bandgap of the QA in HWC228.

The figure 3.7 shows the PL results obtained from the 4 samples. The red line represents the bandgap of ZnSe at 77K (~2.79 eV), whilst the green line represents the desired QA bandgap (2.94 eV). Table 3.3 shows the bandgap, FWHM and separation from the ZnSe bandgap,  $\Delta E_g(\text{ZnSe})$ , for the four samples. HWC228 has a separation of 133meV and although this is less than the 150meV desired, it is sufficient for the SCD2 structure.

	Energy (eV)	FWHM (meV)	$\Delta E_g(\text{ZnSe})$ (meV)
HWC225	2.873	9.1	78
HWC226	2.896	9.6	101
HWC227	2.968	11.0	173
HWC228	2.928	9.7	133

Table 3.3. The PL emission characteristics of the ZnSe rich QA calibrations samples.

### 3.3.1.2. XRD Characterisation

004 XRD measurements were made for all four samples. A representative curve (from HWC228) is shown in figure 3.8, it shows a series of sharp features with pendellösung fringes indicative of a fully strained, high quality structure. The QA

peak is to the right of the substrate peak at ~150 arcsecs.

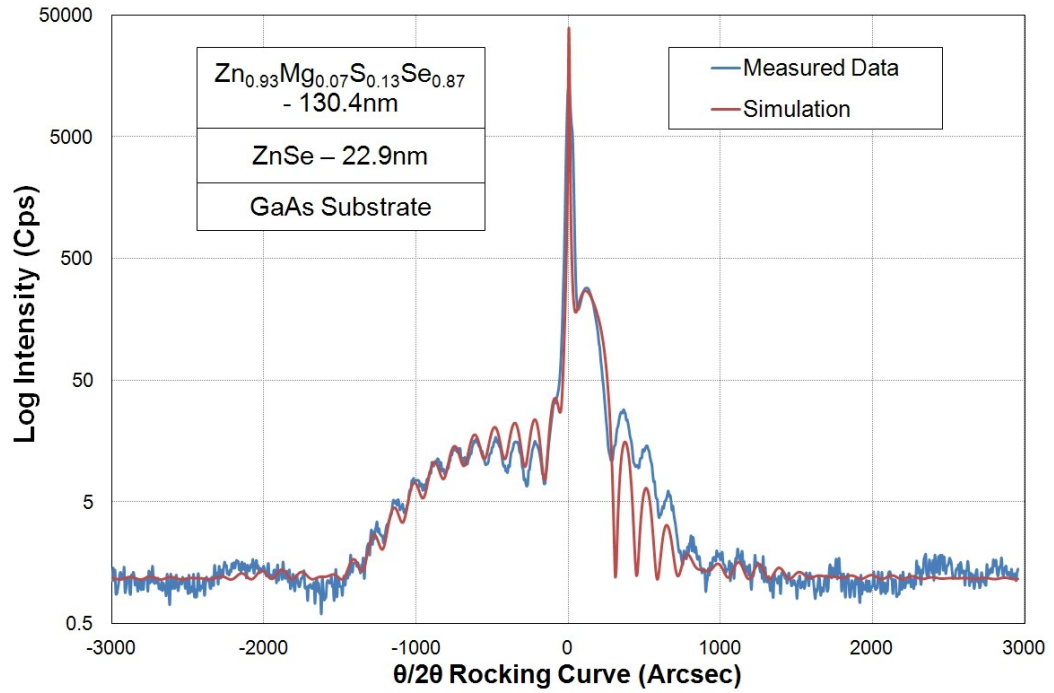


Fig. 3.8. Measured and modelled 004 XRD rocking curve for HWC228. The structure used for the modelling is shown inset. The measured data is shown in blue and the simulated data in red.

A composition of  $\text{Zn}_{0.93}\text{Mg}_{0.07}\text{S}_{0.13}\text{Se}_{0.87}$  produced the best fit. However as will be discussed in chapter 5, QA can have a range of compositions with identical lattice constants and these will all produce extremely similar XRD curves. Therefore from the XRD measurement the QA in HWC228 can only be said to have a lattice constant of  $\sim 5.650\text{\AA}$ . Table 3.4 shows the QA growth rate ( $G_R$ ), lattice constant, GaAs mismatch and GOF for the four ZnSe rich QA samples.

	QA $G_R$ ( $\text{\AA}/\text{s}$ )	Lattice Constant ( $\text{\AA}$ )	Mismatch (%)	GOF
HWC225	0.62	5.636	-0.31	0.127
HWC226	0.70	5.644	-0.16	0.105
HWC227	0.72	5.657	0.07	0.102
HWC228	0.72	5.650	-0.06	0.098

Table 3.4. XRD modelling data for ZnSe rich QA samples.

### 3.3.1.3. Compositional Characterisation

Although the XRD or PL data alone does not allow a composition to be determined for a QA layer, by combining them a composition can be determined as the emission energy (bandgap) and lattice constant change at different rates with composition. Figure 3.9 shows the composition (magnesium (x) and

sulphur (y) percentage) required to produce the correct lattice constant (dotted lines) and emission energy (solid lines). The composition at the intersection of the two lines therefore is the true composition of the QA in the samples.

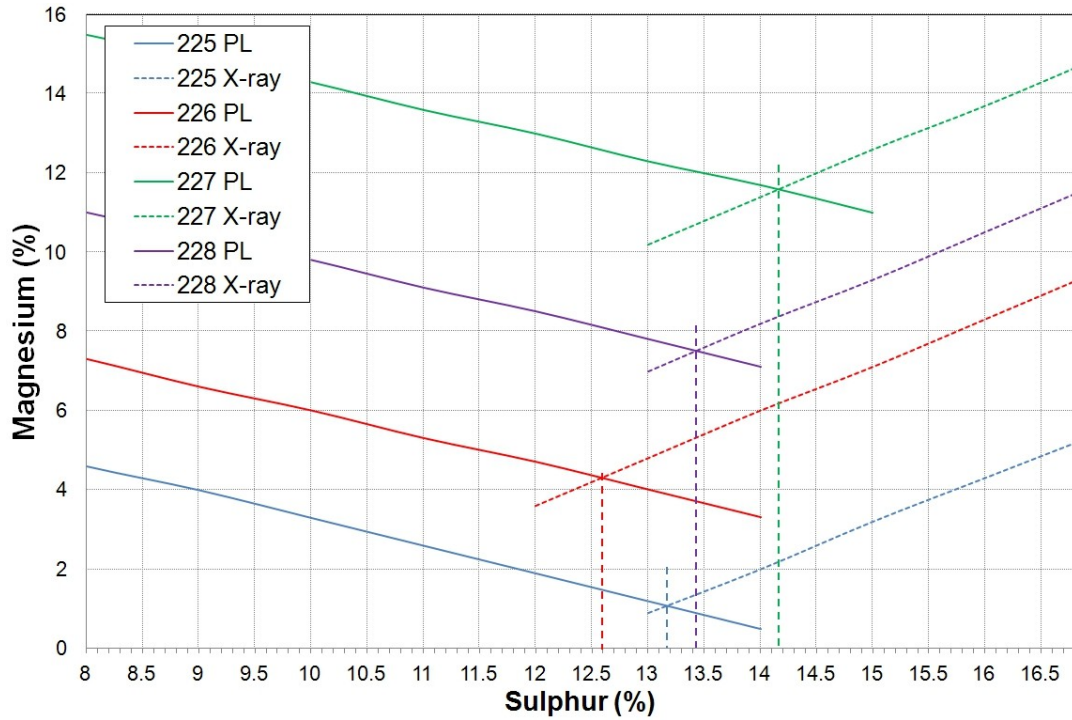


Fig. 3.9. Variation of the required magnesium and sulphur molar ratio for the measured lattice constant and bandgap. Solid lines represent the variation of required composition from the X-ray measurements and the dotted lines the variation of the required composition from the PL measurements. The dashed lines show the position of the intersection on the y (sulphur) axis. The same was done for the x (magnesium) axis, but this is not shown for clarity.

The compositions produced by the figure will have an error associated with them, as the bandgap and lattice constants for the four binary compounds that form the corners of the ZnMgSSe compositional space (ZnSe, ZnS, MgSe and MgS) are only known to limited precision, see chapters 5 and 6. However as all four samples contain ZnSe rich alloys, and ZnSe is the best characterised of the four binaries, the error should be small.

### 3.3.2. Structure and Growth of SCD 2

Figure 3.10 shows the structure of the SCD2 samples. It is very similar to the SCD1 structure but with QA internal barriers. All the sample were grown using identical zinc and selenium fluxes and shutter times to HWC222 but with the Mg and ZnS fluxes used for HWC228.



ZnMgSSe Cap – 5nm
MgS Barrier – 5nm
<b>ZnCdSe Well – 4-5nm</b>
ZnMgSSe Barrier – 20nm
ZnSe Absorption Region ~ 100nm
ZnMgSSe Barrier – 20nm
<b>ZnCdSe Well – 10-12nm</b>
MgS Barrier – 5nm
ZnSe Buffer Layer – 12nm
GaAs Substrate

Fig. 3.10. Spin current detector 2 (SCD2) structure schematic. Again the two QWs are shaded in green and blue.

The first SCD2 sample (HWC229) did not have the correct emission energy, see fig. 3.11, so two further samples (HWC230 and 232) were grown with the same fluxes as HWC229 but increased ZnCdSe QW thicknesses. The RHEED was extremely good throughout the growth of all the samples and again showed no signs of deterioration during the growth interruptions.

### 3.3.3. PL Characterisation of SCD2 Samples

Figure 3.11 shows the PL spectra measured for the three SCD2 samples. All three samples show emission from both ZnCdSe QW and from the ZnSe layers in the sample (primarily the wide absorption layer) at ~2.795eV. HWC229 and HWC230 both also show a further peak at ~2.81eV, which is identified as the light-hole (LH) exciton emission from the ZnSe layer caused by the strain in the layer (see chapter 6). The properties of all the samples are shown in table 3.5.

In addition to the peaks listed in the table, HWC229 also shows 2 further peaks at 2.710 and 2.698eV. It seems likely these are associated with emission peak 2.722eV, as 2.710eV emission is separated by 12meV (which is similar to the 11meV splitting seen between the LH and HH for the ZnSe peak) and the 2.698eV peak is separated by 24meV - consistent with the expected LO phonon

energy. However as no power or temperature dependence data are available for these peaks, it is impossible to determine their origin with any certainty.

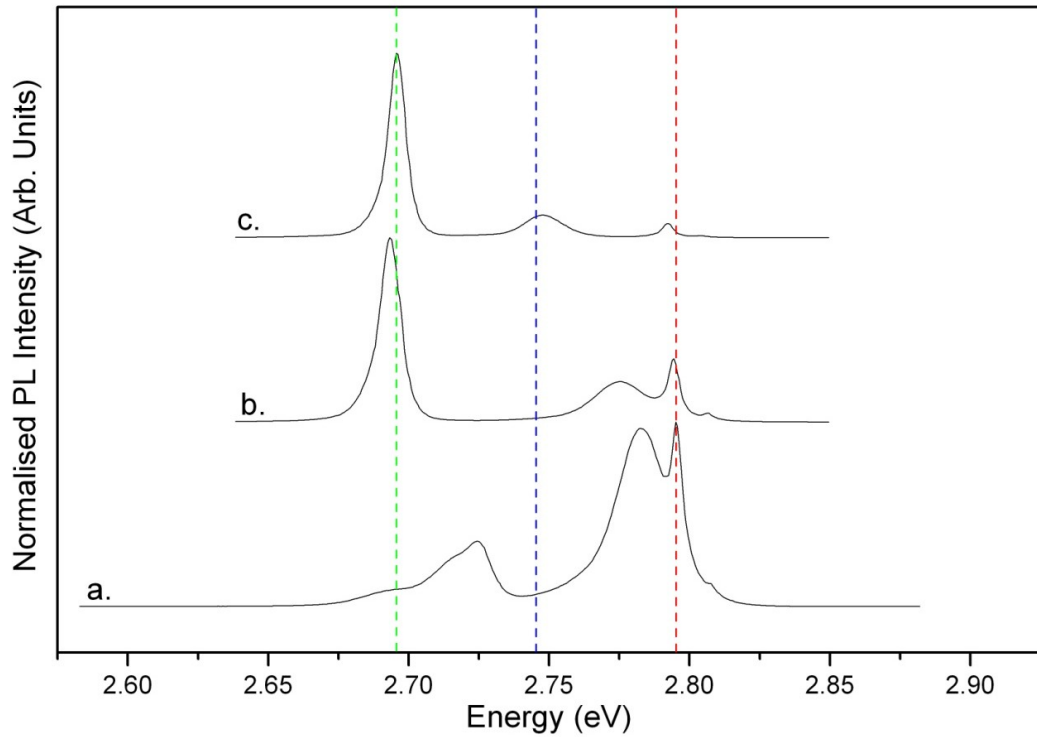


Fig. 3.11. PL spectra from HWC229 (a), 230 (b) and 232 (c) – SCD2 samples. Red line shows the 77K ZnSe bandgap. The blue and green lines the desired QW emission energies.

The ZnSe peaks small FWHM suggests all the samples are of high structural quality. The QW emissions from HWC232 are separated by 100 and 47meV from the ZnSe peak and as they are also sharp and well defined, this sample meets all the PL requirements for the SCD2 design.

	Peak 1			Peak 2			ZnSe Peak		
	Energy (eV)	FWHM (meV)	Rel. Int.	Energy (eV)	FWHM (meV)	Rel. Int.	Energy (eV)	FWHM (meV)	Rel. Int.
HWC									
229	2.722	22.0	0.4	2.783	26.0	0.9	2.795	8.7	1.0
230	2.693	9.2	1.0	2.775	28.1	0.2	2.794	5.5	0.3
232	2.695	7.4	1.0	2.748	18.6	0.1	2.792	4.7	0.1

Table. 3.5. PL emission characteristics of the SCD2 samples.

### 3.3.4. XRD Characterisation

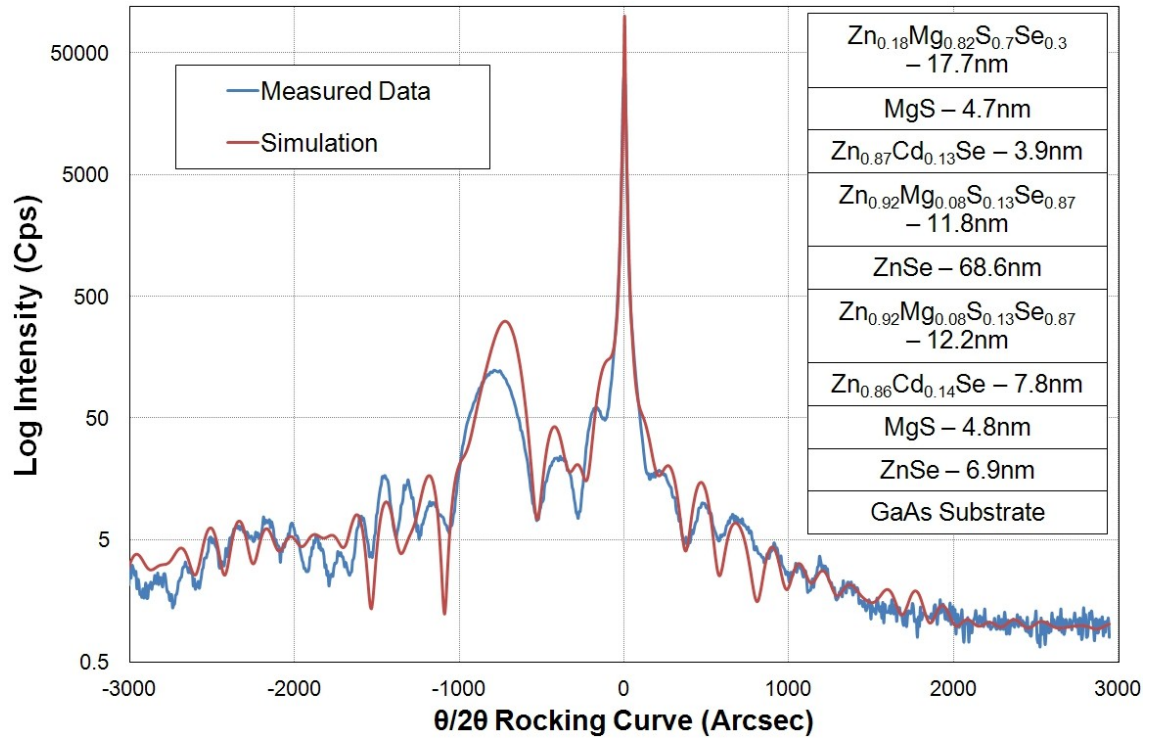


Fig. 3.13. Measured and modelled X-ray diffraction curves for HWC229. The structure used for the model inset. Again the blue line is the measured data and the red the simulation.

Figure 3.13 shows the measured and modelled 004 XRD scan for HWC229, which is representative of the SCD2 samples. The measured data again show sharp pendellösung fringes indicative of a structure that is pseudomorphic. The complexity of this structure again makes modelling difficult. However by using realistic constraints, based on the calibration work, it was possible to generate reasonable fits to the data, see table 3.6.

# HWC	$G_R$ (Å/s)				Composition			GOF
					QA		ZnCdSe	
	ZnSe	MgS	ZnCdSe	QA	x	y	x	
229	0.38	0.40	0.49	0.40	0.08	0.13	0.135	0.160
230	0.39	0.40	0.52	0.41	0.07	0.13	0.128	0.164
232	0.38	0.40	0.53	0.41	0.08	0.12	0.129	0.158

Table 3.6. Spin current detector 2 (SCD2) sample structural properties.

### 3.4. Problems with SCD Design

HWC222 and 232 were sent to the ESP group in Marburg. They found that under standard PL excitation the samples performed identically to the HWU measurements. However when the samples were excited with the femtosecond 400 and 800nm pulses to generate the spin current, no emission was observed and the samples rapidly degraded, resulting in discoloration and poor subsequent PL emission.

The reason for the lack of emission and sample degradation is due to the need to use high intensity 800nm light, due to the low two-photon absorption cross section. As even when highly focused, to further increase the 800nm lights intensity, a large percentage (>95%) is not absorbed by the ZnSe layers. But this residual light is absorbed by the GaAs substrate, which causes significant localised heating and damages the samples.

This problem could be resolved by simply removing the SCD structure from the GaAs substrate but as the SCD structures are very thin and not designed for this, it is likely to result in them becoming damaged (see chapter 4). It would also make collecting any emitted light difficult due to the wide emission angle from the samples edge facet, but the ESP group intend to investigate this possibility in the future. However there are other solutions that might be more elegant and these will be discussed in the future work section in chapter 8.

### 3.5. Conclusions

This chapter explained the growth and characterisation of a series of structures grown for ESP groups at Philipps-Universität Marburg. Details of the PL and XRD characterisation of these structures along with a series of ZnSe rich QA samples were presented.

Samples that met the SCD1 and SCD2 designs were successfully produced and characterised at HWU and showed strong PL emission and sharp XRD features consistent with pseudomorphic growth. The failure of these samples as actual spin current detectors shows one of the key problems faced by semiconductor epitaxy groups when collaborating with others, the need to fully understand the way the samples are to be used and to explain the exact properties of the materials used. This failure resulted in a design being agreed that is fundamentally flawed for the experimental purpose it was designed for.

## 4. Epitaxial Lift-Off

In this chapter my work to further develop and extended the epitaxial lift-off (ELO) process pioneered by the MBE and nano-optics groups at HWU for II-VI semiconductors will be explained. This ELO process was originally developed by Andrea Balocchi and Arran Curran using samples grown by Richard Moug, Christine Bradford and Jessica Morrod [4.1, 4.2]. Some of these samples are re-used in this work together with a series of new ones grown by myself and Akhil Rajan.

Section 4.1 gives a brief overview of the ELO process, its historical background and some examples of its uses. As ELO will be used extensively in chapters 5 and 6, it is explained thoroughly in this chapter drawing particular attention to its benefits and limitations. A brief explanation of the reasons behind a minimum MgS thickness for ELO is also given, full details of which are in [4.3].

In section 4.2 my work to further develop the ELO process for samples containing an MgS sacrificial layer is explained. This work is focussed on investigating the causes of the cracking seen in deposited material to improve the process. This optimisation is necessary if ELO is to be useful for commercial work as currently it has low reproducibility.

My work to extend the ELO process to samples containing an MgSe sacrificial layer will be presented in section 4.3. This is the first time that MgSe has been demonstrated as a sacrificial layer and was undertaken as a collaboration with the City College of New York (CUNY) who grew the samples used for the work. Again during this work every effort was made to try and optimise the process to produce high quality deposited material.

Finally section 4.4 contains conclusions and suggestions for future work.

## 4.1. Introduction

Epitaxy requires a substrate and its properties will determine both which materials can be grown and many of the eventual structure's characteristics. As there are only a limited range of substrates commercially available, the choice of substrate often has to be a compromise. For growth the substrate's lattice constant is the main factor in determining its suitability with all its other properties being of lesser concern.

II-VI semiconductors are typically grown on III-V substrates (GaAs, InP, etc.) due to their availability, relatively low cost and high quality. However as all of these III-V substrates have relatively narrow band-gaps it means that (with the exception of some tellurides) any light emitted by the II-VI layers incident on the substrate will be absorbed. Often this is a serious problem and it would be highly advantageous to be able to remove the substrate after growth. ELO provides this ability, as it allows material to be transferred to a new substrate. In collaboration with the Nano-Optics group at HWU we have previously demonstrated this by using ELO to transfer II-VI material to dielectric mirrors to produce extremely high quality optical cavities [4.2].

Sometimes the mechanical or thermal properties of a substrate may also inhibit efficient post-growth device performance, for example in a device that is subjected to a large heat load during operation. Here the thermal conductivity of the substrate may be too low and another substrate might prove to be better suited and again ELO would be advantageous.

Typically the most expensive item in epitaxial growth is the substrate and so the ability to re-use them provides another reason why ELO is highly desirable. This is of particular importance in the field of photo-voltaic (PV) solar cells where cost is currently seen as a critical issue in increasing device usage.

#### 4.1.1. Overview of the ELO Technique

Any process which coherently removes epitaxial layers from their substrate can be termed 'epitaxial lift-off', but in this thesis and in most on the papers of the subject the term signifies a process that etches away a sacrificial layer built into a structure, here either MgS or MgSe. However there are other ways to remove the epilayers from their substrate:

1. Chemically or mechanically etching away the whole substrate. This method has been developed for a number of material systems [4.4-4.6] but has the drawbacks that the etching will often damage the epitaxial layers and the substrate cannot be re-used afterwards.
2. Thermal lift-off where the substrate is chosen to have a very different constant of thermal expansion to the epilayers results in delamination during cool down [4.7]. This has the major advantage that it does not require any specific post growth processing but may require the substrate to be patterned prior to growth (to control or assist the delamination process) and typically causes significant damage to the epilayers
3. Laser lift-off is where the entire structure is be exposed to short, high intensity pulses of laser light that are preferentially absorbed by either the epilayers or substrate causing a small volume to decompose [4.8]. This allows layers to be etched rapidly but is likely to introduce damage.

The use of a sacrificial layer for ELO was first described by Konagai et al. [4.9], although they used the term 'Peeled Film Technology' rather than ELO. They showed that a 30  $\mu\text{m}$  thick GaAs layer on top of a 5 $\mu\text{m}$  thick  $\text{Al}_{0.7}\text{Ga}_{0.3}\text{As}$  sacrificial layer could be lifted by exploiting the difference in etch speeds of AlAs and GaAs in hydrofluoric acid (HF). To support the epitaxial layers, the top surface of the sample had a metal structure evaporated on to it and was then coated with Apezion W wax to protect it. The process was found to etch pieces up to a few millimetres wide but would fail for larger pieces. This was explained by the etchant and reaction products no longer being efficiently exchanged through the narrow etch channel.



This work was later extended by Yablonovitch et al. [4.10] who found that by annealing the sample before etching the Apezion wax would form a domed shape, straining the epilayers underneath. This produced a wider etch channel and allowed larger areas to be lifted. Further work examined the handling and Van der Waals (VDW) bonding of the lifted material [4.11, 4.12]. VDW bonding is advantageous as it allows material to be attached to a new substrate without an adhesive.

Using these techniques double-heterostructure GaAs/AlGaAs diode lasers [4.13], GaAs light emitting diodes[4.14], GaAs metal-semiconductor field-effect transistors [4.15] and strained single quantum well InGaAs/GaAs high electron mobility transistors [4.16] have been produced. Other groups have extended the technique by developing ways to strain the epilayers without cracking them, to allow larger areas to be lifted. Examples include the weight-induced epitaxial lift-off process (WI-ELO) [4.17] and the use of a flexible plastic carrier to allow a whole 2" wafer to be lifted and deposited successfully [4.18].

However using strain to increase the etch speed and lifted area size has been shown to cause the formation of 'cleavage cracks' [4.19]. These cracks are a problem in electrical devices as they break the circuit increasing its resistance. Later work by Yablonovitch et al. found that after ELO the epilayers have little mechanical strength and strains as small as 0.1% can form cracks. Therefore the layers need to be handled carefully [4.20].

To provide sufficient support the last published paper by Yablonovitch on this topic describes the use of a rigid silicon backing structure for ELO and is depicted in figure 4.1 [4.20]. The structure has thin channels cut in it and is attached using photoresist. The slots are illuminated with UV light to remove the photoresist before the epilayers are exposed to a non-selective etch through the channels to access the sacrificial layer (1). This is then etched away (2), and the epilayers removed still attached to the support structure (3). One application for the lifted material produced by this technique was in PV panels as the thin

strips of material produced can be connected up in series or parallel to produce the individual cells necessary for the panels.

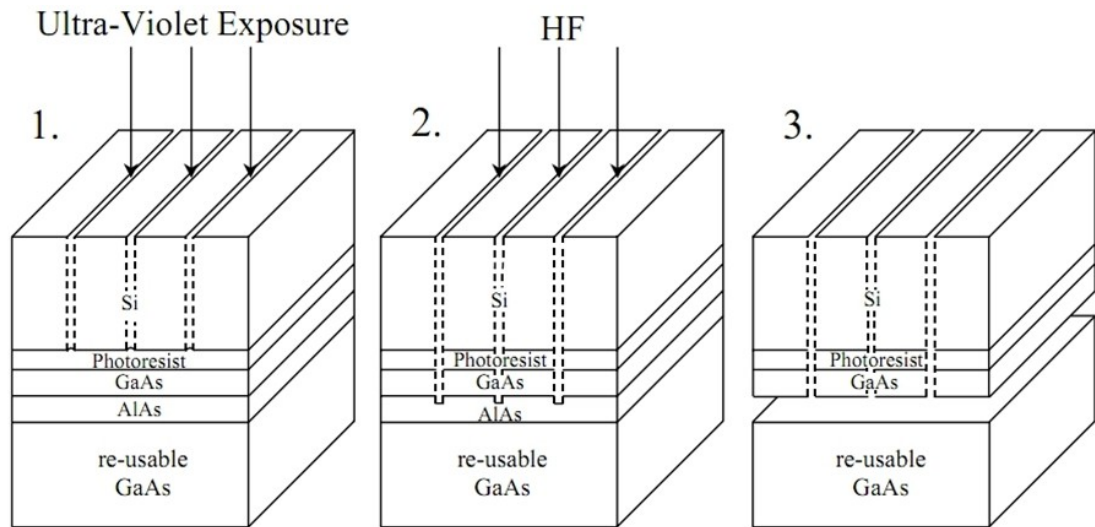


Fig. 4.1 – Schematic of rigid silicon epitaxial liftoff technique adapted from [4.20].

#### 4.1.2. II-VI Epitaxial Liftoff

Although it would be possible to grow II-VI samples on a wafer with an AlGaAs layer and use the Yablonovitch III-V ELO technique, it is more convenient to use a native II-VI compound. The MBE group at HWU has pioneered this by developing a II-VI ELO process that uses MgS as the sacrificial layer. This technique works by exploiting the large difference in etch speed between MgS and ZnSe in acidic solutions, typically 30% HCl where it is at least  $10^7$  times faster [4.1]. An example lift-off of a ZnSe/ZnCdSe QW structure is shown in figure 4.2.

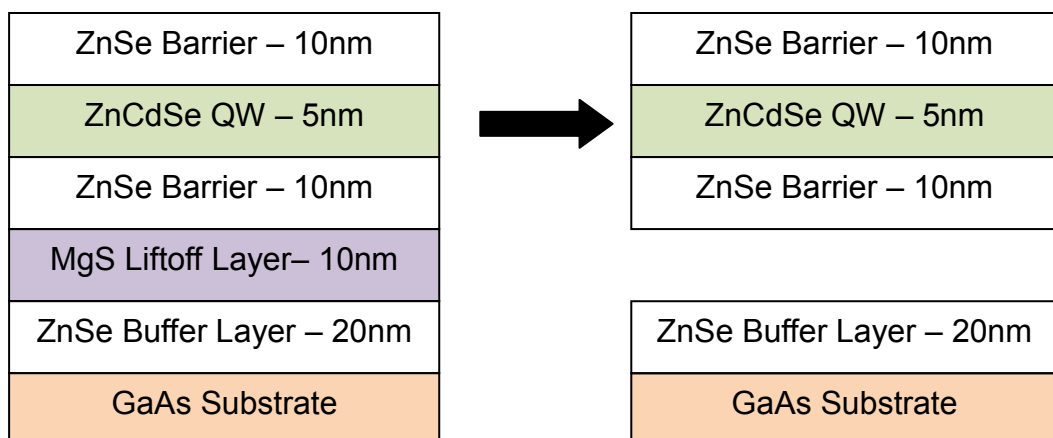


Fig. 4.2 – An example ZnSe/ZnCdSe QW liftoff Structure. MgS layer highlighted in purple.

#### 4.1.2.1. Minimum Sacrificial Layer Thickness

During previous work on MgS ELO a minimum sacrificial layer thickness necessary for lift-off of ~3nm was found, arising from the VDW interaction between 2 layers in close proximity. The VDW force is very short ranged, typically over 10s of Angstroms, varying with the layers separation cubed [4.3, 4.24]. In the case of ELO samples the separation is simply the thickness of the sacrificial layer.

The size of the force resulting from the VDW interaction can be estimated by considering the values calculated by Gusso et al. for GaAs and Si [4.25]. These show a force per unit area equivalent to a pressure >18 atmospheres when the layers are separated by 2nm, decreasing to ~5 atm. at 3nm. Although the total force acting to separate the epilayers from the substrate is unknown, the wax cap produces an upward pressure of the order of 10s of atmospheres due to its surface tension ( $0.065 \pm 0.003 \text{ Nm}^{-1}$ ) [4.26]. From this it is apparent that at 2-3nm the VDW forces will match the force of the wax and stop the epilayers from lifting.

#### 4.2. Development of the MgS Based ELO Process

The II-VI epitaxial lift-off (ELO) process is a 6 stage process and is shown schematically in figure 4.3. The first step is to cleave a sample into a series of small pieces (1). These range in size from ~1mm<sup>2</sup> up to 5mm<sup>2</sup>. The pieces then have Apezion wax applied to their top surface by our standard deposition technique of heating the sample to ~130°C, so the wax runs [4.27], and then place small wax pieces on the surface to form a smooth dome (2). Alternatively the wax can be dissolved in a solvent (such as n-Propyl bromide (NPB)) and then a small volume deposited on the surface so that when the solvent evaporates the wax is left behind.

The wax in solvent technique is not used here as it was found that the wax was not uniform and contained 'channels' through which the solvent had evaporated,

and this reduced the waxes ability to support the epilayers. Yablonovitch et al solved this problem by annealing the samples after the solvent had evaporated [4.10], but as this adds an additional step to the process, the hotplate method was chosen as our standard technique.

After wax deposition, the samples are placed in a solution of 30% HCl for several hours to allow the acid to etch away the MgS (3). The time required varies depending on the dimensions of the sample, the thickness of the MgS layer and whether any of the edges of the sample have been accidentally coated in wax. The etch rate also varies from sample to sample but has a maximum speed of  $\sim 3\text{mm/hr}$  [4.1].

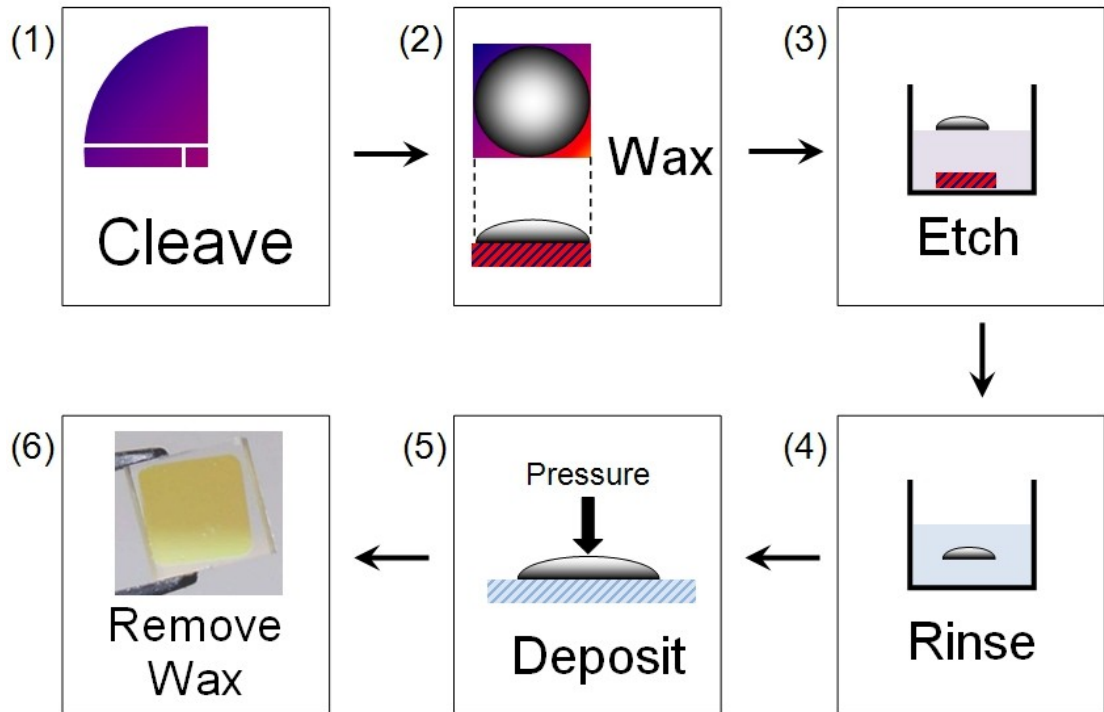


Fig. 4.3. Schematic representation of the epitaxial liftoff process.

After etching the waxed epilayers separate from the substrate and normally float to the surface of the solution. The lifted material can then be carefully removed, rinsed in deionised water (4), and then deposited on to a new substrate (5). All the samples are bonded using VDW bonding, as this produces excellent adhesion of the layer to the substrate and avoids the need to use an additional adhesive. The VDW bonding is achieved by removing the lifted material from the final rinse on the new substrate, partially drying it and then applying a small amount of pressure to the top surface. Typically a pressure of  $\sim 500\text{Nm}^{-2}$  is used but samples have also bonded without any force being applied.

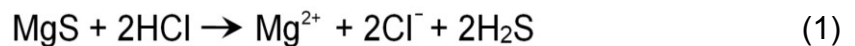
The samples are left for 6-24 hours, to allow any remaining water to evaporate and the VDW bonding to occur and can then have the protective wax removed (6). This is achieved by placing the entire sample in a beaker of solvent and allowing all the wax to dissolve. The sample can then be cleaned in acetone or IPA and deionised water before use. An image of a thick ZnSe layer deposited on glass after the wax has been removed is shown in fig. 4.3 (6).

Considerable care must be taken when handling the sample prior to depositing onto its new substrate as the entire structure (epilayers and wax) is very brittle and easily damaged if handled roughly. This is especially important when any pressure is being applied to the sample during the VDW bonding step, as applying too much force is found to crack the samples.

The only other problem encountered with VDW bonding was when using diamond substrates. These were found to have a hydrophobic surface termination which would not wet properly and this stopped the II-VI material bonding. A more thorough investigation will be presented later in this chapter.

#### **4.2.1. Etch Mechanism**

Our standard etch solution is 30% (~12 molar) HCl. The reaction is shown in equation 1. It produces hydrogen sulphide, which is toxic. However only a very small amount is produced (~ $15 \times 10^{-6}$  moles for a  $5\text{mm}^2 \times 5\text{nm}$  sacrificial layer), so it is not sufficient to cause a hazard.



Hydrogen sulphide does cause problems for the etch itself, as it has only a limited diffusion rate and could form a bubble if its concentration exceeds its solubility limit. Both of these effects inhibit the etch reaction by blocking the exchange of the reactants and fresh  $\text{H}^+$  ions.

Yablonovitch et al proposed the maximum etch speed in the AlGaAs system was based on the diffusion rate of hydrogen away from the etch reaction site

[4.11]. The maximum etch speed we see (3mm/hr) is compatible with the predictions of this model once the increased solubility of H<sub>2</sub>S compared to H<sub>2</sub> is taken into account. However as bubbles are seen at the edge of our samples during etching it is possible the Yablonovitch model is not valid here, as it assumes no bubble formation.

#### 4.2.2. Cracking

Typically lifted material shows some additional cracking. But for a small number of lifted samples there is either no additional cracking (which suggests it's avoidable) or the cracking is very minor and large continuous areas (typically 200-500µm<sup>2</sup>) can be deposited. This makes the technique suitable for optical characterisation work, even though the total percentage of usable samples is low, but may cause problems for electrical work in the future.

Figure 4.4 shows a schematic of the individual stages of the etch process along with a series of pictures taken of the samples at various stages. Images 1-3 show a visible 50x, visible 500x and UV 1000x magnification images of a freshly cleaved sample. Images 4-6 show the 50x, 500x and 1000x visible images of a sample that has been repeatedly heated and cooled. Images 7-9 are the visible 50x, 500x and 1000x images of the surface of a sample after applying and removing wax. All three sets of images show that no cracking occurs prior to etching. Even after the full ELO process was performed on these samples, the cracking in the deposited material was identical to other samples that had only been heated, waxed and etched once. This suggests that the cracking is not caused by the wax deposition process alone.

Images 10 and 11 show the 50x magnification of the top and bottom surface of a piece of waxed and etched material respectively. A series of curved cracks run from the edge of the sample to the centre along with a smaller number of cracks that run either parallel to the edges of the cleaved samples along either [110] or  $[1\bar{1}0]$ . Crystalline materials typically fracture on cleavage planes and so the curved cracks must be due either to sample handling or the wax.

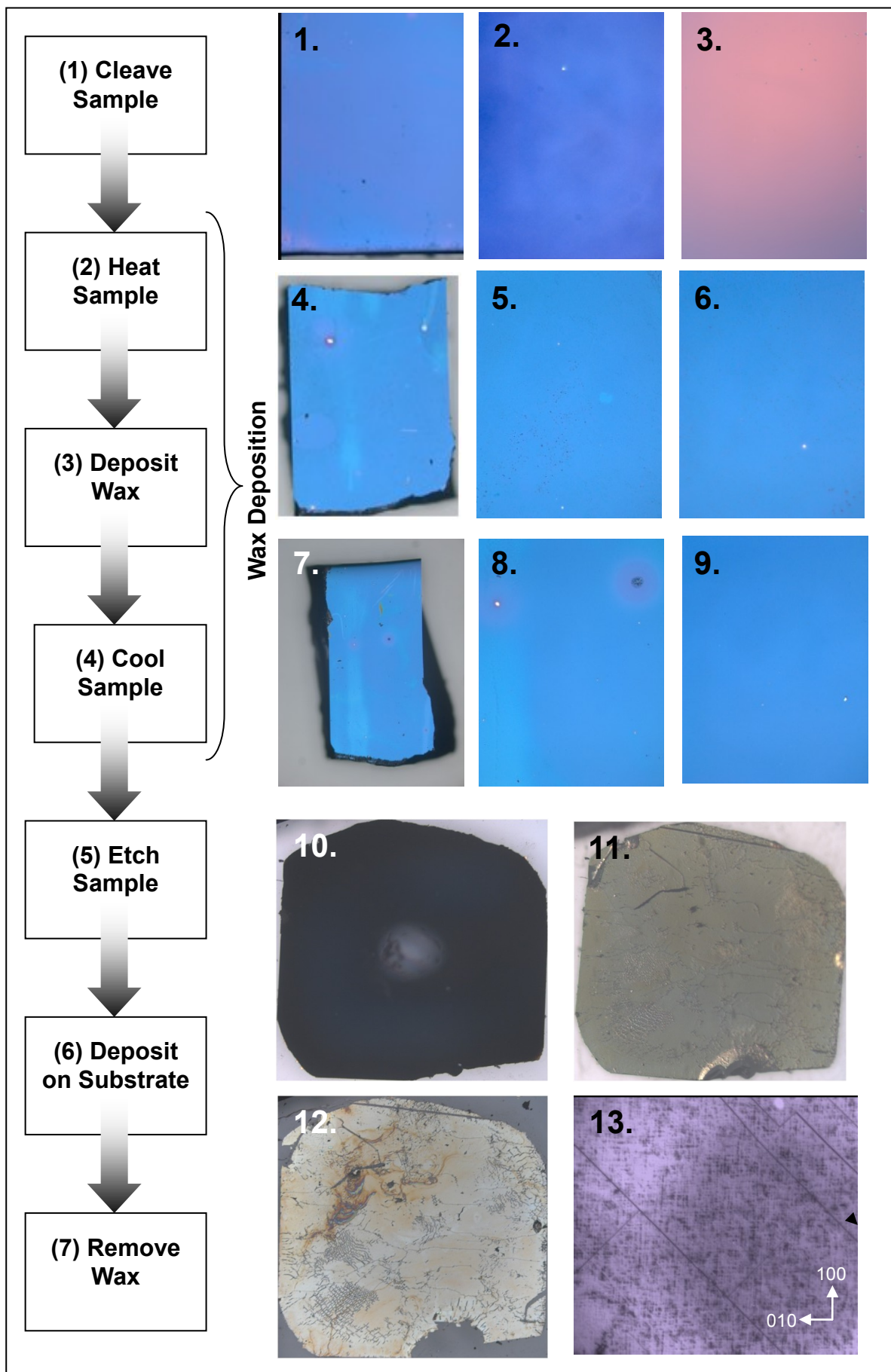


Fig. 4.4 – Epitaxial lift-off process schematic and images.

Image 12 shows the same sample from images 10 and 11 once it has been deposited and the wax dissolved. It shows the same curved and straight cracks as the pre-deposited images confirming that the cracks are in the II-VI layer and are not the underside of the wax imaged through the semi-transparent II-VI layer. Finally image 13 shows a 1000x magnification image of another piece of deposited material showing cracks only on  $[110]$  or  $[1\bar{1}0]$ , which is more typical.

How the etching process is causing the cracking is hard to determine as the fragile epilayers could be damaged by even a slight force and it is difficult to investigate the reaction while it is occurring. However, the two most likely mechanisms are: the formation of bubbles in or at the edge of the etch channel and the uneven relief of stress in the epitaxial layers. The stress would be a mixture of the force applied by the wax to the epilayers and the residual stress introduced by growing ZnSe (or other II-VI materials) on GaAs.

Although  $H_2S$  is highly soluble in water ( $\sim 4g$  per litre at  $20^\circ C$ ), making bubble formation unlikely, some bubbles are seen during the etching process. This is probably due to the geometry of the etching, as a thin etch channel is formed that inhibits gas diffusion, allowing the concentration to increase locally to saturation and a bubble to form. However as the most likely location for the bubble is the end of the etch channel (due to the discontinuity there) any static force it does exert on the epilayers will be small due to the small contact area.

If pieces of unwaxed ELO samples are added to the etch solution they are etched. However rather than the epilayers etching as a single piece, they instead break up into small fragments. The mechanism that causes this break-up may also cause the cracking in the waxed layers. Therefore although the wax may enhance this mechanism, it cannot be the sole cause.

The stress induced by strain in the layer does not appear to be sufficient to explain the cracking, as a minority of samples do not show cracks and these



contain identical strains to those that do. However an uneven release of any strain in the epitaxial layer during etching is a possible cause as this could vary from sample to sample depending on the conditions of the etch.

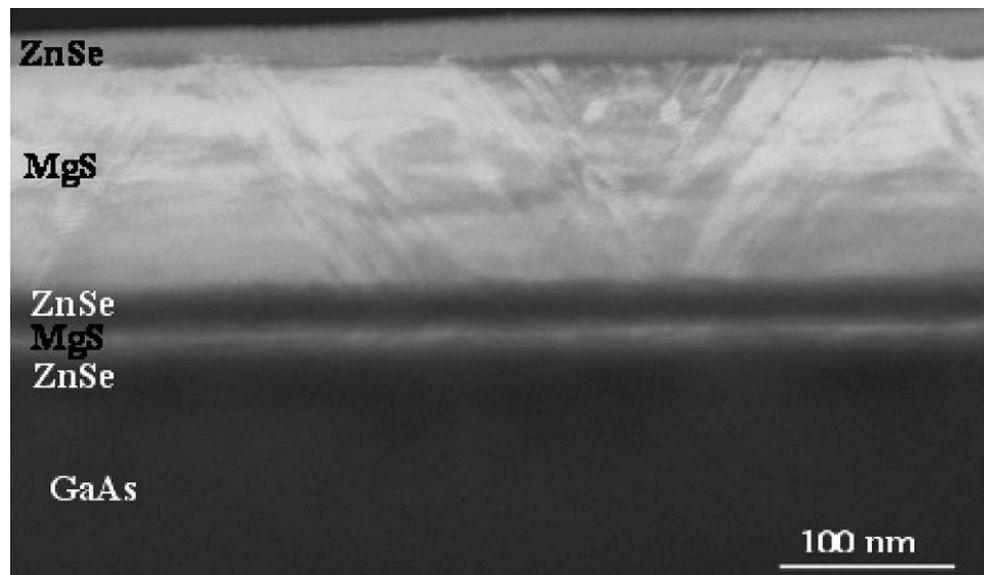


Fig. 4.5. A TEM image of ZnSe/MgS layers on GaAs showing stacking fault propagation [4.31].

The surfaces of ZnSe and MgS layers are known to be nearly atomically smooth and pseudomorphic (as can be seen in fig. 4.5), so it is unlikely that the interface between these layers causes uneven strain release. Another possible source of anisotropic strain in the epitaxial layers is the wax cap, as the samples always cleave into rectangles and the wax forms a more rounded shape, see figure 4.6. This difference is likely to produce areas of the epilayers with different strains as the sacrificial layer is etched. But without further work it is impossible to determine if this is the cause of the cracking.

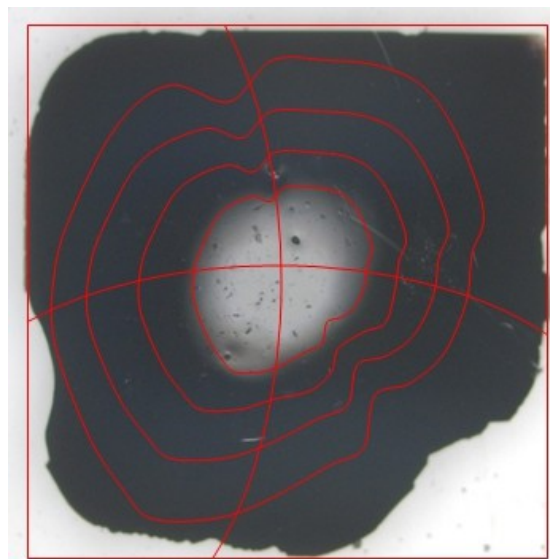


Fig. 4.6 – Image of the top surface of a waxed sample prior to wax removal. Red lines added to show the contours of the wax.

### 4.2.3. Deposition onto a New Substrate

The deposition stage is another potential source of cracking and failure, as the lifted material is removed from the deionised rinsing water, dried and then pressure applied to encourage it to stick to a new substrate whilst only being supported by the wax capping layer. However if care is taken during these steps successful deposition can be achieved with a success rate typically over 90%.

One problem that can cause cracking or failure is the presence of dust or particulates between the epilayer and the new substrate. Figure 4.7 shows a trapped particle causing localised cracking. After wax removal (not shown) the area around the particle had not bonded to the substrate presumably because it was not in contact with the surface.

The solution to this problem is to clean the substrates thoroughly before use and remove the epilayers from their final rinse using the new substrate. This ensures the substrates surface is free from contamination and no opportunity for further contamination occurs before bonding.

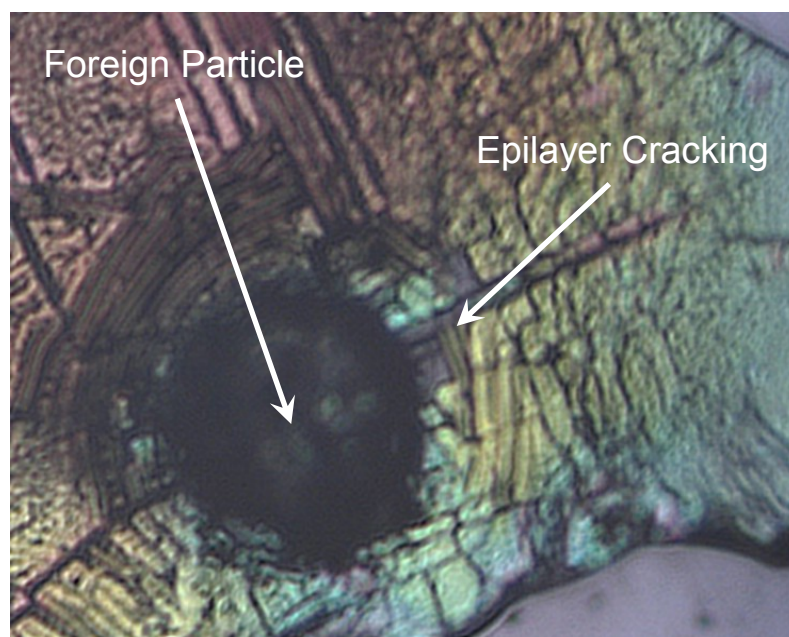


Fig. 4.7 – 500x magnification image of the underside of a waxed layer deposited on a substrate with a trapped particle. The layer has been imaged through the glass substrate it's been deposited onto.

#### 4.2.3.1. Deposition onto Diamond Substrate

As part of a collaboration with the Institute of Photonics at Strathclyde University, II-VI material was deposited on to diamond substrates. This proved more difficult than anticipated as the deposited layers were typically poor quality, see figure 4.8. The diamond surface was determined to be hydrophobic and would not wet properly. One solution would be to use a non-polar solvent such as benzene or chloroform but as these are hazardous, modification of the diamond to produce a hydrophilic surface was investigated.

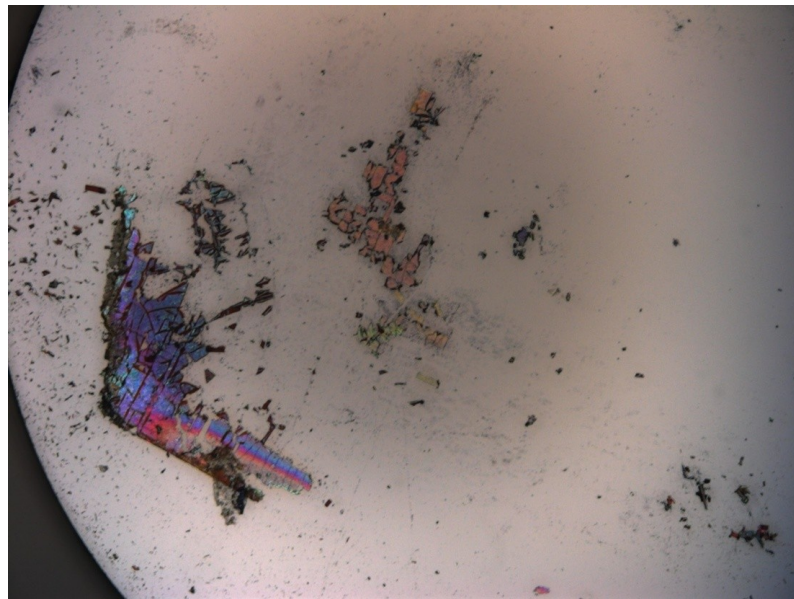


Fig. 4.8. Image of a failed attempt to deposit II-VI material onto diamond. The image shows a few very cracked pieces of II-VI material randomly distributed around the substrate.

To achieve this, the surface was oxidised using the normal GaAs etching solution -  $\text{H}_2\text{O}_2:\text{H}_2\text{O}:\text{H}_2\text{SO}_4$  1:1:7.5. Which replaced the hydrogen terminated surface with an oxygen terminated one. After treatment water wets the surface well and material could be successfully deposited.

#### 4.2.4. Optical Characterisation of ELO Samples

By using ELO, II-VI layers can be investigated by transmission measurement without concern for the GaAs substrate they were grown on. This allows measurement of a sample's absorption and examples of this are reported in chapters 5 and 6 (sections 5.2.3, 5.3.3 and 6.2.1). Structures containing QWs

and QDs have also been lifted (section 5.2.5) and shown to have near identically PL emission after ELO. Typically the only difference that is seen is slight shifts in the emission energy due to the change in strain state.

#### **4.2.5. Recent Problems with MgS ELO Samples**

For a period of time after the HWU MBE machine was moved a dramatic increase in the failure rate of MgS ELO samples was encountered. Two possible ELO failure modes have previously been identified:

1. The MgS layer would be too thin resulting in etching failing due to strong VDW forces, as explained in section 4.1.2.
2. The MgS could have a zinc incorporation >15% resulting in Zn-Zn chains forming in the layer inhibiting etching [3.3].

And both of these were initially suspected as the cause. However as it was found that changing the ZnS flux or substrate temperature (which should affect the zinc incorporation) or growing a thicker MgS layer had no effect on the behaviour of the samples, these could not be the cause. Therefore a new failure mechanism was required. The problem was eventually solved by reducing the Mg flux and this will be discussed along with the new failure mechanism in section 4.5.

### **4.3 Extension of ELO to an MgSe Sacrificial layer**

The MBE group at The City College of New York (CUNY) produces ZnMgCdSe based material using InP substrates. Figure 4.9 shows the emission energy vs. lattice constant for ZnMgCdSe and that a range of compositions can be grown on InP that cover nearly the entire visible range.

The MgS ELO technique cannot be used with ZnMgCdSe due to the difference in lattice constant. However as the benefits of ELO are equally valid, we developed a lift-off process based on MgSe. In contrast to MgS, MgSe (and

MgTe) does not dissolve in HCl but instead react to form insoluble selenium, which inhibits etching. However from previous ZnSe electrochemical CV profiling work we have already developed a technique to make these selenium deposits soluble. This technique relies upon the reaction of sulphite ions with the solid selenium to produce soluble sulfo-selenite ions [4.28].

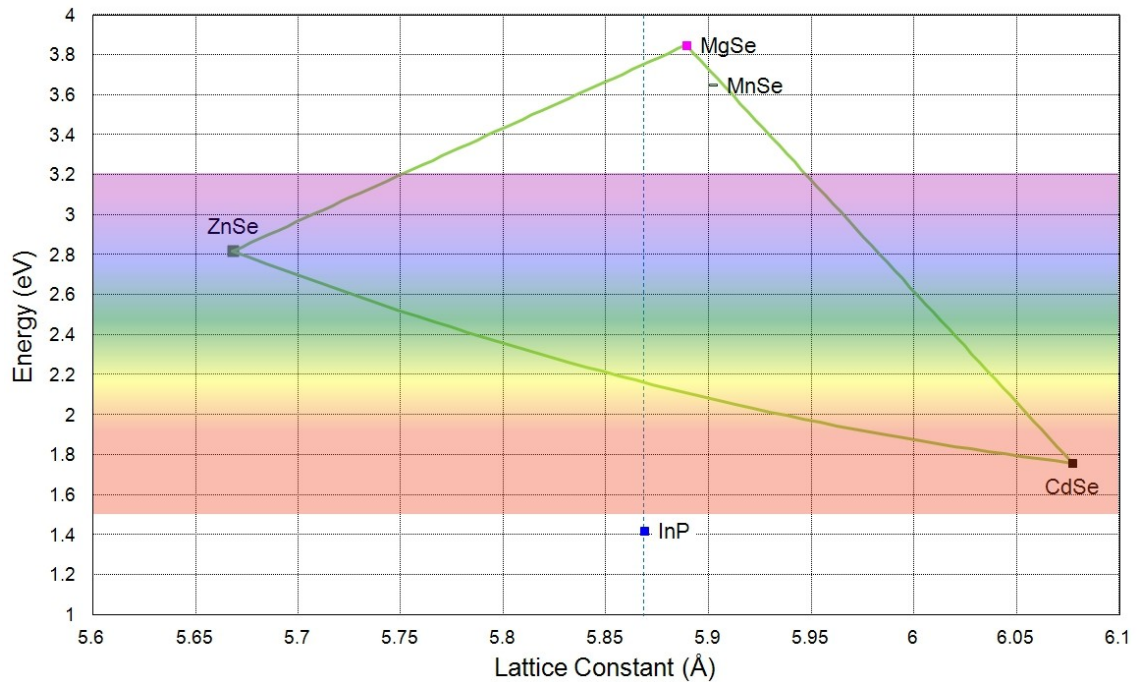
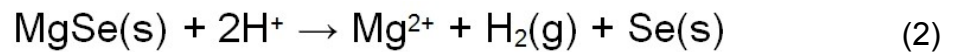


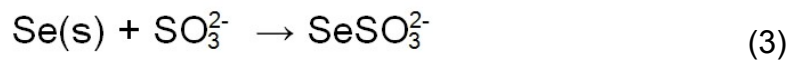
Fig. 4.9 - ZnCdMgSe lattice constant vs. bandgap. A series of binary compounds (squares) and the ternary alloys between them (green lines/curves) are indicated. The line of lattice match to an InP substrate is also shown (blue dotted line).

#### 4.3.1. Etch Mechanism

Equation 2 shows the reaction between MgSe and HCl which has insoluble reaction products of hydrogen gas and elemental selenium. The reason these products are formed rather than hydrogen selenide ( $H_2Se$ ) is that  $H_2Se$  is far more readily oxidised than  $H_2S$  and will therefore rapidly decompose in solution



However by adding sulphite ions to the solution, the solid selenium is converted to soluble sulposelenite ions, as in equation 3 [4.28].



Sulphite ions are very sensitive to pH and in an acidic environment are rapidly

converted to bisulfite ions. However, theoretically bisulfite ions should behave in the same way as sulfite and remove any selenium deposits.

#### 4.3.2 MgSe/ZnCdSe Samples from CUNY

Two set of samples were grown at CUNY for the ELO project, shown schematically in figure 4.10. All the samples were grown by MBE on (001) semi-insulating InP wafers in a dual chamber Riber 2300P system [4.29]. The InP wafer (substrate) was de-oxidised and had a lattice matched 200nm thick InGaAs buffer grown on it at 400 °C in a III-V chamber before being transferred under ultra high vacuum to a II-VI chamber. The samples were then heated to 170 °C, exposed to a Zn flux for 40s and then a ~5nm low temperature ZnCdSe buffer layer grown on them. These steps are known to optimize the III-V to II-VI interface and improve the quality of the epitaxial layers grown above [4.30]. After the low temperature layer, the substrate temperature was raised to 270 °C for the remainder of the growth.

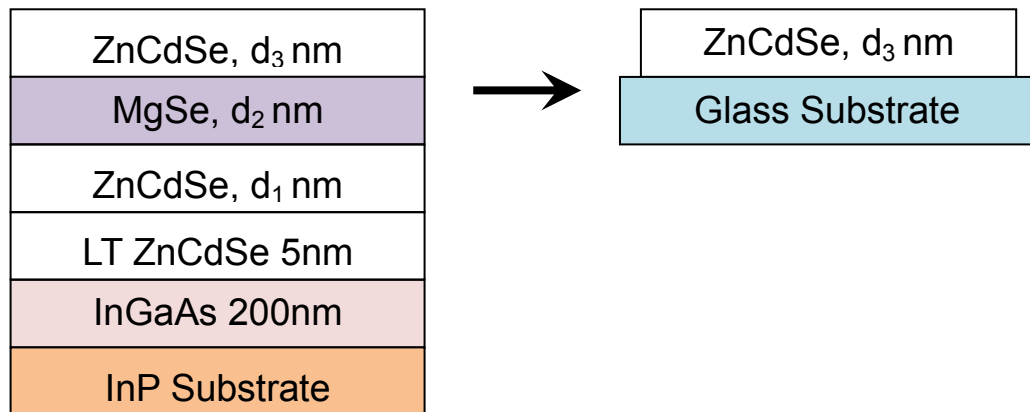


Figure 4.10. Schematic of the MgSe ELO structure pre and post lift. MgSe layer is highlighted in purple.

All the samples have the same structure: two thick ZnCdSe layers separated by a thin MgSe layer. The details of both sets of samples are shown in table 4.1. The thickness of the MgSe layer was varied in the first set of samples, so that the effect of thickness on the etch could be investigated. The composition of the ZnCdSe layers in the 1<sup>st</sup> set of samples was also deliberately chosen not to be latticed matched so that XRI could be used to determine the MgSe layers thickness and calibrate its growth rate [4.31]. The thicknesses for the second series of samples (A30XX) were determined by a series of calibration growths.



Sample	Thickness (nm)			$\text{Zn}_x\text{Cd}_{1-x}\text{Se}$	
	ZnCdSe, $d_1$	MgSe, $d_3$	ZnCdSe, $d_3$	X	Mismatch
A2820	90	3.9	92	0.55	-0.27%
A2846	93	4.8	91	0.54	-0.20%
A2821	103	7.5	105	0.55	-0.27%
A2831	110	7.7	108	0.56	-0.34%
A2849	112	8.8	101	0.58	-0.49%
A3009	100	5	~700	0.60	-0.61%
A3010	100	5	~700	0.59	-0.55%
A3012	100	5	~400	0.56	-0.34%
A3013	100	5	~400	0.55	-0.27%
A3039	100	5	~700	0.49	0.15%

Table 4.1. MgSe/ZnCdSe ELO sample details

#### 4.3.3. XRI Measurements

To calibrate the MgSe growth rate both 004 and 115 XRI scans were performed at HWU for all the first series samples. Examples of the 004 and 115 scans are shown in figure 4.11 and show a series of broad peaks consistent with relaxation having occurred in the upper ZnCdSe layer. The values used for the modelling are inset and in table 4.1.

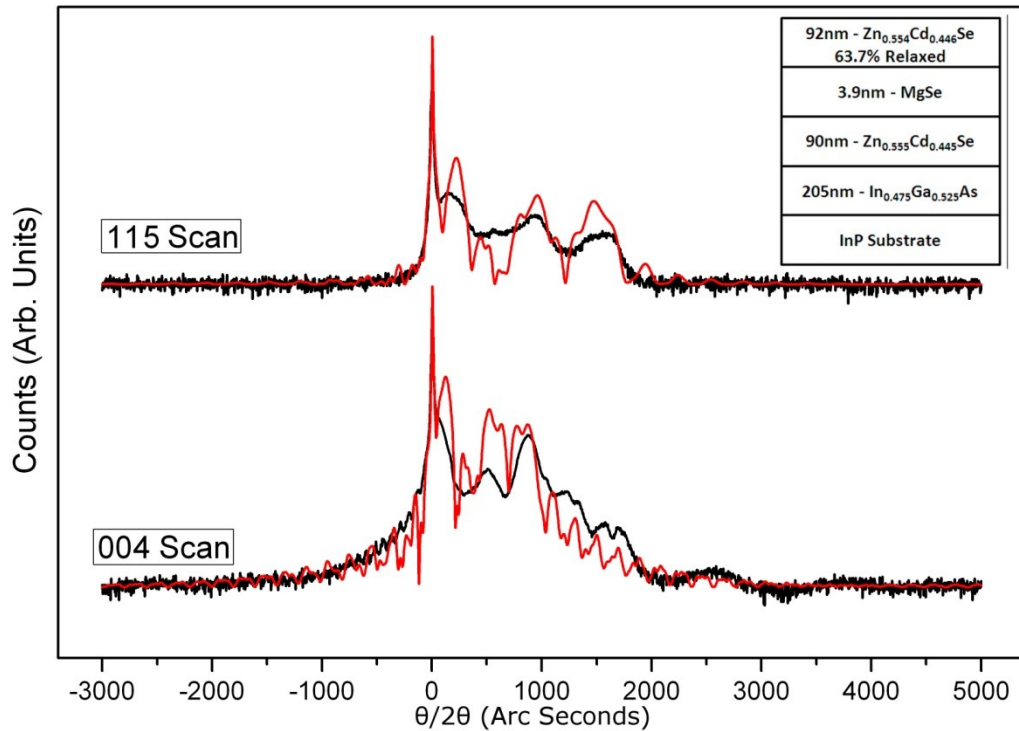


Fig. 4.11.  $\theta/2\theta$  rocking curve and model for sample A2820. The measured data is the black curve and the red curve is the simulated data. The structure used for the modelling is shown inset.

The X-ray scans from all first series samples showed relaxation, as expected as the total ZnCdSe thicknesses and mismatches are large and the samples have therefore exceeded the critical strain-thickness product. Averaged across all the scans, the ZnCdSe composition was  $\text{Zn}_{0.55}\text{Cd}_{0.45}\text{Se}$  with a variation of  $\pm 2\%$  between samples.

The composition determination should not be affected by the relaxation significantly, as the software copes with changes in lattice parameter well, but to test this, the variation of the strain-thickness product was plotted for each structure for different ZnCdSe compositions, as shown in figure 4.12. Assuming the critical strain-thickness product is  $\pm 0.4$  as for ZnSe [4.32], then the critical thickness for a given composition of ZnCdSe can be determined and compared with the values produced by the x-ray modelling.

Figure 4.12 demonstrates that the top layer will have started to relax if the composition contains more than 53% zinc (or 54% for the structures with 100nm ZnCdSe layers). And if the composition is as high as 55% (57% for the 100nm layer samples) then the entire structure will have relaxed. This produces error bounds for the compositions produced by the X-ray modelling of  $\pm 0.5\%$  per sample, which is insignificant, compared to the  $\pm 2\%$  compositional variation over the series of samples.

The determination of the MgSe thickness is complicated by both the relaxation of the samples and the cyclical nature of the XRI spectra with thickness (as discussed in chapter 5). However by plotting the GOF as a function of the MgSe thickness it is possible to produce values with a small error bound (not shown).



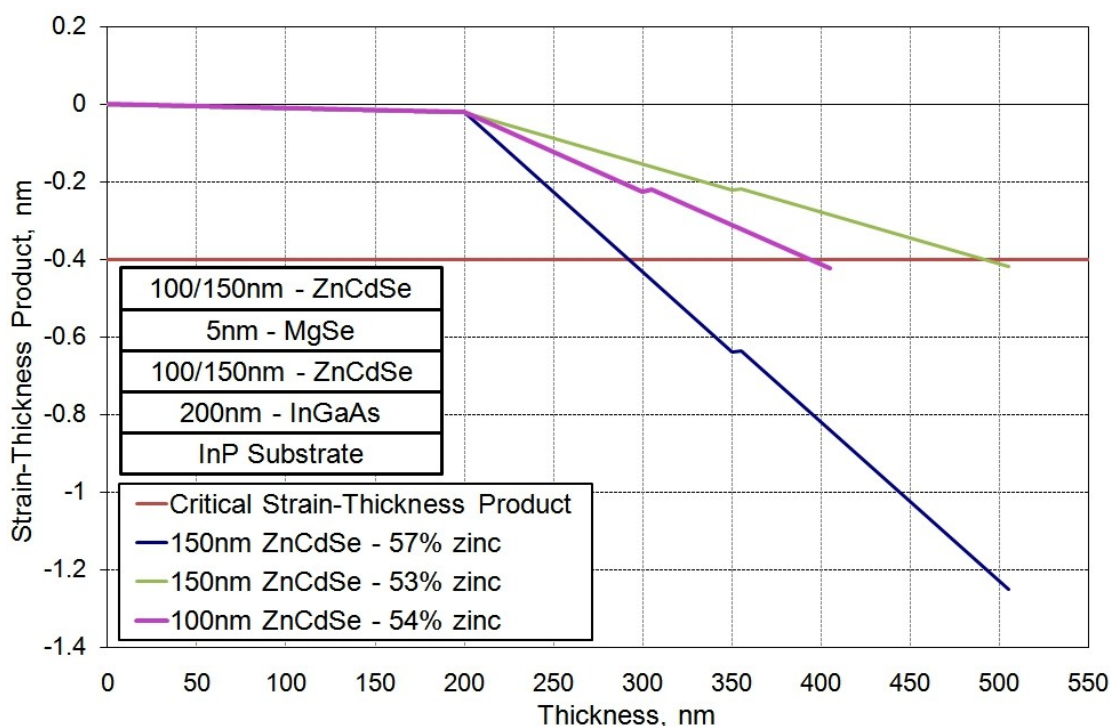


Fig. 4.12 – Strain-Thickness product vs. Thickness for the MgSe/ZnCdSe liftoff structure. The structure used to generate the plot is shown inset. Lines as per the legend.

The thicknesses and error bounds determined for the samples are shown in figure 4.13 and show a growth rate of  $1.2\text{\AA}/\text{sec}$ , which although higher than expected is realistic. Using least squares fitting and allowing any intercept results in an offset of  $1.4\text{\AA}$  and the same growth rate, but as forcing the line through the origin only changes the  $R^2$  value by 1%, this is not significant.

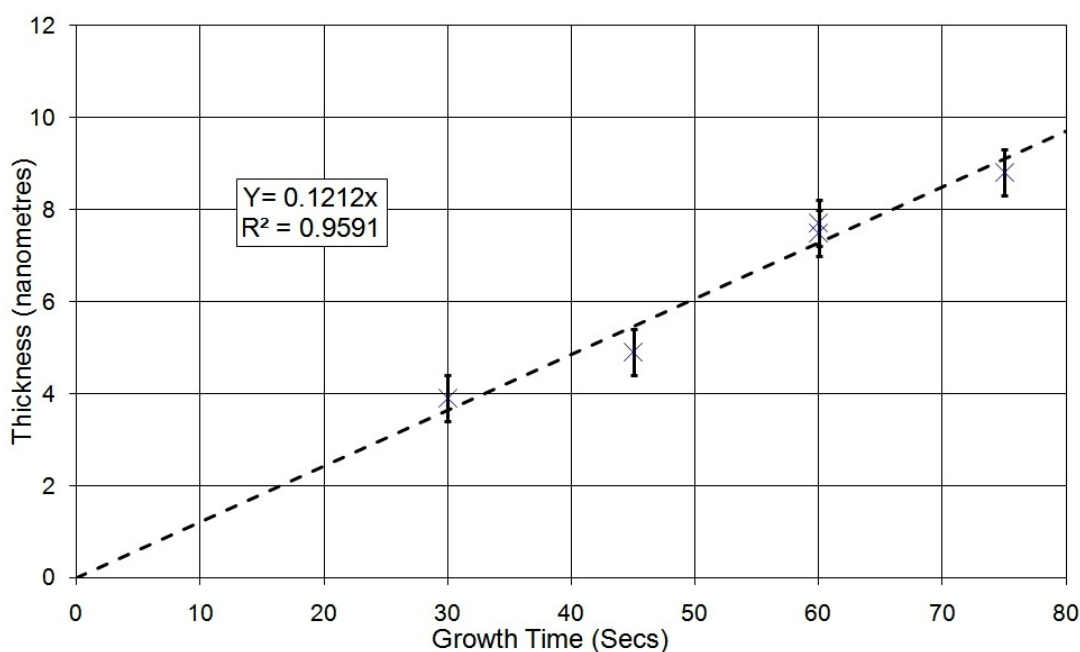


Fig. 4.13 – Growth time vs. Thickness graph for the 1<sup>st</sup> set of MgSe samples

#### 4.3.4. Structural Calibration of the 2<sup>nd</sup> Sample Set

The characterisation of the 2<sup>nd</sup> set of sample was undertaken at CUNY and was based on the growth and characterisation of a series of calibration samples. These samples (and the 2<sup>nd</sup> set of ELO samples based on them) were grown under different conditions to the 1<sup>st</sup> set of samples, making comparison difficult.

Initially a series of thick ZnCdSe samples were grown to determine the ZnCdSe growth rate. Subsequently a series of superlattices consisting of thick ZnCdSe layers separated by thin MgSe layers were grown. The separation of the superlattice peaks gave the total period thickness. Subtract the ZnCdSe thickness gives the MgSe thickness. By varying the thickness of the ZnCdSe and MgSe layers, the large error that would normally be associated with this calibration technique can be reduced.

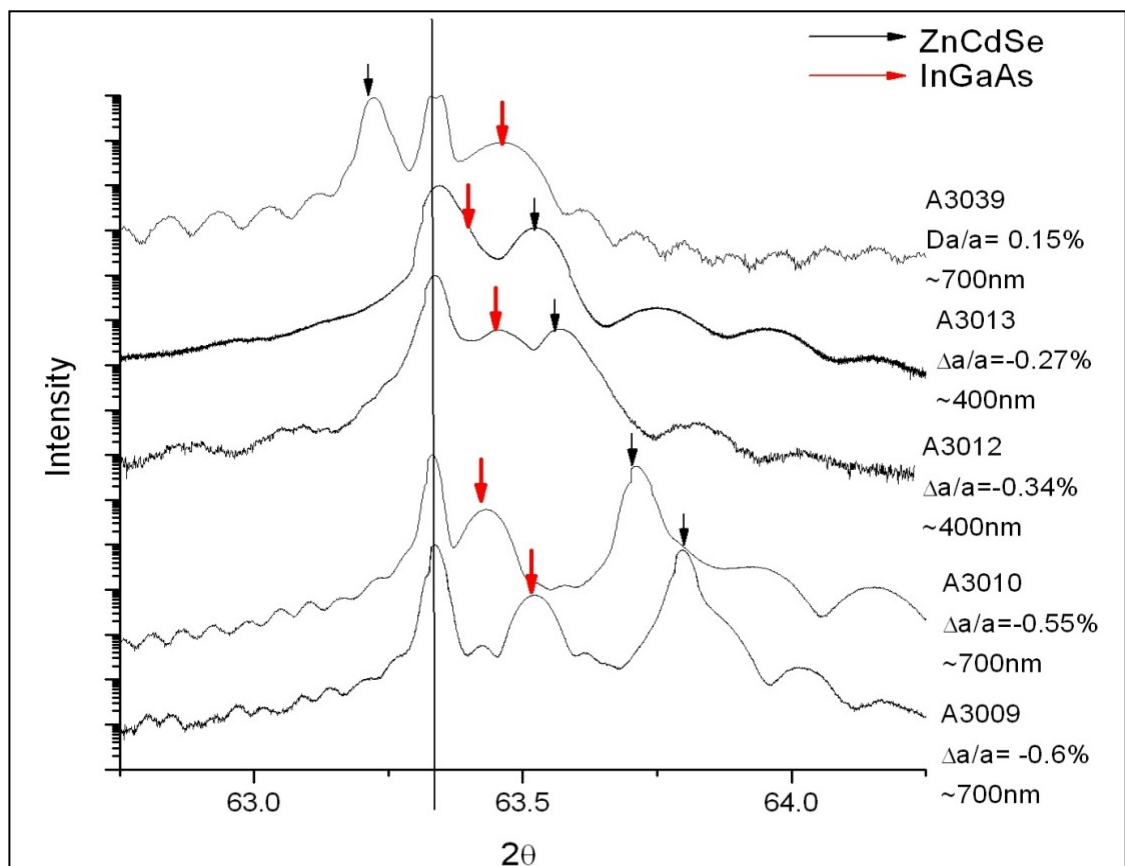
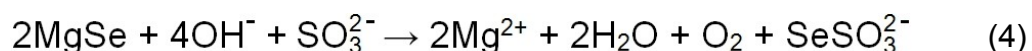


Fig. 4.14 – X-ray diffraction data for MgSe series 2 samples as measured at City College in New York. The black curves are the measured data. Red and Black arrows have been introduced to identify the ZnCdSe and InGaAs peaks. The sample each dataset is measured from, its ZnCdSe layers mismatch and thickness is shown to the left of the scans.

All of the 2<sup>nd</sup> series samples were also measured by XRD, as shown in figure 4.14. Again the ZnCdSe layers are not lattice matched with mismatches ranging from -0.6% through to 0.15%. As the peaks upper ZnCdSe layers are thick and the XRD peaks are again quite broad the structures are likely to be relaxed.

#### 4.3.5. Etching Results

Initially two samples from series 1 (A2831 and A2849) were etched using 1 molar 1:1 NaOH:Na<sub>2</sub>SO<sub>3</sub>, see equation 4. The samples were prepared in the same way as MgS samples and left in solution overnight. Seven samples lifted, three from A2831 and four from A2849. However it was necessary to use tweezers to detach the waxed epitaxial layers from the substrate, unlike the samples with an MgS sacrificial layer which typically floated to the surface of the etching solution unassisted.



Another series of samples was prepared from A2849 and placed in either 30% HCl solution or a solution of 30% HCl and 1 molar Na<sub>2</sub>SO<sub>3</sub>. After 48 hours none of the samples had etched. In the case of the HCl solution this was as expected, but the failure of the HCL:Na<sub>2</sub>SO<sub>3</sub> solution was not.

Subsequently different solutions and concentrations were tried. All work was undertaken using samples from the 1<sup>st</sup> series and several pieces of each sample were used in each solution to remove any effect from individual sample preparation. Table 4.2 shows the results along with the acidity of the solutions, whether or not the samples floated free and any comments.

The table shows that even mildly acidic solutions do not result in successful lift-off, whereas all the basic solutions do. An additional factor that must be considered is the oxidising potential of the solution. The acidic solutions have a higher oxidising potential than the basic ones and this effects the phase diagram of the sulphoselenide system. Under oxidising conditions selenium is stable even in the presence of sulphite ions [4.33].

Solution	Acid/ Base	Etched ?	Floated to the surface?	Comments
30% HCl	Very Acidic	No	n/a	As anticipated
30% HCl : Na <sub>2</sub> SO <sub>3</sub>	Very Acidic	No	n/a	Na <sub>2</sub> SO <sub>3</sub> was expected to produce an etch
Na <sub>2</sub> HSO <sub>3</sub>	Mildly Acidic	No	n/a	Even after 48hrs+ in solution samples did not etch
Na <sub>2</sub> SO <sub>3</sub>	Mildly Basic	Yes	Yes	Samples etched very cleanly and floated free
1M NaOH : Na <sub>2</sub> SO <sub>3</sub>	Fairly Basic	Yes	No	Samples etched but needed to be detached from substrate
Saturated NaOH : Na <sub>2</sub> SO <sub>3</sub>	Very Basic	Yes	No	As 1M NaOH : Na <sub>2</sub> SO <sub>3</sub>
1M NaOH	Very Basic	Yes	No	Waxed epilayers needed significant force to be freed from the substrate

Table 4.2. – Results of investigation into etching of first series of MgSe samples.

The effect of MgSe layer thickness was also investigated using pieces of all five samples from series 1 by placing them in the 1 molar 1:1 NaOH:Na<sub>2</sub>SO<sub>3</sub> solution for ~12 hours. However as the etch took a long time and the epilayers did not float free it was impossible to determine any time dependence with layer thickness. The MgSe thickness was found to have an effect on the quality of the lifted material though, with the thinnest MgSe layer producing the deposited material with the fewest cracks. This will be discussed in the next section.

The second set of samples were prepared in the same way, with a wax cap being deposited using the hot plate. Unfortunately none of the samples resulted in the successful lift-off of material under any conditions. Applying small amounts of pressure to the wax on the top of the samples resulted in some appearing to float free, a couple even appeared to lift on their own without force. However when these were deposited onto a new substrate, no ZnCdSe was left after the wax had been removed. Examining the underside of the wax that had lifted also showed no ZnCdSe.

The wax caps detaching from the samples was a new phenomenon and was investigated by re-waxing and etching the same sample pieces. But the same thing was observed, the wax caps either floated free or could be detached from the substrate with a small amount of force but no material came with them. The reasons for this have not been determined but it may be related to the interaction of the sodium hydroxide/sodium sulphite solutions with the wax or ZnCdSe surface.

The failure of any of the second set of MgSe samples to etch is difficult to explain as the minimum thickness of MgSe in these samples is 5nm and based on the 1<sup>st</sup> set, this should be more than sufficient for liftoff. The only differences between the two sets of samples are the growth conditions and the much thicker top ZnCdSe layer and although these do not immediately suggest a viable failure mechanism, one will be proposed in section 4.4.

#### **4.3.6. PL Characterisation**

Figure 4.15 shows a comparison of the PL emission from one of the series 1 samples (A2849) before and after lift-off. The measurements were made at 77K in a LN2 cryostat using ~10mW excitation from a 40mW 405nm laser diode. The beam was focused using a 70mm focal length lens to produce a ~6 $\mu$ m diameter spot. The emitted light was collected using the same lens and imaged using a fibre coupled 100mm focal length spectrometer and CCD. Spectra were typically recorded using an integration time of 10 seconds.

There is little difference between the spectra which are both dominated by excitonic recombination. Both spectra have identical FWHM and peak emission energies, within experimental error ( $\pm 2.7$  meV for both measurements). No defect related features were seen in the PL taken from the lifted samples, which is similar to our previous work with ZnSe and ZnCdSe structures [4.1-4.3, 4.34].

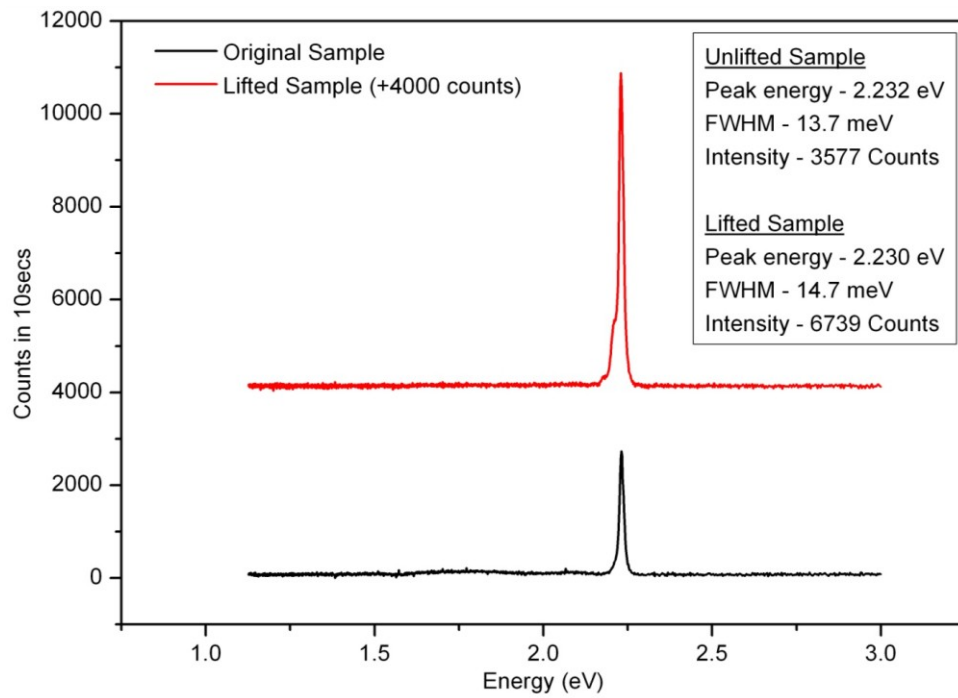


Fig. 4.15. PL comparison of pre and post lifted MgSe sample. The black curve shows the data measured from the original unlifted sample and the red curve the lifted and deposited material offset by 4000 counts. The position, intensity and FWHM of both peaks is shown inset.

The lack of change in the peak emission energy is interesting, as previously we have observed small shifts in emission energy due to the change in strain state of the ZnSe structures [4.34]. However this is compatible with the results of the X-ray diffraction measurements, which showed the layers are relaxed.

There is a noticeable increase in the emission intensity following lift off. There are probably a number of factors for this but the removal of both the InGaAs buffer layer and InP substrate is likely to be the largest, as these are both strongly absorbing at 2.2eV. Hence their removal will result in a significant reduction in the number of carriers being absorbed.

#### 4.3.7. Surface Characterisation and Cracking

As explained at the start of this chapter, the major problem with the ELO process is its inability to reliably produce high quality, crack-free deposited material. To investigate this, the surfaces of the samples can be compared before and after liftoff using an optical microscope and crack densities measured.

#### 4.3.7.1. First Series Samples (A28XX)

Figure 4.16 is a typical image of the surface of one of the 1<sup>st</sup> series of ZnCdSe/MgSe samples (A2820) prior to cleaving. The surface is already rough and covered in features, unlike the MgS based samples shown in figure 4.4. The samples have two types of features, in addition to scratches and dust spots. The first is a network of 'orange lines' along the  $[110]$  or  $[1\bar{1}0]$  and the second, are large 'pink structures' distributed across the surface. Compared to the orange lines, the pink features are shorter and more significantly raised above the surface, see figure 4.17. There is some correlation between the two types, but the pink structures do not always coincide with the orange lines.

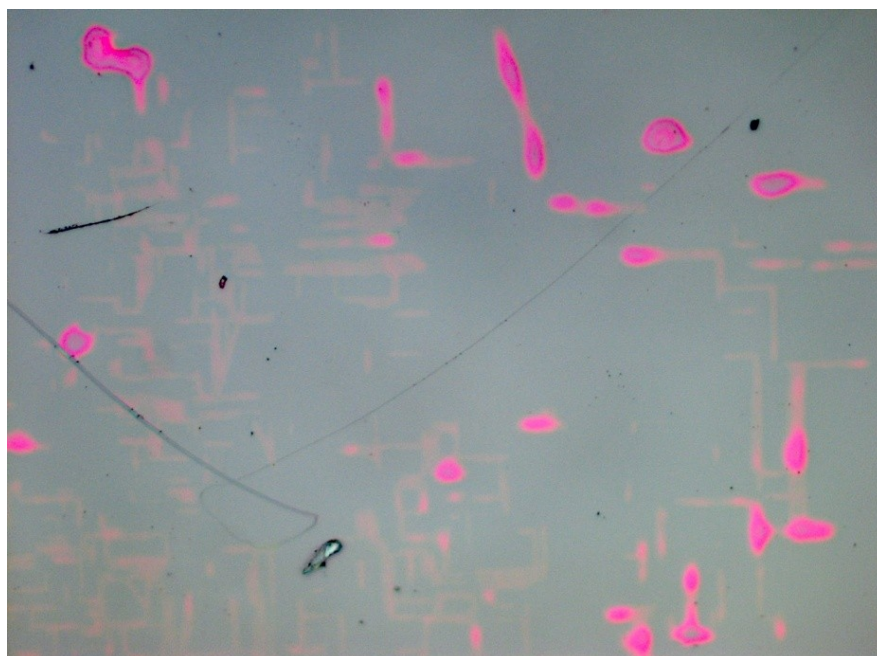


Fig. 4.16 – A 500x magnification visible light image of the surface of sample A2820 showing the orange and pink features seen on the samples surface.

The size and number of features were counted and the results are shown in table 4.3. The density of the orange lines varies significantly across the surface of each sample but the average density is constant across all the samples. The pink structures show a more consistent distribution over each sample but a large variation between samples, although this may be due to the lower total number of features visible and the small sample set.

The phase contrast feature of the microscope allows the vertical dimensions of the features to be visualised and shows that both the orange lines and the pink



structures are raised above the surface. A representative phase contrast image (a) is shown in figure 4.17. A PL microscope image (b) of the same area is also shown demonstrating that the pink structure features are absorbing.

Sample No.	MgSe Thickness (nm)	'Orange Lines' density (cm <sup>-2</sup> )			'Pink structure' density (cm <sup>-2</sup> )
		Minimum	Maximum	Average	
A2820	3.9	2.1±0.4x10 <sup>3</sup>	6.0±0.3x10 <sup>5</sup>	1.5±0.5x10 <sup>5</sup>	268±13
A2846	4.8	1.7±0.1x10 <sup>3</sup>	4.8±3.7x10 <sup>5</sup>	1.2±0.9x10 <sup>5</sup>	134±9
A2821	7.5	1.3±0.2x10 <sup>3</sup>	4.5±1.6x10 <sup>5</sup>	0.8±0.7x10 <sup>5</sup>	551±38
A2831	7.7	2.0±0.3x10 <sup>3</sup>	7.3±0.5x10 <sup>5</sup>	1.8±0.2x10 <sup>5</sup>	412±19
A2849	8.8	3.1±0.1x10 <sup>5</sup>	6.0±1.0x10 <sup>5</sup>	1.5±0.2x10 <sup>5</sup>	464±26
Average	6.5	6.3±0.1x10 <sup>4</sup>	5.7±2.5x10 <sup>5</sup>	1.4±0.5x10 <sup>5</sup>	366±35

Table 4.3. Details of the feature density of the pre-etched samples

The deposited material was also analysed and the size and density of any cracks/features counted. Typically the deposited material was quite badly broken with a large number of cracks and pieces missing, an example of this can be seen in figure 4.18. As the unetched material has imperfections, cracking in the deposited material is not unexpected but observing any changes should still allow the effect of altering the etch process to be investigated.

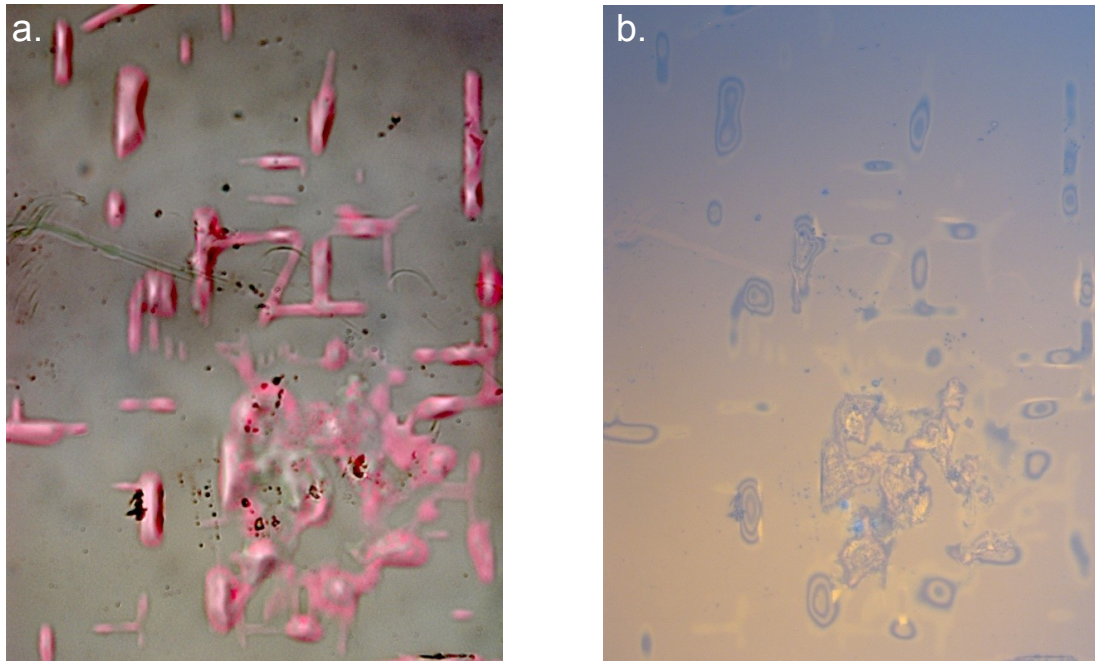


Fig. 4.17. Phase contrast (a) and PL(b) microscope images of the un-etched surface of A2821 showing the orange line and pink structure features.





Fig. 4.18. A 50x magnification visible image of a piece of deposited epitaxial material demonstrating the difficulty in measuring crack densities for those samples that do not lift/deposit well.

One complication is the need to produce deposited material that approximately fills the area imaged by the microscope (so a known area can be used to calculate the crack density) and this was not always possible. When it wasn't the dimensions of the largest area available were estimated and this used to calculate the density. However some deposited material was of such poor quality that the largest area deposited was not sufficient to allow any analysis.

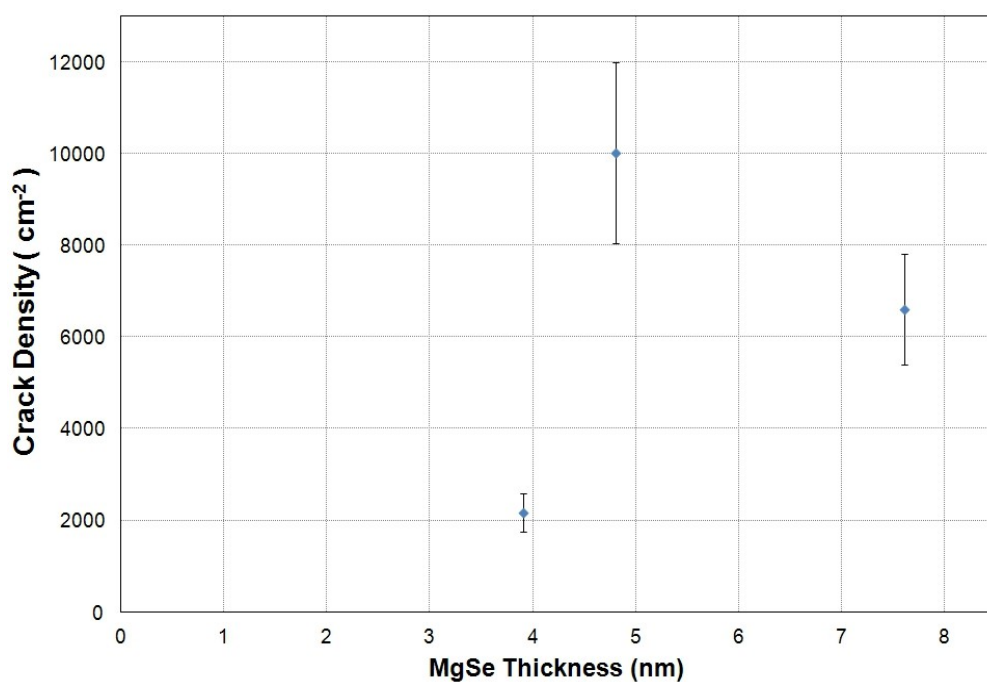


Fig. 4.19. Crack density of deposited layer vs. MgSe thickness

Fig. 4.19 shows the result obtained using the 1 molar, 1:1 ratio NaOH:Na<sub>2</sub>SO<sub>3</sub> solution. No results are shown for sample A2849 (MgSe thickness 8.8nm) as the largest area deposit was too small to be analysed. The sample with the smallest MgSe thickness (A2820) has the lowest crack density but the other points do not show a linear trend. The crack density measured for all the samples seems to be close to the minimum 'orange line' density found in the un-lifted samples.

Figure 4.20 shows the variation of crack density with solution concentration. Pieces of A2820 and A2846 were also etched in 2 and 0.5 molar solution respectively, but the largest piece successfully deposited was not sufficient for analysis. The deposited material again has crack densities similar to the orange line features seen in the un-lifted samples. However as the errors on each data point are large and it is not possible to look at the full concentration range for either sample, it is difficult to determine any trend in the data. But it does appear that there is little correlation between solution strength and cracking density.

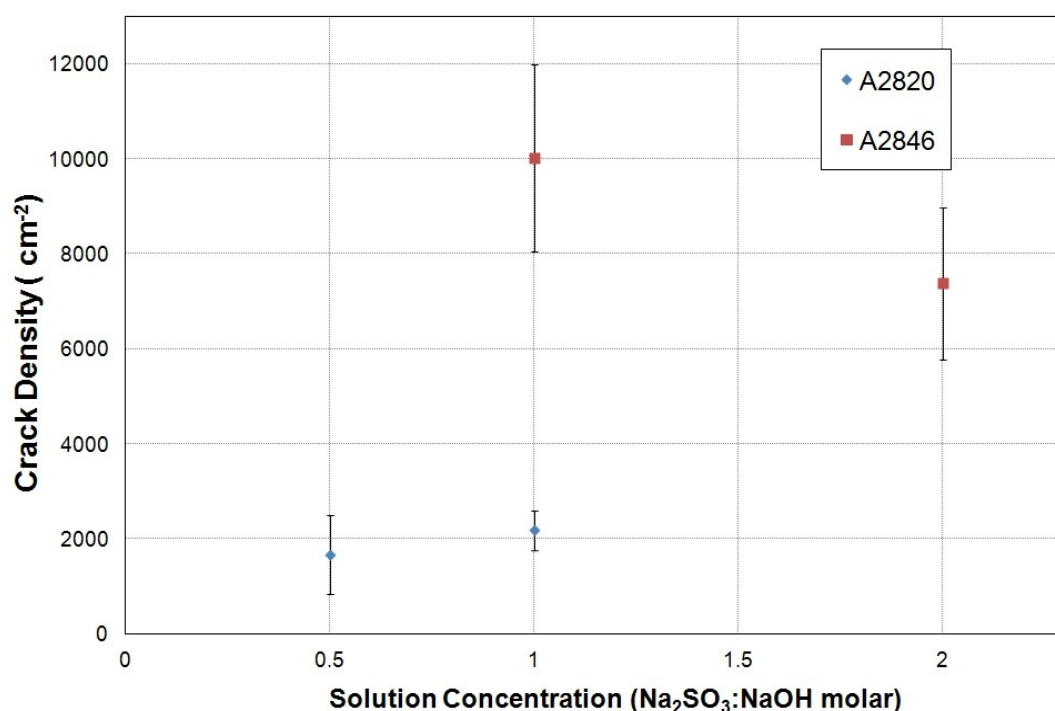


Fig. 4.20. Crack density vs. Solution concentration for A2820 and A2846.

Samples were successfully etched with solutions of either pure NaOH or Na<sub>2</sub>SO<sub>3</sub> alone, see figure 4.21. For pure NaOH, this was entirely unexpected and suggests that the etching process is very insensitive to the solution used.

As no correlation between the etching conditions and the quality of the deposited material could be determined, no further investigation was undertaken.

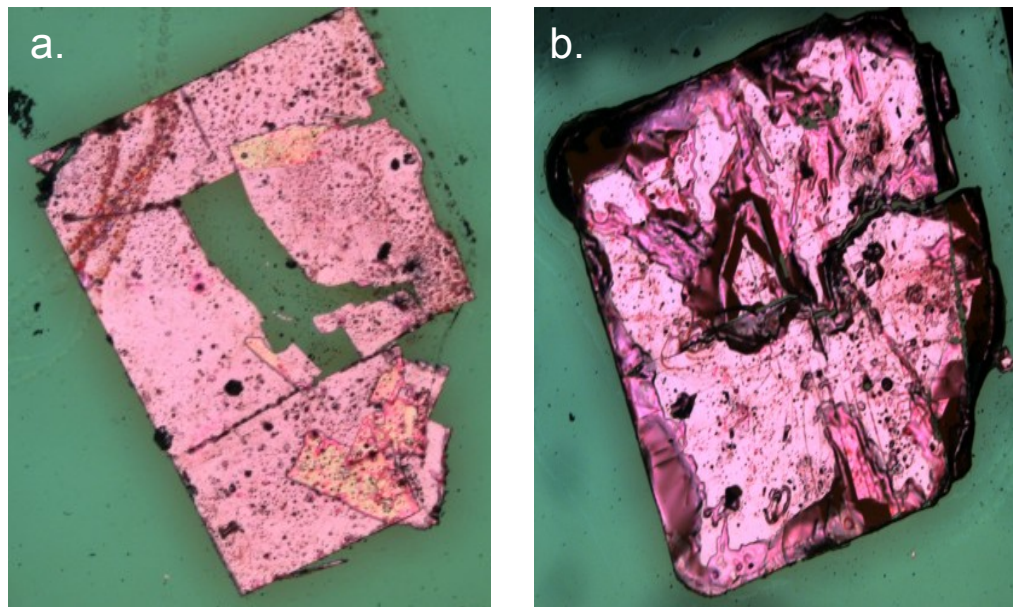


Fig. 4.21. 50x magnification images of samples lifted using (a) NaOH and (b) Na<sub>2</sub>SO<sub>3</sub>.

Using the MgSe ELO process it is possible to deposit continuous pieces of material as large as 200-250 $\mu\text{m}^2$  for all the samples except A2849. These areas appear identical to the unlifted material as can be seen in Figure 4.22, which shows 1000x magnification images (an area of 280x210 $\mu\text{m}$ ) of A2831 before (a) and after (b) ELO.

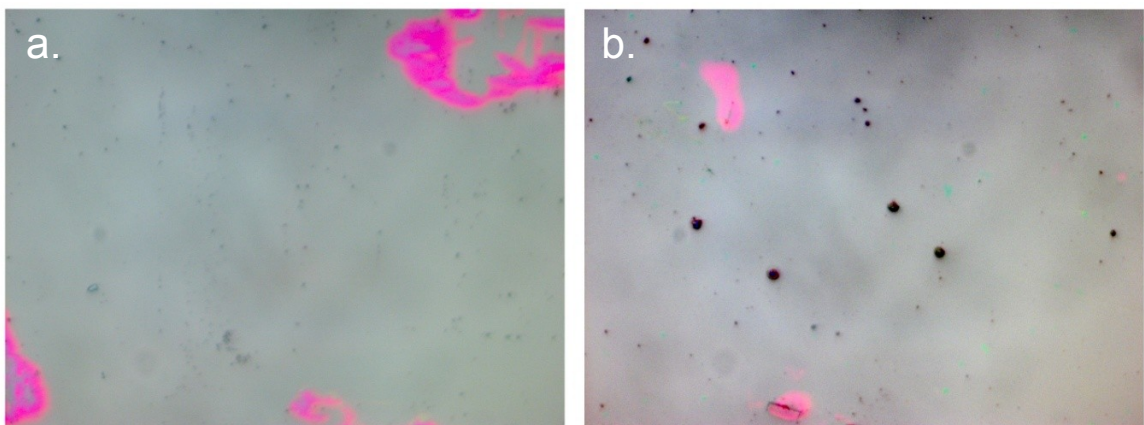


Fig. 4.22. 1000x magnification visible images of the surface of A2831 before (a) and after (b) lift-off.

#### 4.3.7.2. Second Series Samples (A30XX)

The 2<sup>nd</sup> set of samples all have smooth feature-free surfaces (unlike the 1<sup>st</sup> set). However under UV illumination and high magnification a network of dark lines can be seen under the surface. These dark lines are consistent with the formation of threading dislocations at a layer boundary due to structural relaxation, an example of this is shown in figure 4.23.

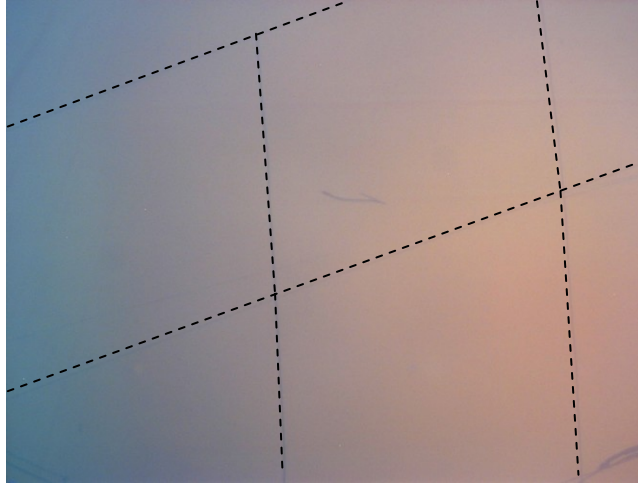


Fig. 4.23. 500x UV image of A3013 showing the dark lines seen below the epilayers. Dotted black lines have been placed over dark lines to improve their visibility.

As no pieces of material larger than a few microns square could be lifted and deposited, no further analysis could be undertaken. The small pieces of material that were deposited typically came from the etched samples where the capping layer had been removed forcibly. An example of this is shown in figure 4.24. This behaviour will be explained in section 4.4.

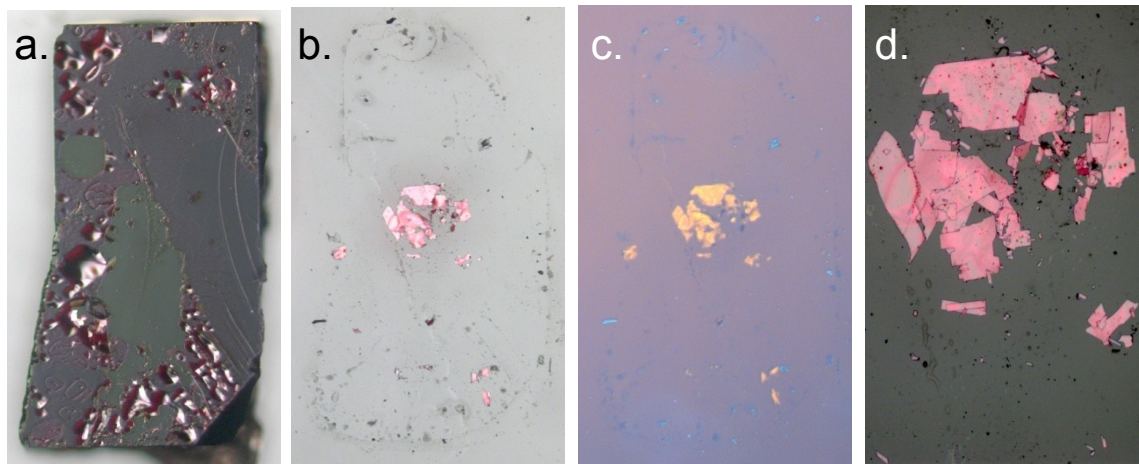


Fig. 4.24. (a) 50x image of the A3039 substrate after forcible cap removal, (b) 50x image deposited material from the cap, (c) 50x PL image of deposited material, (d) 200x image deposited material.



#### 4.4. MgS and MgSe ELO Failure Modes

As described in sections 4.2.6 and 4.3, a number of problems have been encountered with ELO with a number of samples. The commonalities between all these failures are:

1. Samples fail to etch even though the sacrificial layer is sufficiently thick
2. Epilayers and cap do not float free, unlike good samples
3. Deposited material is very poor quality

As the objective for the development of the ELO process was to improve its reproducibility and ensure high quality deposited material, these failures were investigated

Previously two failure modes for the MgS ELO process have been identified: there could be too much zinc in the MgS layer or the MgS layer could be too thin. These failure modes are assumed to be shared by the MgSe ELO process. However the problems encountered after the MBE system was moved with MgS samples and the CUNY MgSe samples did not seem to be explained by either of these modes. This suggests that there must be at least one additional failure mode that had not previously been identified.

Previously MgS grown with a magnesium cell temp of 375°C had a growth rate ( $G_R$ ) of  $\sim 0.4 \text{ \AA/s}$ . After the MBE machine was moved the same magnesium temperature resulted in a growth rates determined by XRI of  $\sim 0.2 \text{ \AA/s}$  and increasing the magnesium cell temperature did not increase the XRI determined growth rate. This reduced growth rate was initially considered as a possible explanation for the etching/ELO failure of these samples, but as no connection could be found between the MgS growth time and the success or failure of the ELO process, it could not be the sole cause.

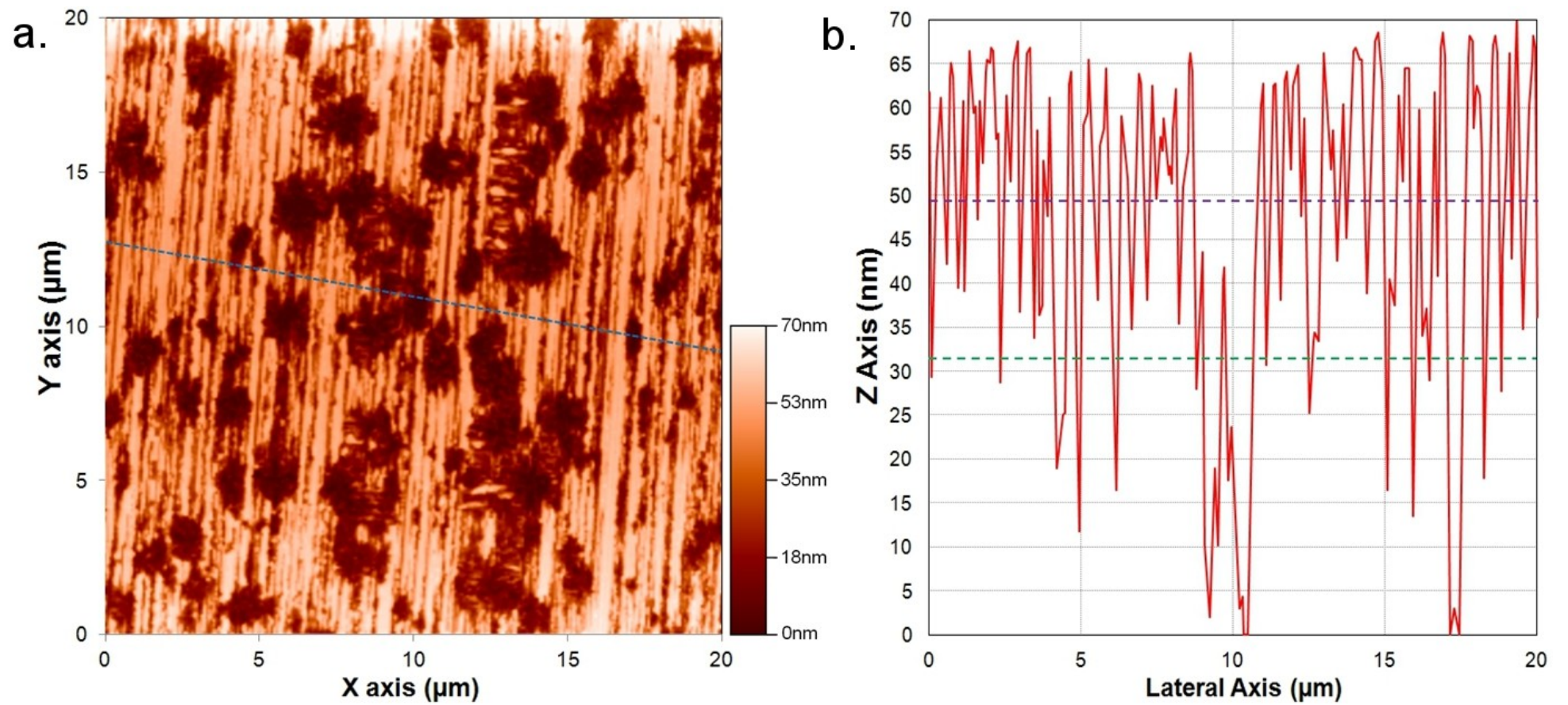


Fig. 4.25. AFM scan of HWC387. (a) shows the surface image produced by the AFM. (b) shows the z-profile of the dotted dark blue line in (a). The dotted green line in (b) shows the average height of the surface oscillations and the dotted purple line the expected thickness assuming a  $G_R = 0.4 \text{ \AA/s}$ .

AFM images taken of the surface of MgS samples show pits in the surface, an example of this is shown in figure 4.25. HWC387 has a 40minute MgS deposition time, considerably longer than that used for ELO samples (typically 5-10mins), however it was chosen as it clearly shows the pits observed. The pits in HWC387 are approx. 50-70nm deep (see fig.4.25 (b)), which is roughly the thickness of the MgS layer. The exact depth is difficult to determine due to the very rough surface caused by the corrugation effect seen in thick MgS samples [4.35]. However pits probably extend through the MgS layer to the ZnSe layer underneath. A schematic representation is shown if figure 4.26.

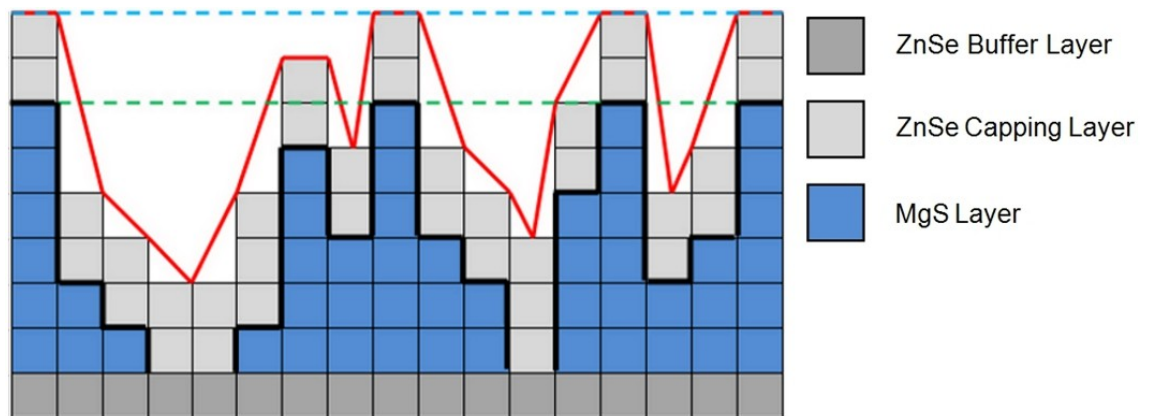


Fig.4.26. Schematic representation of a capped rough MgS surface like the one in figure 4.25.

Although the schematic has very different lateral and vertical scales it is designed to show that when a rough layer of MgS is covered with a thin layer of ZnSe, some of the MgS will either be only very thinly covered (~1-2ML of ZnSe perhaps) or completely exposed to the air. If this sample were etched the pits would produce 'gaps' in the lifted material where the ZnSe cap is in direct contact with the buffer layer. The presence of the pits would also produce gaps in the sacrificial layer and reduce the etch speed by providing partial barriers to the etch solutions progress through the layer. Slow etch speeds were also seen with the most problematic MgS and MgSe samples.

When the capping layer thickness is greater than the roughness of the sacrificial layer, then a rough but continuous capping layer will be formed, which has thin pillars extending through the sacrificial layer joining it to the layer underneath, see fig. 4.27. The sacrificial layer is now fully covered by the capping layer but when etched these pillars will remain and stop the epilayer from lifting. If the pillar density is small then a small amount of force will cause them to break and

release the epilayers. However if the density of pillars is greater, then the force required to break them may exceed the structural strength of the epilayers and wax causing them to fracture. This effect was again seen with both the CUNY MgSe and post system move MgS samples.

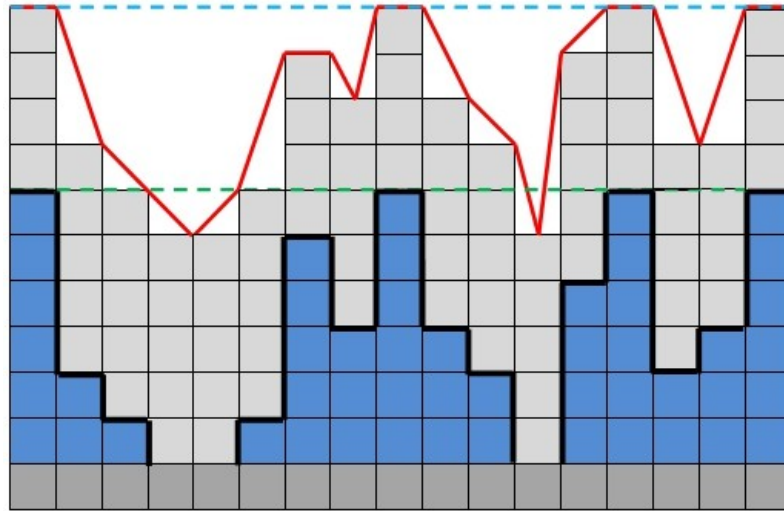


Fig. 4.27. Schematic representation of a sample with a rough MgS layer when the capping layer thickness  $\geq$  the MgS layer roughness.

Spectroscopic ellipsometry (SE) measurements were also made of a number of MgS samples grown under similar conditions to HWC387 (see chapter 6). The MgS thicknesses determined from these measurements the growth rate was found to be  $0.4\text{\AA/s}$  MgS or higher (for samples grown with a higher Mg cell temp). Using these thicknesses and considerable effort some of the XRI models were refined to produce better fits but some could not be improved.

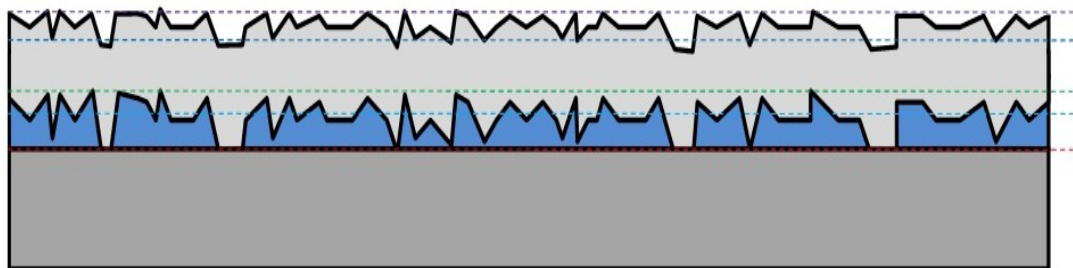


Fig. 4.28. An MgS/ZnSe XRI sample showing the effect of a rough MgS layer on the samples structure. Colour scheme is the same as fig. 4.26 and 4.27 but the horizontal scale is larger. The coloured lines are included to visualise the various regions of the sample.

The presence of a rough MgS layer and ZnSe pillars can also explain the discrepancy between the MgS growth rate predicted by XRI and SE for these samples and the historical rate. Figure 4.28 is a schematic of a generic MgS/ZnSe XRI sample with a rough MgS layer. The roughness of the MgS layer



is roughly mirrored in the surface of the sample, as although ZnSe usually reduces the surface roughness, an insufficient amount has been grown in these samples to eliminate it. HRXRD is very sensitive to tilts in the sample layers (see chapter 6) so the small tilts introduced at the numerous interfaces will reduce the measured intensity.

This will reduce the MgS and upper ZnSe layer thicknesses that produce the best modelled fit to the XRI spectra and result in a lower growth rate being determined than by SE. This is often seen with the ZnSe layers in these samples, as typically a better fit is achieved with a significantly thinner ZnSe upper layer compared to the lower, although both will have the same nominal growth time.

#### 4.5. Conclusions

The work contained in this chapter shows that it is possible to use the epitaxial lift-off process developed by the MBE group at HWU to lift material grown on both GaAs and InP substrates by utilising either an MgS or MgSe sacrificial layer. It also showed that when performed under ideal conditions the lifted material will be identical, in terms of both physical and optoelectronic properties, to the as-grown material.

Any additional cracking caused in the material lifted using an MgS layer has been shown to be due either to the etching process or rough handling of the material after it has been etched. The causes of this cracking were investigated, to understand its origin and reduce its appearance.

A model of the samples microstructure was presented to explain the unexpected behaviour of both some MgS and MgSe samples based on the sacrificial layers being very rough with columns of cladding material through them. This model accurately describes the behaviour seen in a number of examples. However no measurements have been made to prove the existence of the pillars in the sacrificial layers at present.

## 5. Development of a Lattice Matched, MgS rich ZnMgSSe Quaternary Alloy

This chapter details all the work undertaken to develop a lattice matched, MgS rich ZnMgSSe quaternary alloy (QA). Initially this alloy was developed as a replacement barrier material for ELO samples, as MgS cannot be used as both a sacrificial layer and a barrier in these samples, but it also has a number of other beneficial characteristics that make its development highly useful. To be a successful replacement barrier material, the alloy must both provide good carrier confinement and a lattice constant close enough to GaAs that it can be grown without introducing significant strain energy. As the intended use of the alloy is in ELO structures it must also be etch resistant.

The initial investigation of an MgS rich QA was undertaken by Richard Moug who grew a series of samples with the composition produced by using the same zinc, magnesium, selenium and zinc sulphide fluxes routinely used to grow ZnSe and MgS. The characterisation of these samples comprised AFM, HRXRD and PL measurements, as well as the use of ELO to allow the alloys absorption to be measured, and will be described in section 5.2.

As these original QA samples were not found to have a composition that is lattice matched, a further series of samples were grown using increased Zn and Se fluxed. The composition of this 2<sup>nd</sup> set of QA samples was investigated using XRD and found to be close to lattice matched. This will be described in section 5.3. During the characterisation of these samples problems were found relating to the interpretation of XRI spectra. This resulted in a thorough investigation of their modelling. Section 5.4 describes this investigation.

As the second series of samples were found to be more zinc rich than desired and the RHEED pattern observed during growth typically change to a spotty 3D pattern after a few minutes, a 3<sup>rd</sup> series of samples were grown. These were

designed for both XRD measurement and (by the incorporating an MgS sacrificial layer) ELO so the QA bandgap and lattice constant can be measured from the same sample. The issues arising from the growth of these samples as well as the background to this method will be detailed in section 5.5. Finally the chapter will be concluded and suggestions for further work made in section 5.6.

## 5.1. Introduction

In any structure where MgS is used as a sacrificial layer it will either be highly difficult or impossible to also use it as a barrier material, as any layer thicker than ~4nm will be etched away[5.1]. It is therefore necessary to use an alternative material for the barriers in an ELO structure.

This new barrier material must meet at least 3 simple criteria to be successful. First, it must have a band-gap substantially larger than that of the material used in a quantum well or dot layer, to provide sufficient confinement for efficient emission (see figs. 4.29(b) & 6.10 for the increase in emission energy for a ZnSe QW and CdSe QWs & QDs). Second, it must be resistant to the etch solution used to remove the MgS layer (30% HCl) otherwise it will be damaged. And finally, it must also have a lattice constant that is compatible with growth on a GaAs substrate.

If the alloys lattice constant is close to that of GaAs it also means it can also be grown thick without relaxation and dislocation formation. This is of particular interest in optical devices where it is often necessary to be able to introduce wave-guiding regions with thicknesses that are comparable to the wavelength of visible light (400 – 800nm). Figure 5.1 shows the variation of the critical thickness before relaxation with lattice mismatch based on our work with ZnSe [5.2]. It shows that to be able to grow a layer >400nm thick without the strain-thickness product exceeding  $0.4 \pm 0.1 \text{ nm}$  requires a layer with a lattice mismatch less than  $0.1 \pm 0.025\%$  of GaAs

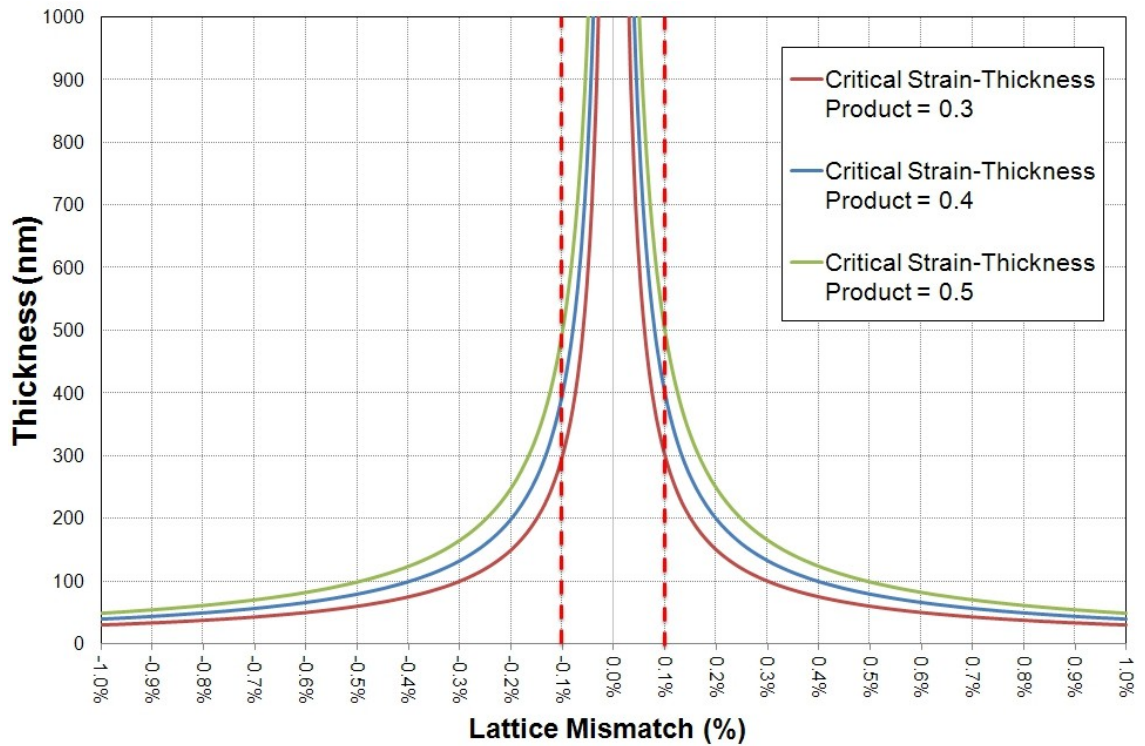


Fig. 5.1. Graphical representation of the variation of the critical layer thickness versus lattice mismatch.

The solid colour lines represent how the maximum layer thickness that can be grown before relaxation occurs varies with thickness for a number of critical strain-thickness values. The dotted red lines show the range of mismatch that would allow waveguide thicknesses to be grown without relaxation.

It is also necessary that the layers grow relatively quickly, ideally faster than  $1\text{\AA}/\text{sec}$  or  $0.36\mu\text{m}/\text{hr}$ , so that thick layers can be grown on a sensible timescale i.e.  $<4\text{-}5\text{hrs}$  so that structures can be grown in a normal  $8\text{hr}$  working day. This should be attainable as high quality ZnSe and MgS are routinely grown at a rates of  $0.6\text{ -}1$  and  $0.4\text{ \AA}/\text{sec}$  respectively and QA will grow faster than these.

As large band-gap material typically also have smaller refractive indices (see chapter 6), this makes them ideal cladding layers for lower band-gap materials. This would ideally require thick lower band-gap/higher refractive index layers (ZnSe for example) to be grown between the QA layers, but as the step between the QA and air or GaAs will be far larger than to ZnSe/CdSe, the QA layer will also be able to act as a wave-guide itself.

The obvious first choice for a replacement barrier material is ZnSSe as this has a band-gap larger than bulk ZnSe and CdSe and can be grown lattice matched to GaAs. The draw back with this material is that in growing it lattice matched,

or with low strain, it can contain only  $\sim 6\%$  sulphur. The result is that its band-gap will only be  $\sim 2.70$  eV at room temperature, roughly 40 meV above that of ZnSe, and its band alignment is such that the 40meV offset is all in the valence band. As such it will not provide much confinement for any carriers generated in a ZnSe QW and will limit the minimum well thickness possible. However it would provide sufficient confinement for any carriers generated in CdSe QDs.

The low confinement energy also has the additional effect that exciton binding energy enhancement would not be sufficient to exceed thermal energy at room temperature ( $k_B T(300K) = 25.9\text{meV}$ ) and hence any structures grown would not show excitonic behaviour at room temperature [5.3]. This would limit the range of applications for any liftoff structures incorporating ZnSSe barriers.

Without the introduction of an additional Knudsen cell to the MBE growth chamber, it would also necessitate a change in the ZnS cell temperature during growth of ELO samples to achieve the 6% incorporation required for a lattice matching. This requires an interruption in the growth to allow the cell to cool and stabilise, increasing the growth time and possibly allowing the surface composition to change due to either unwanted species (sulphur etc.) present in the chamber absorbing on the surface or material evaporating from the surface layer, as discussed in chapter 3.

Another possible solution would be to use a lattice matched  $\text{MgS}_{0.88}\text{Se}_{0.12}$  layer. This would have a band gap around 4.4 eV, which would be more than sufficient for carrier confinement. However, as was demonstrated in the previous chapter, the introduction of only selenium into a magnesium alloy is not a reliable way to render it etch-resistant. The growth of MgSSe would also again require the flux of one of the cells to be changed during growth and as stated, this is not ideal. This leaves only one viable option, which is to use a quaternary ZnMgSSe alloy.

This alloy has a number of advantages, principally the ability in theory to tailor both band-gap and lattice constant separately. However in the case of

ZnMgSSe there are thermodynamic limitations due to the large difference in the heats of formation of the component binary compounds. As Sorokin et al state, *“the binary compound with the maximal standard enthalpy (MgS) does not have the lowest lattice parameter. Thus, the segregation of MgS-enriched phase gives a gain in chemical constituent of free energy without an increase in the deformation contribution”*[5.4], the result is that a large decomposition region exists in the centre of the compositional space, see figure 5.2. Within this region stable growth is not possible as the alloy will decompose (phase segregate) either immediately (spinodal decomposition) or after nucleation of one of the constituent compositions (bimodal decomposition).

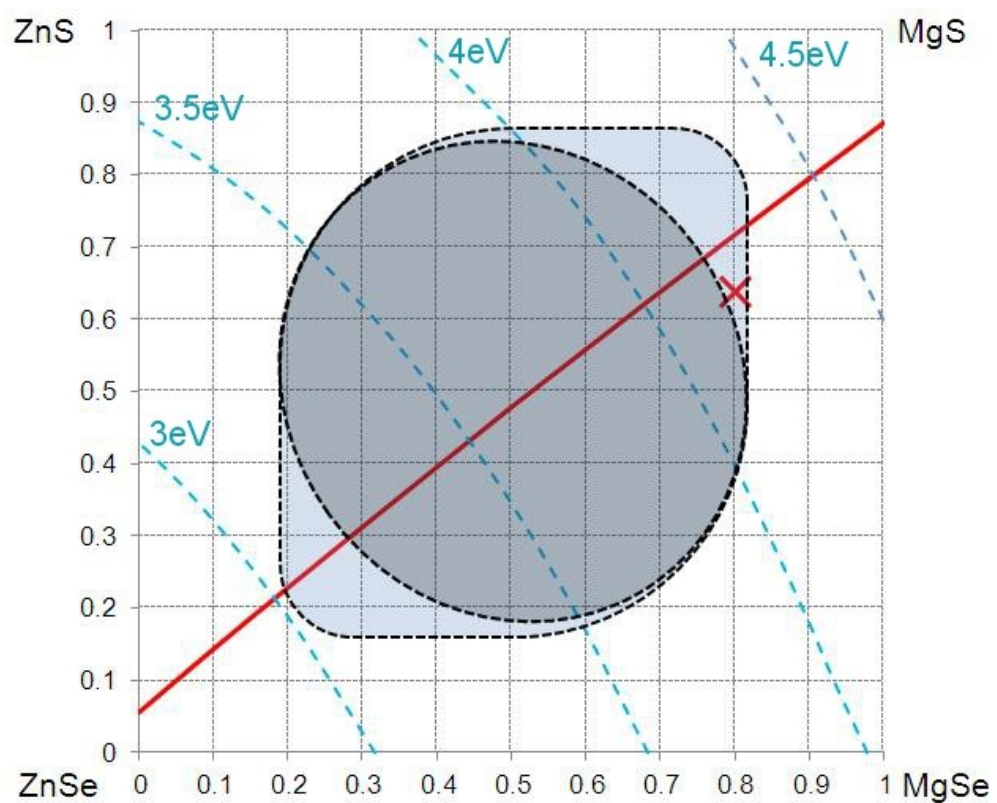


Fig. 5.2. ZnMgSSe compositional square. The light and dark grey areas are schematic represents of the binodal and spinodal decomposition region based on ref. [5.4]. The red line the GaAs lattice match line, the dotted blue lines are lines of constant bandgap and the red cross the composition determined for the 1<sup>st</sup> series of QA samples

Typically there would be an additional strain energy term associated with the alloy decomposing into two binary compounds but in the case of ZnMgSSe as the tie lines (the lines that link any unstable composition to the nearest stable binaries on either side of the decomposition region) run almost parallel to the lattice constant lines, this is not the case and instead it is possible for the alloy to decompose without any increase in strain energy. In some material systems

(GaMnAs for instance) it is also possible to grow at a sufficiently high growth rate that the atoms on the surface do not have sufficient time to reorganise into two separate phases, and this allows meta-stable alloys to be grown. But in the case of ZnMgSSe the need grow MgS inside a narrow growth window and the ZnSe in such a way as to achieve smooth pseudo-morphic growth, this is not possible.

The apparent lack of a binodal decomposition region in the ZnS and MgSe rich regions of the compositional space is caused by the four points that define the binodal and spinodal regions all having to lie on a line of lattice match and as these move away from the line of lattice match they must eventually converge on the same point. As such if the regions had been drawn accurately (which they are not) there would be only one point with no binodal region with a small area around it where the area is extremely small. .

However even with a large decomposition region where stable growth is impossible, there is still an area in the MgS rich portion of the square where it is possible to grow an alloy that matches all of the conditions required to replace MgS in an ELO structure - large bandgap, lattice matched and etch resistant.

## 5.2. Initial Work

One of the main issues relating to the growth of semiconductor samples by MBE is the need to precisely control the temperature of the Knudsen sources, as a change of 1 degree in the zinc and selenium cells will change the flux produced by 5-10%. It is this need to control the cells temperature accurately and allow them to stabilise that puts limits on the viability of varying fluxes during a growth. This is especially true with the ZnS cell as the granular nature of the source material available results in a large thermal lag between changes in cell temperature and the source material and results in significant difficulties in maintaining the temperature of the material.

For these reasons, the first attempt at HWU to produce an etch-resistant ZnMgSSe QA focussed on using the fluxes routinely used to grow ZnSe and MgS. These fluxes produced an alloy with a lattice mismatch of less than 1% and it could therefore to be grown over 100nm thick without any noticeable deterioration in the structural quality (meaning it was outside the bimodal decomposition region), was etch resistant and provided a wide enough band-gap to produce extremely good confinement on a par with pure MgS [5.5]. The etch resistance and ability to grow thick layers allows samples for XRI, XRD and ELO measurements to be grown so both the lattice constant and bandgap of the QA could be measured.

These first ZnMgSSe containing structures were initially believed to have a composition of  $\text{Zn}_{0.2}\text{Mg}_{0.8}\text{S}_{0.64}\text{Se}_{0.36}$  with a variation of approximately  $\pm 2.5\%$  in both group II and VI mole fractions between all the samples grown. However, as will be discussed later, the use of XRI to determine the composition of these samples has since been called into question and the analysis of the one sample thick enough to produce an XRD peak suggests that that even the lattice constant associated with this composition may not be accurate.

The bandgap, measured by transmission/absorption measurement, was found to be  $4.19 \pm 0.05$  eV [5.6]. Using these figures a red marker is shown in fig. 5.2 showing this initial alloys position in the compositional square.

### **5.2.1. Growth**

All the growth work undertaken for the development of the QA was undertaken in the C-end of the HWU MBE machine. Initially a series of XRI samples were grown consisting of a thin layer of the QA sandwiched between thick ZnSe layers (see fig. 5.3), as prior to their growth there was no way of knowing the exact alloy composition and hence whether thicker layers would be possible.

All the samples were grown using our standard growth technique (see chapter



2) and ZnSe and MgS fluxes on semi-insulating (100) orientated GaAs wafers prepared using our standard technique. The structures for the XRI samples (HWC167, 178 and 180) and the ELO sample (HWC200) are shown in figure 5.3. All of the samples showed good RHEED patterns throughout growth. The samples were cooled after growth under a selenium flux until under 200°C and then removed from the growth chamber.

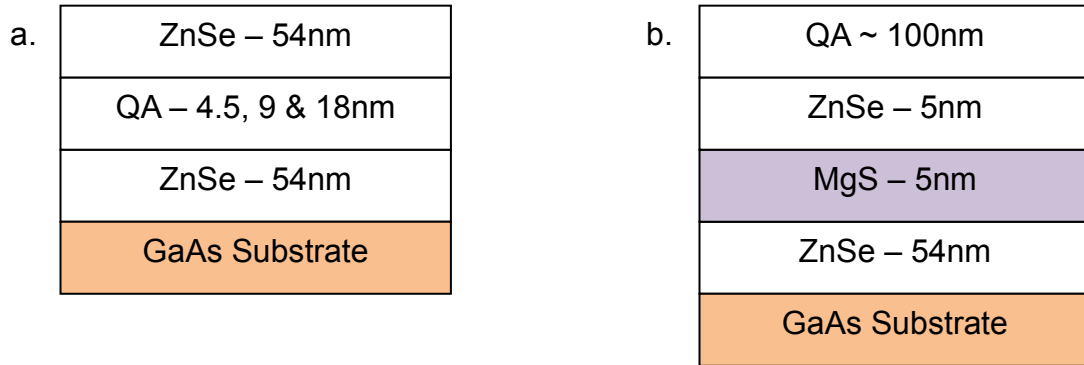


Fig. 5.3. Schematic of X-ray interference (a.) and epitaxial lift-off (b.) QA samples. The MgS layer in the lift-off sample has been highlighted in purple

### 5.2.2. X-ray Characterisation

To determine the composition of the QA, 004 and 115 scans were obtained from all three XRI samples. All of the XRI samples were well modelled by a simple three layer model, i.e. without intermixing of ZnMgSSe and ZnSe, as can be seen in table 5.1. A better fit could be achieved by the introduction of thin intermixing layers, but was not sufficient to justify their inclusion.

TEM measurements of other ZnMgSSe samples grown under identical conditions are in agreement with this model, as they show that the interface between ZnSe and ZnMgSSe layers is extremely sharp with only approximately one monolayer of intermixing [5.5]. As this is far narrower than the thickness of the quaternary layers, it is therefore acceptable to model them using only 3 layers.

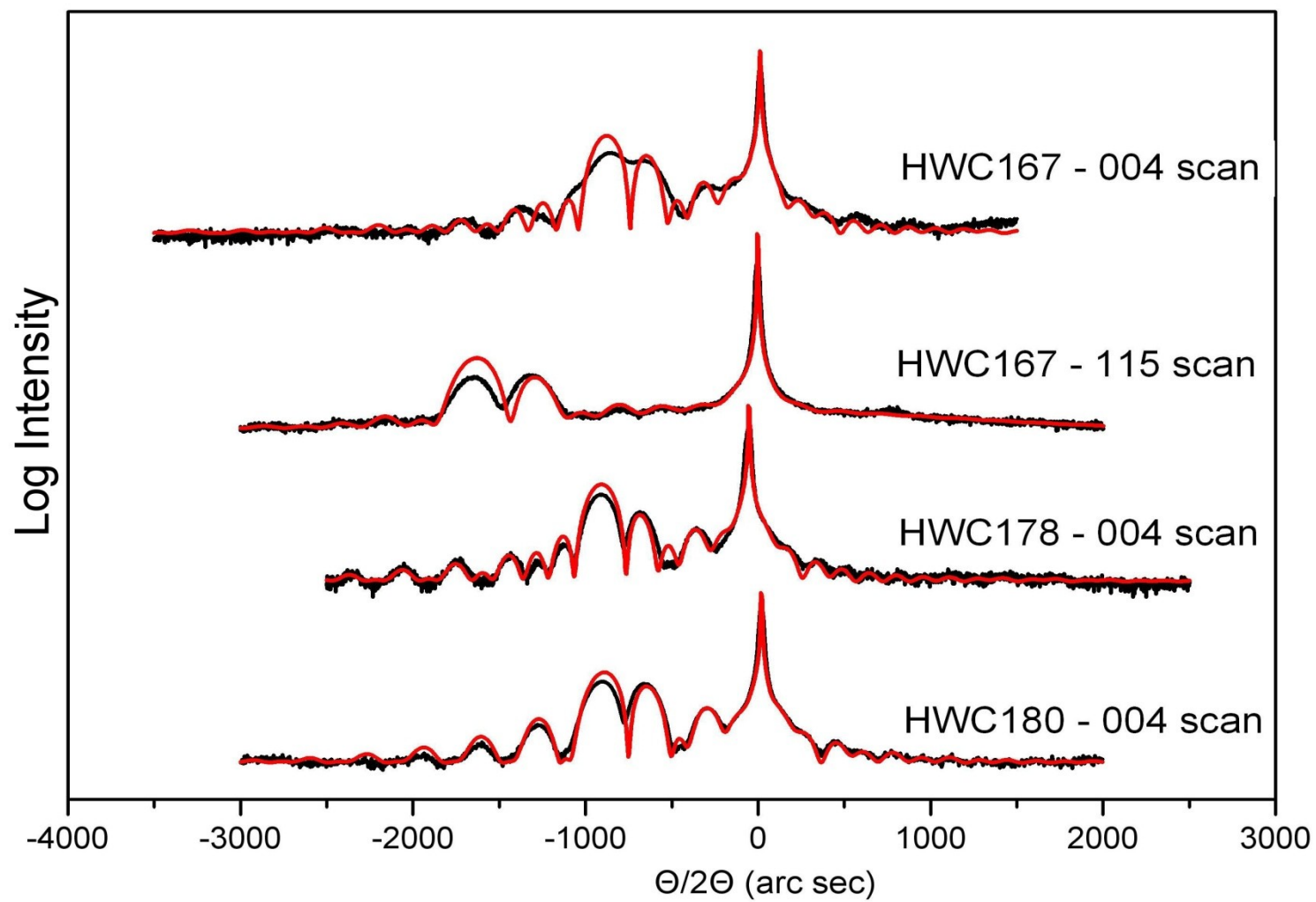


Fig. 5.4. X-ray interference scans (black curves) and simulations (red curves) for HWC167, 178 & 180 , the three initial ZnMgSSe x-ray interference calibration samples . The layer thicknesses and compositions used for the modelling are shown in table 5.1

The only constraint applied during the modelling was that the two thick ZnSe layers were of near-identical thickness and that the composition of the QA was in the MgS rich region of the  $\text{Zn}_{1-x}\text{Mg}_x\text{S}_y\text{Se}_{1-y}$  composition space, i.e.  $x = 0.7-1.0$  and  $y = 0.6-1.0$ , as bandgap measurements (see section 5.2.3.) showed that the alloy bandgap was greater than 4 eV.

Figure 5.4 shows a selection of the data obtained from the samples and the fits to them produced by the simulations based on the parameters in table 5.1. This table also shows the goodness of fit (GOF, as defined in chapter 2) achieved based on these parameters. A series of GOF figures are also quoted for the best 5 layer models, the only additional constraint imposed was that the intermixing layers should be thin (<1-2nm) compared to the total layer thickness and have a composition between the middle layer (QA) and the cladding (ZnSe).

# HWC	Layer Thickness (nm)			QA Composition		GOF 3 layer model		GOF 5 layer model	
	ZnSe, $d_1$	QA, $d_2$	ZnSe, $d_3$	Mg (X,%)	S (Y,%)	004	115	004	115
167	51.4	15.8	50.6	80	64	0.10	0.14	0.09	0.14
178	55.8	9.1	56.1	79	63	0.13	0.11	0.13	0.10
180	54.2	4.8	55.4	81	67	0.17	0.12	0.19	0.11

Table 5.1 – Modelling parameters and GOF for ZnMgSSe XRI samples

Although only limited constraints were placed on the composition during modelling, the modelling algorithm consistently selected a composition of  $\text{Zn}_{0.2}\text{Mg}_{0.8}\text{S}_{0.64}\text{Se}_{0.36}$ , with a variation of approximately  $\pm 2.5\%$  in both the group II and VI mole fractions between samples and scans. However as a quaternary compound can have a range of compositions ( $x$ ,  $y$ ) with the same lattice parameter which generate nearly identical XRI simulations for a given thickness, further investigation is necessary to check that the true composition has been determined.

This analysis was carried out by fixing the thicknesses of all the layers and

either the value of  $x$  or  $y$  and then determining how the GOF varies as a function of the other compositional variable. Initially the best fit  $x = 0.8$  value chosen by the simulation software was used and  $y$  was varied between 0 and 1 for different values of  $d_2$ . Figure 5.5 shows the variation of the GOF with  $y$  mole fraction for various QA thicknesses for the 004 scan of HWC 180 and is representative of the analysis of all the XRI sample both in terms of  $x$  and  $y$ .

As can be clearly seen, for each QA thickness,  $d_2$ , there are a series of minima in the GOF as  $y$  is varied. Each GOF minimum represents a potential best fit value and is related to the movement of the modelled ZnSe peaks as the composition changes relative to the measured data as will be explained in section 5.4.

A number of the minima in both the  $x$  and  $y$  analysis fall well within the decomposition region of the compositional space and can therefore be discounted [5.4]. The remaining possible minima are marked by dotted black or red lines. As the alloy was found to have a large bandgap (4.19 eV at 300K) and the literature shows that the bandgap of ZnMgSSe does not suffer from severe bowing, it is therefore possible to also discount those minima from the low  $x$  and  $y$  fraction region [5.7].

This leaves only a small range of possible minima. For these the  $Y$  value is a sensitive function of  $d_2$ , except for the value of  $y = 0.64$  which is independent of  $d_2$ . It is also apparent that for most (if not all)  $d_2$  values this particular minimum is the lowest. This analysis therefore shows us that there is a particular value of  $y$  (0.64) which consistently results in a better fit and hence appears to be the most likely composition. This analysis can be repeated for  $x$ , this time with  $y$  held constant and from this we obtain the best fit value  $x = 0.8$ .

This result that one composition returns a unique best fit solution to the measured data initially seems strange, as it would appear that any composition

with the same lattice constant should produce the same simulated data. This however neglects the differences between the end member compounds, each of which has a different Poisson ratio, density and atomic constituents. So a MgS rich composition will produce a slightly different modulation than a more ZnSe, ZnS or MgSe rich one with the same lattice constant.

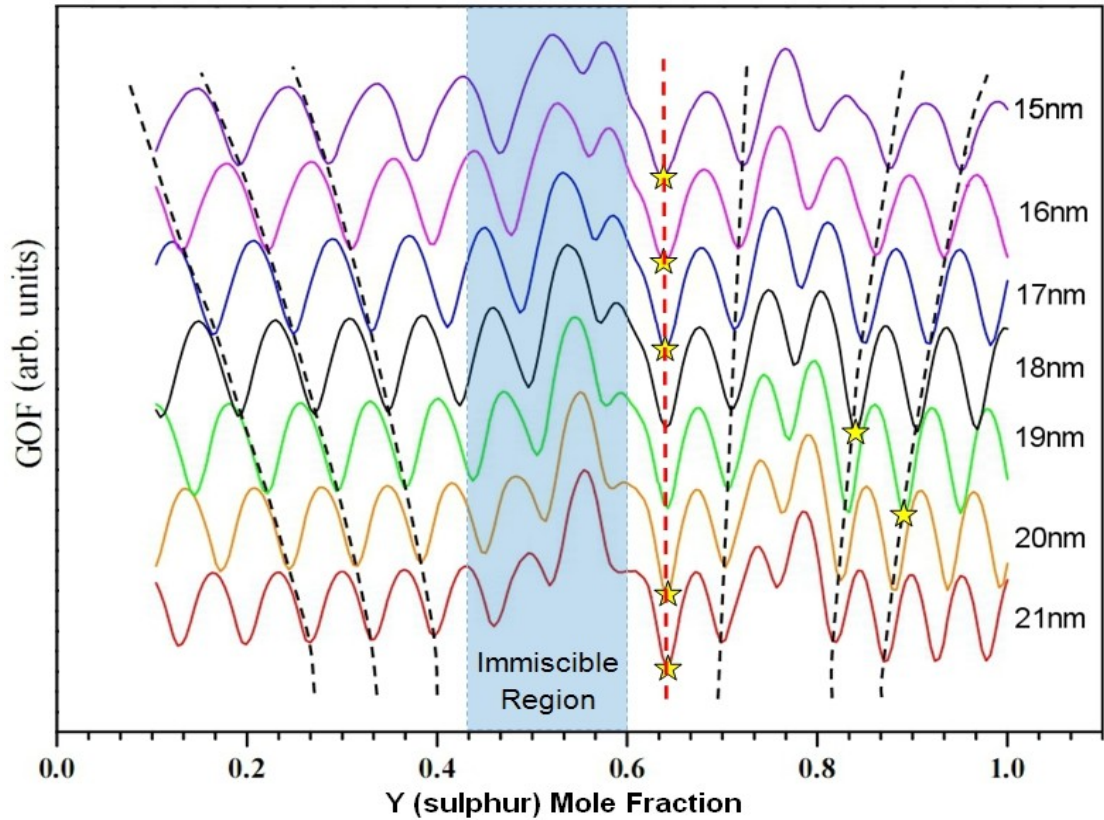


Fig. 5.5. Goodness of fit values for simulations to the HWC180 X-ray interference 004 measured data with different central thickness  $d_2$  plotted as a function of  $y$ . Curves have been displaced vertically as a visual aid. The dotted lines are a guide to the eye for minima in the miscible regions of the composition space. The red dotted line shows the composition chosen by the software. The stars show the minima at each QA ( $d_2$ ) layer thickness.

Over the series of three samples, there is a slight variation in the  $x$  and  $y$  determined by this process, despite the growth conditions being relatively constant for the entire series. As a result, the composition of the series of samples is given as  $x=0.80\pm0.02$ ,  $y=0.645\pm0.025$ .

This composition falls just within the spinodal decomposition region predicted by Sorokin et al. and would hence not be stable. But the sharp fringes in the XRI data, single transition in the absorption data and TEM images show this is not the case [5.4, 5.5]. This apparent problem can be remedied by reducing the

enthalpy of formation for MgS from -235 to -231 kJ.mol<sup>-1</sup>, as the model then places Zn<sub>0.2</sub>Mg<sub>0.8</sub>S<sub>0.64</sub>Se<sub>0.36</sub> outside the spinodal decomposition region. This refinement is justifiable as both the entropy and enthalpy of formation for ZB MgS had been estimated from the known values from RS MgS.

As the thickest QA sample grown (HWC167) is best modelled by a QA layer 15.3nm thick, it is possible to increase the range of  $\theta/2\theta$  values measured and find the XRD peak associated with this layer in both 004 and 115 scans. Figure 5.6 shows these scan along with a model based on the previously determined composition, Zn<sub>0.2</sub>Mg<sub>0.8</sub>S<sub>0.625</sub>Se<sub>0.375</sub>. The model fits the modulated ZnSe XRI part of the scan very well but does not match the XRD peak from the QA.

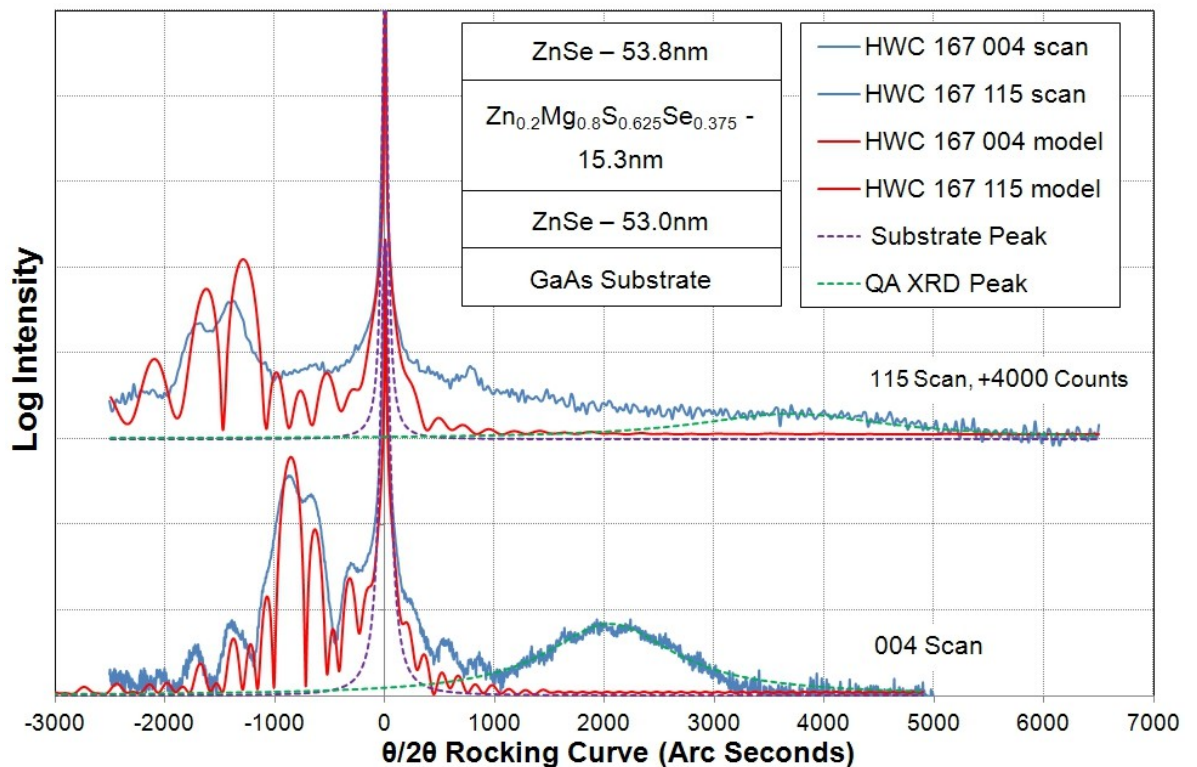


Fig. 5.6. The measured and simulated XRD plots of HWC167. The blue curves are the measured data, the red are the simulations produced by the modelling software based on the inset structure, the green and purple dashed lines are Lorentzians that have been fitted to the substrate and ZnMgSSe layer X-ray diffraction peaks by had to determine their lattice constant.

To correctly fit the measured data including the XRD peaks a composition with a lattice of ~5.6146Å is required, such as Zn<sub>0.2</sub>Mg<sub>0.8</sub>S<sub>0.86</sub>Se<sub>0.14</sub>. However a number of other compositions will also produce nearly identical GOF for this sample. The inability to find a unique composition with is to be expected, as the XRD peak is simply due to the alloy diffracting the beam at an angle determined by

its lattice constant rather than the more subtle case of XRI.

The fact that the XRD result here does not agree with the earlier XRI results is troubling. The XRI results indicate an alloy with a lattice constants of  $\sim 5.6786\text{\AA}$  (0.44% mismatch), whereas the XRD result suggests an alloy with a lattice constant of  $5.6146\text{\AA}$  (-0.69% mismatch) and these are obviously very different. However looking again at figure 5.5, one of the other minima corresponds to a composition of  $x=0.8$ ,  $y=0.86$ , the value obtained from the XRD analysis. Later on in section 5.4 a further investigation into the modelling of the XRI technique will be presented and an attempt made to clear up the discrepancy between the values obtained by XRI and XRD. But at the time the initial XRI analysis was completed the XRD result had not been obtained, so for continuity reasons the discussion will be presented later.

### 5.2.3. Measurement of the Bandgap of the Alloy

The thick QA ELO sample, HWC200, was grown under the same conditions as the XRI samples so that the alloy layer should share the same composition. It also contains an MgS sacrificial layer so it can be lifted, deposited on to a transparent substrate and then its transmission/absorption measured. This was performed using the Shimadzu UV-3100 UV-VIS spectrometer as described in chapter 2. The absorption of the lifted QA sample is shown in figure 5.7 and shows the expected sharp increase at the band edge of the alloy.

To determine the bandgap from this data, the modified Tauc relation for a direct band-gap semiconductor, equation 5.1, was used.

$$(\alpha - \alpha_1)hv = C_1(hv - E_g^d)^{1/2} \quad (1)$$

Where  $\alpha$  is the absorption co-efficient,  $\alpha_1$  is the minimum absorption found below the band edge,  $C_1$  is a constant and  $E_g^d$  is the direct band-gap.

HWC200 has a thin ZnSe layer between the QA layer and the substrate to



minimise any intermixing, but this is sufficiently thin that it acts only as an effective filter reducing the intensity of the light passing through the sample. This is then accounted for by the introduction of the  $\alpha_1$  term.

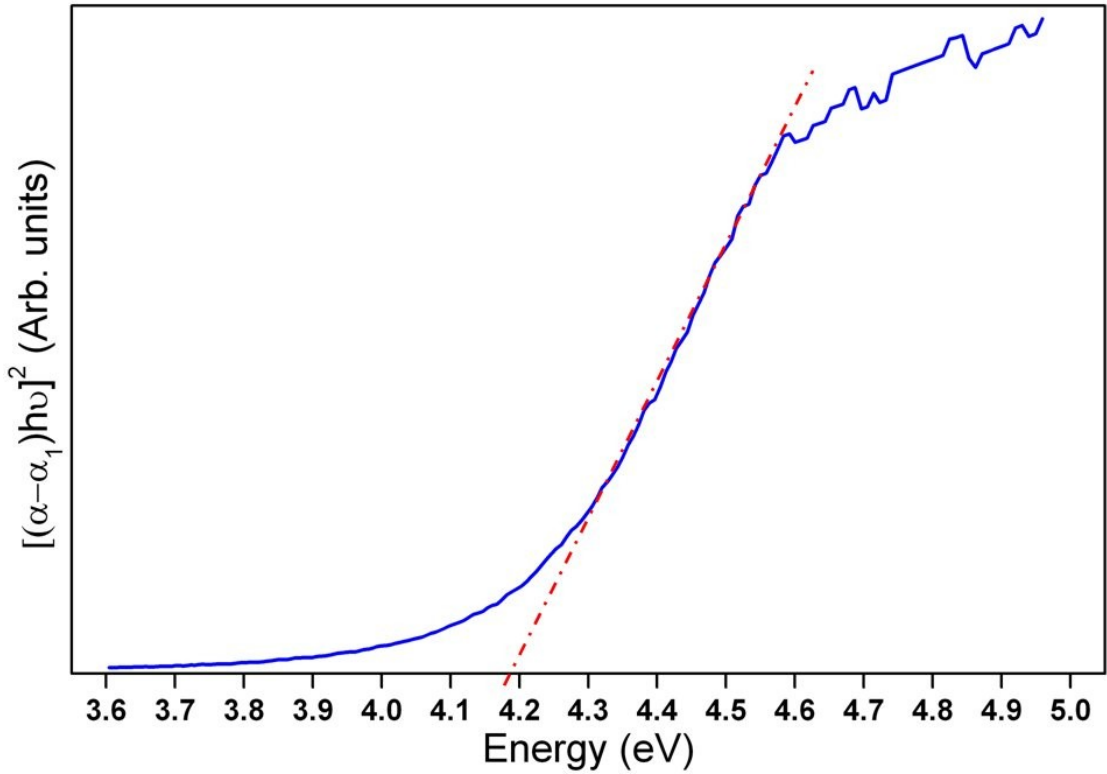


Fig. 5.7. Near band edge absorption of the lifted quaternary alloy layer. The red dashed and dotted line shows the extrapolation of the absorption back to the origin, so as to determine the bandgap.

$E_g^d$  for the alloy is obtained by extrapolating the rapid change in the absorption to zero, as shown in fig. 5.7. From this  $E_g^d = 4.19 \pm 0.05\text{eV}$  can be determined. This value will differ from that obtained by other means, such as PL, due the Stokes shift caused by a number of effects, such as band filling [5.8]. However as the alloy is strained, undoped and single-phase, any change in the bandgap energy should be well within the stated error.

When the transmission spectrum is plotted using the Tauc relation for an indirect semi-conductor (not shown), it is worth noting that there is also a much weaker change in the absorption observed which suggests that the alloy could also have an indirect gap of around  $3.55 \pm 0.05\text{eV}$ . However as this feature is much less intense than that seen for the direct bandgap, it is highly likely that it is not a true bandgap transition but merely an apparent one due to noise in the measurement. This is something that could be investigated further, as it is also



possible that MgS possesses an indirect band-gap, as this is one of the theoretical predictions [5.9] and could be the reason there are no reports of emission from MgS.

#### 5.2.4. PL Comparison of ZnSe QWs with QA and MgS Barriers

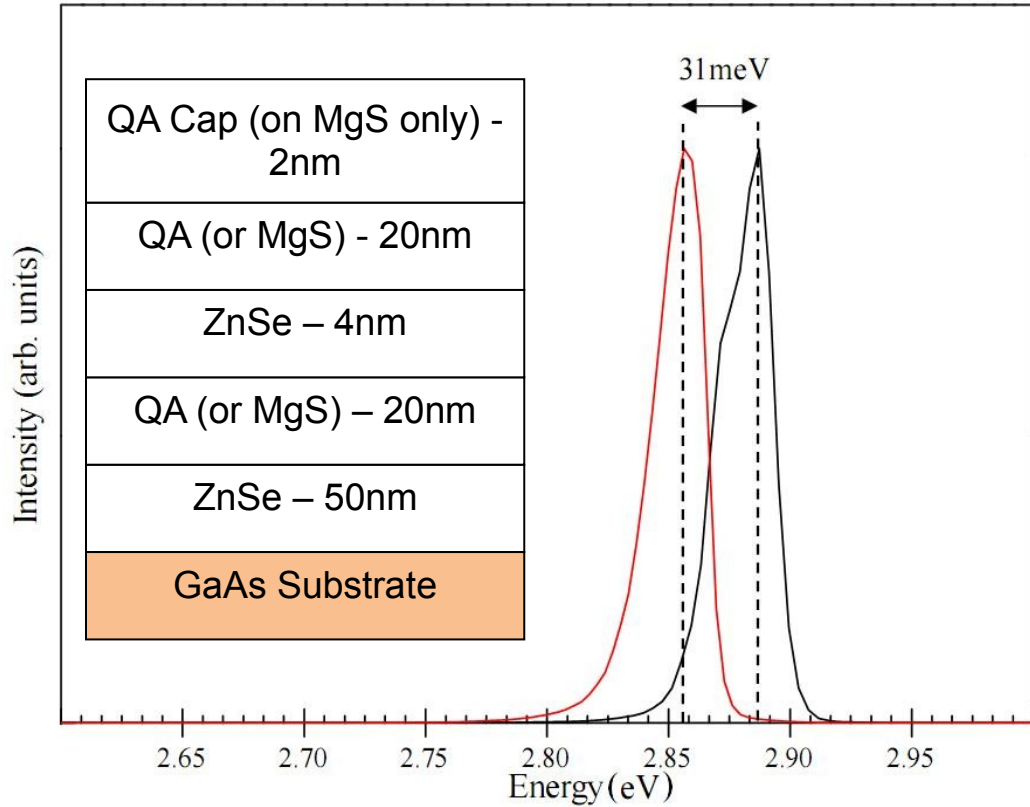


Fig. 5.8. PL spectra from HWC122 and 176, ~4nm ZnSe quantum well with MgS (red curve) or ZnMgSSe (black curve) barriers respectively. The structure of the samples and the emission energy difference are also shown in the figure.

As the alloy is to be used as a replacement barrier material in ELO structures, it is important to ensure that it is able to function as one. Figure 5.8 shows the 77K PL spectra of 2 samples, HWC 176 and 122, with a schematic of their structure inset. As can be clearly seen, the sample with QA barriers, HWC176 (black curve), shows almost identical spectral profile to the one with MgS barriers, HWC122 (red curve). The slight shift in energy is attributed to a ~1.5ML difference in well width due to the samples being grown on different dates. There is also a slight shift in the FWHM between the 2 samples (15.1 meV for the QA vs. 16meV for the MgS), this may be due to very smooth interface between the QA layer and ZnSe, as was observed by TEM [5.5].

In the case of CdSe QDs when compared to a similar sample with MgS barriers,

the QA again performs almost identically. This can be seen in figure 5.9, which shows the PL spectra of 2 samples, HWC 224 and HWA1569, which both contain QDs with ~3.5ML of CdSe grown by thermally activated MEE with QA and MgS barriers respectively. A schematic of their structures is again shown inset. The 2 structures show slightly different FWHM, 134meV for HWC224 vs. 164meV for HWA1569. This may be due to differences in either the amount of CdSe deposited or the thermal annealing used to induce dot formation.

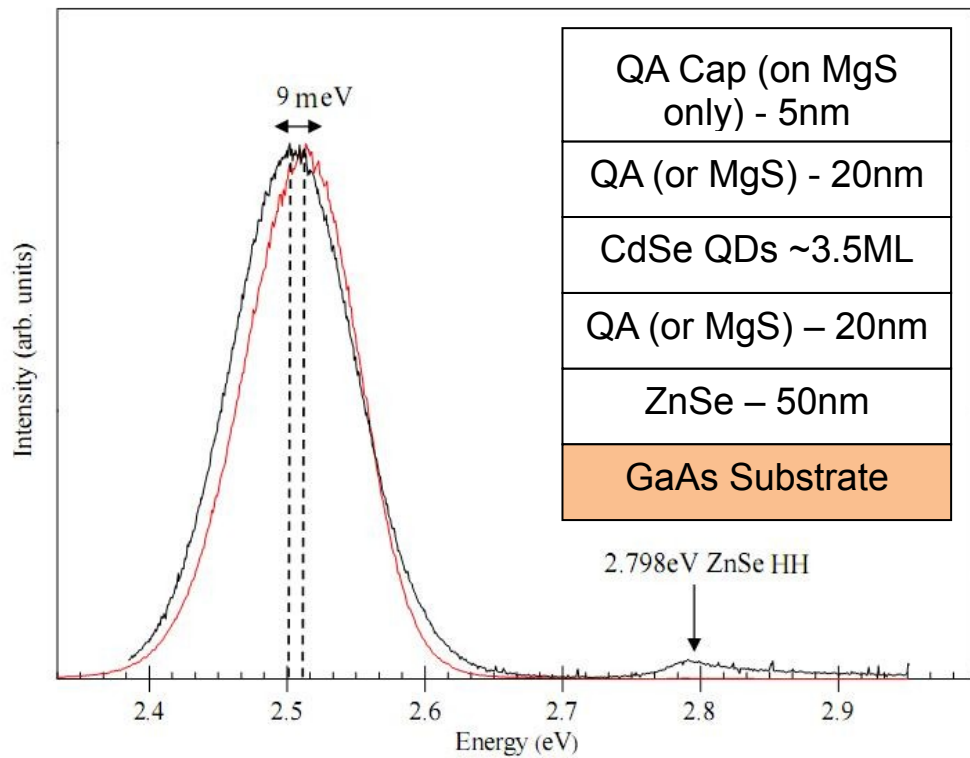


Fig. 5.9. PL Spectra from HWC224 and HWA1569, QA and MgS barriered CdSe QD samples. The samples structure, emissions peak identity and the shift in the quantum dot emission are also shown.

A number of other comparable structures have been grown, including a series of other QD samples that will be discussed further in chapter 7, and in all of these the QA performs virtually identically to MgS. Therefore it is concluded that MgS rich QAs are an effective replacement barrier material for lift-off structures.

### 5.2.5. Lift-Off Results

The final desired characteristic for a QA was that it should resist our standard MgS etch solution (30% HCl) and the easiest way to test this was to grow a ZnSe/QA QW sample with an MgS sacrificial layer and then compare the original and lifted samples in terms of their structural and optical properties.

Figure 5.10 shows the 77K PL spectra of HWC186, before (curve a) and after (curve b) lift-off. It shows that most intense emission from this sample (both before and after liftoff) is excitonic emission from the 60nm thick ZnSe spacer layer at around 2.78/9eV. This is due to the much higher absorption cross-section presented by the thick ZnSe layer compared to the 4nm ZnSe QW layer and to how effectively the QA barriers are confining the carriers generated in it.

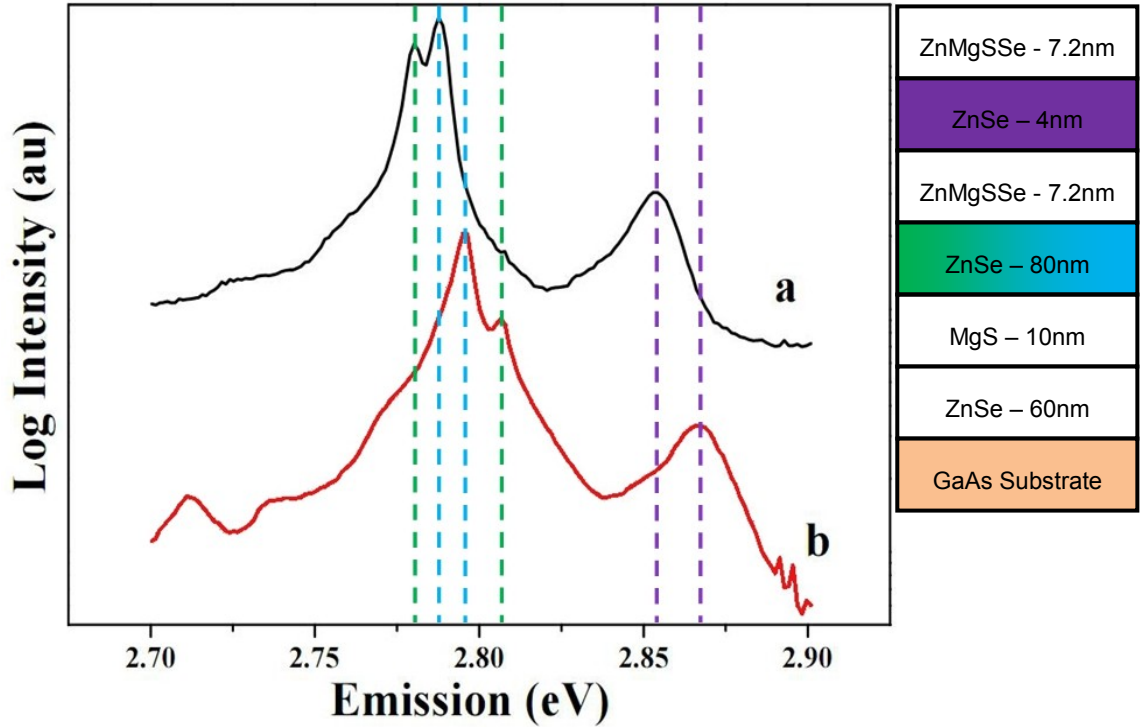


Fig. 5.10. Pre (red curve labelled b) and Post (black curve labelled a) liftoff PL Comparison. The structure of the unlifted sample is shown to the right of the graph with the layer responsible for the emissions shaded the same colour as the dotted line through the emission peak for identification.

The main changes between the 2 spectra are the shift in energy of the main peaks and the disappearance of the feature at 2.713eV. This low energy feature is at the correct energy to be a acceptor-bound exciton feature and as it is weak and not present in the lifted layer it can be assigned to either As-doping or Zn vacancies present in the 60nm ZnSe buffer grown directly on the GaAs substrate [5.10].

The energy shift shown by all the peaks is due to the change in strain state during ELO. Before lift-off the whole structure is strained to the GaAs substrate, while after its etched it will instead minimise its internal energy by adopting a lattice constant which is the weighted average of the individual layers. This

weighting arises from the differences in thickness and elastic constant of each layer.

The split ZnSe peak from the 60nm buffer layer is caused by the lifting of the light-hole/heavy-hole degeneracy due to the strain and the peaks can be assigned, due to their relative intensities, as the heavy-hole (HH) emitting at 2.795eV in the unlifted sample (2.784eV in the lifted one) and the light-hole (LH) at 2.808eV in the unlifted sample (2.778eV in the lifted). The shift in the position of the LH relative to the HH from higher to lower energy is again caused by the change in strain-state with the ZnSe layer changing from being under compressive strain in the unlifted material to tensile in the lifted [5.11].

Under the microscope at up 1000x magnification, prior to lift the samples are smooth and relatively featureless, whereas after liftoff they typically show some degree of cracking. However the large areas between the cracks appear to be identical to the material prior to lift-off. AFM measurements agree with this analysis and show that the uncracked areas of the lifted material are virtually identical to the original sample and show RMS roughness's around 10nm, identical to the substrates they've been deposited on.

### 5.3. Second Set of Samples

As all the initial samples contained alloys that were not lattice matched to GaAs, the work was continued to attempt to produce a composition that was. Between the initial work and the growth of a second set of samples the normal growth rate of ZnSe (and hence the fluxes of zinc and selenium) was increased. For the reasons discussed in the introduction to this chapter it was again considered undesirable to change fluxes during growth, so these increased fluxes were used for the growth of a fresh set of samples.

Although the exact composition of the original set of samples has still not been precisely determined, the lattice constant (determined in section 5.2.2) is  $\sim 5.615\text{\AA}$  and therefore smaller than that of GaAs ( $5.6533\text{\AA}$ ). Therefore the

introduction of more Zn and Se should increase the lattice constant of the alloy, bringing it closer to lattice match. However, it could also result in the new composition falling within the spinodal decomposition region, making its growth thermodynamically impossible.

If so, it could cause further problems as the obvious way to compensate for this would be to increase the Mg and ZnS fluxes. But as there is only a very limited window, in terms of fluxes, within which MgS growth is possible and this significantly limits the range that can be used.

### 5.3.1. Growth

Four samples utilising the increased fluxes were grown in two sets. The first set comprised two XRI samples (HWC 298 & 302) with QA layers grown for 25 and 50 seconds, expected to produce QA thicknesses of ~4 and 8nm respectively. The 2<sup>nd</sup> set comprised an additional XRI sample (HWC340) with a ~10nm QA layer and an ELO XRD sample (HWC333) with a ~140nm thick QA layer. The samples structures are shown schematically in figure 5.11. The ELO XRD sample is shown on the right and contains both a thick QA layer (which should produce an XRD peak allowing the lattice constant to be measured) and an MgS sacrificial layer so the QA layer can be lifted to allow its band-gap to be measured.

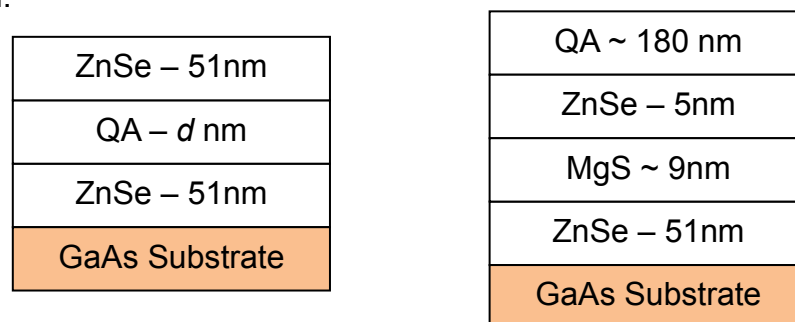


Fig. 5.11. Structure of HWC 298, 302 & 340 - QA XRI samples (left) and HWC 333 (right).

During the growth of the first two samples, the RHEED showed a streaky but faint 2x1 reconstruction throughout. This is in opposition to the strong and streaky c(2x2) and 2x1 typically seen during the growth of the QA layers in the original samples. The faintness of the ZnSe pattern may be due to the low

Zn:Se ratio, as typically a 1:2-2.5 ratio is optimal. The low ZnS flux during quaternary growth could then similarly be the reason for it not displaying both of the strong patterns normally seen. However as the RHEED did not deteriorate during growth it suggests the growth was smooth and pseudomorphic.

The growth of HWC333 produced a strong and streaky 2x1 RHEED pattern during the growth of the ZnSe layer and a c(2x2) during the MgS layers. The QA layer showed a faint but streaky 2x1 and c(2x2) during the first 3 minutes of its growth but the pattern slowly became spotty as the growth proceeded, indicating a roughened surface.

HWC 340 showed both a strong & streaky 2x1 and a faint c(2x2) during the growth of the lower ZnSe layer, indicative of near-stoichiometric growth conditions, which is more zinc rich than ideal. During the growth of the QA layer, the RHEED initially showed a strong and streaky 2x1 and c(2x2) pattern, this then started to become spotty towards the end of its growth. The upper ZnSe layer showed only a very strong & streaky 2x1, suggesting the Zn:Se ratio had increased closer to 1:2.

### 5.3.2. X-ray Characterisation

HWC 298 and 302 were measured along both the 004 and 115 planes and produced the expected XRI pattern, see figure 5.12 for an example. Modelling these scans resulted in best fits with the parameters shown in table 5.2. It was again found that a range of different compositions and thicknesses could produce nearly identical GOF and this lead to a thorough investigation of the XRI technique (including a re-evaluation of the original QA samples) the results of which will be discussed in the section 5.4.

Sample No.	ZnSe 1 Thickness	Zn <sub>1-x</sub> Mg <sub>x</sub> S <sub>y</sub> Se <sub>1-y</sub>				ZnSe 2 Thickness	GOF	
		Thickness	X	Y	Mismatch		004	115
298	48.03	4.88	0.996	0.740	0.66%	48.64	0.101	0.105
302	42.15	11.85	0.850	0.628	0.66%	42.95	0.080	0.073

Table 5.2. Modelling parameters for HWC 298 & 302.

During modelling the RADS software was again given the constraints of ZnSe layers that are approximately the same thickness ( $\pm 0.5\%$ ) and between 30-70nm thick (a growth rate,  $G_R$ , of 0.5–1.2Å/s), QA layers thickness representing a  $G_R = 1.5 - 2.5\text{Å/s}$  and composition in the MgS rich part of the compositional space ( $x=0.75-1$ ,  $y=0.6-1$ ). With these constraints the software found the values in table 5.2 resulted in the lowest GOF.

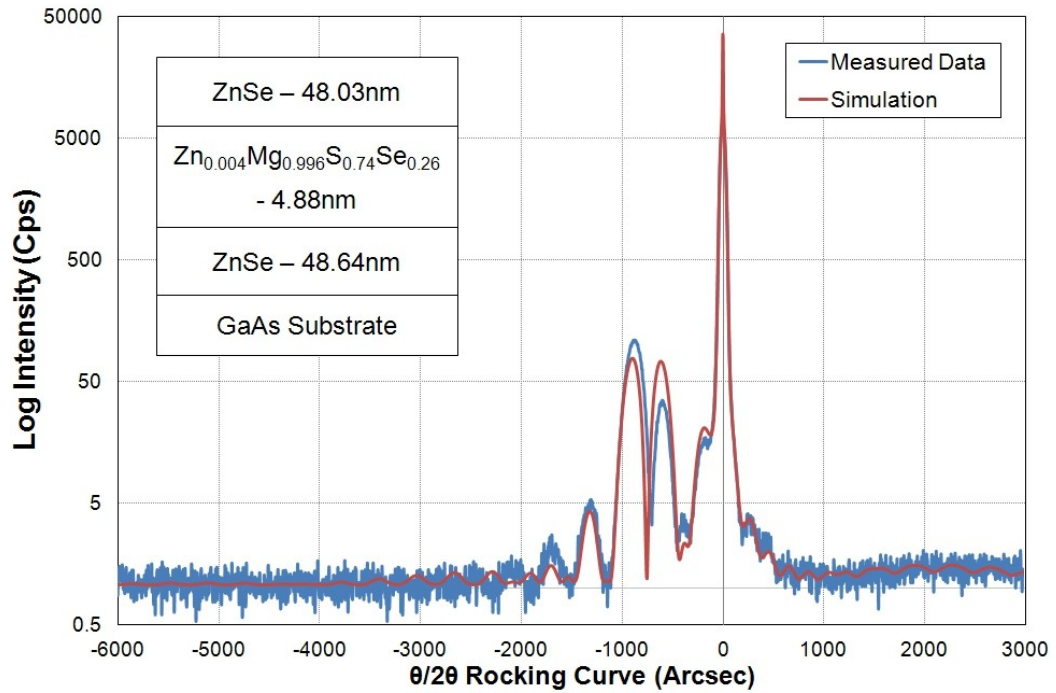


Fig. 5.12. 004 x-ray interference  $\theta/2\theta$  rocking curve for HWC298. The blue curve is the measured data and the red the simulation. The structure used for the simulation is shown inset.

Comparing the new alloy with the one produced in the first series we see that the mismatch has changed sign. This is to be expected as the zinc and selenium fluxes have been increased, resulting in lattice constant moving towards that of ZnSe. However, as the mismatch has increased beyond that of ZnSe toward MgSe (see fig. 5.13) points to the alloy compositions sensitivity to the selenium flux. It also suggests the need to either increase the sulphur or decrease the magnesium fraction if the alloy composition is to be changed to a lattice matched one.

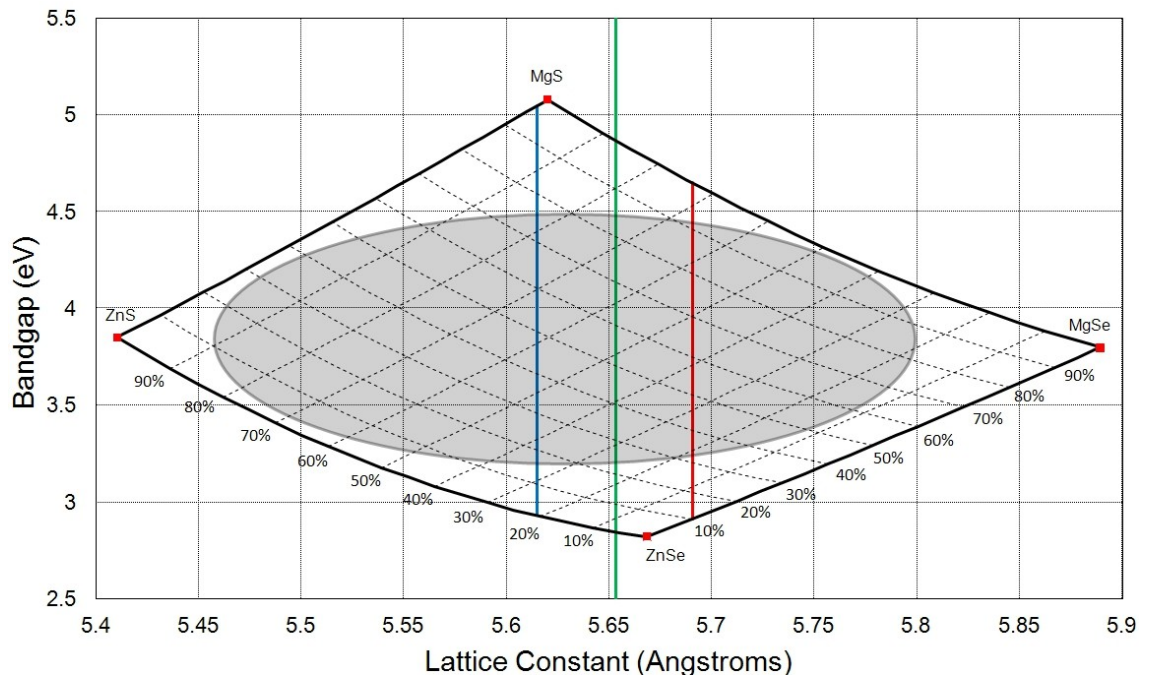


Fig. 5.13. ZnMgSSe compositional square. Green line is the GaAs lattice matching line, blue and red lines represent lattice constant of series 1 & 2 QA samples respectively. Grey region roughly represents the spinodal decomposition region, note that the boundaries are not accurate. The percentages around the square represent the incorporation percentages  $x$  and  $y$ .

This sensitivity to selenium flux is due to the differing incorporation coefficients (the fraction of the atoms incorporated into the alloy for a given flux arriving at its surface) of the species used in the growth of the alloy at the specific substrate temperature used. During the growth of ZnSe, the Zn co-efficient has been determined to be  $\sim 0.67$  [5.12]. But as our work on MgS has lead us to believe that magnesium atoms incorporate by displacing zinc atoms, this will reduce the zinc incorporation co-efficient and reduces its alloy mole fraction [5.13].

Magnesium itself has an incorporation coefficient of approximately 0.5 in MgS and this if varies with selenium mole fraction this will have a very strong effect on the composition. ZnS has a very low incorporation coefficient and it is extremely hard, at the substrate temperatures used here, to get more than a monolayer of ZnS to stick to the surface (hence the very large overpressure used during growth) and this results in a very low sensitivity to changes in ZnS flux. This leaves selenium as the species with the greatest effect on the alloy composition.



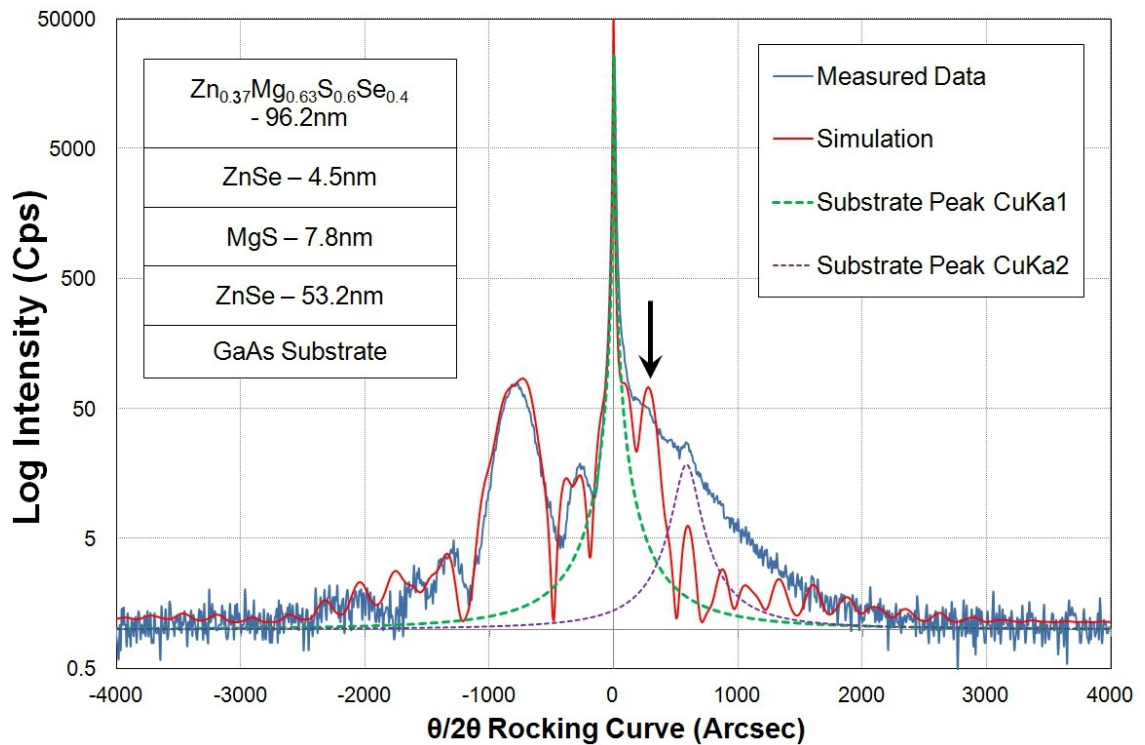


Fig. 5.14. Measured and hand modelled 004 scan of HWC333. The black arrow shows the position of the QA XRD peak. Overlaid are Lorentzian curves representing the GaAs substrate peak (green dotted line) and GaAs peak due to Cu  $K_{\alpha 2}$  emission (purple line). The structure used for the modelling is inset.

HWC333 was also investigated using both the 004 and 115 reflections and produced the rocking curves shown in figure 5.14. There is no obvious XRD peak for the QA layer in either scan. Modelling the scans resulted in the software fitting the QA XRD peak to the small peak seen at ~600 arc seconds (~850 in the 115), however this peak is actually due the substrate reflection of the Cu  $K_{\alpha 2}$  emission from the X-ray source, as discussed in chapter 2. Any attempt to force the software to fit the peak elsewhere resulted in it choosing either an unrealistically thin layer (<5nm) and/or a composition that falls outside the scan range which longer range scans (12000 to -12000 arcsecs., not shown) prove is not the case

However, when Lorentzian curves representing the Cu  $K_{\alpha 1}$  and  $K_{\alpha 2}$  emissions are fitted to the measured 004 and 115 scans, a small peak/shoulder on the positive side of the main GaAs substrate peak at around ~200 arc seconds (~350 in the 115) is seen, as marked by the black arrow in fig. 5.14. By either removing the  $K_{\alpha 2}$  peak from the data or constraining the RADS software to use a composition that places the QA XRD peak at the 200 (350) arc seconds

shoulder, a good fit to the data was found. The best fit simulation is also shown in figure 5.14. The fit is consistent with a lattice constant of  $5.6503 \pm 0.0013 \text{ \AA}$  (a lattice mismatch of approx. -0.05%) and a  $G_R \approx 1.8 \text{ \AA/s}$ . This lattice constant was modelled using a composition of  $\text{Zn}_{0.37}\text{Mg}_{0.63}\text{S}_{0.63}\text{Se}_{0.4}$ .

Figure 5.15 shows the 004 scan of HWC340, it shows the anticipated XRI pattern but there is no again sign of an XRD peak. If the alloy is growing at the anticipated  $1.8\text{-}2 \text{ \AA/s}$  rate obtained from the other samples in this series, the QA layer would be expect to be 10-12nm thick so a small peak should be visible. The fact that it is not suggests the peak must therefore fall close to the substrate peak.

Modelling the scans was again difficult with the best fits either predicting QA layers that are too thin or had compositions consistent with a large lattice mismatch, which does not seem realistic. However after a repetition of the process used to fit HWC333, a composition of  $\text{Zn}_{0.25}\text{Mg}_{0.75}\text{S}_{0.63}\text{Se}_{0.37}$  with a lattice constant of  $5.665 \text{ \AA}$  (a mismatch of 0.22%) was found to produce the best fit. This mismatch is close to those of ZnSe and is very different from that determined for HWC333, which is surprising considering both samples were grown under similar conditions. However as QAs seem very sensitive to changes in cell temperature/flux this is not entirely unrealistic.

This sensitivity to cell temperatures/fluxes does indicate an important point, that it may be difficult to consistently produce lattice matched alloys and to ensure that the composition of an alloy layer is homogenous. In the majority of applications this would not be critical but if very thick layers are to be produced, as explained at the start of this chapter, it could be. This may warrant further investigation in the future if quaternary alloys are going to be used as optical waveguides.

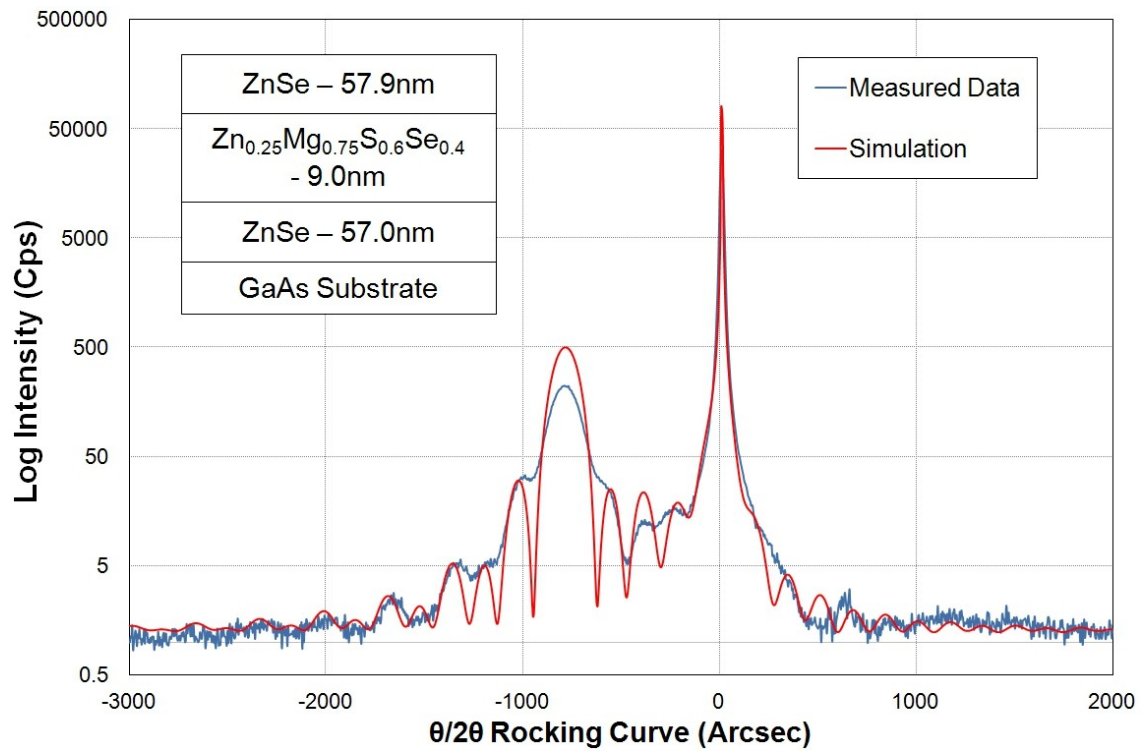


Fig. 5.15. Measured (blue curve) and modelled (red curve) 004 x-ray scan of HWC340. The 004 data has had the Cu  $K_{\alpha 2}$  peak removed by hand.

### 5.3.3. Measurement of the Bandgap of the Alloy

Several pieces of HWC333 were lifted using our standard technique and deposited onto pieces of glass. The lifted pieces were then placed in the J. A. Woollam V-Vase ellipsometer described in chapter 2 and their transmission/absorption measured. Figure 5.16 shows representative absorption measurements of the deposited samples and a blank piece of glass substrate.

The measured spectra of the QA sample show 2 transitions, the first is at an energy of 2.64eV and is identified as the direct transition of the ZnSe buffer layer. The second transition is at 3.72eV and is identified as the transition due to the QA layer. Comparing the spectra of the deposited sample to that of the blank glass substrate, no transition is seen at 2.64eV and the glass begins to absorb at 3.78eV which is distinct from the QA transition.

The magnitude of any Stokes shift present in this measurement is hard to

determine as it varies depending on the material and its structural quality, and as we have no information on it for either MgS or MgS-rich ZnMgSSe alloys it is impossible to accurately predict. However from reviewing various values in the literature and the work reported in chapter 6, a figure of 50-100meV should be more than sufficient to cover any possible shift [5.14]. This error bound should also be more than large enough to cover any other errors that may have been introduced in the measurement of the bandgap.

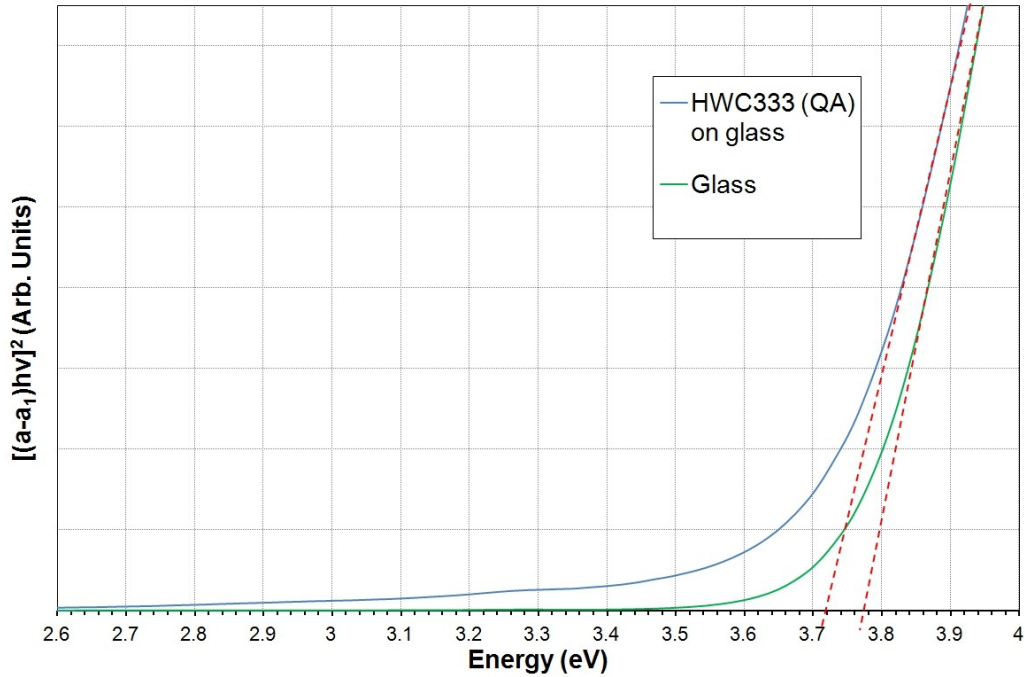


Fig. 5.16. Tauc absorption plot of HWC333 (blue line) and a piece of glass substrate (green line). The dashed red line shows the extrapolation of the linear region of the absorption curve back to the origin and hence its band-edge.

#### 5.3.4. Determination of the QAs Composition

As both the lattice constant and bandgap of the alloy in sample HWC333 have been determined it should be possible to determine the composition of the alloy. However as the bandgap of MgS is unknown and those of ZnS and MgSe are still matters of slight debate [5.7, 5.15-5.18], the degree of accuracy possible is limited. By plotting a lattice constant line (at  $5.6503 \pm 0.0013 \text{ \AA}$ ) on the compositional diagram and then looking at where the lines of constant bandgap representing the alloys bandgap ( $3.8 \pm 0.1 \text{ eV}$ ) intersect it, the range of compositions can be determined.

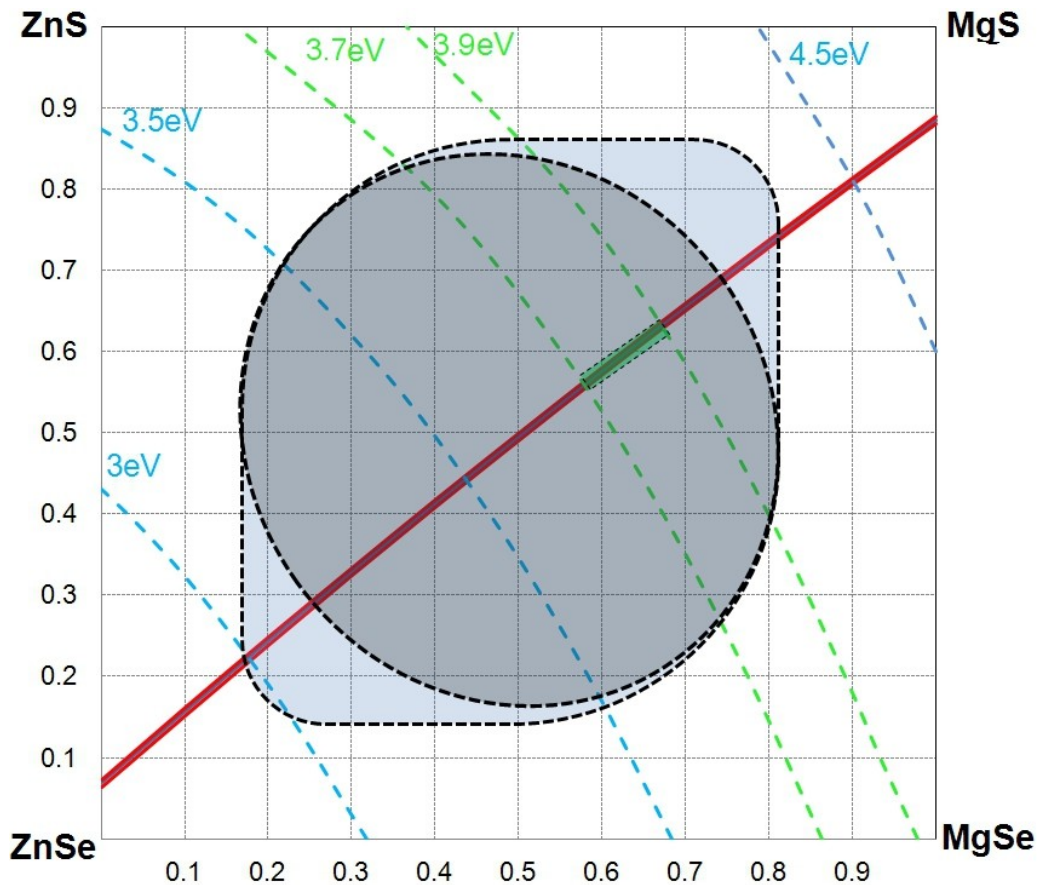


Fig. 5.17. ZnMgSSe compositional square with the lattice constant line (red line) and bandgap (green lines) for HWC333. The other blue lines represent bandgap values of 3, 3.5 and 4.5eV. The light and dark grey areas are the bimodal and spinodal decomposition regions respectively. The compositional space occupied by HWC333 has been marked by a green shaded region.

Figure 5.17 shows this for HWC333 assuming room temperature bandgap for ZnSe, ZnS, MgSe and MgS of 2.68, 3.66, 4.05 and 4.8eV respectively [5.7, 5.19]. Using these figures the composition of the QA in HWC333 would be in the region  $x = 0.58 - 0.67$  and  $y = 0.56 - 0.63$ . This composition range falls well within the spinodal decomposition region but as the absorption measurement shows only two transitions, one from the alloy and one from the ZnSe layer, the alloy has not decomposed. This suggests that one or more of the bandgap values used may be wrong.

Of the 4 binary compounds that make up the ZnMgSSe compositional space, ZnSe is by far the best characterised. However its quoted room temperature bandgap still varies, ranging from 2.6 - 2.75eV [5.7, 5.20, 5.21]. ZnS and MgSe have both been grown as single phase cubic crystals and then characterised by a number of groups and methods [5.15-5.18]. ZnS is reported as having a

bandgap of 3.54 – 3.77eV at 300K while MgSe is reported as 3.59 - 4.05eV [5.7, 5.15-5.18]. Currently no-one has managed to measure the band-gap of MgS directly but experimental values as high as 5.47eV have been determined and calculated values ranging from 3.4-6.5eV reported [5.22-5.25].

The uncertainties in each quantity (the bandgap and lattice constant of the alloy and binary compounds) contribute differing amounts to the overall uncertainty in the composition of the alloy and it is therefore necessary to consider them individually. The lattice constants of both the alloy and the binary compounds are all known to  $\pm 0.05\%$ , and as such contribute very little to the overall uncertainty ( $\sim 0.5\%$  in x and y) and can therefore be ignored.

The uncertainty in the bandgap of ZnSe is also small and hence again only introduces a limited amount of uncertainty,  $\sim 0.5\%$  in x and y, to the composition. The uncertainties in the bandgap values of ZnS and MgSe are larger ( $\sim 3$  and  $6\%$  respectively) but as the alloy is MgS rich it is less effected by them and at most these uncertainties combined only produce a  $\sim 1\%$  variation in x and y. The uncertainty of 100meV in the measured bandgap of the alloy introduces a  $\sim 8\%$  uncertainty in x and y values but as the 100meV figure was chosen simply to be larger than any possible error it is likely the true error, and hence uncertainty in the composition, is much smaller than this.

The value that has the most significant effect on the uncertainty of the composition is as anticipated the bandgap of MgS, as the  $\sim 1\text{eV}$  range of values quoted for this figure (4.3-5.3eV at 300K) results in an approximate 15 and 12% uncertainty in the x and y values of the alloy respectively. This dominates the uncertainty and is why this value needs to be determined more accurately if alloy compositions are to be determined with reduced error bounds. Combining all the values together we end up a compositional range of  $x = 0.55\text{-}0.87$  and  $y = 0.54\text{-}0.79$ , which is obviously quite large.

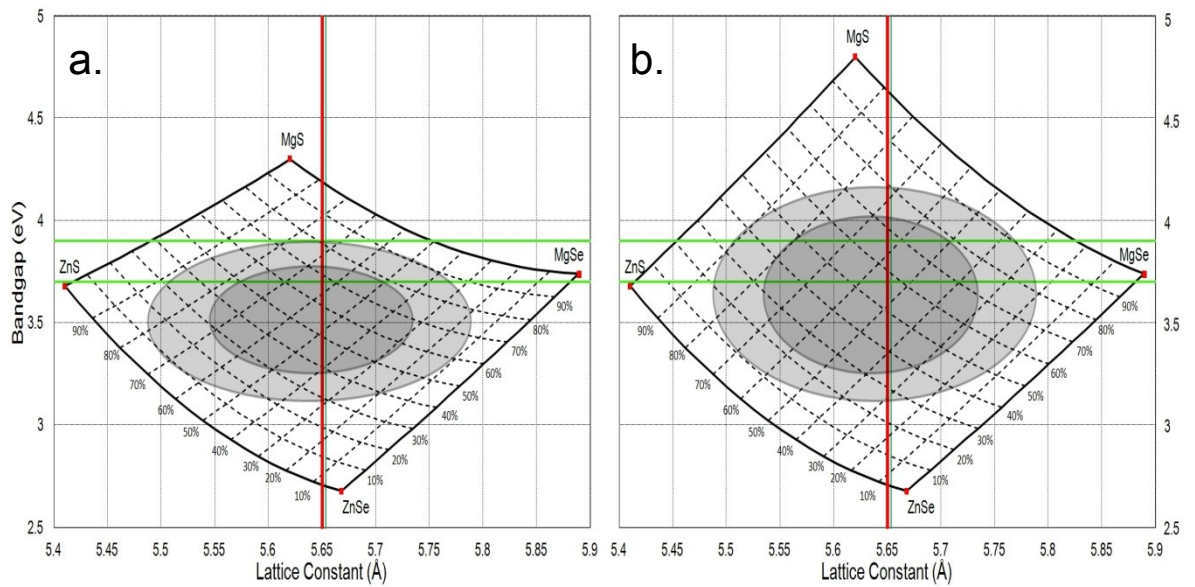


Fig. 5.18. Schematic of the ZnMgSSe compositional square assuming a 300K MgS bandgap of 4.3 (a) and 4.8 eV (b). The red line is the lattice constant of the alloy in HWC333 and the green lines represent the possible bandgap values. The light and dark grey areas again represent the binodal and spinodal decomposition regions but the boundaries are not plotted accurately.

Figure 5.18 shows how the QA compositional square varies as the MgS bandgap is changed. An increase in the MgS bandgap value used results a decrease in the values of  $x$  and  $y$  required for the alloy to have a  $3.8 \pm 0.1$  eV bandgap.

As it is known that there are thermodynamic limits on the range of compositions that can be grown, this will limit the range of values that the bandgap of MgS can possess. However as the thermodynamic data required by the theory are difficult to measure it is not possible (at present) to use this theory to help determine the composition of the alloy, but it does allow a very rough limit to be placed on the maximum value of the MgS bandgap. In figure 5.18 (b), the compositional range of the alloy is  $x = 0.58 - 0.65$  and  $y = 0.64 - 0.72$  and these values are likely to fall within the binodal decomposition region. If the 300K bandgap of MgS is any higher, then the composition would certainly fall within the spinodal region where growth is not possible. It is therefore possible to say that the maximum bandgap value is likely to be  $\leq 4.9$  eV at 300K and certainly less than 5.3 eV (as by this value the composition range would be centred on  $x$  and  $y$  values equal to  $\sim 0.5$ ).



## 5.4. Quaternary Alloy XRI/XRD Modelling Problem

As has been mentioned already in this chapter during the work to develop these QAs a number of issues arose concerning the use of the XRI technique to measure the composition of the alloys. The main problem is that for a number of the samples investigated, a range of different compositions and thicknesses resulted in identical GOF, thereby making it either hard or impossible to report either a lattice constant or composition for the alloy layer.

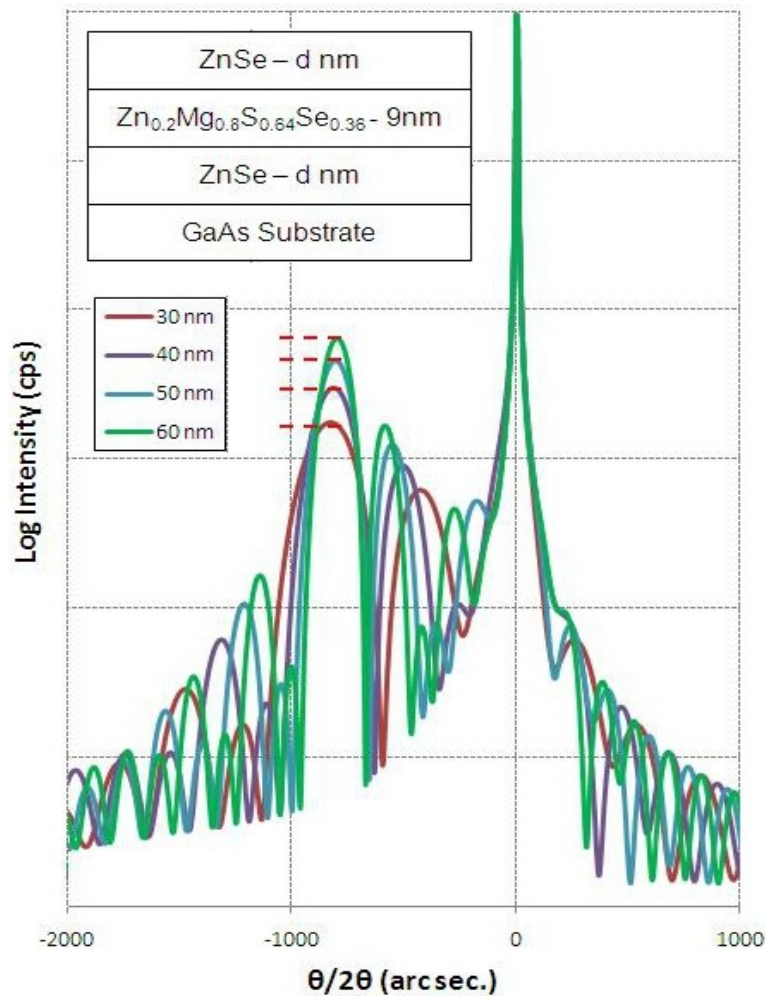


Fig. 5.19. Variation of the rocking curve of the simulated data from a generic XRI structure with ZnSe thickness  $d_1(=d_3)$ . Inset is a schematic of the structure. The four curves show the variation of the peak height with cladding layer thickness.

The XRI technique requires samples where a thin layer of a material of interest has been grown between two nearly identical thickness layers of another material whose lattice constant is known. In samples produced at HWU this is typically ZnSe. When the samples XRD spectrum is obtained the thin layer modulates the XRD peak from the thick layers in such a way that its thickness



and lattice constant can be determined. An advantage of this technique, compared to XRD, is that as only a very thin layer of the material of interest is required, it will still work even for materials that either are metastable or have a large lattice mismatch

During the analysis of an XRI sample there are 6 parameters that need to be determined if structural relaxation has been avoided and can be ignored. These are the thicknesses and lattice constants of the 3 layers. Typically the lattice constant of the 2 thick layers ( $a_1$  &  $a_3$ ) will be identical and known (as is the case for ZnSe) and as their thicknesses ( $d_1$  &  $d_3$ ) are chosen to be nearly identical, this immediately reduces the number of free parameters to  $\sim 3$ .

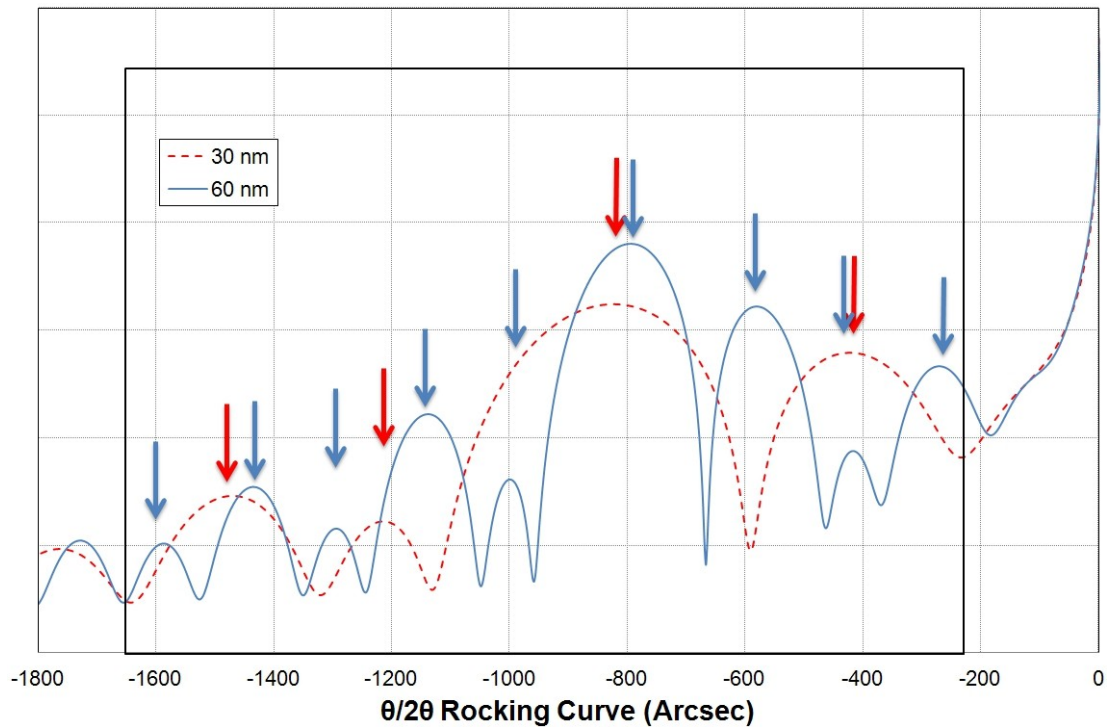


Fig. 5.20. Variation of the simulated rocking curve for a generic XRI structure with ZnSe thickness  $d_1(=d_3)$ , demonstrating the increasing number of peaks with increasing thickness. The structure is identical to that shown in fig. 5.19. The red dashed curve has a cladding layer thickness of 30nm and the blue 60nm .

Figure 5.19 and 5.20 show the variation of a simulated XRI structure with the thickness parameter  $d_1$  (which is set equal to  $d_3$ ). An increase in  $d_1$  has two effects, first it causes the intensity of the ZnSe diffraction peaks to increase, fig. 5.19 and second it increases in the number of peaks in the region from -200 to -1600 arc seconds (when  $d_1=30\text{nm}$  there are 4 peaks – the red arrows in fig. 5.20,  $d_1=60$  there are 9 peaks – the blue arrows in fig. 5.20). As the exact

diffracted intensity measured from a sample is affected by a number of factors (alignment, sample structural quality etc.), fitting the intensity of the main ZnSe XRD peak it is not a precise way to determine the ZnSe layers thicknesses.

The thickness can be far more accurately determined by matching the number and position of the simulated peaks with the measured ones. Often the position is not completely accurate across the entire scan range but only a very small thickness range produces the correct number of peaks.

Changing the thickness or lattice constant (mismatch) of the thin layer changes the spacing between the ZnSe layers and therefore the modulation of their peak. Figure 5.21 shows the 004 simulated rocking curves for a generic XRI structure as the QA layer thickness is increased from 0.5nm to 10nm (the structure used is inset). The dotted red line shows the curve for a single 52nm thick ZnSe layer grown on GaAs plotted at four times the intensity of the XRI samples (due to the summation of the intensities from the two ZnSe layers).

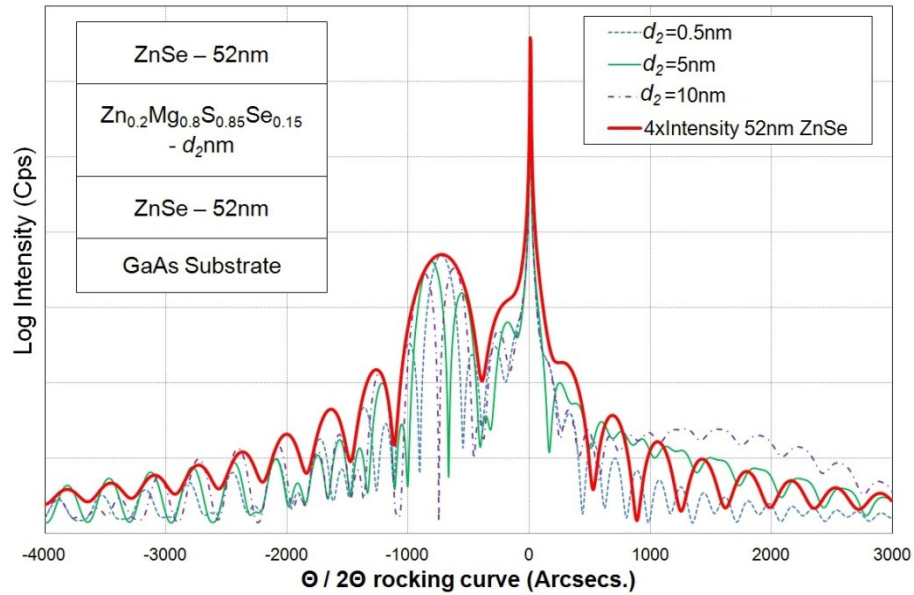


Fig. 5.21. Effect of varying  $d_2$  on the simulated XRI 004 rocking curve. The structure used is inset. The figure demonstrates that the XRI curves trace out the XRD peak of cladding layer.

The various XRI plots are within the envelope of the ZnSe XRD peak. Figure 5.22 shows the progression of the ZnSe peaks with thickness. As well as moving towards the right with increasing  $d_2$ , the peaks intensity also increases

until they are at the ZnSe XRD peak position and then decrease. If a wide enough range of thicknesses are modelled the arrangement of the 2 main peaks repeats, although the other outlying peaks will not be in exactly the same position.

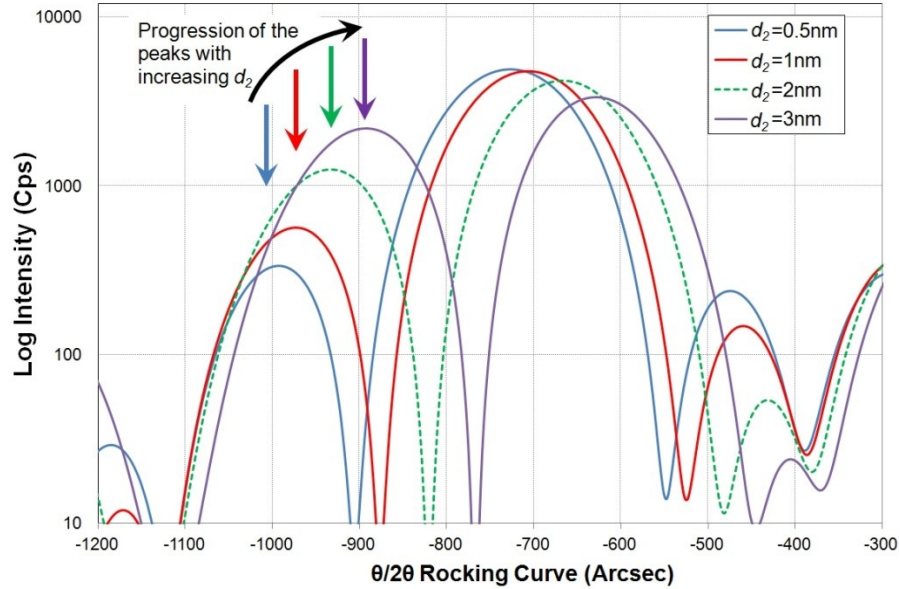


Fig. 5.22. Progression of the ZnSe XRD peaks with increasing  $d_2$  thickness. Same structure as fig. 5.21 used to generate data.

Increasing  $d_2$  also causes an XRD peak for the QA layer to appear, in the case of fig. 5.19 at  $\sim 2000$  arcsecs. In the figure the intensity of the x-ray source has been set at a higher flux than is typically, to improve the clarity of the diagram, and this results in the XRD peak becoming visible at around 3-4nm. Normally the layer thickness needs to be 10-15nm before an XRD peak is seen, and this places an upper limit on the thickness of the  $d_2$  in an XRD samples if a peak is not observed.

Varying the thin layers lattice constant,  $a_2$ , produces an identical effect to changing  $d_2$ . The resulting modulation of the ZnSe peak causes the double peak to trace out the shape of the ZnSe XRD peak, and it is again possible to find different lattice constants where the simulated XRD pattern is nearly identical. However as shifts caused by changes in the lattice constant for samples with  $d_2 < 10\text{nm}$  will not result in the appearance of an XRD peak, a wider range of lattice constants has to be considered.

The two thin layer parameters are also coupled, meaning that combinations of thicknesses and mismatch will result in good fits to the measured data, where the individual values would not have. This increases the range of parameters that will produce low GOF figures. An example of this is shown in figure 5.23, which shows a colour map of the variation of the GOF of a 3 layer 004 simulation to a synthetic dataset produced using the structure in figure 5.21. The synthetic data has noise added representing a 30s count time and the x-ray intensity and background count set to a representative level (50k and 1.4 counts respectively) to more closely resemble actual measured X-ray data.

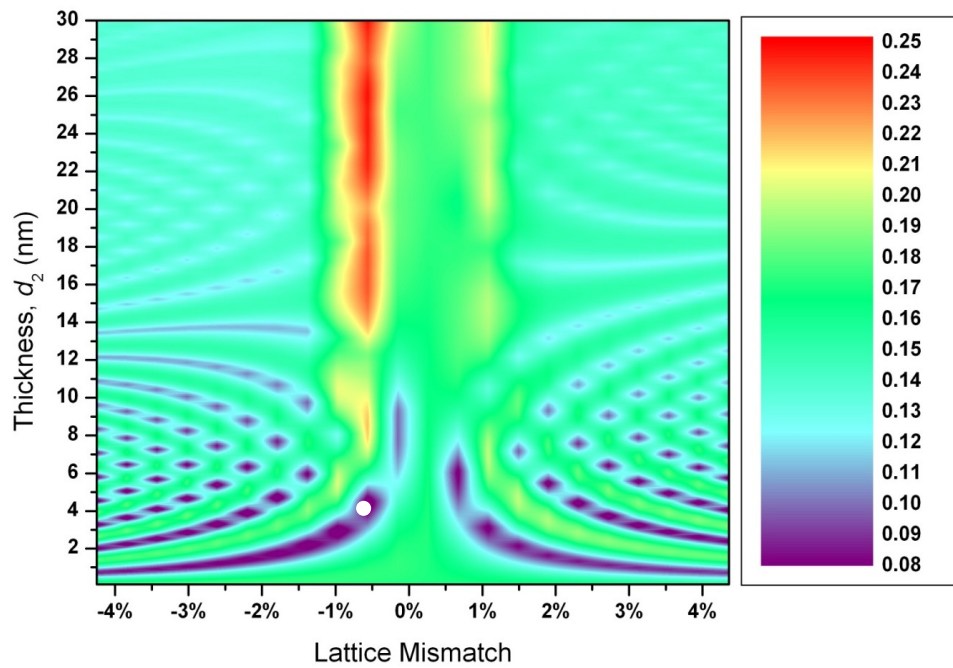


Fig. 5.23. Variation of the goodness of fit for a simulation of a generic XRI structure with  $d_2$  and  $a_2$  (mismatch). The white dot marks the  $d_2$  and mismatch value used to generate the original data.

The figure shows that even when modelling simulated data there are a wide range of thickness and lattice mismatch values that produce good fits. When modelled with the correct original values ( $d_1 = d_3 = 52\text{nm}$ ,  $d_2 = 4\text{nm}$  and  $a_2 = 5.617\text{\AA}$  [( $x=0.8$ ,  $y=0.85$ ) =  $-0.64\%$  mismatch]), RADS returns a GOF of 0.051. However when modelled using the normal limits ( $d_1 = d_3 = 30\text{-}70\text{nm}$ ,  $d_2 = 0.1\text{-}10\text{nm}$  and  $x=0.7\text{-}1$ ,  $y=0.6\text{-}1$ ) it opts for a solution with the right ZnSe thicknesses ( $\pm 0.5\%$ ) but a QA layer thickness of  $4.2\text{nm}$  (a  $5\%$  error) and a lattice constant of  $5.619\text{\AA}$  ( $x=0.8313$ ,  $y=0.8670$ , a mismatch of  $-0.61\%$ ), producing a GOF of 0.046. Although the composition is different, again its lattice constant is almost the same.

So far all of the work described has been based on 004 scans and modelling but it is equally true for 115 scans - again there are a range of  $d_2$  and  $a_2$  values that will produce good fits to the measured data. However these values maybe different to those from the 004 analysis. By repeating the analysis for the 115 scan and then adding it to the 004 plot, a new plot (figure 5.24) that describes the variation of the GOF for both scans is produced.

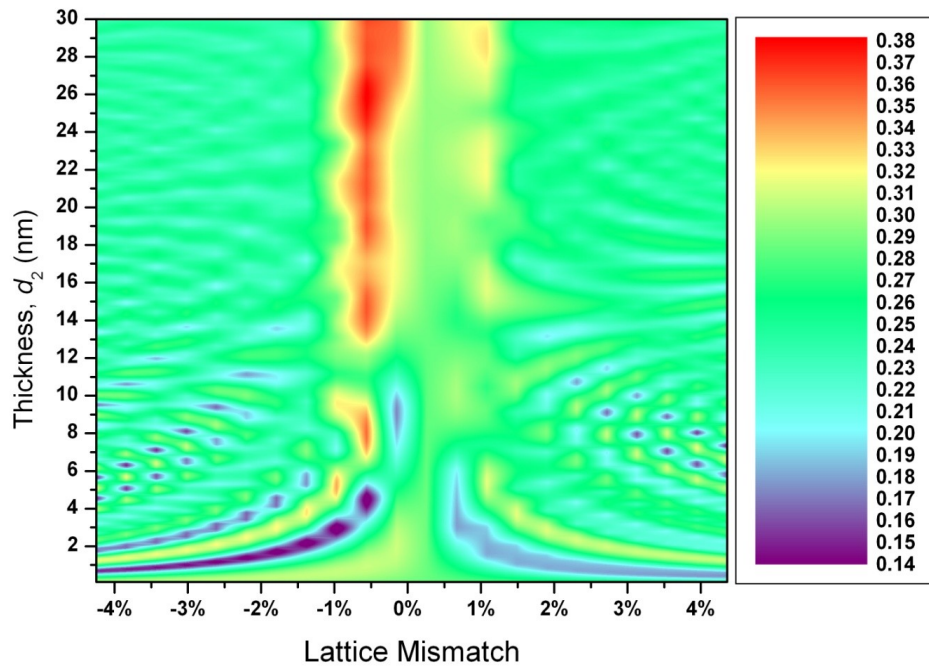


Fig. 5.24. Variation of the simulated structures combined 004 and 115 goodness of fit vs. thickness and mismatch.

This analysis shows that even when both scans are used there are still a range of values that will result in the RADS software producing a low GOF value. By combining the analysis of the two scans the range of values is reduced, but it is still difficult to accurately determine a lattice constant and thickness. In the case of the generated structure being modelled in fig. 5.24, there are actually a wide range of values around the ones used to produce the data ( $d_2=4\text{nm}$  and a mismatch of  $-0.56\%$ ) that would all appear to be reasonable values if the analysis were of a genuinely unknown sample.

The reason why a range of values are able to produce nearly identical GOF figures arises from the way the GOF is calculated. As it is a measure of how closely related a simulation is to the measured data, the largest features in the measured data will determine to a large degree the GOF. Therefore anytime the

large modulated ZnSe peaks in the simulation coincide with the measured data a low GOF value is produced. The coincidence of the other smaller features also affects the GOF but unless these are very different, they are less important than the main peaks. This is especially true when noise and samples with a low diffracted intensity are considered, as is often the case with real samples, as it will mask the low intensity differences between compositions.

These low intensity differences are the reason the RADS software can select one QA composition in preference to another and is the result of each of the four binary compounds at the corners of the ZnMgSSe compositional square have different densities, Poisson's' ratios and atomic constituents (Zn or Mg, S or Se). This results in different compositions with the same lattice constant producing slightly different simulated rocking curves. However as these differences are extremely small, once noise is taken into account the differences become impossible to distinguish. So although the software will still find that one composition has a smaller GOF than another, it is debatable whether this is the true composition of the alloy or just the one that fits the noise best.

So far, all of the samples analysed have been QA, but this analysis is equally applicable to ternary alloys or binary compounds with unknown values. In these cases each composition produces a unique lattice parameter, but there is still a problem with different thicknesses combining with different lattice constant to produce nearly identical fits.

In all of these situations XRD measurements will produce more reliable results, as a thick layer of a compound will definitely produce a unique scattering angle and hence lattice constant. The only issue is then determining if the layer has begun to relax. However by first growing a thick (>100nm) layer and determining its lattice constant, it is then possible to determine if a thinner layer has started to relax.



#### 5.4.1. Re-Analysis of the XRI Samples

Having determined that XRI gives unreliable results, especially with noisy or low intensity spectra, it is worth looking at a selection of the samples previously analysed to see whether or not the results obtained are meaningful. This was undertaken by performing the same analysis used in figures 5.23 and 5.24 to see how the GOF of the simulated data varies with  $d_2$  and  $a_2$  and whether either a unique lattice constant or composition can be obtained for the samples.

##### 5.4.1.1. Series 1: HWC167

Both the XRI and XRD scan spectra were re-analysed to investigate any differences between them. Figure 5.25 shows the combined 004 and 115 GOF for the XRI (a) and XRD (b) scans. The XRI data shows a series of different compositions and thicknesses that will produce good fits. The XRD data (b) shows only a very limited range of values produce a good fit and match the expected layer thickness. These are centred on the mismatch line that matches the XRD peak, -0.7% marked with the dotted red line. The data appears to show a poor fit at the thickness and lattice constant previously found to produce the best fit ( $d_2=15.3\text{nm}$ , -0.7% mismatch). However this is simply due to the mismatch step size of the data ( $\sim 0.4\%$ ) causing it to miss the exact value.

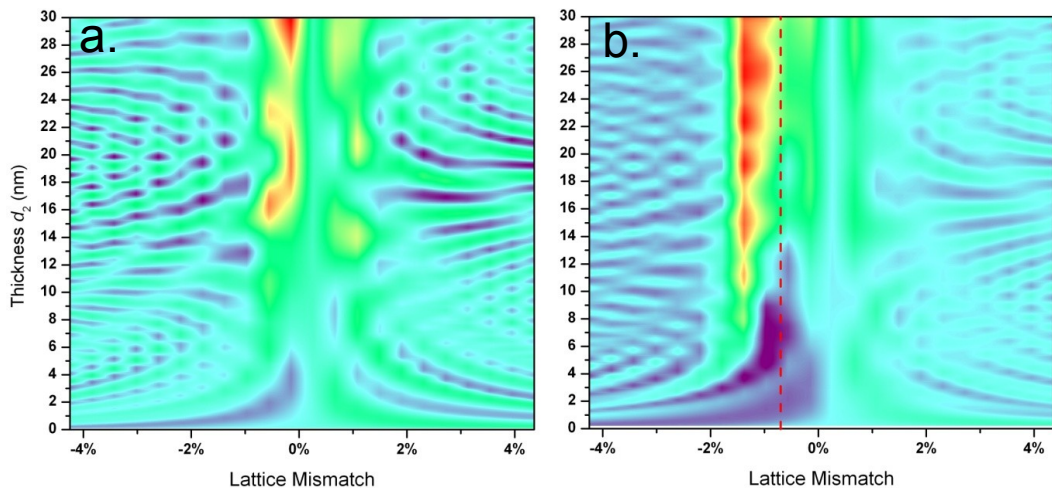


Fig. 5.25. Variation of goodness of fit with thickness and mismatch for the XRI(a) and XRD(b) data from HWC167. The colour regions represent the same values as in fig. 5.24.

Figure 5.26 shows the 115(a), 004(b) and combined(c) data for the XRD scan with a smaller mismatch step size ( $\sim 0.2\%$ ) around the mismatch determined for

the QA layer. In the 004 and combined data (b&c) a region of good fit is now found at the correct position. The lack of a good fit in the 115 spectra at this position is due to the very low intensity of the XRD peak. However if the background count is increased from 1 cps to 1.9cps and the width of the Gaussian scattering term (introduced to simulate the use of a wide detector slit) is reduced from 7000 to 3000 arc seconds the good fit returns (not shown).

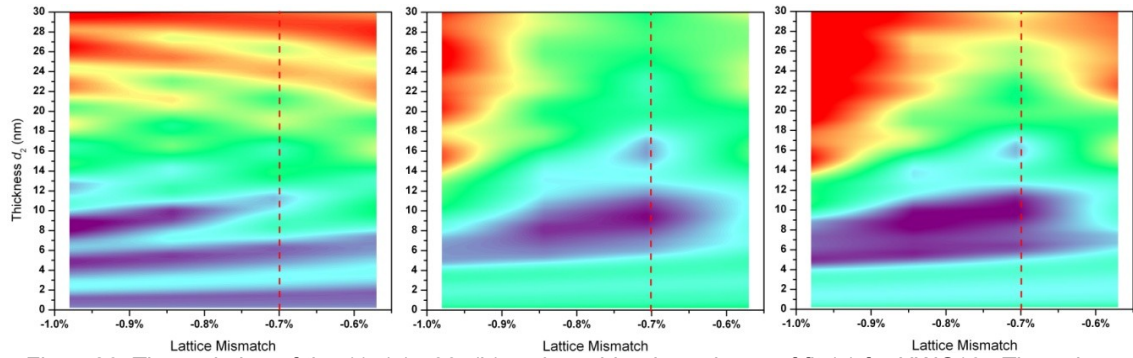


Fig. 5.26. The variation of the 115(a) , 004(b) and combined goodness of fit (c) for HWC167. The colour regions represent the same values as in fig. 5.24.

#### 5.4.1.2. Series 1: HWC 178 and 180

Both samples showed similar GOF plots to the XRI results for HWC167 and as such they are not shown. However they confirm that a number of different mismatch and thickness combinations will produce good fits including values of 8.1nm and -0.89% for HWC178 and 4.6nm and -0.82% for HWC180. These are close to the values predicted by the extrapolation of the XRD result in HWC167.

#### 5.4.1.3. Series 2: HWC 298 and 302

The combined 004 and 115 GOF data for HWC298 is shown in figure 5.27. HWC302 show nearly identical behaviour to 298 and both 298 and 302 are very similar to the original QA work. However the analysis of these XRI scans also shows antiphase lines where the simulated ZnSe peak is at a maximum between the split peak of the measured data, an example is shown in fig. 5.28 for HWC298. Figure 5.27 also shows large areas of poor fit for thicknesses greater than 10nm, this is due to no XRD being present in any of the scans of HWC298 or 302. This would be expected as the QA layer in both samples should be too thin to see this.



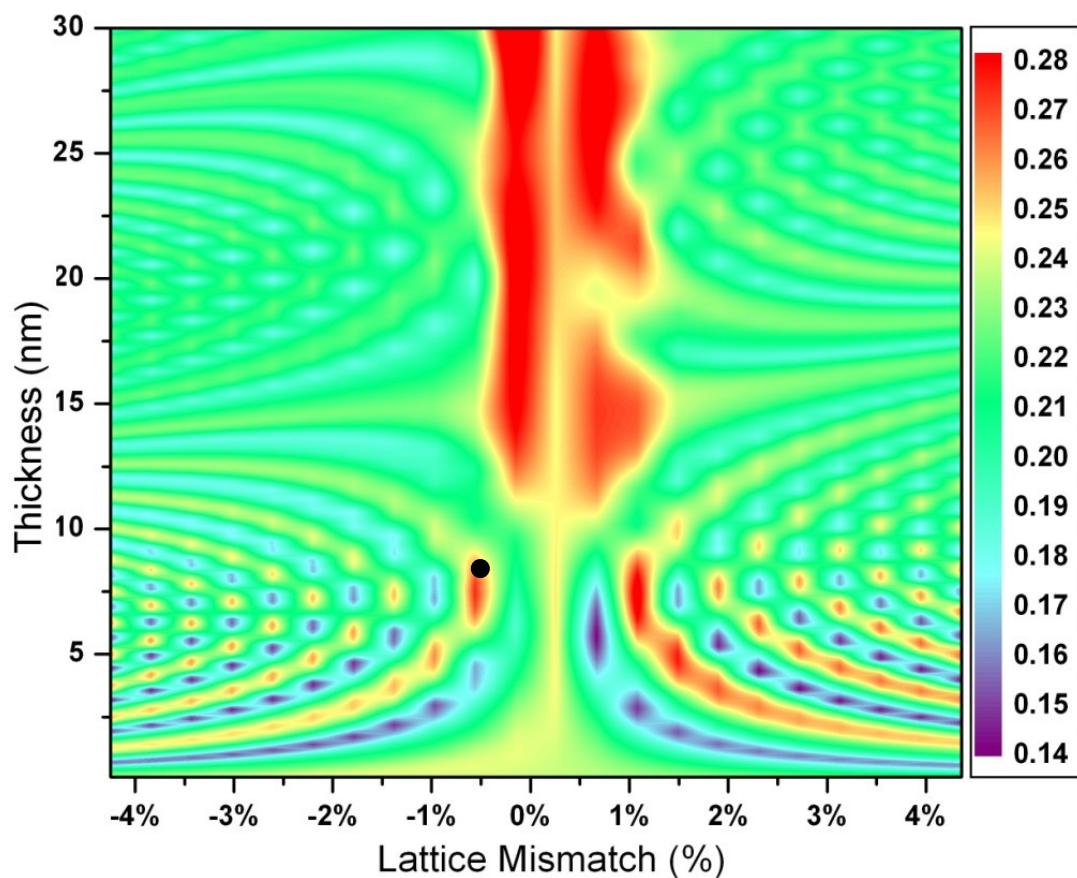


Fig. 5.27. Variation of goodness of fit with mismatch and  $d_2$  thickness for HWC298. The black spot shows the thickness and mismatch used to generate the model used in fig. 5.28

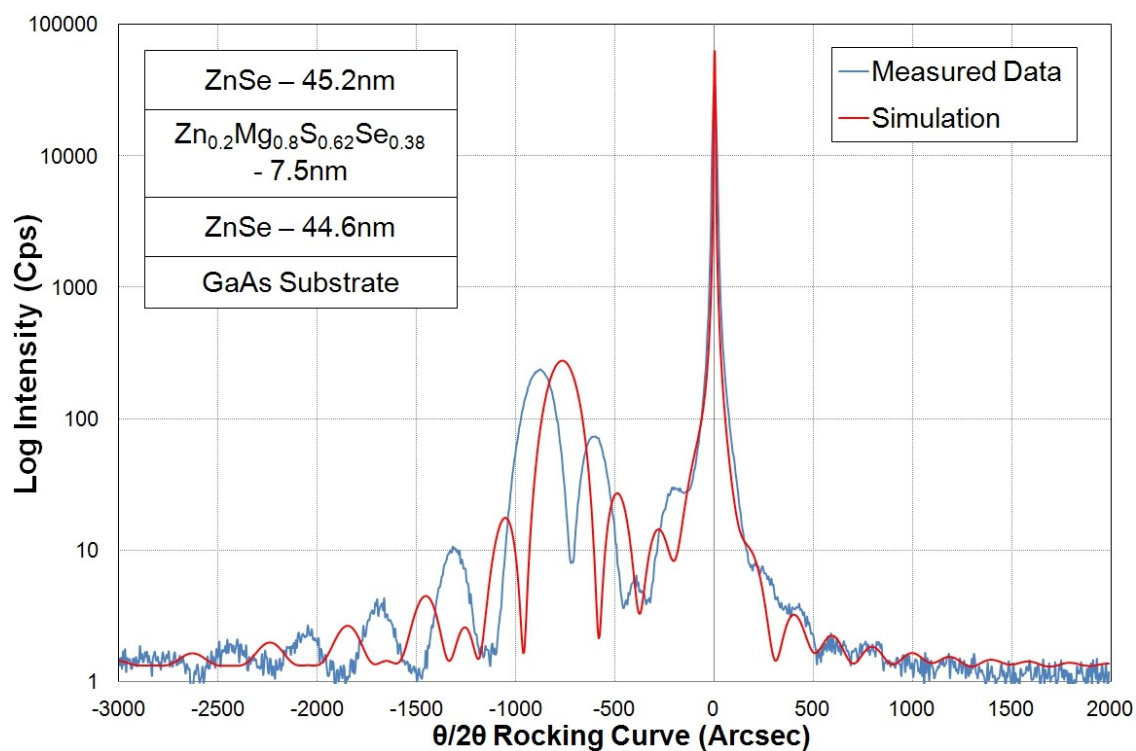


Fig. 5.28. Measured and modelling 004 scan of HWC298 showing a composition (mismatch) and thickness combination that produces a bad fit due to the peaks being out-of-phase. The blue data is the measured curve and the red, the simulation

#### 5.4.1.4. Series 2: HWC 333

As HWC333 is not an XRI sample the GOF vs. thickness and lattice mismatch plot is somewhat different. Instead of showing the periodic features as a function of thickness and mismatch, it instead shows straight lines over the majority of the possible thickness range, see figure 5.29. The plot shows that in the region measured in the 004 and 115 scans there is only a very small area around zero mismatch with a low GOF. Outside this region, the composition must have a large mismatch before a reasonable fit is again achieved, but as scans do not show an XRD peak at large mismatch then this cannot be the case. The actual range of lattice constants that produce a good fit is so small that it is necessary to use a much smaller mismatch step size (0.02%) to see the region of best fit, this is shown in the inset diagram in the figure.

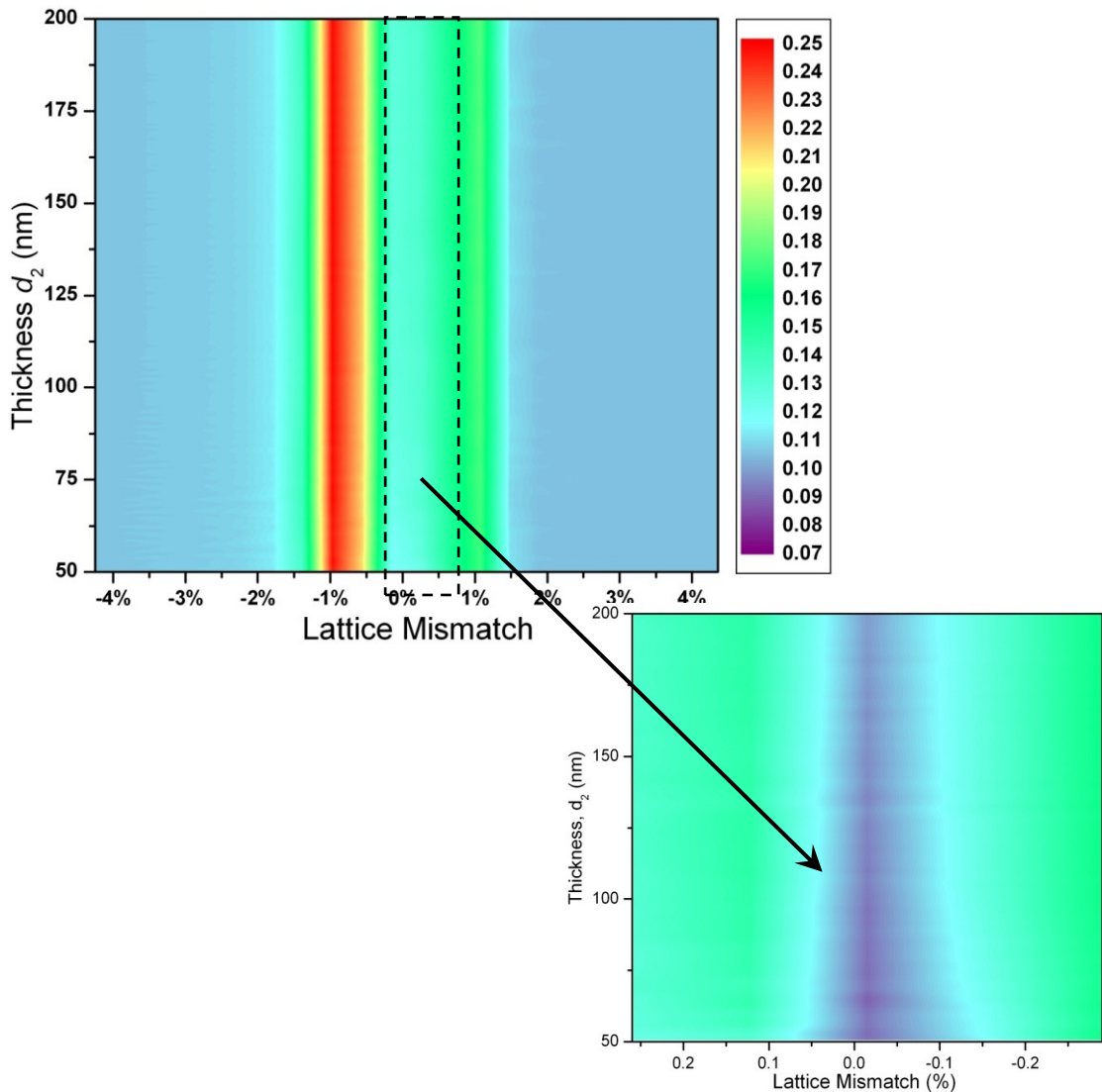


Fig. 5.29. Variation of the goodness of fit for HWC333 with mismatch and QA thickness. The second (lower) graph shows a higher resolution plot of the region around lattice match

#### 5.4.1.5. Series 2: HWC 340

HWC340 is another XRI sample with a similar series of lines of best fit. However on this occasion the only range of mismatches that are physically realistic are those centred on 0.25% as the expected thickness is >10nm. The plot (figure 5.30) again also shows two regions of poor fit and these again demonstrate that the sample does not contain a visible XRD peak.

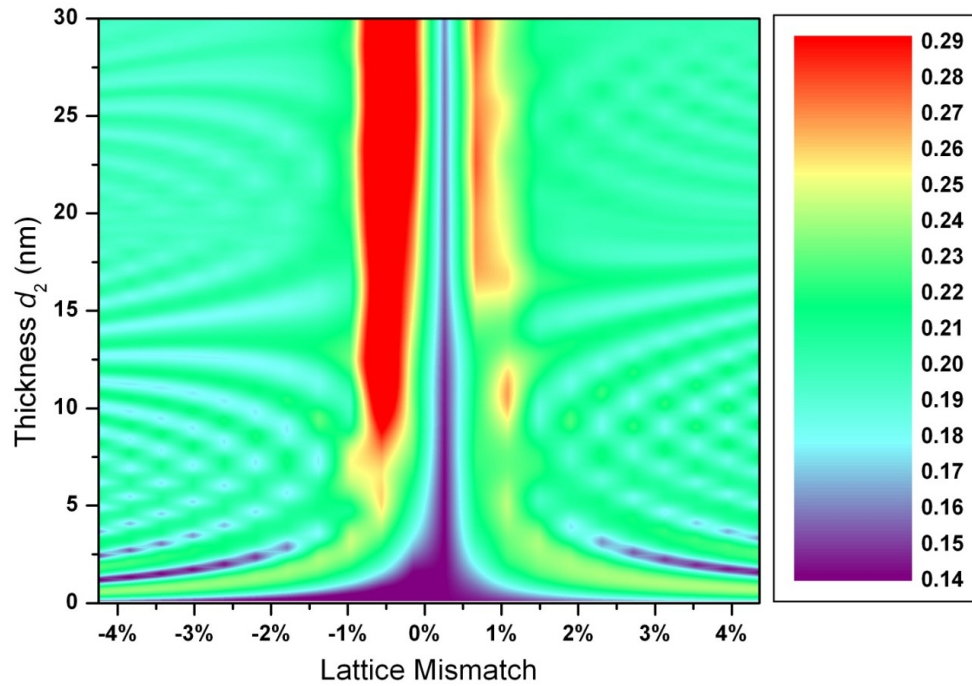


Fig. 5.30. Variation of goodness of fit with thickness and mismatch for HWC340.

### 5.5. Third Set of Samples

Although the 2<sup>nd</sup> set of samples produced an approximately lattice matched sample, the  $\text{Zn}_{1-x}\text{Mg}_x\text{S}_y\text{Se}_{1-y}$  contained a large ZnSe fraction ( $x=0.71\pm0.16$ ,  $y=0.66\pm0.13$ ,  $E_g(300\text{K})=3.9\pm0.1\text{eV}$ ) and this means it probably within the binodal decomposition region. As one of the objectives of this project was to develop a lattice matched alloy that can be used to grow thick layers, it would therefore be better to use an alloy composition that has a lower ZnSe fraction.

To achieve this, a new series of samples were grown utilising fluxes closer to those used for the 1<sup>st</sup> set of samples (HWC167-180). This work also has the added benefit that additional QA samples with different compositions may allow

the determination of the bandgap of MgS to be improved and hence our ability to determine the composition of alloys in the future.

As the previous section shows the XRI technique can produce inaccurate figures for the lattice constant or layer thickness, an XRD and 2 ELO XRD samples were grown for this 3<sup>rd</sup> set of QA samples. The ELO samples were characterised using XRD, but due to problems with the growth of the MgS layers, none of the ELO samples were able to be lifted and hence their bandgap could not be measured.

A subsequent ELO sample (HWC 356) containing a double ZnSe/QA QW separated by an MgS sacrificial layer, was grown primarily to investigate the use of the alloy as a barrier. But this also failed to lift and as the PL lab was being relocated, the sample has so far not been analysed using PL spectroscopy.

#### **5.5.1. Growth**

Initially the XRD sample (HWC 355) and the ELO double quantum well sample (DQW, HWC 356) were grown and characterised. As these showed partial relaxation, the 2 ELO XRD samples (HWC 359 and 368) were then grown with slightly different conditions; the ZnS flux was increased for HWC359 and the Zn flux then also increased for HWC368. A schematic of the structure of the samples is shown in figure 5.31.

HWC 356, 359 and 360 all showed  $c(2 \times 2)$  and both  $2 \times 1$  and  $c(2 \times 2)$  RHEED patterns during the growth of the MgS and QA layers respectively. However the RHEED pattern of HWC356 started to become spotty after the first QA layer, this became more diffuse during the growth of the MgS layer before deteriorating significantly during the next QA layer to a series of very diffuse spots. This suggests that the surface of the sample had become rough and flat, pseudomorphic growth stopped occurring.

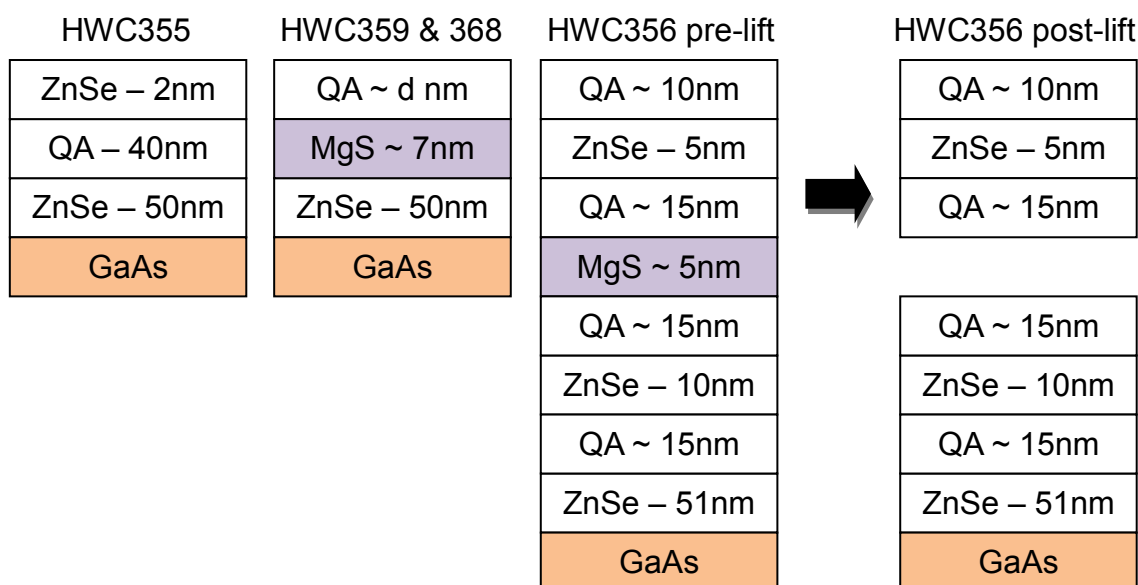


Fig. 5.31. Schematic representation of the 3<sup>rd</sup> series of QA calibration samples, HWC355, 359/368 and 356 respectively including the intended post liftoff appearance of HWC356.

Both HWC359 and 368 showed good RHEED patterns up until 3 minutes of QA had been grown, at this point the patterns became diffuse and began to get spotty. Due to the deteriorating RHEED pattern, the growth of HWC359 was stopped at 3 minutes whilst HWC368 was grown for another 8 minutes by which time the RHEED pattern had become a series of sharp spots. Again this suggests that the end of the growth was not smooth and pseudomorphic.

### 5.5.2. X-ray Characterisation

All of the samples were investigated using HRXRD and showed fairly broad features consistent with samples that have undergone some form of relaxation resulting in increased dislocation densities. HWC 355, 359 and 368 all showed XRD peaks and these, along with 356, were all fitted using the normal constraints ( $x=0.7-1$ ,  $y=0.6-1$ ). The best fit values are shown in table 5.3.

The growth rates determined for the ZnSe, MgS and QA layers are all lower than expected but these may be underestimated due to the structural relaxation. If correct, the low MgS growth rate would explain the samples failure to lift as  $G_R \geq 0.33 \text{ Å/s}$  is required to grow the 4nm minimum thickness required for ELO (see chapter 4). Previously an MgS growth rate of  $\sim 0.4 \text{ Å/s}$  had been determined and was used to calculate the growth times used here.

Sample No.	Quaternary Alloy				ZnSe	MgS	GOF	
	Mg %	S %	Mismatch %	$G_R$ (Å/s)	$G_R$ (Å/s)	$G_R$ (Å/s)	004	115
HWC355	88	63	-0.37	0.94	0.39	-	0.084	0.074
HWC356	76	70	-0.07	1.00	0.40	0.30	0.099	0.118
HWC359	100	71	0.79	0.94	0.39	0.30	0.107	-
HWC368	94	68	0.71	0.37	0.43	0.34	0.133	0.117

Table 5.3. Data obtained from fitting x-ray data from QA series 3 samples.

Figure 5.32 shows the 004 scan of HWC356, it shows a broad feature at the correct position for ZnSe and a few other small broad features. The lack of sharp diffraction features make interpreting any model of the sample difficult as a range of structures will fit the data. However the model shown inset produces a GOF of 0.099 which is a very good fit. The best fit composition of the QA is also one that is close to lattice match (-0.07% mismatch) which would be ideal if correct, but on the basis of this spectrum alone it is difficult to conclude whether that is true or not.

All of the XRD structures show similar rocking curves with a broad ZnSe peak present at ~650 arc seconds and a broad QA XRD peak at a position further from the substrate peak consistent with relaxation in the layers, see fig. 5.33. In all three cases the modelled spectrum also has a substrate peak that is narrower than the measured peak. This is most likely due to the software having difficulty in modelling the relaxed ZnSe and QA layers and selecting an unrealistically low X-ray beam intensity to solve this. This makes interpretation much harder, as the calculated lattice mismatch values differ from the true value for the alloy as the extent of the relaxation is unknown. Repeating the fitting but allowing the QA layers to relax results in the expected change in lattice constant, the mismatch increasing.



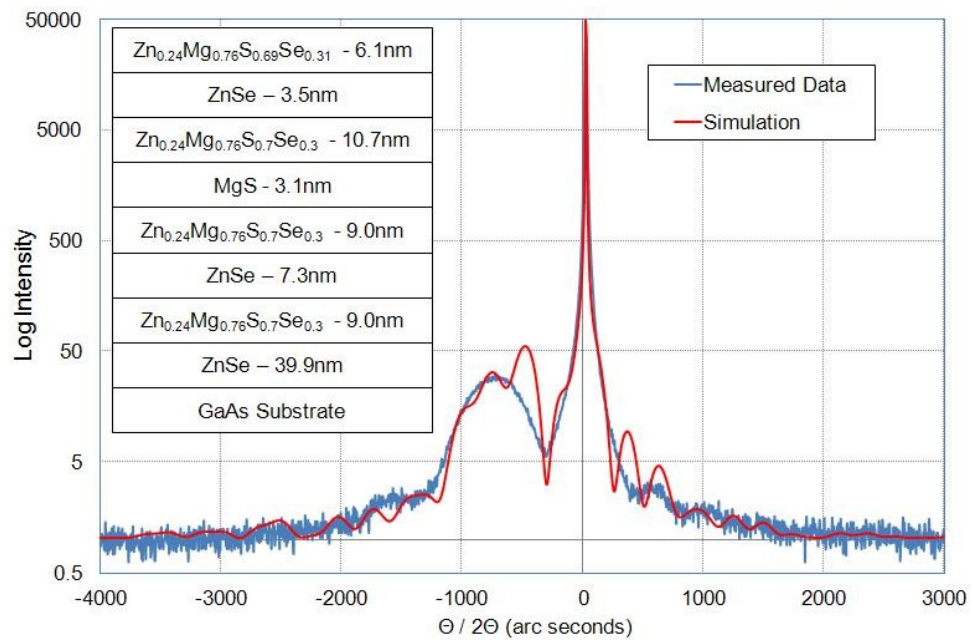


Fig. 5.32. 004 XRD scan and model of HWC 356. The structure used for the simulation is shown inset. The blue curve is the measured data and the red the simulation.

For example in HWC 368 the best fit has a mismatch of 0.71% when the layer is completely strained to the substrate, but if allowed to relax the best fit changes to a mismatch of 0.88% at 25% relaxation. This allows a much wider range of possible lattice constants for the alloys. However a complete analysis of this variation has not been performed at present. It should be noted that the change in lattice constant with relaxation is a function of the composition of the alloys (as all the binaries have differing Poisson's ratios), so it might actually be an aid to determining the composition of an alloy.

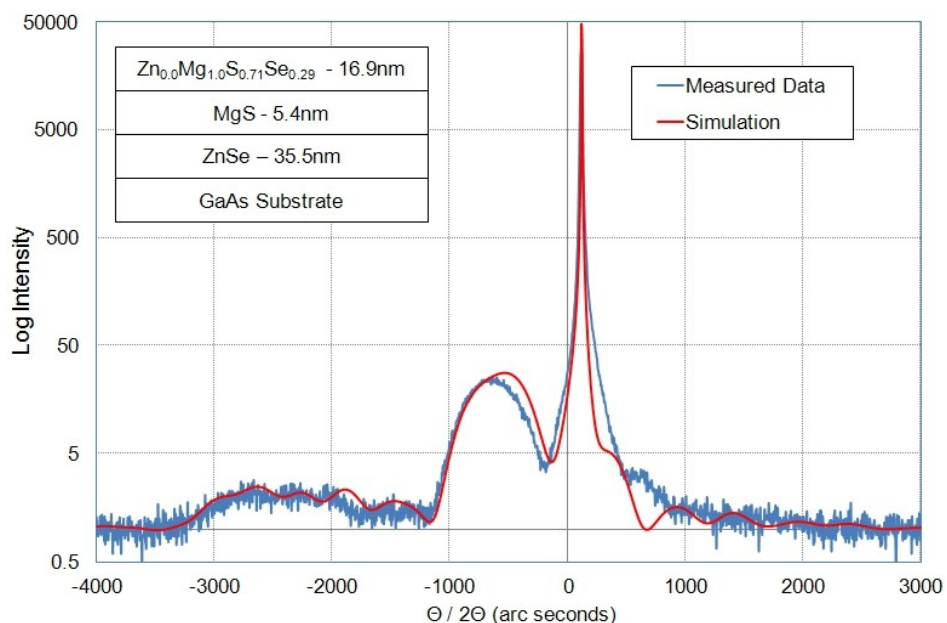


Fig. 5.33. The XRD rocking curve for HWC359 a QA liftoff sample. The blue curve is the measured data and the red the simulation.

## 5.6. Conclusions

This chapter has detailed all of the work I have undertaken to attempt to develop a lattice matched, wide bandgap, etch resistant quaternary alloy. During this work an alloy was produced with the desired properties of having a wide band-gap and a lattice matched composition.

In section 5.2, all of the work on the initial samples grown by Richard Moug was explained with particular attention paid to the x-ray analysis of these samples as a prelude to the work in section 4 discussing the reliability of the XRI technique. This section also detailed the determination of the bandgap of this alloy ( $4.19 \pm 0.05\text{eV}$  at 300K) and this value represents a minimum value of the bandgap of MgS. Finally in section 2 the performance of the alloy as a barrier layer both before and after ELO was presented.

Section 5.3 described the work undertaken to produce a new QA with a lattice matched composition and shows that this can be achieved. The bandgap of this lattice matched alloy was measured and found to be  $3.8 \pm 0.1\text{eV}$ . Using this value allows a maximum bound for the band-gap of MgS of  $4.9\text{eV}$ . From this measurement and the one in section 5.2 then the bandgap of MgS at 300K will fall in the range  $4.55 \pm 0.35\text{eV}$ . This is still a very large range, but is an improvement on the 3.4-6.5eV range reported in the literature[5.22-5.24].

The work also demonstrated the effect that varying some of the flux ratios has on the composition, showing that varying the selenium flux has a larger effect than varying the zinc. This also shows that it may be hard to grow thick layers of lattice matched alloy consistently as even small (2-5%) changes in the fluxes seemed to have a significant effect on the composition of the resultant alloy.

The work in section 5.4 showed that while the original idea that a unique composition could be obtained from XRI measurements alone is correct, in practice it is almost impossible to achieve, due to the noise present in real



experimental data. It also detailed my reanalysis of all the XRI and XRD samples in the initial and second series of QA samples, and shows that although for any given composition it may be possible to obtain a unique lattice constant from an XRI measurement. This is more easily achieved with an XRD sample.

Finally section 5.5 described the continuation of the work to develop a lattice matched alloy again using reduced zinc and selenium fluxes to produce an alloy that is further from the decomposition region. This work was not successful as all the layers produced appear to have large mismatches to GaAs so that relaxation had occurred after only very thin layers had been grown. This failure was compounded by the inability to get any of the samples to lift due to the uncertainties in the growth rate of MgS.

Despite this, this work has shown that it should be possible to grow lattice matched, wide band-gap ZnMgSSe alloys for use as a replacement barrier in ELO samples. The alloy should function in a nearly identical way to MgS and therefore provide excellent optical confinement. The only issue with growing very thick layers is that small fluctuations in fluxes during and between growths may result in it being difficult to grow lattice matched compositions consistently.

## 6. Optical Characterisation of II-VI compounds and Distributed Bragg Reflector Development

This chapter details all the work I have undertaken to optically characterise the different compounds grown by the MBE group at HWU and to design a distributed Bragg reflector (DBR) based on them. The samples investigated in this chapter have been grown by a number of the members of the group over several years and comprise almost the full range of materials produced. A series of ZnCdSe/MgSe samples produced by the MBE group at the City College of New York (CUNY) for our collaboration to extend the ELO process to MgSe (as discussed in chapter 4) were also investigated, to enable the bowing parameter of the ZnCdSe ternary alloy to be determined.

A brief outline of the significance of the optical properties along with the techniques used to measure them will be presented in section 6.1. A summary of the relevant work undertaken by other groups to characterise II-VI compounds will also be included and used for comparison later in the chapter.

Section 6.2 details the work I have undertaken to determine the band-gaps of a number of our samples. This work mainly comprises 77K PL spectroscopy but a number of results have also been obtained through transmission/absorption measurements. A number of the results used in this section relate to work reported elsewhere in this thesis, but are used here to determine the bowing parameter of the ZnCdSe system mentioned above.

Section 6.3 contains a brief explanation of the work I have performed to investigate the use of reflection measurements to determine the thickness of ZnSe overgrowth (OG) samples and demonstrates that this method is preferable to x-ray analysis for this purpose.

All the spectroscopic ellipsometry (SE) work undertaken to measure the optical constants of our II-VI compounds will be detailed in Section 6.4. This section will also describe the development of a novel technique to use XRI structures to measure the optical properties of a number of the compounds that we have grown and the attempts to develop SE into a general structural characterisation technique. I have also investigated the reported dispersion curves for ZnSe and tried to gain an understanding of the oxide layer that forms on ZnSe.

Final conclusions and suggests for further work will be presented in section 6.5.

## 6.1 Introduction

Semiconductors are used extensively in optoelectronic applications due to their unique properties including optical emission under electrical excitation. However the integration of semiconductors into useful devices requires detailed knowledge of how they interact with light. There are principally 3 parameters that need to be measured: the band-gap ( $E_g$ ), refractive index ( $n$ ) and extinction coefficient ( $k$ ). These are all related but still need to be measured individually as their relationship can only be expressed through general, empirical formulae [6.1-6.3].

A number of semiconductor compounds have already been thoroughly investigated and widely accepted values exist for their optical parameters [6.4-6.8]. However the bulk of this work has focussed on the Si/Ge and III-V material systems with II-VI compounds received less interest, with the possible exception of ZnS and ZnSe. If II-VI materials are to be used in useful optoelectronic devices it is important that they are also fully characterised.

### 6.1.1. Bandgap Measurement and PL Spectroscopy

As has been demonstrated throughout this thesis there are a number of ways to measure the bandgap of a semiconductor, such as PL or absorption. These two techniques determine the bandgap due to emission and absorption respectively,

so typically a small shift in the value reported is observed and is termed the Stokes shift. Typically in MBE grown semiconductors it is less than 50meV [6.9]. An example of this is given in section 6.2 where a shift of 32meV is measured for two 50nm thick ZnSe samples.

PL is used extensively to characterise the optical (and by extension structural) quality of semiconductor samples as the number, energy and FWHM of the emission peaks gives valuable information about the samples. Widely accepted bandgap values are therefore available for many II-VI compounds [6.10-6.13]. However some (such as MgS) do not and are therefore still an area of active research.

So far in this thesis the bandgap value for MgS has been inferred to be  $4.7 \pm 0.35 \text{ eV}$  at low temperature ( $\sim 4.5 \text{ eV}$  at 300K). However even the lowest energy in this range is sufficiently high that a pump source is not available at HWU to allow PL measurements to be made (one with an emission energy  $> 4.7 \text{ eV} / 260 \text{ nm}$ , in the DUV) would be needed. Thus an alternative technique must be used.

One such method (as will be proposed in the future work section in chapter 8) would be to measure the transmission of an MgS layer removed from its absorbing substrate and then determine its band-edge. But the use of MgS as the sacrificial layer and need to protect it from oxidation make this measurement difficult.

SE represents another way to measure the bandgap of MgS (or any other material that cannot easily be investigated by PL), as it allows the absorption of thin layers within multi-layer samples to be determined over a wide energy range ( $\sim 0.8\text{-}5.3 \text{ eV}$  and even further into the IR or UV if systems with a vacuum chamber and the correct light source and detector are available). This is achieved by measuring the absorption of the whole sample and then, *assuming*

*the properties of all the other layers in the sample are known, modelling the sample to deduce the band-edge of the MgS (or other unknown layer).*

### 6.1.2. Reflectometry

Reflectometry is also regularly used to investigate the thickness of ZnSe overgrowth (OG) samples (the very thick layers of ZnSe grown to both calibrate the ZnSe growth rate and simultaneously coat the inside of the MBE chamber to bury contaminants), as it provides an efficient and accurate way to obtain thickness figures for these layers [6.14] - as will be demonstrated in section 6.3. However it only works for layers that are ~200nm or thicker, as otherwise the intensity fluctuations needed to determine the thickness are not seen. An example of this can be seen in fig. 6.1, where there are clear fringes for the 500nm thick sample within the wavelength range studied, while the 160nm thick layer does not and therefore cannot easily be modelled.

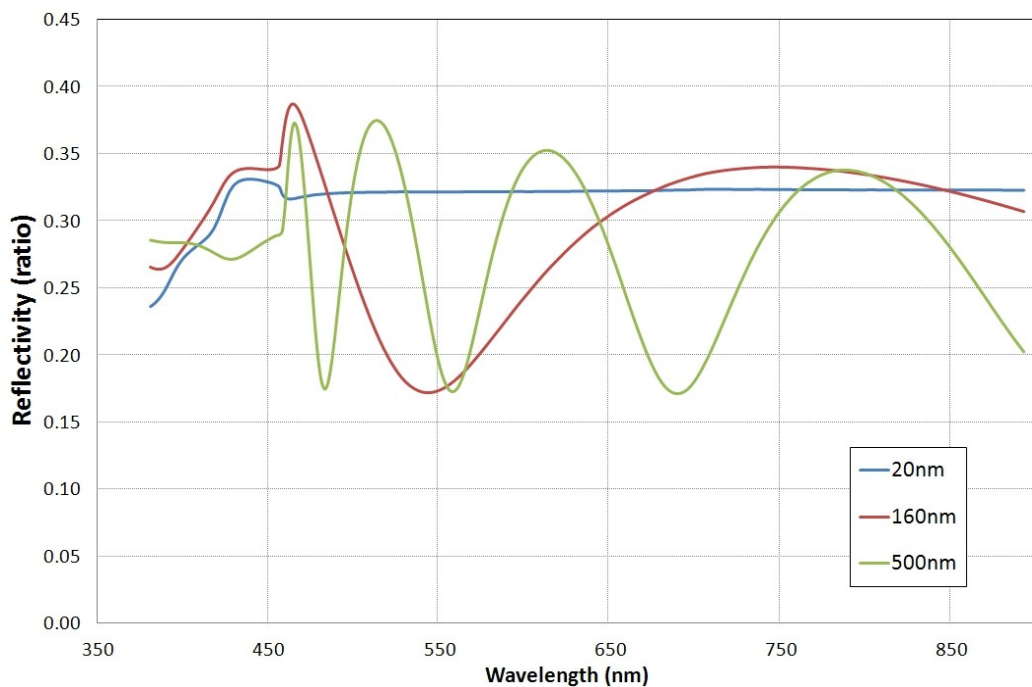


Fig. 6.1. Reflectivity vs. Wavelength for various ZnSe thicknesses

Reflectometry could alternatively be used to measure the refractive index of a layer, if the thickness of the layer is precisely known, but would again only work with thick layers of material. It is also likely to produce relatively large errors due to any uncertainties in the value of the layer thickness used.

### 6.1.3. Refractive Index Measurement and Spectroscopic Ellipsometry

There are a number of techniques (in addition to reflectometry) to measure the complex refractive index ( $\tilde{n} = n + ik$ ) of a material - such as refractometry, the 'prism-coupler technique' and various interferometric methods [6.15-6.17]. However all of these techniques work best when dealing with either bulk material or thick layers and as such are not ideal for the samples grown at HWU, as most are relatively thin (<500nm) and can contain layers as narrow as a few nm.

A technique that is sensitive to this range of thicknesses is therefore required and spectroscopic ellipsometry (SE) is one option. It achieves this by measures both the intensity and phase-shift of the *p* and *s* polarisations of light at a given wavelength. SE also has a number of other major advantages (as detailed in chapter 2) but as it is an indirect method requiring the measured structure to be modelled before useful data can be obtained, uncertainty can be introduced.

The ability of SE to handle absorbing layers should also allow the issue of complex surface oxide formation and the reactivity of some compounds, such as MgS, to be avoided. This can be achieved by measuring samples where the layer of interest has been capped by a non-reactive layer with a known dispersion relation, such as ZnSe. In this case, the capping layer will still be oxidised but its effects can be removed and the optical data for the rest of the structure determined. In the case of ZnSe previous work shows that the oxide layer formed will be relatively thin and the material underneath will be protected [6.18]. However as this technique has not been reported for the characterisation of new materials before, it will be carefully evaluated in this chapter.

The added benefit of working with samples where a thin layer has been capped by ZnSe is that these are identical to the XRI/XRD samples commonly grown at HWU for structural characterisation work. Therefore X-ray determined structural data available exist for all of them. Some compounds are also rarely produced elsewhere, such as MnS, and therefore the dispersion data reported here may

be the first for these compounds.

SE can also produce structural information for multilayer samples and this has been used extensively in industry for the Si/Ge and III-V material systems [6.19, 6.20]. However it is less commonly used with II-VI materials due to the lack of high quality dispersion data for many compounds. As it would complement XRI/XRD measurements very well and could result in more accurate layer thickness information, a thorough evaluation of its use with II-VI samples will be presented later in this chapter.

#### **6.1.4. ZnSe Dispersion**

The use of structures with ZnSe cap and buffer layers for the determination of the optical properties of other compounds requires that the dispersion of the ZnSe layers be known with a high degree of accuracy. Luckily, ZnSe is a material that is used widely in a number of applications and a number of dispersion curves have been measured and reported for it [6.21-6.27].

As ZnSe oxidises in air, the reported dispersion curves fall into 3 categories: (1) *in vacuo* measurements, (2) those where the oxidised material has been chemically etched prior to measurement and (3) those where the layer is 'removed' by modelling its effect and subtracting it from the dispersion measured. The final method is often used in conjunction with the second, so that information on the ZnSe layer can be determined to improve the oxide model. Multi-sample techniques have also been used where the oxide is removed entirely mathematically [6.28].

##### **6.1.4.1. *In vacuo* ZnSe Dispersion Measurement**

There is only one published *in vacuo* dispersion curve for ZnSe, produced by Kato et al. [6.21]. They made the measurements on a 4.9 $\mu$ m thick MBE grown layer while it was still in their growth chamber. The published data was the raw

measurements, but modelling it returns a thickness of  $4.85\mu\text{m}$  and the dispersion curve shown in figure 6.2. A second *in vacuo* dispersion curve is reported in the thesis of Bernard Jobst from Würzburg University [6.27], but this data does not appear to have been published elsewhere. It is also shown in figure 6.2. The two curves are nearly identical with only slight variations in the  $k$  values. However as the data of Kato et al. covers a wider range it will be used throughout the remainder of this chapter.

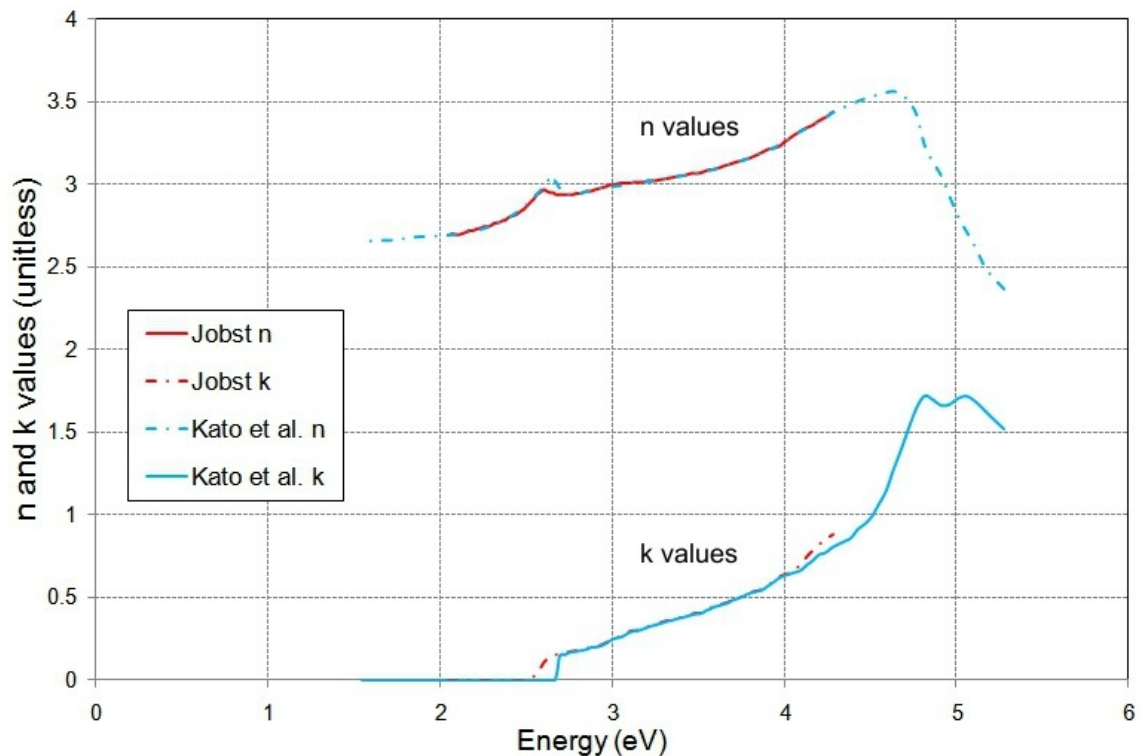


Fig. 6.2. Dispersion curves for ZnSe measured by in-vacuo SE. Red curve is taken from B. Jobst PhD thesis [6.27] and the blue from Kato et al., [6.21].

#### 6.1.4.2. Etched ZnSe Sample Dispersion Measurements

Different etch solutions have been used to remove the oxide layer present on the ZnSe layer including methanol (Adachi et al. [6.23], Dahmani et al. [6.22]) and a range of ammonia:methanol solutions of varying concentration (Kim et al. [6.25], Koo et al. [6.26]). All these curves are shown in fig. 6.3. Typically samples were etched repeatedly until no further increase in the value of the E1 critical point (CP) of the  $\epsilon_2$  curve could be achieved. Although the 2 methanol rinsed samples seem to show higher E1 values in the figure, this is due to it being an  $n$  and  $k$  graph not an  $\epsilon_1/\epsilon_2$ , which has inverted the order.



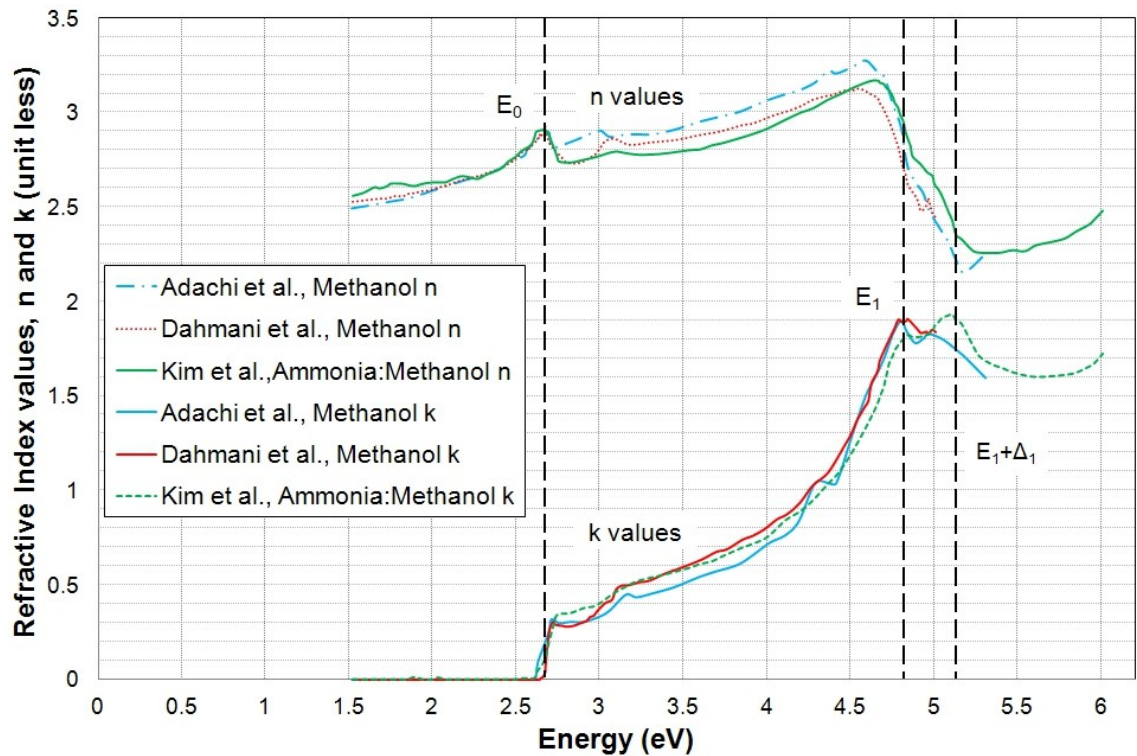


Fig. 6.3. Dispersion curves determined for etched ZnSe samples from refs. [6.23, 6.22 & 6.25].

#### 6.1.4.3. Mathematical Modelling of the ZnSe Dispersion Curve

An example of the dispersion curves obtained by mathematically modelling the oxide layer and removing its effect using multi-sample analysis is shown in figure 6.4 alongside an example of the *in vacuo* and etched results. The multi-sample analysis curves are adapted from Franta et al. [6.28]. The native oxide layer was modelled using a series of different models (Cauchy, Cauchy-Tauc and Lorentzian) and found to be thin, having little effect in the visible region (1.5-3.5eV) but a strong influence in the near-UV (4 – 5.6eV). They conclude that they were unable to determine the true optical dispersion of the oxide layer, but that all three models used to describe the oxide layer are equally effective and that it would be necessary to perform additional non-optical characterisation of the oxide layer if its dispersion is to be determined conclusively.

The figure shows that the Franta et al. *n* values are close to those of Kato et al. whilst the *k* values are closer to those of Kim et al. and are higher than that of the Kato data. This suggests that the multi-sample analysis produces similar or slightly better results than etching the sample but that it is still not as good as measurements made *in vacuo*.

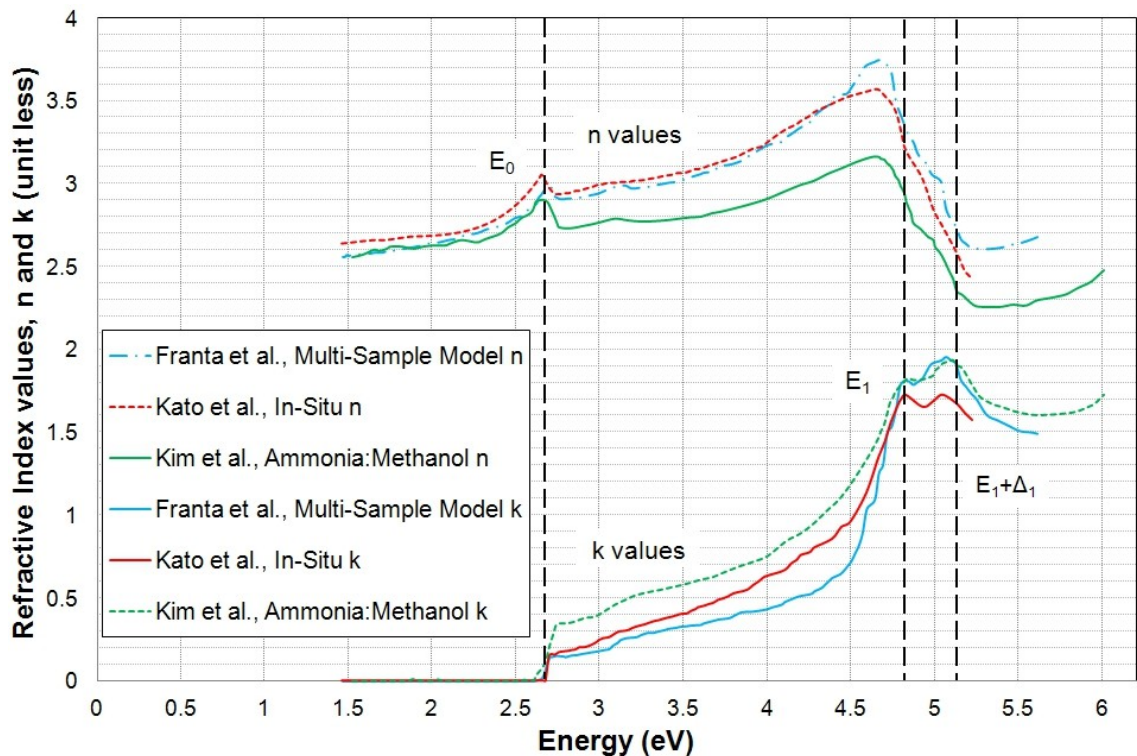


Fig. 6.4. ZnSe dispersion curves for multi-sample modelled, etched and in-vacuo samples from refs. [6.28, 6.21, 6.25] respectively.

#### 6.1.4.4. ZnSe Oxide Layer

The two most obvious constituents of a ZnSe oxide layer are ZnO and SeO<sub>2</sub>, as these are the most stable oxidation products of zinc and selenium. In the case of selenium there are other possible oxides (SeO<sub>3</sub>, Se<sub>2</sub>O<sub>5</sub>) but as they are less stable, they are likely to decompose to SeO<sub>2</sub> after a period of time [6.29]. As SeO<sub>2</sub> is also known to be a strong oxidising agent and has been found to compete with zinc for the available surface oxygen it is possible that samples may initially have elemental selenium deposits on their surface [6.26, 6.30]. However over a prolonged period of time this selenium will also be oxidised by the atmosphere.

AFM measurements of the surface of ZnSe samples commonly find small structures generally referred to as selenium clusters [6.31]. However these structures may be made up of both selenium and SeO<sub>2</sub>, as XPS measurements of the surface find peaks for both elemental selenium and selenium bonded to oxygen [6.32-6.36]. None of the papers reporting XPS measurements of ZnSe surfaces report peaks related to ZnO. But as the shift between a Zn atom

bonded to a selenium or oxygen atom is very small this is to be expected and does not rule out the existence of ZnO on the surface [6.32].

ZnO may also be the eventual stable oxide layer that forms on ZnSe, as any elemental selenium will eventually oxidise to selenium dioxide and as this is volatile, it will slowly evaporate/sublime away even at room temperature [6.30, 6.37, 6.38]. This would leave behind a ZnO layer that would act to protect the ZnSe underneath. An attempt to test this hypothesis will be reported later.

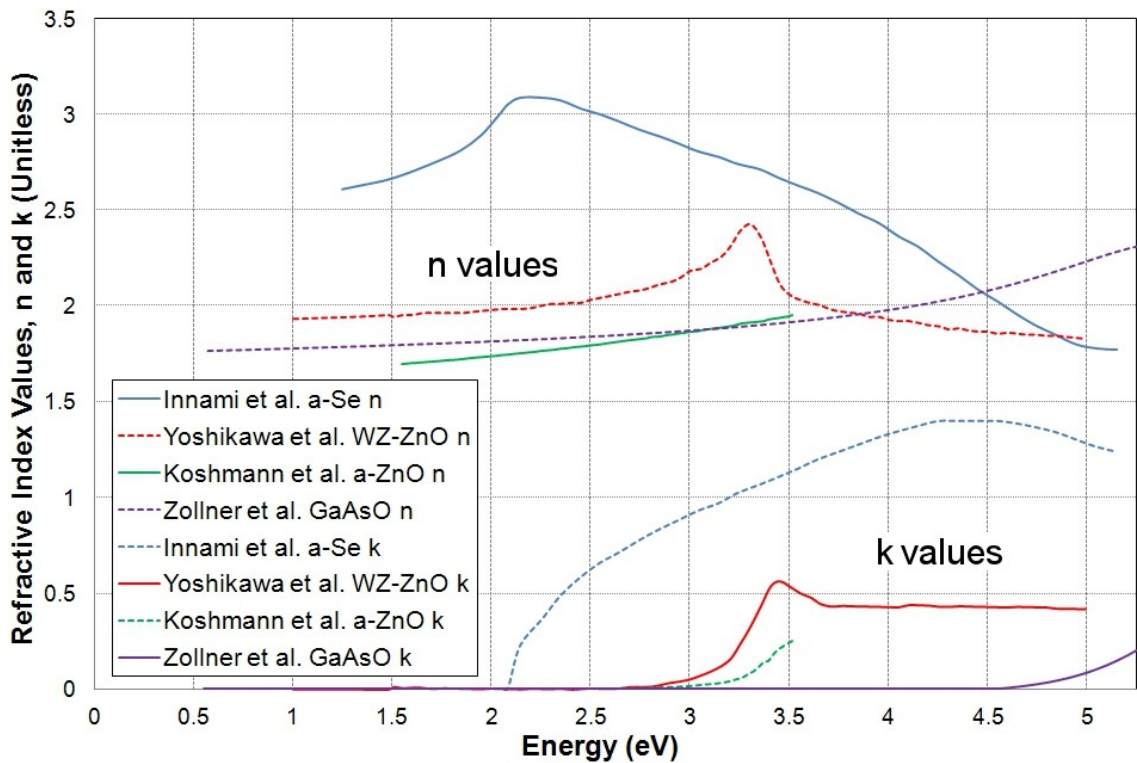


Fig. 6.5. Dispersion curves determined for a-Se, GaAsO, WZ-ZnO and a-ZnO taken from refs. [6.39-6.42].

Figure 6.5 shows the dispersion curves for amorphous selenium (a-Se) and GaAsO, as used by Kim et al. to model the oxide layer [6.39, 6.40], as well as dispersion curves for wurtzite (WZ) and amorphous ZnO (a-ZnO)[6.41, 6.42]. No information could be obtained for material in the ZB phase, however it is thermodynamically unlikely that any ZnO formed will adopt that phase. Additionally no curve could be obtained for  $\text{SeO}_2$  and the only information reported is that it is transparent in the visible and has a refractive index greater than 1.76 [6.43].

The curves in figures 6.2 – 6.5 will be used later in the chapter to model the dispersion of the ZnSe layers in the measured samples. An attempt to determine which represents the most accurate representation of a ZnSe layer and its native oxide will also be presented.

#### 6.1.5. Distributed Bragg Reflectors

DBR are an extremely common form of reflector, particularly in semiconductor devices, due to their ease of production and the high reflectivities. Typical commercial DBR are produced by depositing alternate layers of 2 dielectric materials with optical thicknesses of  $\lambda/4$ , where  $\lambda$  is the design wavelength.  $\text{TiO}_2$  and  $\text{SiO}_2$  are popular materials for their production, as they have both a number of useful mechanical properties and a refractive index difference/step ( $\Delta n$ ) of  $\sim 1$  over a range of wavelengths. A large index step ( $\Delta n \geq 1$ ) is beneficial as it results in both an increased reflection at each interface ( $R(\Delta n=0.1) \approx 0.06\%$ ,  $R(\Delta n=1) \approx 6.3\%$ ), reducing the number of layers required for a specific overall reflection value and increasing the wavelength range over which the DBR will work [6.44, 6.45].

DBRs have previously been realised in both III-V and II-VI semiconductor epitaxy and allow for the production of monolithic micro-cavity structures such as laser diodes [6.45-6.49]. In (Al,Ga)As the choice of the two different materials is relatively simple as AlAs and GaAs have  $\Delta n \approx 0.8$  and are lattice matched, but for the II-VI material systems things are more complicated.

With ZnSe based alloys it would be ideal to find a material that is also roughly lattice matched to GaAs and has a  $\Delta n \approx 1$  to ZnSe, which has an index of  $\sim 2.7$  at 500nm. However no common binary II-VI material available meets this criterion. MgS would work (as it has an index of  $\sim 2.2$  at 500nm, as will be shown later) but the need to grow multiple thick layers (pairs of  $\sim 45\text{nm}$  ZnSe/ $57\text{nm}$  MgS) will result in a structure that relaxes (see figure 6.42), which is not ideal.

The need to find a low index material compatible with the growth on GaAs has

resulted in a number of other groups opting for more complex solutions. Kruse et al. [6.50] have demonstrated the use of 48nm  $\text{ZnS}_{0.06}\text{Se}_{0.94}$  high index layers and a 24.5 period superlattice consisting of 1.9nm MgS and 0.6nm ZnCdSe for the low index layer, and have shown reflectivities as high as 95%. However as each structure requires ~2400 layers to be grown to achieve this, it results in a structure that is time consuming and difficult to grow reproducibly (due to the possibility of shutter failures). However this technique has also been extended to materials grown on ZnTe [6.51].

DBR production is slightly easier in the ZnMgCdSe on InP system, as it is possible to grow both CdSe and MgSe rich alloys lattice matched to InP with indices of ~2.9 and 2.5 respectively. However the need to grow two roughly lattice matched ternary or quaternary alloys with compositions at either end of the ZnMgCdSe compositional space is challenging and is again likely to result in a structure that is hard to grow reproducibly.

The solution proposed here is the use of a close to lattice matched MgS rich QA, as this possess an index of ~2.3 and allows thick layers to be grown between ZnSe layer without the structure relaxing. Although the work discussed in chapter 5 shows that repeatedly growing thick layers of QA with a lattice matched composition is highly difficult, a design based on 12 pairs of a ZnSe and QA will be shown to produce a simulated reflectivity of >95% and its feasibility discussed.

## 6.2. ZnCdSe Bowing Parameter

Although a large number of PL measurements are routinely made at HWU, the majority are made to determine the optical quality of samples and as such are not interesting. However a small number allow some more interesting parameters to be investigated.

One example is the bowing parameter of ZnCdSe, as a range from 0 – 1.26 eV

has been reported [6.52, 6.53]. There are likely to be a number of reasons for this variation but the most obvious are that either samples with an insufficient compositional ranges have been investigated or that differing techniques have been used. By looking at a series of samples grown at both Heriot-Watt and CUNY, virtually the entire compositional range can be investigated using the same technique, resulting in a more accurate value for the bowing parameter. The investigation of each sample will be detailed in the following sections. All the PL measurements were made at 77K.

### 6.2.1. ZnSe Bandgap

Figure 6.6 shows the PL spectra from HWC248, a 50nm ZnSe sample measured at 77K using the Ar<sup>+</sup> laser and PMT set-up. In the region just below the ZnSe bandgap 6 peaks can be resolved. Their emission energy, energy separation and relative intensities are listed in table 6.1. Comparing these to published values, allows the identity of the peaks to be determined [6.54-6.59].

Peak Label	Emission Energy (eV)			Energy Separation (meV)		Relative Intensity
	300K	77K	4K	X <sub>HH</sub>	X <sub>LH</sub>	
BB <sub>LH</sub>	2.7016	2.8243	2.8387	28.9	17.8	0.01
BB <sub>HH</sub>	2.6907	2.8134	2.8278	18	6.9	0.02
X <sub>LH</sub>	2.6838	2.8065	2.8209	11.1	0	0.12
X <sub>HH</sub>	2.6727	2.7954	2.8098	0	-11.1	1.00
LO(X <sub>LH</sub> )	2.6539	2.7766	2.7910	-18.8	-29.9	0.02
LO(X <sub>HH</sub> )	2.6383	2.761	2.7754	-34.4	-45.5	0.01

Table 6.1. HWC248 emission peak details.

At 77K the emission from the sample will be dominated by excitonic emission due to the large exciton binding energy of ZnSe [6.60]. As the sample comprises only a ~50nm thick ZnSe layer, it will still be fully strained to the GaAs substrate and under compression. This results in the heavy hole exciton (X<sub>HH</sub>) being emitted at a lower energy than the light hole (X<sub>LH</sub>), hence the dominant peak can be identified as X<sub>HH</sub> and the peak at 2.8065eV as X<sub>LH</sub> [6.61].

The 2 peaks at a higher energy (labelled BB<sub>LH</sub> and BB<sub>HH</sub>) are identified as the

direct band-to-band emission of an unbound electron to the heavy and light-hole respectively as their 4K emission energy (scaled using the Varshni formula [6.62]) is close to the low temperature bandgap of ZnSe found in the literature [6.57]. This then allows the exciton binding energy value of  $17.9 \pm 0.1 \text{ eV}$  to be determined from the energy separation between the excitons and these band-to-band peaks. This is extremely close to the  $\sim 20 \text{ meV}$  value reported in the literature [6.55, 6.60].

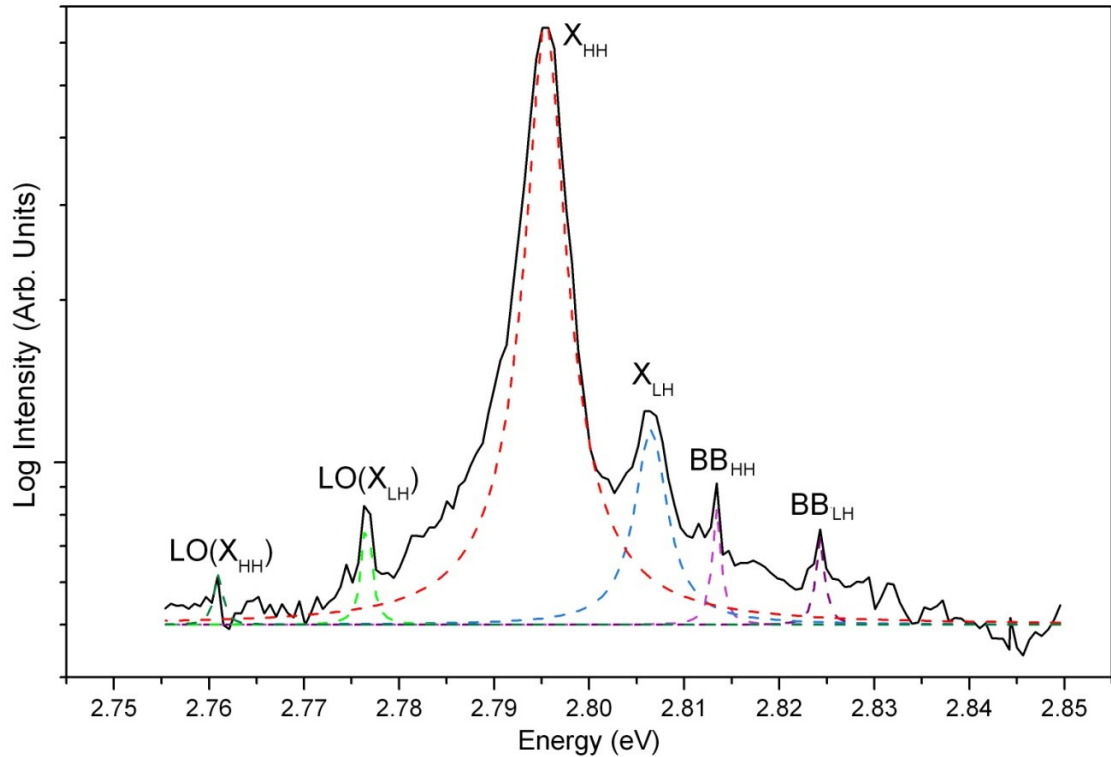


Fig. 6.6. PL spectra for HWC 248 a  $\sim 50 \text{ nm}$  ZnSe sample. Identities of the emission lines are in table 6.1. The black solid curve is the measured data and the coloured dashed lines are Lorentzian fits to it.

The 2 peaks labelled  $\text{LO}(X_{\text{HH}})$  and  $\text{LO}(X_{\text{LH}})$  are separated from the HH and LH exciton by 29.9 and 34.4 meV respectively (average 32.2 meV) which is close to the 31.5 meV value reported for the LO phonon energy in ZnSe, hence these are identified as LO phonon replicas of the exciton peaks [6.61, 6.63—6.65]. However to definitely confirm the peak identifications it is necessary to obtain additional power and polarisation dependent PL spectra, which this has not been performed for this sample.

Figure 6.7 shows the room temperature absorption plots for HWC310, a  $\sim 50 \text{ nm}$  thick piece of ZnSe lifted and deposited using the ELO technique on to a glass substrate (blue line) and for comparison, a piece of the bare glass substrate



(green line). The ZnSe shows two transitions at 2.560 and 2.651eV (equivalent to 2.679 and 2.770eV at 4K). The 2.651eV transition is identified as the band-edge transition of the ZnSe [6.57]. The transition at 2.560eV is harder to identify as it does not appear to correspond to any reported transmission/absorption feature of ZnSe. However as it is at a lower energy than the band-edge transition it likely to be due to some sort bound state possibly caused by dislocations or surface states introduced by the lift-off process.

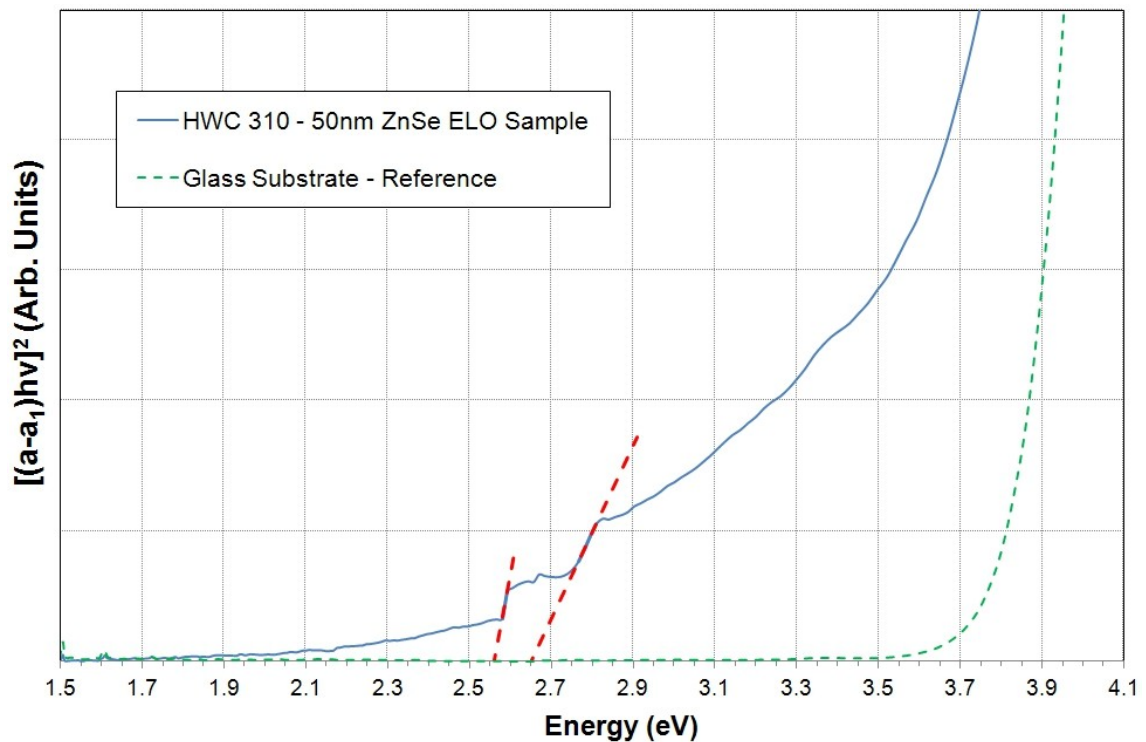


Fig. 6.7. Tauc absorption plot for HWC310 a ~50nm thick ZnSe ELO sample deposited on glass (blue line) and the bare substrate (green line).

Comparing the band-edge measured in figure 6.7 with an estimate of the unstrained bandgap (the average of the light and heavy hole excitons) determined from figure 6.6, scaled to 300K, there is a Stokes shift of 32.2meV. This is similar to the values reported in the literature and small enough to suggest that the deposited ZnSe layer is of a high quality [6.56, 6.66]. It also provides a rough estimate to use when looking at the transmission/absorption measurements made of other deposited ELO samples.



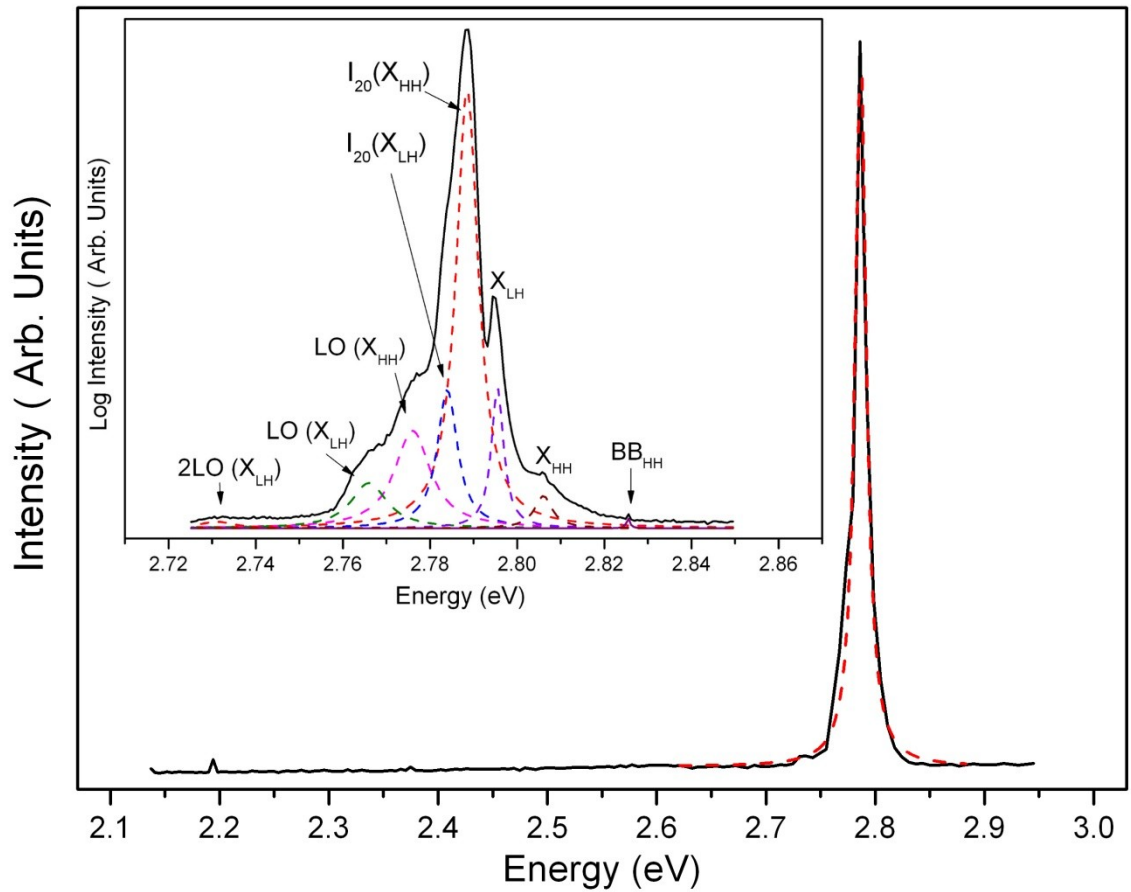


Fig. 6.8. PL Spectrum from HWC249, a 1450nm thick ZnSe sample. Inset Spectrum shows the identity of the various peaks that make up the emission peak. The black solid curve is the measured data and the coloured dashed lines are Lorentzian fits to it.

Figure 6.8 shows the PL spectra obtained from HWC 249, a ~1420nm thick ZnSe OG sample. The thickness was measured using reflection measurements, as will be described later. It shows a single peak at 2.787eV with a small shoulder on the low energy side. However the FWHM of the peak is quite broad at 12.3 meV. The inset higher resolution scan shows that the broad peak is an envelope for a series of peaks. These have also been identified by their emission energy and separation with regard to published values and are reported in table 6.2.

As all of the peaks, except those at 2.7887 and 2.7837eV, can be associated with peaks seen in HWC248 (see table 6.1). The 2 extra peaks are therefore identified as additional neutral donor bound states ( $I_{20}$ ) most likely caused by gallium diffusion ( $Ga_{Zn}$ ) brought about by the introduction of dislocations in the material due to relaxation [6.61, 6.67].

The peaks at 2.797 and 2.808eV are identified as  $X_{LH}$  and  $X_{HH}$  respectively. These energies are close to the values reported for HWC248 but as the thick layer of ZnSe will have relaxed during growth, the HH will now be at a higher energy than the LH due to the thermal strain induced by cooling from growth temperature ( $\sim 570K$ ) to 77K. The LH/HH splitting is 11meV and is brought about by the difference in thermal expansion in the GaAs and ZnSe [6.61, 6.68].

The LO phonons are separated from the free excitons peaks by  $\sim 32$  meV and the 2LO phonon by  $\sim 64$ meV. There may also be an additional 2LO phonon related to the HH exciton but at too low an intensity level to be resolved. The presence of these strong multiple phonon replicas of the free exciton peaks shows that while the ZnSe layer has relaxed, it is still of a very high crystalline quality, as would be expected for MBE grown material [6.55].

Peak Label	Emission Energy (eV)			Energy Separation (meV)		Relative Intensity
	300K	77K	4K	$X_{HH}$	$X_{LH}$	
$BB_{LH}$	2.7067	2.8260	2.8262	18.5	29	0.01
$X_{HH}$	2.6882	2.8075	2.8077	0	10.5	0.06
$X_{LH}$	2.6777	2.7970	2.7972	-10.5	0	0.18
$I_{20}(X_{HH})$	2.6694	2.7887	2.7889	-18.8	-8.3	1.00
$I_{20}(X_{LH})$	2.6644	2.7837	2.7839	-23.8	-13.3	0.29
$LO(X_{HH})$	2.6562	2.7755	2.7757	-32	-21.5	0.43
$LO(X_{LH})$	2.6457	2.7650	2.7652	-42.5	-32	0.10
$2LO(X_{LH})$	2.6137	2.7330	2.7332	-74.5	-64	0.02

Table 6.2. HWC249 emission peak details.

As both HWC248 and 249 are measured under strain their exciton emission values will be shifted slightly with regard to the bulk ZnSe value. However as the 2 samples are under opposite strains of roughly equal magnitude and the splitting between the light and heavy hole excitons is similar (11.1 vs. 10.5 meV), averaging all 4 values produces a value of 2.809eV at 77K or 2.690eV at 300K for the bandgap of bulk ZnSe, which is close to the values reported elsewhere [6.54-6.61]. Comparing this value to the transmission/absorption measurement allows an error bound to be placed on the bandgap value. Therefore a bulk ZnSe bandgap value of  $2.670 \pm 0.02$ eV at 300K is determined.

### 6.2.2. CdSe Bandgap

As CdSe is most stable in the WZ phase and has a ZB lattice constant of 6.077Å, significantly mismatched to GaAs (~7.5%), it is not possible to grow thick layers of ZB material without it relaxing and introducing significant numbers of dislocations or roughening the layer [6.69]. The result of this is that the values reported in the literature are either from relaxed material or extrapolate from ZnCdSe [6.54]. ZB-CdSe has been grown on ZnTe but as ZnTe and CdSe have a type II band alignment, this makes PL measurements and analysis more complicated [6.70]. However by looking at a series of thin CdSe/MgS QW samples and then extrapolating their emission energy back to that of a thick layer, a reasonably accurate value for the CdSe bandgap should be obtained. CdSe/MgS QWs, rather than CdSe/ZnSe, have been chosen due to the lack of intermixing between CdSe and MgS, see chapter 7[6.71].

Figure 6.9 shows the PL spectrum measured for sample HWC233 with the structure of the sample shown inset. It was intended to be a QD sample but due to the small CdSe thickness deposited it shows a strong QW emission in addition to a weaker QD emission. All of the layers were grown at a pyrometer temperature of 240 °C, the CdSe layer was deposited by 6 MEE cycles followed by a 4 minute thermal annealing. The other layers were grown by normal MBE.

The PL spectrum from the sample shows 3 peaks at 3.167 eV, 2.778eV and 2.621 eV. These are identified as the emission from the CdSe QW, ZnSe buffer layer and CdSe QDs respectively. The CdSe QW emission is very broad with a FWHM of 346meV. As intermixing is extremely small in the CdMgSSe compositional system (see introduction to chapter 7), this broad peak is caused by variations in the layer thickness due to it being around the critical thickness for spontaneous QD formation.

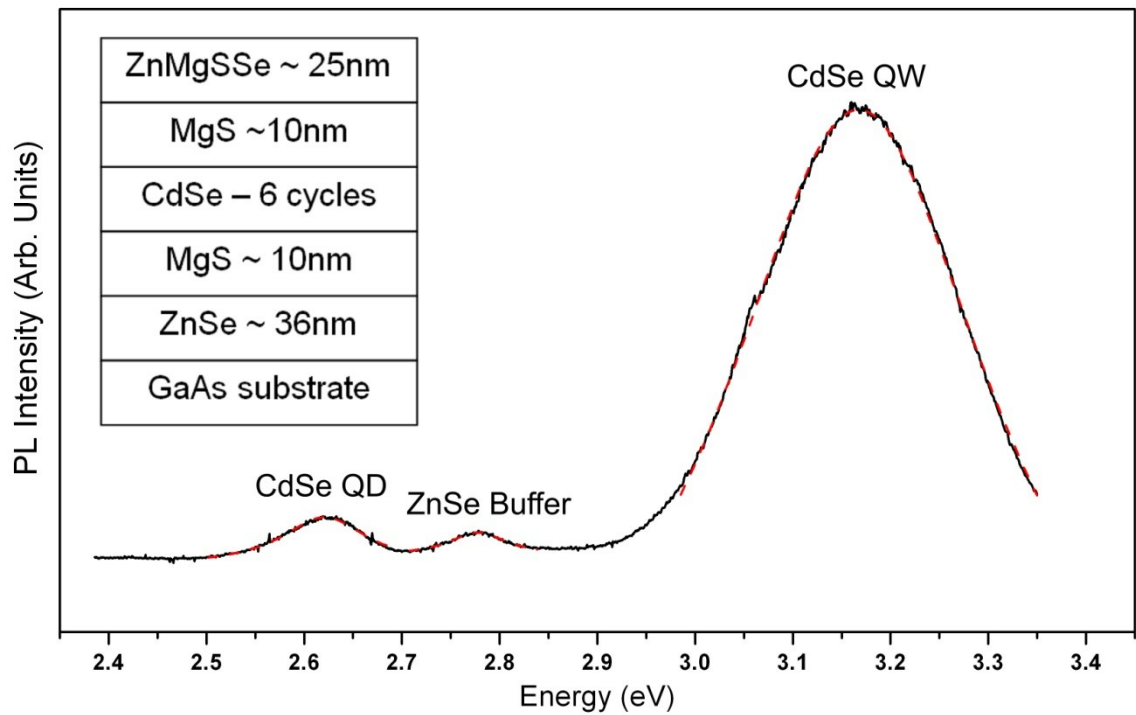


Fig. 6.9. PL spectrum from HWC233, a MgS/CdSe QD/QW. PL performed at 77K using  $\text{Ar}^+$  ion laser and PMT. Inset is the structure of the sample. The black solid curve is the measured data and the red dashed lines are Gaussian fits to it.

Modelling the emission from the QW for different CdSe bandgaps assuming a 77K bandgap for MgS of 4.8eV, and taking the effects of carrier confinement and binding energies into account, produces a series of roughly parallel curves like those shown in fig. 6.10 [6.72-6.74]. Although the bandgap of MgS is still not accurately known (see chapter 5) any of the values in the range determined ( $4.7 \pm 0.35\text{eV}$  at 77K) will produce virtually identical results as they are all far larger than CdSe, which is typically reported in the literature as  $\sim 1.75\text{eV}$  at 77K ( $\sim 1.65\text{eV}$  at 300K). The blue curve is calculated using this bulk bandgap value.

Comparing the emission energy with the blue curve, it suggests that the well width would be  $2.1 \pm 0.4$  ML, which would fit well with the thickness expected from 6 MEE cycles. However as the well could be as thick as 3ML, this is compatible with a relatively large range of possible CdSe bulk bandgap values, as a value of 2.1eV would produce 3ML well emitting at 3.167eV.

It is therefore necessary to obtain structural information from the x-ray analysis to attempt to reduce the possible range of well widths and therefore bandgap

values. Unfortunately CdSe QD samples are not routinely x-rayed, as the typically highly disordered QD layer makes analysis difficult and therefore no information is available for HWC233. Looking back at an older sample (HWC156) does provide both a PL spectrum and a XRI measurement.

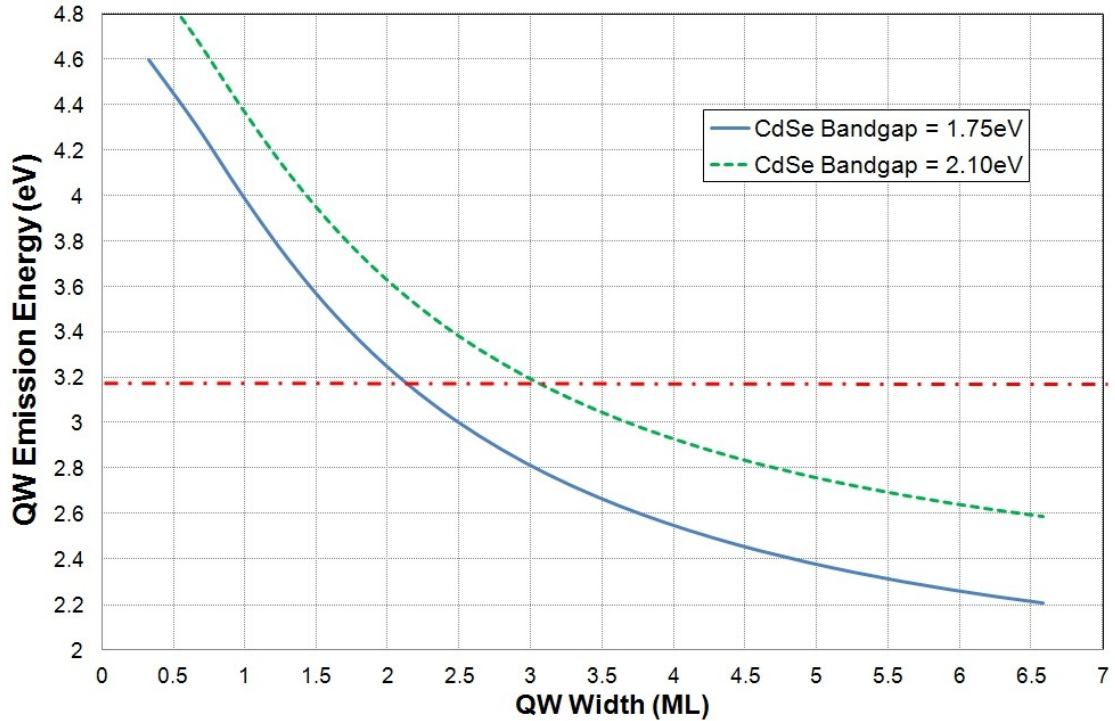


Fig. 6.10. Variation of CdSe QW emission energy with well width. Blue line represents a bulk ZB CdSe bandgap of 1.75eV at 77K while the green dotted curve a bandgap of 2.1eV. The emission energy of the QW in HWC233 is shown by the dashed red line.

Figure 6.11 shows the measured and simulated XRI spectra for HWC156 including an inset schematic of the structure used for the modelling. Although the structure is relatively complex the simulated fit is good, returning a GOF of 0.106. The lack of intermixing between the CdSe and MgS helps by reducing the number of free variables. This results in the simulation being extremely sensitive to changes in the CdSe thickness and as such, a thickness of  $0.75 \pm 0.02 \text{ nm}$  is determined. This is equivalent to  $2.46 \pm 0.06 \text{ ML}$ .

The PL spectra from the sample has one main emission peak centred on  $2.978 \pm 0.002 \text{ eV}$  with a FWHM of 119meV. Again using the modelling data for the variation of emission energy with well width, results in a predicted ZB CdSe bandgap of  $1.65 \pm 0.05 \text{ eV}$  at 300K. This value will be subjected to significant strain but is still close to the values reported in the literature for other thin layers,

relaxed layers on GaAs and layers on ZnTe [6.54, 6.70].

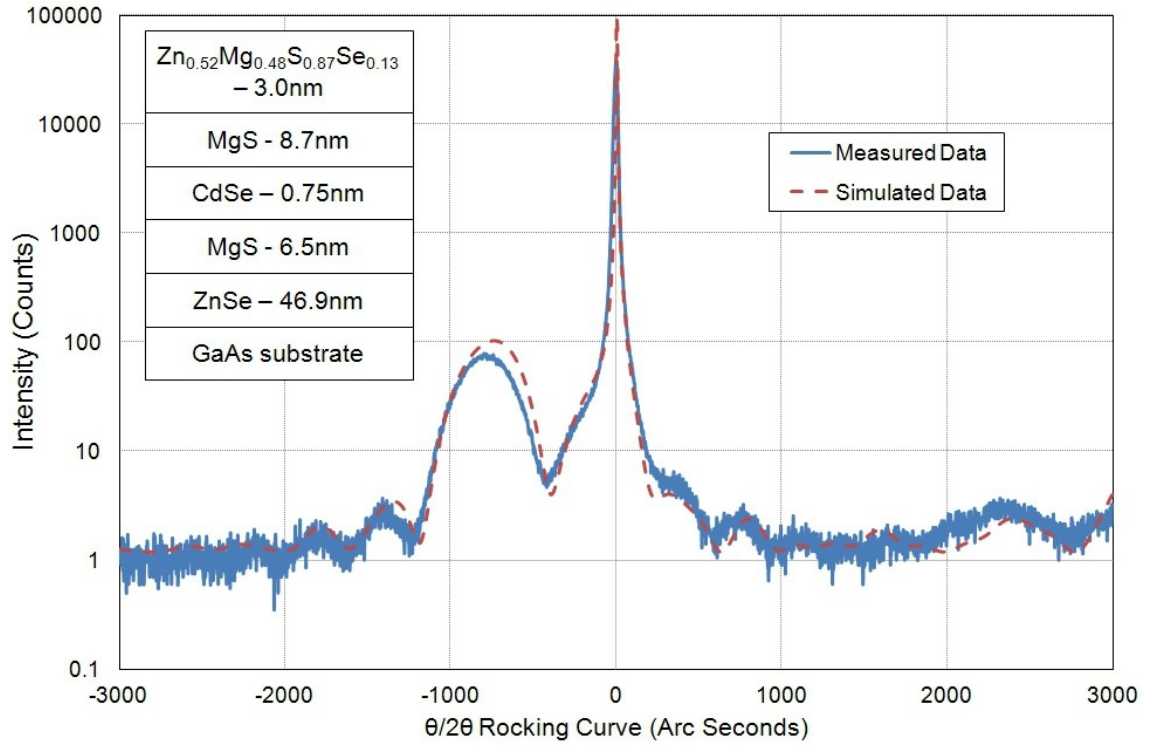


Fig. 6.11. XRD plot for HWC156. Structure predicted by simulation is shown inset. The blue curve is the measured data and the red dashed curve the simulated data based on the inset structure.

### 6.2.3. ZnCdSe Bandgap

Two different types of ZnCdSe containing samples were available for investigation: a series of thin ZnSe rich ZnCdSe QW samples grown at HWU (including the SCD samples discussed in chapter 3) and the series of thick  $\text{Zn}_{0.55}\text{Cd}_{0.45}\text{Se}$  samples grown at CUNY. All of these samples were investigated using XRD and PL measurement.

The characterisation of the SCD samples will be omitted here as they were discussed in chapter 3. The thick ZnCdSe samples from CUNY were grown as part of the work to extend the ELO technique to MgSe and were therefore discussed in chapter 4, so again will not be discussed further here. However the data from all of these samples will be used to determine the bowing parameter used in section 5.3.4.

### 6.2.3.1. ZnSe rich ZnCdSe QWs

Three ZnSe rich ZnCdSe QWs were grown following our standard procedure at 240°C. The zinc and selenium fluxes were kept constant across all 3 samples with a Zn:Se ratio of 1:1.7. The cadmium flux was increased throughout the 3 samples from a Zn:Cd ratio of ~15:1 to ~7:1. The structure of all 3 samples (ZnSe- $d_1$  nm/ZnCdSe- $d_2$  nm/ZnSe- $d_3$  nm) is shown schematically inset in figure 6.12 with the exact thicknesses detailed in table 6.3.

After growth all 3 samples were analysed by HRXRD and show the normal XRI pattern. This was then modelled to produce the thicknesses and compositions shown in table 6.3. As expected the models that result in the best fits show a trend of increasing Cd concentration with increased Cd flux. However as the variation in Cd percentage is quite small compared to the change in measured Cd flux it suggests that the ion gauge ionization coefficients for zinc and cadmium are quite different.

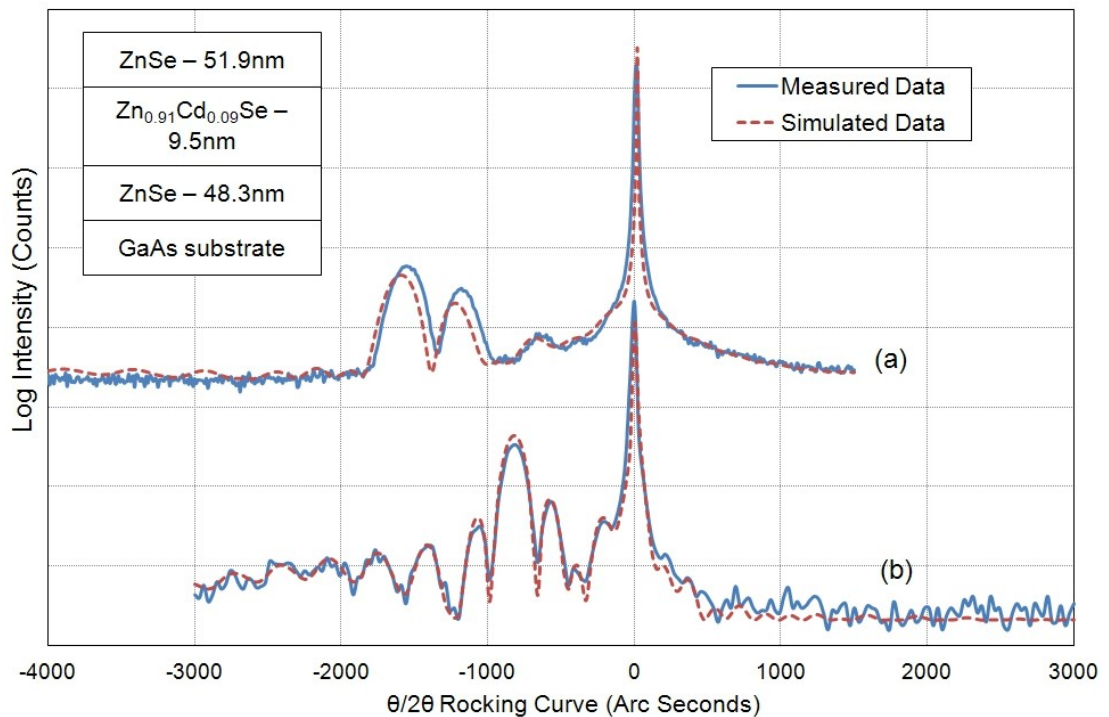


Fig.6.12. Measured and simulated XRI data for sample HWC251. Curve (a) is the 115 scan and (b) the 004. The structure modelled is shown inset. The blue curves are the measured data and the red dashed lines the simulated curves based on the inset structure.

As was discussed in chapter 5, the ability of the XRI technique to unambiguously find a single solution for a sample can be questioned, so it is



therefore necessary to look at the data produced more carefully to check its validity. This was achieved in the same way as chapter 5, by plotting the variation of the GOF with ZnCdSe composition (lattice constant) and thickness. A representative example of this for HWC 250 is shown in figure 6.13.

#	Thicknesses (nm)			Cd %	Lattice Constant (Å)	GOF		Emission (eV)
	d <sub>1</sub>	d <sub>2</sub>	d <sub>3</sub>			004	115	
250	52.5	8.3	48.3	7.3	5.701	0.114	0.126	2.707
251	51.9	9.5	48.3	9.6	5.705	0.100	0.099	2.676
252	51.4	9.9	48.5	10.8	5.711	0.124	0.133	2.636

Table 6.3. Structural and optical properties of HWC 250-252.

The figure shows the variation of GOF for the combined 004 and 115 scans for HWC 250. The solution of 8.3nm and 8.0% Cd chosen by the software falls in the middle of a region of good fit. Assuming that the ZnCdSe growth rate is similar to the ZnSe, then the two dashed lines on the graph represents the thickness range of the layer. The range of compositions producing low GOF figures with in this are  $7.25 \pm 1.25\%$  Cd. Repeating the analysis for HWC 251 and 252 results in best fit ranges of  $9.6 \pm 1.0\%$  and  $10.8 \pm 1.2\%$  respectively. Although all of these are quite large ranges and will reduce the level of accuracy of the bowing figure, they should still be sufficient to allow an estimate to be made when combined with other values.

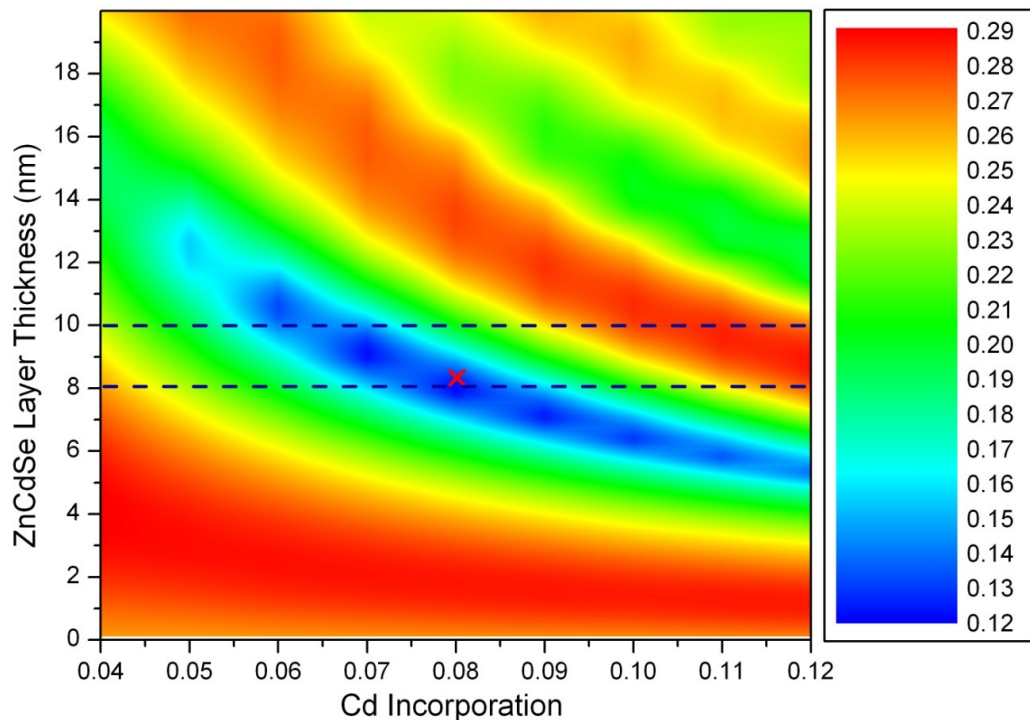


Fig. 6.13. Variation of averaged 004 and 115 GOF with Cd incorporation and layer thickness for HWC250. Dashed lines show the expected thickness region. The red cross the value chosen by the RADS software.



Figure 6.14 shows the PL spectra obtained from samples HWC 250, 251 and 252. These have sharp peaks at the energies indicated in the figure. The low FWHM suggest that the amount of alloy broadening is quite limited, in apparent contradiction to the XRI result. However this is to be expected as the XRI result signifies an inability to determine a single best-fit composition, and not that the composition necessarily varies in each sample.

The emission from the QWs were again modelled using the thickness and composition data determined by XRI, this time using values for the 77K bandgap of CdSe and ZnSe of 1.65 and 2.80eV respectively. The bulk layer emission energies were found to be  $2.69\pm0.04\text{eV}$ ,  $2.66\pm0.02\text{eV}$  and  $2.62\pm0.03\text{eV}$  for HWC 250, 251 and 252 respectively. The error bounds are again quite large due to the uncertainty in layer thickness and composition.

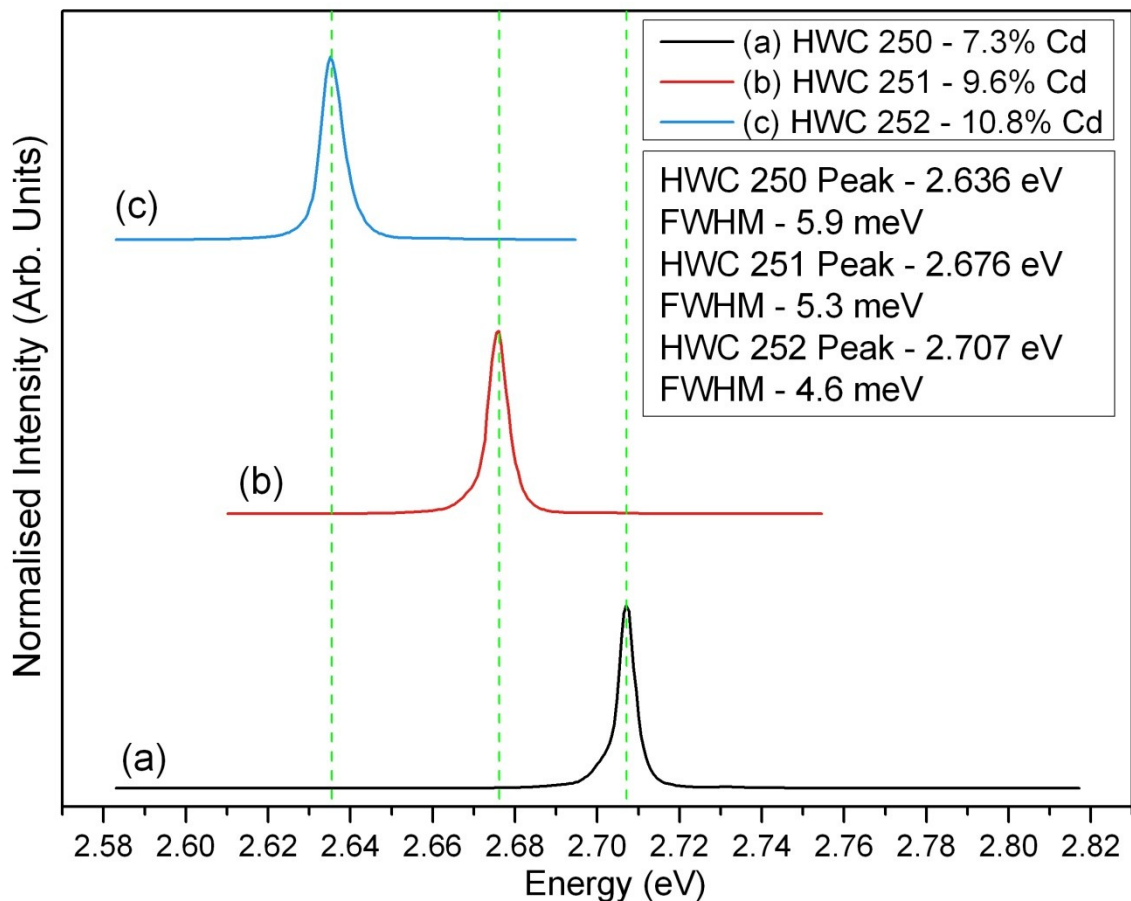


Fig. 6.14. PL Spectra for HWC 250( a), 251(b) and 252(c). The green dashed lines have been added as a guide to the eye.

As each SCD contained two ZnCdSe QWs of nearly identical composition this would potentially reduce the error in both the composition and bulk layer

bandgap. However this was not found to be the case, as the X-ray rocking curves for these structures were more complex and harder to model accurately. This introduced significant uncertainty to the well widths and compositions and this translates into even larger uncertainties in the associated bandgaps. The details of the investigation of the SCD samples are not repeated here but the parameters measured or determined are reported in table 6.4.

Table 6.4 also contains the details of the ZnCdSe samples produced at CUNY. As these have compositions nearly lattice matched to the InP substrate, thick layers can be grown and this dramatically reduces the errors in the thickness, composition and bandgap (although the possible relaxation of the samples does introduce a small uncertainty). These samples also have compositions in the middle of the compositional range which, as can be seen in figure 6.15, causes them to have a strong influence on the calculated bowing parameter.

#	Emission Energy (eV)	FWHM (meV)	Layer Thickness (nm)	Cd %	$\Delta\text{Cd}$ %	a (Å)	$\Delta a$ (Å)	Bulk $E_g$ (eV)	Bulk $\Delta E_g$ (eV)
250	2.707	5.9	8.3	7.3	1.3	5.698	0.012	2.69	0.04
251	2.676	5.3	9.0	9.6	1.0	5.707	0.008	2.66	0.02
252	2.636	4.6	10.4	10.8	1.2	5.712	0.010	2.62	0.02
232	2.696	7.3	8.6	12.8	2.5	5.709	0.020	2.63	0.05
	2.748	17.8	4.4	-	-	-	-	-	-
230	2.693	9.1	8.8	12.9	2.5	5.708	0.020	2.63	0.06
	2.776	27.7	3.4	-	-	-	-	-	-
221	2.616	10.6	7.5	19.0	2.5	5.738	0.020	2.55	0.06
	2.733	20.1	3.7	-	-	-	-	-	-
211	2.546	14.9	7.7	23.3	2.5	5.763	0.020	2.48	0.06
	2.686	20.5	2.9	-	-	-	-	-	-
a2849	2.232	13.7	~200	41.9	0.5	5.839	0.004	2.23	0.01
a2846	2.173	12.4	~180	45.9	0.5	5.856	0.004	2.17	0.01

Table 6.4. Emission energy, composition, lattice constants & bulk layer band gap for all the ZnCdSe samples. The samples shaded grey are those produced at CUNY

#### 6.2.4. ZnCdSe Bowing Parameter

Figure 6.15 shows all the measured alloys and a series of bowing parameter fits to the dataset. The solid blue line represents a value of 0.37eV which is the best

fit solution (with an  $R^2$  of 0.9979 to the measured data). However the large error bounds present on the data points means that any of typical literature values (0.33-0.5eV [6.53, 6.54]) could also be correct. However from this work the bowing parameter of ZnCdSe is found to be  $0.37 \pm 0.05$  eV.

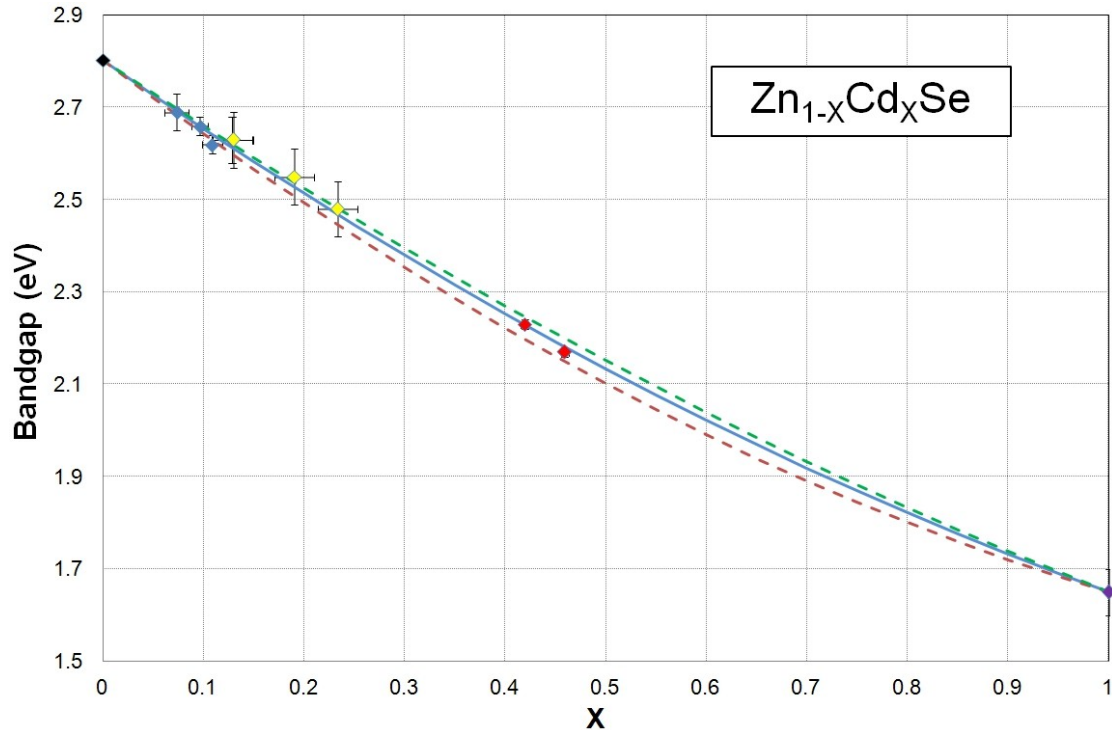


Fig. 6.15. Variation of ZnCdSe bandgap with composition. Blue dots represent ZnCdSe QWs, yellow dots SCD samples and the red dots, CUNY ZnCdSe samples. The blue line is the best fit representing a bowing parameter of 0.37 eV. The red and green dotted lines represent the commonly quoted 0.5 and 0.3 eV parameters.

### 6.3. Reflectometry

To determine the optical thickness of the ZnSe OG samples their reflected spectra were measured as described in chapter 2. These measurements produce reflected intensity vs. wavelength plots similar to the one shown in figure 6.1 which comprise a series of peaks and troughs below the band-edge of the material. The peaks represent the points where the reflections from the top surface of the sample and the ZnSe/GaAs interface interfere constructively while the troughs indicate the destructive interference.

As the dispersion of ZnSe is well known (see sections 6.1.4. and 6.4.1.), the physical thickness of the samples can be determined from these plots. The

sample shown in figure 6.16 (HWC 249) is found to be  $1419 \pm 8 \text{ nm}$  thick, a growth rate of  $1.15 \pm 0.01 \text{ Å/s}$  ( $\sim 0.4 \mu\text{m/hr}$ ).

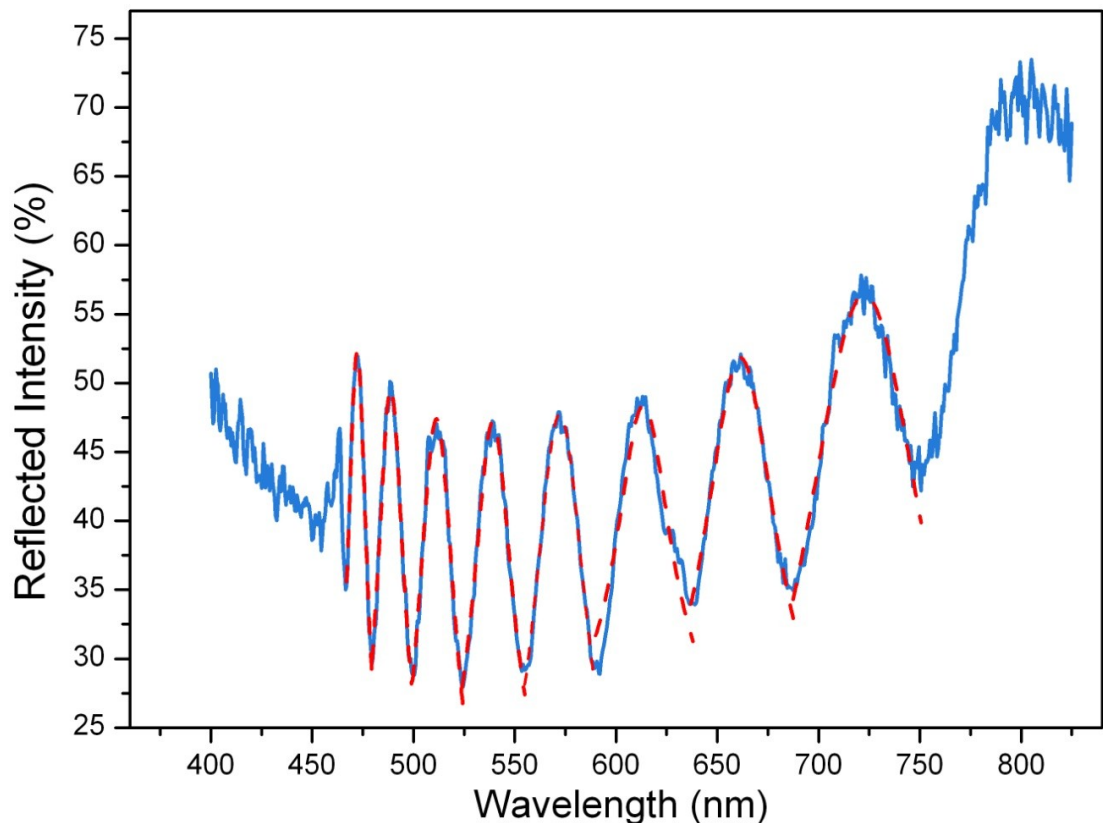


Fig. 6.16. Reflection spectra from HWC249 (blue curve). The 5 peaks visible below the ZnSe band-edge (462nm at 300K) have been fitted with Lorentzians (red dashed curves).

A sample this thick should show a very strong XRD peak under. However (see figure 6.17) the peak is much weaker than would be expected for a layer of  $\sim 1420 \text{ nm}$  thickness and if not properly constrained the modelling software will select a layer thickness of only 70nm. The reason for this serious modelling failure is due to the relaxation mode of the layer once the critical thickness has been exceeded ( $97.5 \pm 2.5 \text{ nm}$  in the case of ZnSe [6.75]).

The onset of relaxation produces an increase in the dislocation density and this introduces a locally varying tilt to the epilayer, which in turn causes the normal to the plane to vary over a small range of angles. The Bede RADS modelling software currently used at HWU is not capable of modelling this effect and fails to account for this. However the latest version of the software contains a feature to model the sample as a 'mosaic' made up of a series of small tilted areas.

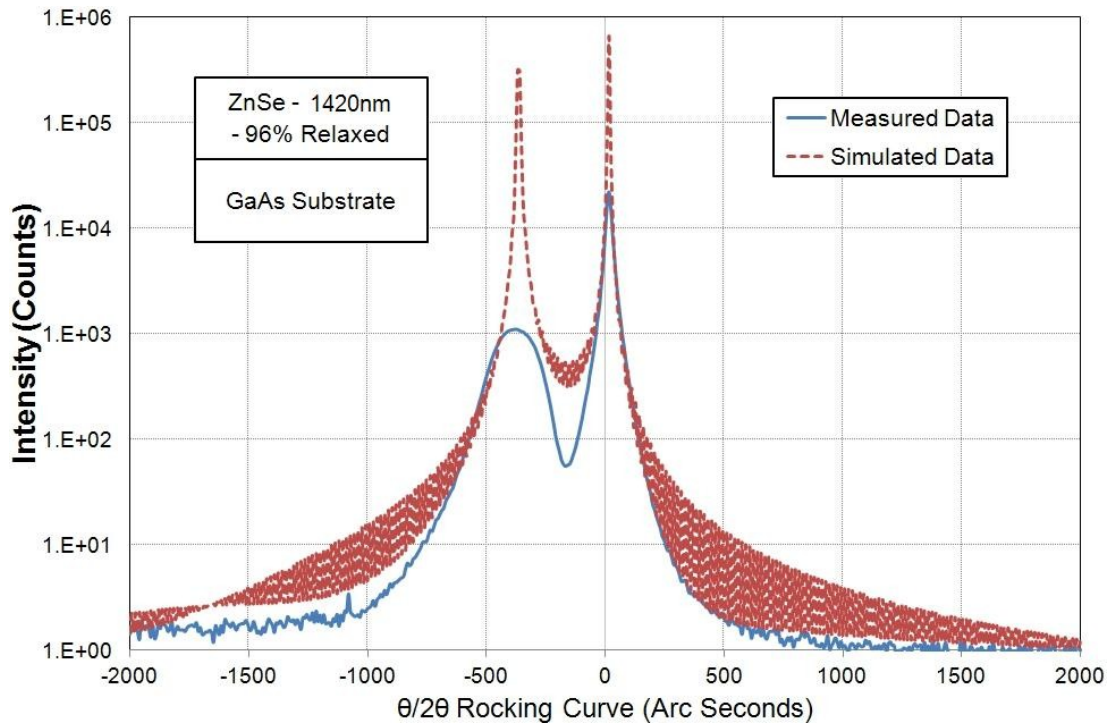


Fig. 6.17. XRD plot for sample HWC249. The structure chosen by the software to generate the simulated data is shown inset.

This produces a far more accurate model of a relaxed sample, blurring out the pendellösung fringes etc, but even with it the software still returns a thickness of 172nm for HWC249. Forcing a thickness of 1420nm and using the mosaic feature returns a GOF of 0.117, far worse than the 0.068 returned for the 172nm layer, hence even this feature does not solve the relaxation issue

Figure 6.18 shows the amount of relaxation, determined by XRD, versus ZnSe layer thickness for a series of the ZnSe OG samples. The thicknesses were all determined by reflectometry except HWC248, a 75nm thick OG sample, which was determined by XRI as it is too thin for reflectometry. The error bounds on the data points are the result of the need to relax the ZnSe layer in HWC248 by 9.4% to produce a good fit, as this is unrealistic and would be in opposition to all the published reports of the relaxation of ZnSe with thickness [6.75-6.81]. Most likely it suggests that either the lattice constant value used for the modelling (5.6681Å) is slightly wrong or that the sample was under some sort of strain when the measurement was made. As these same factors could also have affected any of the other measurements, a ~10% error bound can be assumed.

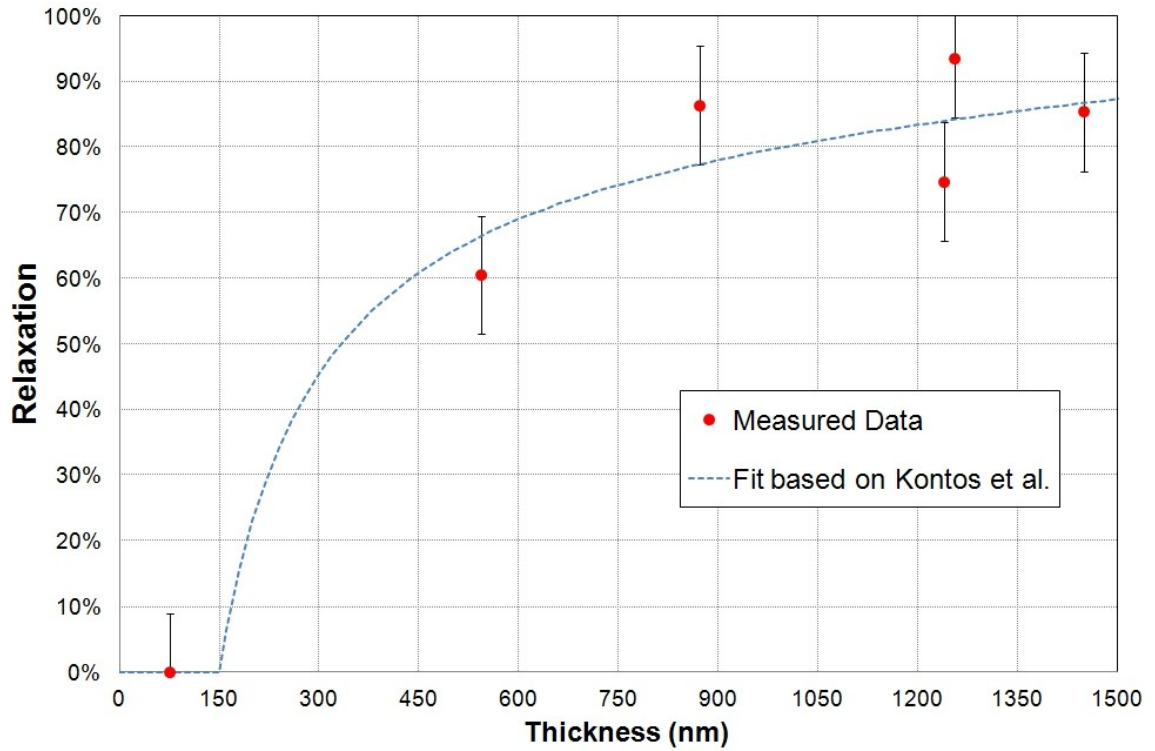


Fig. 6.18. ZnSe OG samples relaxation vs. thickness. Blue dashed line was calculated from the work reported in Kontos et al. [6.76]. The red circles are the measured ZnSe relaxation vs. thickness data.

The blue dashed line was generated based on the work reported by Kontos et al. [6.76] modelling ZnSe relaxation data using a geometrical model (based on the work of Dunstan et al. [6.77]). To fit the measured data here it was necessary to set the critical thickness to 150nm, which is a commonly reported value [6.78-6.81], and the residual strain to -0.07%. These values differ from those of Kontos et al. (130nm and -0.05%) but this may be due to the small dataset used here.

Attempts to model the relaxation data using a model based on balancing the ZnSe layers strain and relaxation energies produced a fit far worse than the geometrical model, hence it was not shown in the figure. This suggests our data supports the use of the geometrical model for strain relaxation.

## 6.4. Spectroscopic Ellipsometry and Refractive Index Measurement

The refractive indices of the majority of the compounds produced at HWU were measured using a J.A. Woollam V-VASE ellipsometry system and then modelled using the CompleteEASE, WVASE32 or RegressPro software, described in chapter 2. This allowed the refractive index of all the samples to be investigated over a range of wavelengths (typically 235-800nm/1.5-5.2eV).

A number of the measurements were made of samples with thick ZnSe (or in the case of a small number of samples ZnCdSe or ZnS) cladding layers, so that the optical properties of compounds could be measured without concern for their reactivity or oxidation. This requires very accurate ZnSe and ZnSe native oxide layer dispersion curves, as described in section 6.4.1 and 6.4.2.

The optical parameters and dispersion curve for each compound are then described and any features of interest detailed in the following sections. In total 8 compounds were investigated including ZnSe, CdSe, ZnCdSe, MgS, MnS, ZnS, ZnSSe, and a range of compositions of ZnMgSSe. The success or failure of the measurement and modelling of each compounds will also be discussed.

### 6.4.1. Zinc Selenide, ZnSe

Figure 6.4 showed a selection of the range of published ZnSe dispersion curves. They were all produced by SE using differing techniques and demonstrate similar but varied refractive indices. Because a range of data exists, no specific curve has been accepted as the de facto standard. The other obvious feature in the figure is that exposure to the atmosphere increases the apparent absorption and decreases the refractive index of the samples irrespective of any pre-SE measurement treatment. This increase in absorption is most likely caused by the formation of a thin absorbing oxide layer on the surface. However the increase could also be caused (or enhanced by) surface roughening, as this scatter incident light away from the detector.

	Kim et al.			Adachi et al.			Dahmani et al.			Kato et al.		
# HWC	Surface Roughness (nm)	Thickness (nm)	MSE	Surface Roughness (nm)	Thickness (nm)	MSE	Surface Roughness (nm)	Thickness (nm)	MSE	Surface Roughness (nm)	Thickness (nm)	MSE
026	0.00	1124	111.9	1.67	1143	67.0	0.17	1137	57.1	5.17	1090	110.1
064	0.00	302	41.4	2.41	305	36.3	0.33	304	31.7	5.44	292	40.6
104	2.94	543	61.4	3.53	552	34.1	2.63	549	23.7	6.12	526	58.4
105	5.90	1049	101.5	6.81	1068	69.3	5.87	1062	63.1	9.29	1018	94.4
256	1.53	69	54.6	1.83	69	33.6	1.33	69	42.8	4.87	65	48.5
323	0.00	1405	128.9	0.00	1429	73.8	0	1421	60.4	3.87	1491	118.1
Avg.	1.73	749	83.3	2.71	761	52.4	1.72	757	46.5	5.79	747	78.4

Table 6.5. Ellipsometry model parameters and mean square errors (MSE) for ZnSe OG samples using dispersion models from ref. [6.21-6.23, 6.25].



To investigate which of the ZnSe dispersion curves/models represents the best fit to the data, a series of ZnSe samples grown at HWU were measured and modelled using a 3 layer model (rough surface/ZnSe/GaAs). The ZnSe was modelled using the various dispersion curves presented in figure 6.4 (plus the Dahmani et al. [6.22] model from fig. 6.3 to check reproducibility).

To compensate for any oxide layer present, the ZnSe layers roughness was varied between 0-10nm. The software models this as an additional Bruggeman effective medium approximation (BEMA) layer with a 50:50 mixture of ZnSe and air ( $n=1$ ,  $k=0$ ). This has been shown to affect the simulated data in a similar way to the presence of an oxide layer (reducing the refractive index and increasing the absorption) and should therefore be a good approximation of the oxide layer [6.82, 6.83]. The MSEs of the different models are shown in table 6.5.

The smallest MSE is that produced using the data of Dahmani et al. closely followed by Adachi et al. However the average surface roughness (BEMA thickness) introduced by these two models is the smallest, which suggests that although they do a good job of modelling an oxidised ZnSe layer, they may not be as good for an unoxidised one. To test this hypotheses a number of MgS samples with the structure ZnSe/MgS/ZnSe/GaAs were investigated, as the lower buried ZnSe layer will be un-oxidised.

Table 6.6 shows the MSE and surface roughness figures for these samples. The samples were modelled between 300-800nm (1.55-4.13eV) using the data in ref.[6.27] for the MgS, which will be discussed later in section 6.4.5, but should not affect the ZnSe modelling. The Kato et al. model produces the lowest average MSE figure, although the Adachi model still produces a low figure. However the Kato model is better at modelling the AFM samples, where the oxidised ZnSe capping layer is thinner and therefore less significant, suggesting that this model is closer to the true values of ZnSe.

	Kim et al.		Adachi et al.		Dahmani et al.		Kato et al.	
# HWC	Surface Roughness (nm)	MSE	Surface Roughness (nm)	MSE	Surface Roughness (nm)	MSE	Surface Roughness (nm)	MSE
107	4.47	35.6	5.33	32.7	4.15	29.8	8.27	17.1
112	4.58	49.2	6.40	27.3	5.32	43.0	10.19	33.0
310	4.15	45.8	4.13	28.1	3.20	34.2	7.70	28.3
367	0.00	61.0	1.10	50.8	0.00	41.2	5.41	36.4
284	36.89	127.5	36.71	93.4	35.35	111.7	40.08	82.3
348	0.04	65.2	0.22	35.7	0.58	45.9	5.18	43.7
352	10.23	50.6	2.93	30.3	4.04	48.2	15.59	24.2
354	21.98	83.0	21.92	47.4	21.44	67.6	27.32	54.4
Avg.	10.29	64.8	9.84	43.3	9.26	52.8	15	39.9

Table 6.6. The surface roughness and MSE figures for the four dispersion models of ZnSe for a selection of ZnSe/MgS/ZnSe AFM and XRI samples. The first four samples are the XRI samples.

In an attempt to further improve the fits, and at the same time see if the *in vacuo* measurements could be improved upon, the Kato data was replaced with a model comprising of seven oscillators with amplitudes, FWHM and energies chosen to fit the Kato data. For simplicity a series of identical oscillators were used. The oscillators have characteristic energies of 2.69, 3.22, 4.75, 5.05, 5.06, 7.00 and 7.40eV, which are close to the values of the  $E_0$ ,  $E_0+\Delta_0$ ,  $E_1$ ,  $E_1+\Delta_1$ ,  $E_2$  and  $E_2+\Delta_2$  critical points (CP) reported [6.22, 6.23, 6.26]. The  $E_1+\Delta_1$  point needed to be modelled with two oscillators, which this suggests that it is more complex than a simple Gaussian.

After the Kato data had been parameterised, the model was then refined by allowing all the parameters to vary slightly while fitting a selection of ZnSe OG samples. During this process the surface roughness was also allowed to vary, in an attempt to stop the model becoming specialised for oxidised layers.

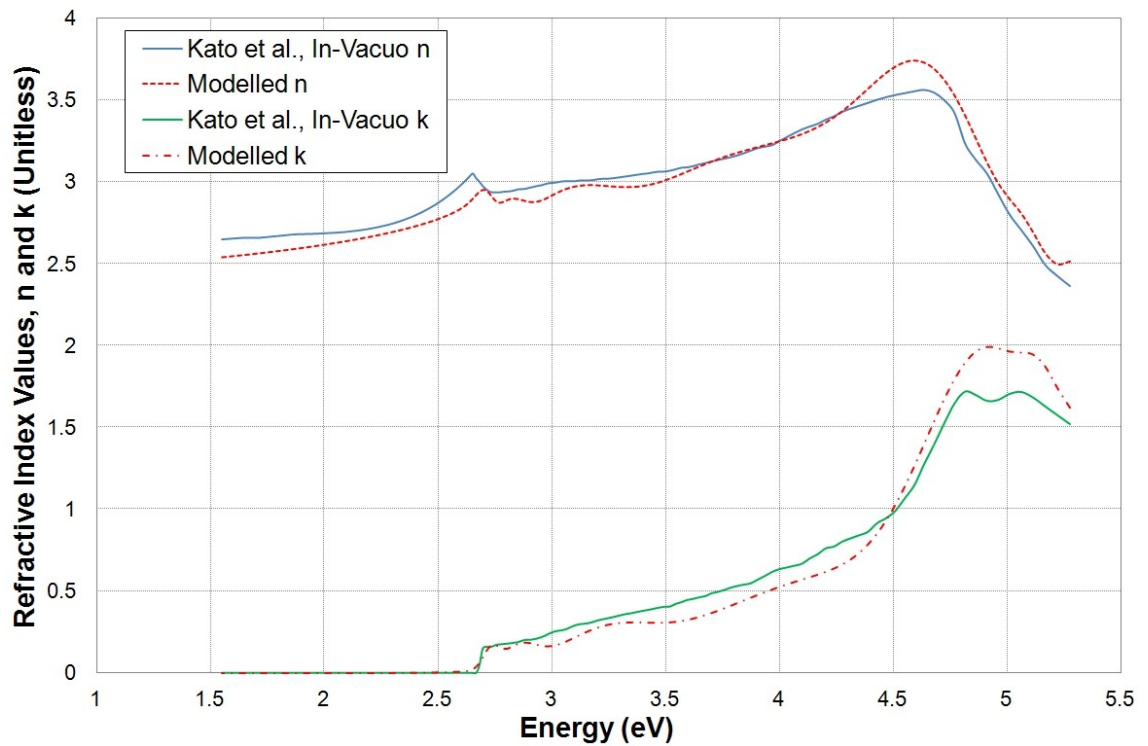


Fig. 6.19. Dispersion curves for Kato et al. and parameterised model vs. energy.

Figure 6.19 shows the final revised model and the Kato data it was based on. The major change is the increase in the magnitude of the  $E_1$  and  $E_1+\Delta_1$  CPs. This suggests that there may be an additional factor in the data of Kato et al. that introduces additional absorption. There would be a number of possibilities for this, such as the samples having a thin selenium layer if they were cooled under a selenium flux, which is standard practice at HWU. However without additional information about how the samples were grown and the measurements made, it is impossible to determine this.

Samples	Adachi et al.		Kato et al.		Modelled	
	Roughness (nm)	MSE	Roughness (nm)	MSE	Roughness (nm)	MSE
Avg. ZnSe	2.7	50.9	5.9	81.9	7.1	30.5
Avg. XRI	4.1	34.6	8.6	28.3	7.6	23.7
Avg. AFM	16.4	53.6	21.1	54.0	19.4	30.5
Avg. All	7.7	46.4	11.8	54.7	11.4	28.2

Table 6.7. Surface roughness and MSE for the Adachi, Kato and 6.4.1 models

Comparing the fits produced by this refined model and those of the Adachi and Kato models (see table 6.7) shows that the model produces much lower MSE values for all the samples. The modelling software also introduces a similar

amount of surface roughening to the Kato model, which suggests that the model should be applicable to both buried and surface ZnSe layers.

Comparing the thickness data produced by the SE modelling and x-ray for the ZnSe/MgS XRI samples, see table 6.8. The growth rates for the ZnSe layers are very similar except for HWC107 and the difference here may be due to the poor x-ray data measured from the sample. The MgS  $G_R$  is more variable between the 2 techniques. However this is likely to be due to the MgS dispersion model used and will be investigated later in this chapter.

# HWC	Modelled				X-ray			$\Delta ZnSe$ $G_R$	$\Delta MgS$ $G_R$
	Surface Roughness (nm)	ZnSe $G_R$ (Å/s)	MgS $G_R$ (Å/s)	MSE	ZnSe $G_R$ (Å/s)	MgS $G_R$ (Å/s)	GOF		
107	7.19	0.62	0.67	24.20	0.56	0.68	0.13	11.8%	-1.0%
112	8.55	0.56	0.66	14.95	0.53	0.60	0.08	5.6%	11.0%
289	5.23	0.82	0.60	14.81	0.77	0.70	0.11	6.5%	-14.3%
310	5.57	0.84	0.48	12.16	0.83	0.36	0.10	1.3%	33.6%
311	8.36	0.77	0.73	21.32	0.69	0.78	0.10	11.6%	-6.4%
367	6.73	1.08	0.61	13.64	1.05	0.58	0.08	3.3%	5.2%

Table 6.8. Growth rates for ZnSe/MgS XRI samples determined by SE and XRI.

Combining the SE and XRD data was found to be beneficial as the fits of both could be improved. An example of this is the modelling of the SE data for HWC367. Initially the MgS  $G_R$  was assumed to be around the  $\sim 0.4 \text{ Å/s}$  rate and modelling it resulted in a best fit with  $\sim 10 \text{ nm}$  of MgS and a very poor MSE of 158. The XRI data was then remodelled with a wider range of MgS thicknesses.  $G_R(\text{ZnSe}) = 0.59 \text{ Å/s}$  was then found to produce an improvement in the GOF from 0.11 to 0.08 and this  $G_R$  was then used to generate the fit in table 6.8.

#### 6.4.2. ZnSe Oxide Layer

The oxide layer on ZnSe samples has previously been investigated by a number of groups and its influence removed with a number of strategies [6.22, 6.25, 6.28]. As HWU does not possess an *in situ* SE system all the samples have to be exposed to the atmosphere prior to measurement and it is therefore

necessary to deal with the effect of the oxide layer either directly through chemical etching or indirectly through modelling.

As chemical etching is both time consuming and may damage the surface of the ZnSe layer it is better to remove the layers effect mathematically. However this requires that the layer can be modelled accurately, so compositional information must be obtained. To achieve this, a number of ZnSe OG samples of different ages and thicknesses were investigated and modelled with differing oxide layer compositions. A selection of these (HWC64, 170 and 268) were then either chemically etched (in a 1:10 solution of  $\text{NH}_3:\text{CH}_3\text{OH}$  or 0.5 molar NaOH solution for 1 min.) or vacuum annealed at  $\sim 200^\circ\text{C}$  for approx. 15 mins as these processes should all the oxide composition to be investigated, see table 6.9.

	vacuum annealing	NaOH solution	ammonia solution	methanol solution
ZnSe	Stable	Weakly Soluble	Insoluble	Insoluble
ZnO	Stable	Very Soluble	Soluble	Insoluble
a-Se	Evaporates	Soluble	Soluble	Soluble
$\text{SeO}_2$	Evaporates	Soluble	Soluble	Soluble

Table. 6.9. Expected effect of processes on ZnSe and oxide layer.

#### 6.4.2.1. Native Oxide Etching

After all the samples had been processed they were then measured with the SE system within 40-100minutes to reduce the chances of the surface becoming heavily re-oxidised (Kim et al. report oxide layer growth rate is less than  $2\text{\AA}/\text{hour}$  [6.84]). The samples were then stored in sample boxes for 76 days before being re-measured to determine the effect of further atmospheric exposure.

Figure 6.20 shows a representative set of SE data for sample HWC 268. The multi-coloured dot-dashed lines represent the values measured immediately after treatment, while the solid lines represent the data measured 76 days later. In the case of the initial measurements, a UV optical fibre was not available for the SE system so the measurement range was limited to  $<4.1\text{eV}$ , while the other measurements (inc. the untreated sample) span the full range, 1.6-5.3eV.

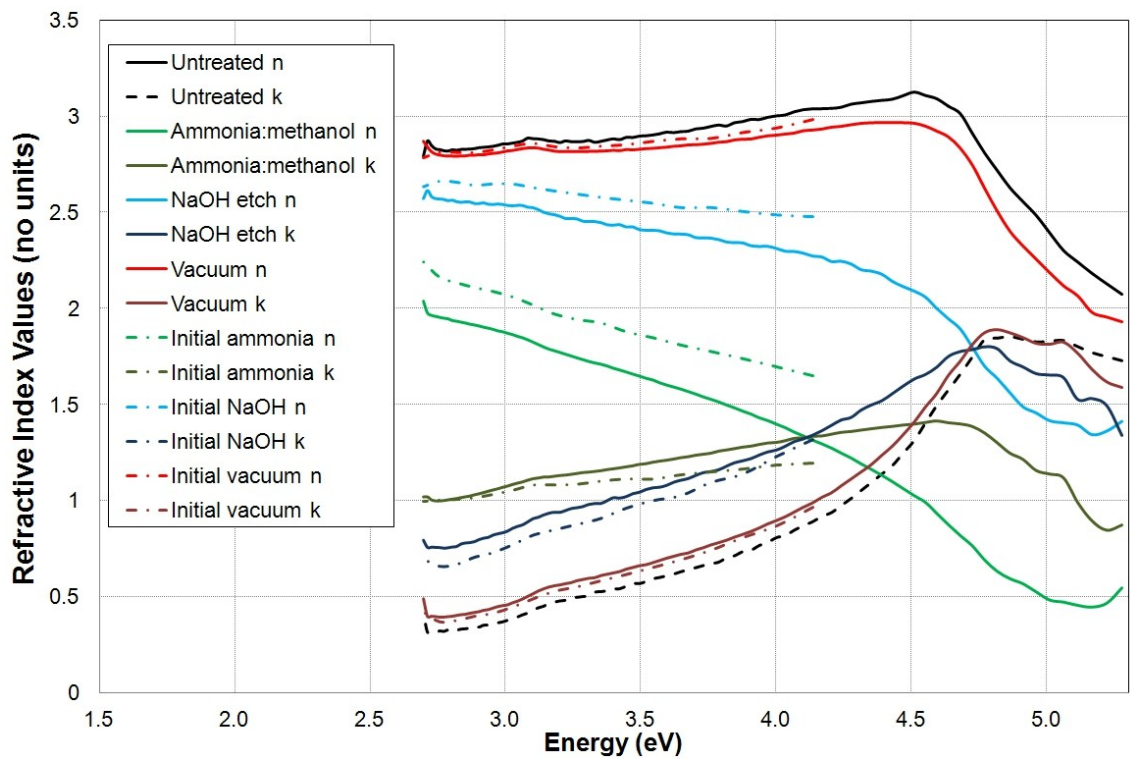


Fig. 6.20. The  $n$  and  $k$  values for HWC268 before and after being etched/annealed. Solid lines represent the  $n$  and  $k$  values for each treatment after 76 days and the dashed and dotted the initial measurements.

Figure 6.20 reveals two interesting points. First, all of the treated samples except the vacuum annealed ones change over time. Second, irrespective of the treatment there is always an increase in the absorption and a decrease in the apparent refractive index of ZnSe. Interestingly it is the  $\text{NH}_3\text{:CH}_3\text{OH}$  solution that has the worst effect on the measured values even though it is one of the most used technique for oxide removal [6.25, 6.26,].

There are also changes in the position of the peaks of the oscillations in the below bandgap region (not shown) for the  $\text{NH}_3\text{:CH}_3\text{OH}$  etched samples consistent with a 12, 36 and 65nm change in thickness for HWC64, 170 and 268 respectively. However as this change depends on the layer thickness, it suggests it is not caused by etching. This effect was unexpected, but has been seen by other groups who attributed it to surface roughening [6.85].

Of the three surface treatments tried only the vacuum annealing produces any improvement to the surfaces, as the amorphous selenium component is removed even though the BEMA thickness is increased. The vacuum annealed

sample also shows the least change over time as demonstrated in figure 6.20. However even the vacuum annealed sample does show changes over time and as there is a reduction in E1 for all the etched or annealed samples, these treatments are not suitable for SE measures of our samples. They do however support the presence of a mixture of ZnO, SeO<sub>2</sub> and amorphous selenium in the oxide layer, and that the final state of the ZnSe surface is a rough ZnO layer.

#### 6.4.2.2. Sample to Sample Variation

	No oxide layer	Surface Roughening	Amorphous Selenium	WZ-ZnO	Amorphous ZnO	GaAsO <sub>2</sub>
Dahmani	27.8	24.8	26.4	25.0	27.8	24.9
Kato	48.9	42.5	48.7	42.8	48.8	42.9
Model	31.3	21.0	30.8	22.0	29.2	22.6
Average	36.0	29.4	35.3	29.9	35.3	30.1

Table 6.10. Variation of MSE for different ZnSe and native oxide dispersion models.

A simple model composed of a ZnSe layer (using the Dahmani, Kato or section 6.4.1. ZnSe dispersion model) and a single layer composed of either WZ-ZnO, a-ZnO, a-Se, GaAsO or roughening individually was used to model all the samples initially. The average MSE from these models are in table 6.10.

	Overlayer Thickness (nm)	Selenium %	Air %	ZnSe Thickness (nm)	MSE
Average	4.62	33.0	45.7	824	25
Std. Dev.	1.60	17.0	8.5	462	18

Table 6.11. Variation of the BEMA parameters for a series of twelve ZnSe OG samples

The results of modelled the samples again using a more realistic BEMA consisting of a-Se, air (roughening) and WZ-ZnO to represent the oxide layer are show in table 6.11.. The change improves the MSE for all 12 samples, but only by a small amount and there is a very large variation in the values from sample

### 6.4.3. Zinc Sulphide, ZnS

Only one ZnS sample, HWA2018, was investigated using SE. The sample consists of a single thick layer of ZnS, comprising 900s of growth directly onto a GaP wafer. When the layers XRD peak is modelled (see figure 6.21) it shows a ~10% relaxed peak best modelled by ~55nm of ZnS, representing a growth rate of 0.61Å/s. This level of relaxation is slightly larger than would be anticipated, as ZnS is only -0.76% mismatched to GaP and therefore the critical thickness for relaxation should be ~53nm. The structure used for the modelling is inset in figure 6.21 and returned a GOF of 0.119 to the measured 004 data.

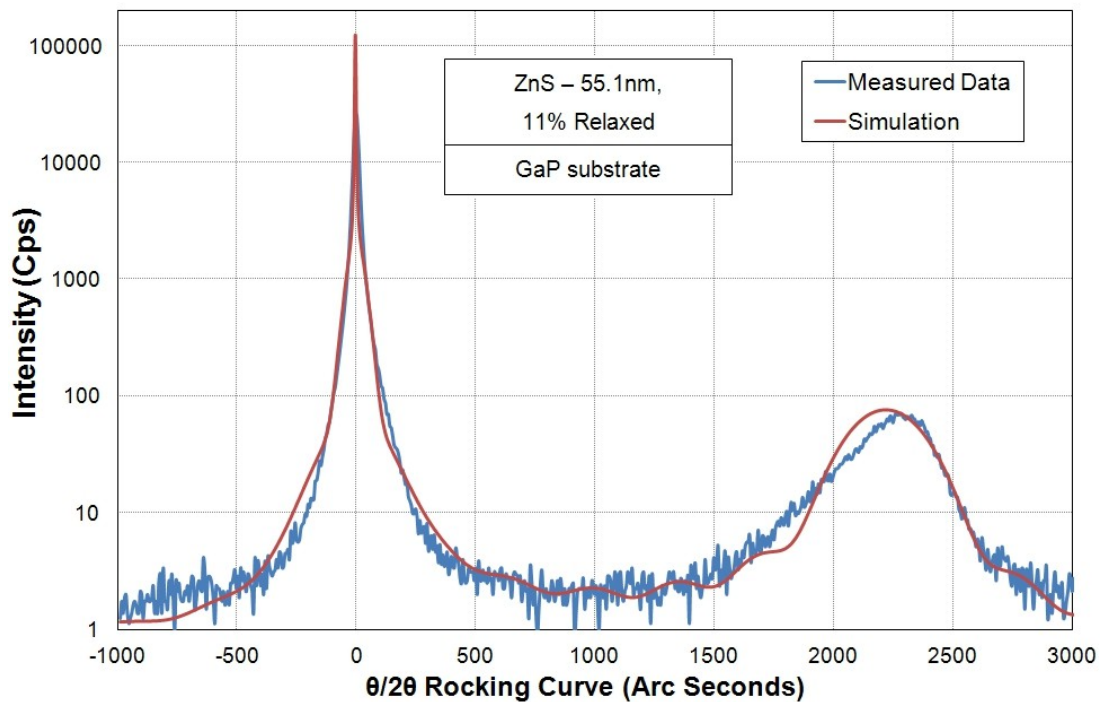


Fig. 6.21. Measured XRD peak from HWA2018 and simulation. The modelled structure is shown inset. The blue curve is the measured data and the red is a simulation based on the inset structure.

Figure 6.22 shows the measured SE data for HWA2018 with a fit made using the refractive index data from Tsuchiya et al. [6.86] and a BEMA roughening layer comprising 50:50 air/ZnS for the oxide layer. The structural details produced by the fitting are shown in table 6.12. The figure shows a series of peaks in the ZnS transparent region representative of a thickness of ~270nm, far greater than predicted by the X-ray modelling and consistent with a growth rate of 3Å/s. However as relaxed layers are not handled well by the modelling software, see section 6.3., it is likely that this growth rate is more accurate.



Palik ZnS Data			Tsuchiya et al. ZnS Data			Multi-Oscillator (MO) Model		
Roughness (nm)	ZnS (nm)	MSE	Roughness (nm)	ZnS (nm)	MSE	Roughness (nm)	ZnS (nm)	MSE
4.31	269.1	63.1	4.76	272.1	27.7	5.81	267.8	17.1

Table 6.12. HWA2018 SE fitting data.

Table 6.12 also shows the details of modelling the layer with the refractive index data from Palik [6.8] and a MO model based on the Tsuchiya data and generated in the same way as that in section 6.4.1. The MO model consists of three Gaussian oscillators with energies of 3.780, 43131 and 6.087eV and a UV pole (to again represent higher order transitions) at 10.057eV. However as only one ZnS sample was available, it is impossible to accurately determine whether or not this refined MO model is a better representation of the ZnS dispersion.

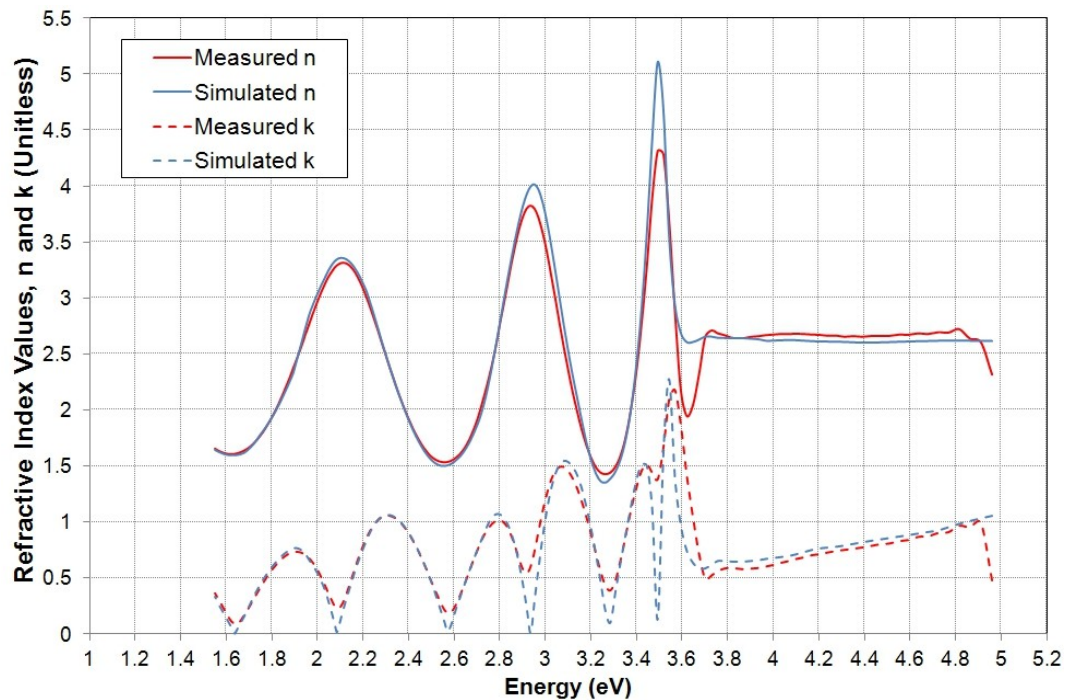


Fig. 6.22. Spectroscopic ellipsometry measurement and modelling of HWA2018.

Modelling the oxide layer with a BEMA composed of Air and either WZ or amorphous ZnO resulted in MSE increases for the Palik and multiple-oscillator (MO) models of 1.4% and 10.4% respectively for the WZ, and 0.3% and 13.0% for the a-ZnO. The Tsuchiya et al. fit was improved by 4.9% for the WZ-ZnO/air BEMA but made worse by 0.3% for the a-ZnO/air BEMA.

#### 6.4.4. Zinc Sulphur Selenide, ZnSSe

Three ZnSSe samples with the same structure ( $\text{GaAs}/d_1 \text{ ZnSe}/d_2 \text{ ZnS}_x\text{Se}_{1-x}$ ) but different layer thicknesses and ZnSSe compositions, as shown in table 6.13, were investigated by SE. As the samples are uncapped, the ZnSSe was exposed to the atmosphere and will have oxidised. However as all the alloys are very ZnSe rich the oxidation will be similar to pure ZnSe as the additional products (sulphur and  $\text{SO}_2$ ) will evaporate rapidly due to their high volatility.

# HWC	Expected Thickness (nm)		XRD Characterisation				
	ZnSe, $d_1$	ZnSSe, $d_2$	ZnSe, $d_1$ (nm)	ZnSSe, $d_2$ (nm)	Sulphur, X (%)	GOF	
						004	115
143	3.6	170	2.8	167	16.7	0.11	-
253	48	86	45	96	15.8	0.09	0.15
254	52	86	55	88	8.6	0.11	0.09

Table 6.13. Expected and XRD determined thicknesses and sulphur content of the ZnSSe samples investigated using SE. XRD GOF figures are also shown.

Figure 6.23 shows the measured XRD spectra for HWC143 and a simulation based on the inset structure. This spectra is similar to all those measured. The sharp pendellösung fringes present in the HWC143 XRD spectra mean the structure is not fully relaxed. Fringes are also seen for HWC253 and 254, but are less well resolved, so these structures are more relaxed.

To produce an accurate XRD model it was necessary to model the ZnSSe layer as two layers with the same composition but different relaxations. The other possibility that might explain the shape of the measured XRD peak is if the composition of the ZnSSe layer changes as function of thickness. Modelling the ZnSSe layers in the three samples using 3-5 layer graded composition models results in a smaller GOF than in table 6.13, but this is simply due to the use of a multi-layer solution. As the ZnS cell used for the growth of these samples is known to produce an initial spike in the flux it produces and the layer thicknesses produced, it seems likely that the best model of the XRD spectra would comprise a model with both relaxation and a graded composition. However by introducing both of these without more information (PL data for

instance) a range of different compositions would be possible.

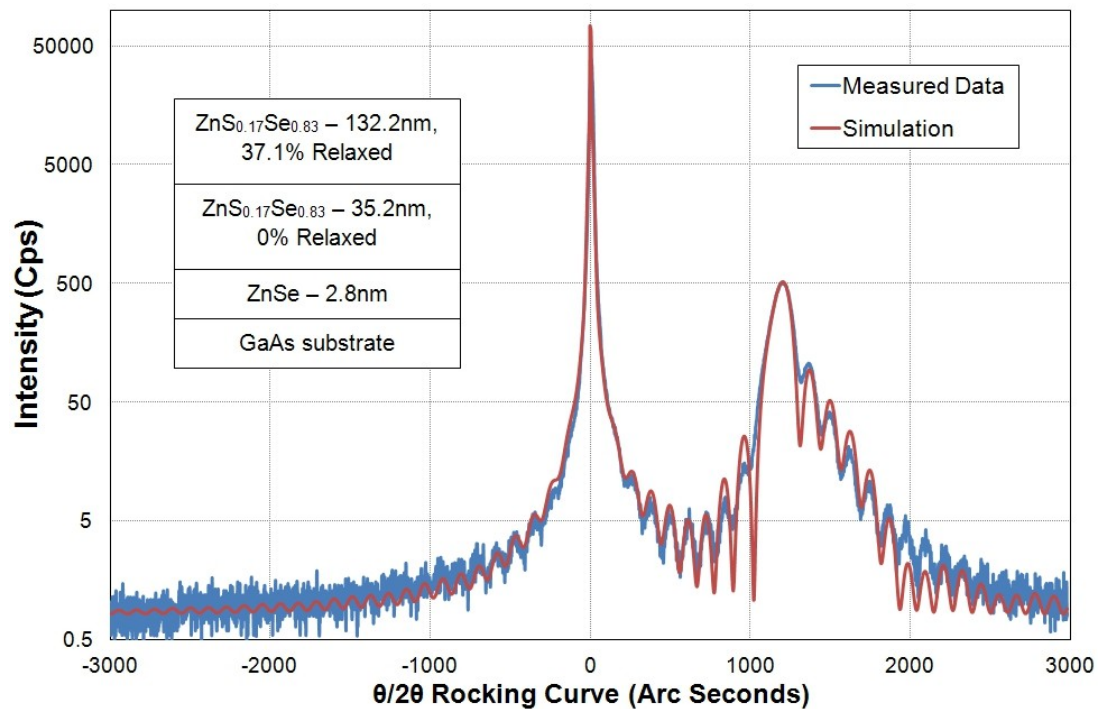


Fig. 6.23. Measured XRD peak from HWC143 and simulation. The structure used for the simulation is shown inset. The blue curve is the measured data and the red a simulation based on the inset structure.

ZnS and ZnSe have bandgaps of  $\sim 3.7$  and  $\sim 2.7$  eV at 300K respectively and as all three samples contain ZnSe rich alloys, it should be possible to model the ZnSSe layer across virtually the entire measured range using a simple BEMA. Figure 6.24 shows the measured and modelled SE data for HWC253, with the structure used for the modelling inset.

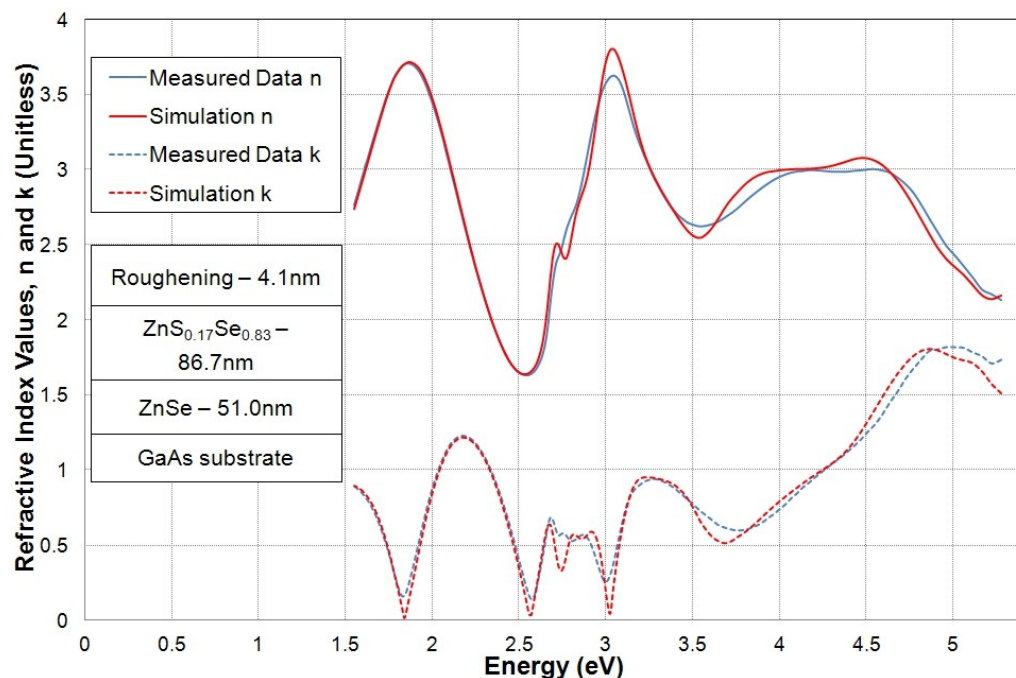


Fig. 6.24. Measured and modelled SE data from HWC253. The structure used for the modelling is inset.

The models used for all three samples are detailed in table 6.14 along with the growth rates predicted by both the SE and XRD measurements. Both the ZnSSe composition and growth rate are in agreement between the 2 techniques. There are slight differences in the ZnSe thicknesses generated but this may be due to the thick, relaxation ZnSSe layer masking their effect.

ZnSSe is a material where SE modelling is very effective at producing both thickness and compositional information, as the SE scans require only ~30 minutes each with minimal time required to setup the scan and analyse it. In comparison the x-ray scans require at least 12 hours each plus an hour or 2 to align the sample and a considerable time to analyse. The comparison is slightly skewed by the SE analysis only being performed to see if it matches the X-ray data, but it is still a faster way to investigate ZnSSe samples.

# HWC	Layer Thickness (nm)			S%	MSE	Growth Rates (Å/s)			
	Roughness	ZnSSe	ZnSe			SE		X-Ray	
						ZnSe	ZnSSe	ZnSe	ZnSSe
143	3.46	153.5	12.2	18.6	25.4	1.02	1.60	0.23	1.74
253	4.13	86.7	51.0	16.5	16.1	1.06	1.44	0.94	1.60
254	3.42	81.4	67.0	10.4	13.3	1.40	1.36	1.15	1.47

Table 6.14. Structural information generated by the SE modelling of the ZnSSe sample.

#### 6.4.5. Magnesium Sulphide, MgS

A series of MgS containing samples were investigated with SE. Samples chosen were selected for a number of reasons including:

1. That as the dispersion (and bandgap) of MgS is not known with any certainty, it is necessary to look at a number of samples to ensure that the derived dispersion relation is at least internally consistent.
2. The use of XRI samples for the determination of materials dispersion has not been reported previously. Hence it should be investigated to ensure that it is justifiable.
3. To allow the various oxide models derived in the last section to be tested and their effect on the dispersion measured for the MgS determined.

The MgS samples also allowed a range of different dispersion modelling techniques (Cauchy relation, SEO, point inversion) to be investigated to determine which produces the best model for MgS.

The majority of the samples investigated are standard XRI structure with an MgS central layer surrounded by thick ZnSe layers. But a smaller number were grown for AFM measurements with a ~5nm thick ZnSe top cap, which should contribute less to the samples total dispersion. However the thin capping layer may be insufficient to protect the MgS underneath, hence it is possible that it will have oxidised to MgO

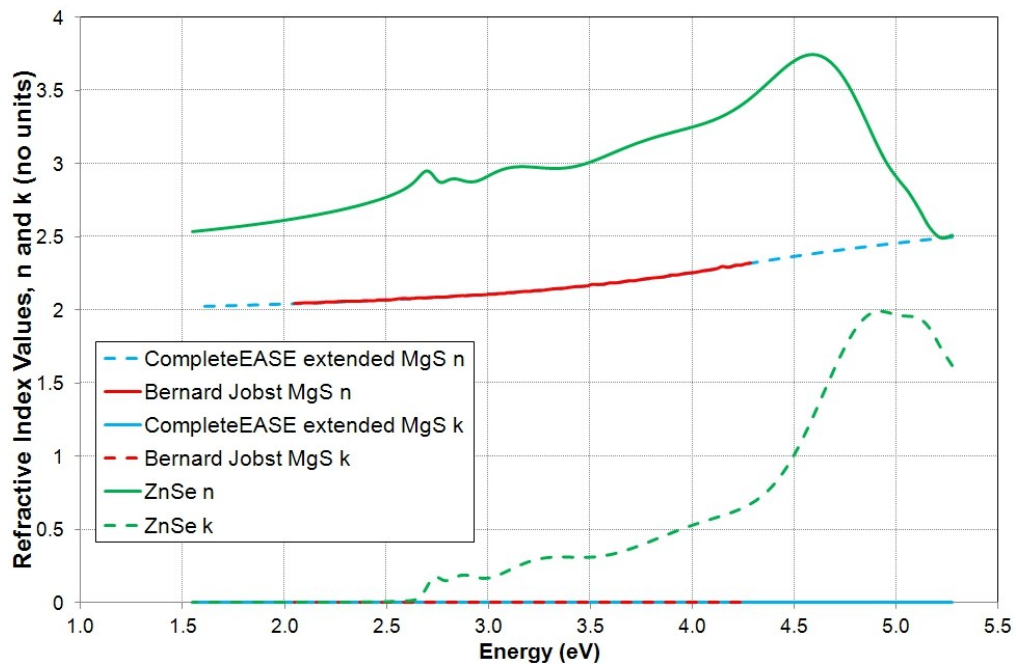


Fig. 6.25. MgS dispersion from B. Jobst thesis [6.27], extended relation and a ZnSe curve for comparison.

There are no published experimental values for the dispersion of MgS (either ZB or rock-salt), most likely due to its rapid oxidation. A number of papers report calculated values based on different models [6.87, 6.88] and these have been used to produce DBRs, so should be close to the true values [6.89]. Bernhard Jobst measured the dispersion of a thin layer (~5nm) over a narrow energy range (2.0-4.3eV) using an *in vacuo* SE system at Würzburg University and presents the result in his thesis [6.27] but has not published the data. A version of his data is presented in figure 6.25 along with the extended curve produced by the CompleteEASE modelling software based on it and a ZnSe curve (for comparison). No transition features are observed in the Jobst data and hence the bandgap must be greater than this.

# HWC	SE Modelled, Jobst Extended					XRI Modelled			
	Roughness (nm)	ZnSe (nm)	MgS (nm)	ZnSe (nm)	MSE	ZnSe (nm)	MgS (nm)	ZnSe (nm)	GOF
107	7.3	56.1	9.1	56.3	22.1	50.1	9.1	50.5	0.09
112	8.7	65.0	6.5	70.5	13.9	62.9	6.0	65.4	0.08
289	5.2	38.8	10.7	39.8	14.8	32.0	13.4	35.1	0.11
310	5.7	49.2	8.8	51.4	13.2	49.3	6.4	50.3	0.10
311	8.4	46.7	13.1	45.9	21.3	47.1	14.2	36.2	0.10
366	3.8	90.1	2.7	92.9	11.6	-	-	-	-
367	3.5	95.8	23.3	99.0	16.4	92.0	22.5	96.6	0.13
283	0.0	4.6	17.5	44.0	44.0	-	-	-	-
284	27.6	6.4	22.5	41.7	77.2	-	-	-	-
348	0.0	2.9	19.4	53.5	42.6	-	-	-	-
349	42.6	11.9	17.0	56.9	70.6	-	-	-	-
352	2.2	3.0	10.6	49.8	27.7	-	-	-	-
354	21.9	1.0	10.9	51.8	36.0	-	-	-	-
Avg.	10.5	36.3	13.2	58.0	31.6	-	-	-	-

Table 6.15. Details of the SE and XRI modelling of the MgS samples.

Table 6.15 gives the best fit parameters based on the extended Jobst model for MgS and The ZnSe model from section 6.4.1. A simple BEMA roughening layer was used to account for the native oxide layer. The details of the X-ray analysis of the samples is also shown (where available). The best fit parameters in table 6.15 differ from those reported earlier in table 6.5 as the measured SE spectrum is now being modelled over the entire 235-800nm (1.55-5.3eV) range. The data shows that although there are differences in the ZnSe and MgS thicknesses determined by SE and XRI they are small, 4.8% and 1.7% respectively.

All of the samples were remodelled using the dispersion relation for MgO from ref. [6.91]. As MgO has a band gap of ~7.8eV (159nm) at 300K, it is transparent across the entire measured range. A number of the MgS samples grown by the group recently were suspected to be intermixed with ZnSe (see chapter 5). The samples were therefore also remodelled with the MgS layer replaced by either an MgS/ZnSe BEMA or an MgO/ZnSe BEMA.

The remodelling showed that the majority of the samples are either oxidised, contain some ZnSe or both. Only samples HWC366 and 367 appear to contain pure MgS, with HWC283, 311 and 352 containing MgS/ZnSe layers. However as the differences between the MSE values achieved is often less than 5%, conclusive layer composition determination is impossible

#### 6.4.5.1. MgS Trial Function Modelling

As neither the extended Jobst data nor the MgO model show a transition, a series of trial dispersion curves for MgS with transition at 4.5, 4.7, 4.9, 5.1 and 5.3eV were generated by adding the scaled, near bandgap region of a ZnSe dispersion curve to the Jobst MgS data. However when generic models with transitions at different energies were compared, the change in the total dispersion was found to be extremely small due to the large increase in the ZnSe  $n$  and  $k$  close to its E1 point ( $\sim 4.5$ eV) masking the trial function transition.

This effect is independent of the ZnSe or oxide layer dispersion models used, as all the ZnSe dispersion curves show a similar large increase between  $\sim 2.7$  and 4.5eV. As the AFM samples have a much thinner ZnSe capping layer this problem is somewhat reduced but the change in  $n$  and  $k$  values is still relatively small for samples with thin MgS layers. Therefore the modelling of the XRI samples did not produce any meaningful information.

The MSE of AFM samples had a greater dependence on the trial function transition energy, with the sample falling into two groups. The first comprises HWC283, 348 and 352, which all show an MSE minimum between a transition energy of 4.7-5eV. The second group show very different behaviour and no apparent minimum.

#### 6.4.5.2. Cauchy-Lorentz Modelling

Although the measured SE data for the XRI samples may not allow a distinct

transition to be determined directly, it still allows the general form of the dispersion to be evaluated and a transition to be obtained. The simplest way to achieve this is to model the below to near-bandgap region using a combination of a Cauchy and Cody-Lorentz relation.

As a Cauchy-Lorentz model can only effectively model the region close to a materials bandgap, the energy range modelled will be important. It is therefore worth investigating what happens as the energy range is varied while modelling the MgS samples with the extended Jobst model. The results of this work are shown in figure 6.26 and shows that again the AFM samples have a greater dependence on the MgS dispersion than the XRI samples.

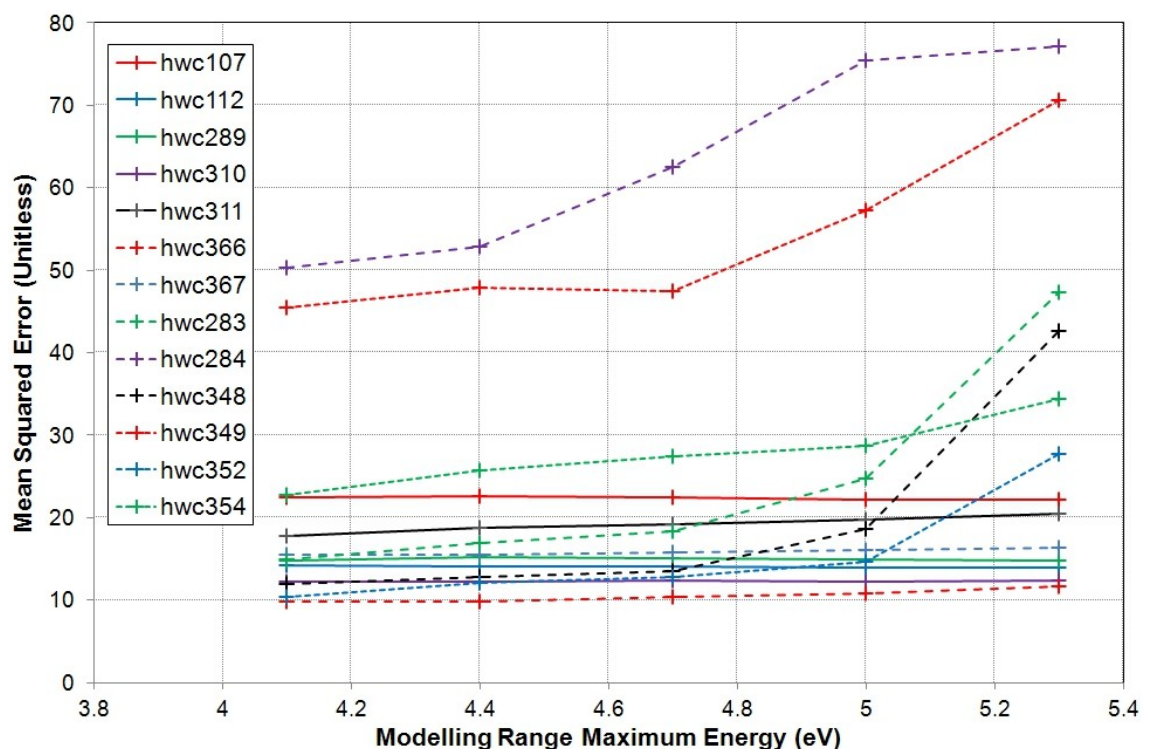


Fig. 6.26. Extended Jobst MgS modelled samples mean squared error vs. the maximum energy of the modelled range.

The Samples can be roughly divided into 2 groups with HWC107, 112, 284, 289, 310, 311, 349 and 354 (referred to as group 1 from now on) all showing similar behaviour with a roughly linear increase in MSE with the maximum energy of the modelling range. The other samples (group 2) all show threshold behaviour around 4.7-5eV consistent with a transition.



Replacing the Jobst extended data with a Cauchy-Cody model produces a similar result, with the group 2 samples being the only ones that showed the expected threshold behaviour in  $n$  and non-zero  $k$  values, in the region above 4.7eV. The models for the group 1 samples either did not show a transition or it was at >6eV, suggesting these samples may contain MgO.

#### 6.4.3.3. Single Effective Oscillator (SEO) Modelling

Another simple technique that has been used to model semiconductors effectively is the single effective oscillator (SEO) model [6.90], where a single oscillator is used to model the near-bandgap behaviour of the material and a second UV pole oscillator at higher energy (typically 8eV+ for II-VI materials [6.82]) to model all of the higher energy transitions. SEO models are again limited in the energy range they can successfully model but as MgS and MgO have bandgaps of  $4.5 \pm 0.35$ eV and >7eV at 300K respectively, it is possible that entire range measured range (1.55-5.3eV) could be measured. However as the modelling data didn't show any trends in bandgap figure this wasn't the case.

A smaller energy range of 1.55-4.68eV (265-800nm) was then chosen and the modelling repeated. The data produced again divide into the same 2 groups, with group 1 having bandgaps >8eV and group 2 having bandgaps in the range 4-6eV. The average  $n$  curve for the group 1 samples (not shown) was also found to be virtually parallel to MgO  $n$  curve but with the wrong values (~2.0-2.2 vs. 1.6-1.8) and a correlation of 0.993 to it, strongly suggesting that these samples contain MgO but with the wrong layer thicknesses. The average dispersion for the group 2 samples was much closer to MgS but didn't show a transition, most likely due to modelled range.

#### 6.4.5.4. Wavelength by Wavelength Point Inversion Modelling

The final technique used to determine the dispersion of the MgS layer is point inversion (PI) at each measured wavelength, where the  $n$  and  $k$  values are

calculated from the measured dispersion once the other layers effect has been subtracted. The drawback with this technique it that it does not attempt to produce a smooth dispersion curves, so is also more likely to be affected by errors in the other layers. Figure 6.27 shows the dispersion curves produced by averaging the curves produced by PI for the group 1, group 2 and all the samples, as well as the Jobst data for comparison. As PI works best when used with multi-sample analysis, all of the curves were averaged.

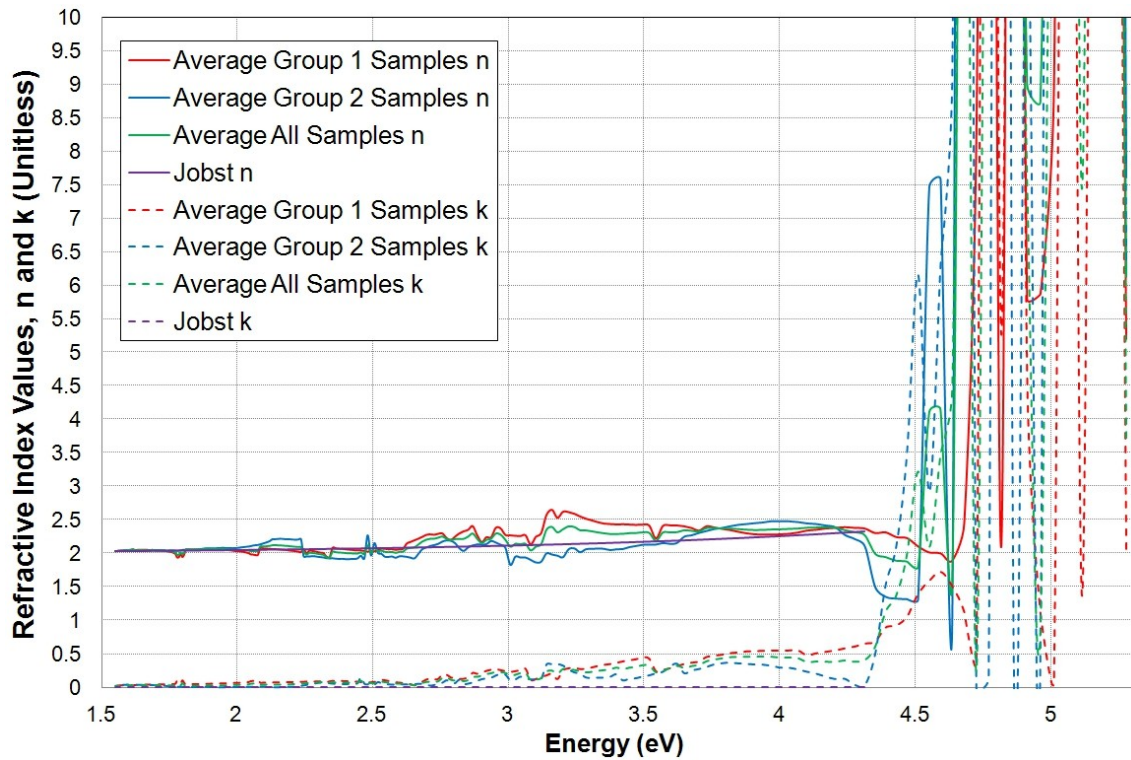


Fig. 6.27. Average dispersion curves obtained by wavelength-by-wavelength point inversion of the MgS samples and the Jobst dispersion curve for comparison.

The curves are rough and show below bandgap absorption, neither of which are realistic. However the absorption may represent the true behaviour of the sample, with one of the layers (most likely the surface oxide layer) absorbing more than has predicted by its model. If this is the case then the only way to remove the feature would be to better model the other layers or to force the MgS layer to be non-absorbing below 4-5eV and accept a worse fit. The PI fitting has a 50% lower MSE than modelling the samples with the extended Jobst data, which suggests that although the dispersion curves are not smooth they must still represent the overall dispersion of the MgS layers well.

The figure also shows that both groups of samples show a rapid increase in both  $n$  and  $k$  above 4.5eV. This would be expected as the region contains the anticipated MgS bandgap transition. However the magnitude of the increases appears un-realistic. Typical above bandgap  $n$  and  $k$  values can reach 10 or more but it is extremely unlikely that values exceed this, as such these fits must be approached with some scepticism. By averaging the sample curves by type (either XRI or AFM, not shown) it becomes clear that the short period, large magnitude oscillations (noise) seen above 4.5eV is due to the XRI samples.

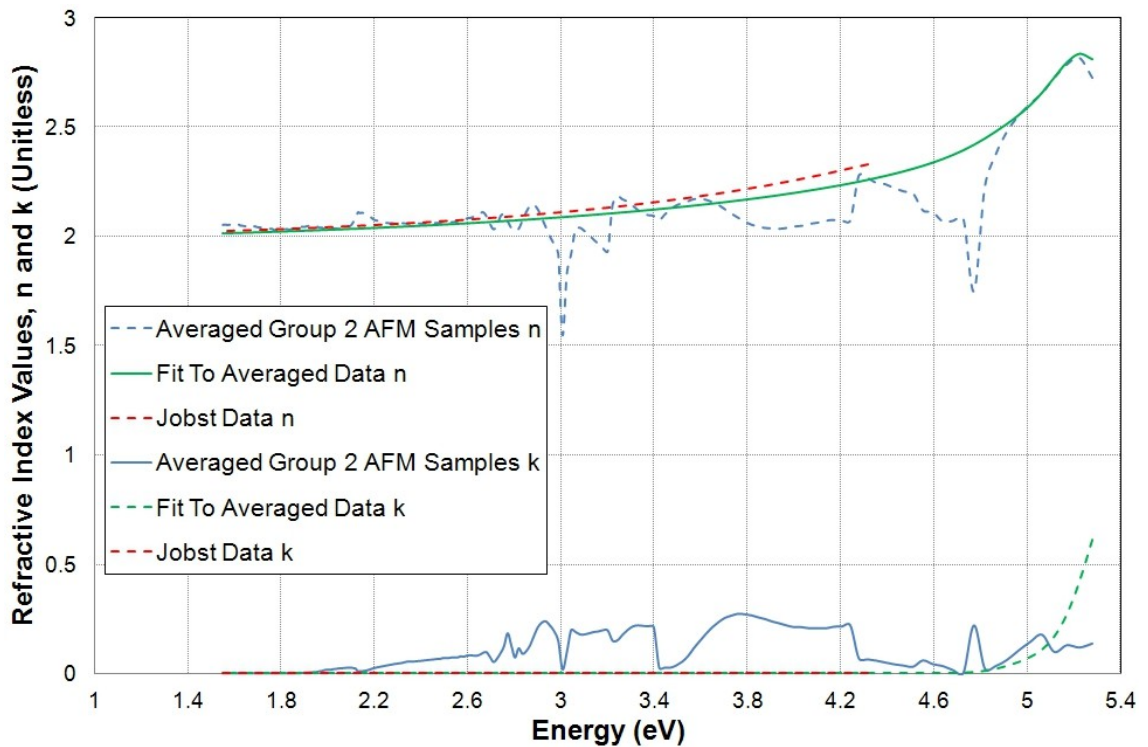


Fig. 6.28. Refractive index values of the averaged group 2 AFM samples, a MO fit to them and the Jobst MgS data, for reference.

The dispersion curves produced by averaging the AFM samples in group 2 are shown in figure 6.28 (blue curves). Although they are still not smooth they are now free from noise  $>4.5\text{eV}$  and are close to the Jobst data (red curves), apart from the below bandgap absorption. Fitting a SEO model (green curves) to the PI data produces an  $R^2$  value of 0.62 to the PI refractive index which although not high, is to be expected due to the noise in the data. The MO model shows a correlation to the Jobst MgS data of 0.95, which suggests that the two measurements are compatible.

The SEO fit to the averaged group 2 AFM samples shows a transition at

~5.22eV, which is higher than anticipated from the work reported earlier in this thesis. However it is still compatible with the values reported in the literature [6.92-6.95]. The absorption (Tauc) plot from the SEO fit  $k$  (not shown) produces a band-edge figure of 5.18eV. Combining this with the value from the modelling a predicted MgS bandgap of  $5.20 \pm 0.02$  eV.

Averaging the PI curves for the AFM samples in group 1 produces a much flatter refractive index curve (not shown). The correlation (and  $R^2$ ) with the MgO and Jobst MgS curves produces coefficients of 0.44(0.19) and 0.39(0.15) respectively. Although these figures are not conclusive, they do support the argument that the group 1 samples may have oxidised to MgO.

#### 6.4.5.5. Oxide Layer Modelling

So far all the modelling work of the MgS samples has used a simple air/ZnSe BEMA roughening layer to model the ZnSe native oxide. To test both the validity of the MgS model generated in the last section and the effectiveness of the roughening layer as a native oxide model, the samples were re-modelled using a BEMA consisting of a ZnO/a-Se with roughening and the MO MgS model generated in section 6.4.3.4. This resulted in a 14.6% improvement in the fits obtained. However 45% of this improvement comes from HWC349 alone and without it the improvement is a more modest 7.9%.

Repeating the PI modelling process with the ZnO/a-Se BEMA layer resulted in virtually identical dispersion curves for the MgS (not shown). When the transitions determined from the fitting and Tauc plot of this new modelling are combined the bandgap of MgS is predicted to be  $5.15 \pm 0.02$  eV.

#### 6.4.6. Manganese Sulphide, MnS

MnS is another metastable compound and little information is available about the ZB phase in the literature. Although there is information about the refractive

index of MnS in the RS phase [6.96], no data can be found for the ZB phase. Therefore the results presented in this section are the first measurements of the refractive index of ZB-MnS

# HWC	Thickness (nm)		
	ZnSe	MnS	ZnSe
1423	5	16.4	5
1476	60	4.2	60
1478	60	6.3	60
1500	60	8.4	60
1616	33	2.0	33
1710	72	2.5	72
1790	18	42.8	-
1838	18	5.0	-

Table 6.16. Expected thicknesses for MnS containing samples.

Two types of MnS containing samples were investigated by SE: six XRI structures and two AFM structures. The expected layer thickness for all the samples are shown in table 6.16. The uncapped AFM samples are of particular interest as they have been exposed to the atmosphere for a considerable period of time (>2500 days) and could therefore have completely oxidised to MnO.

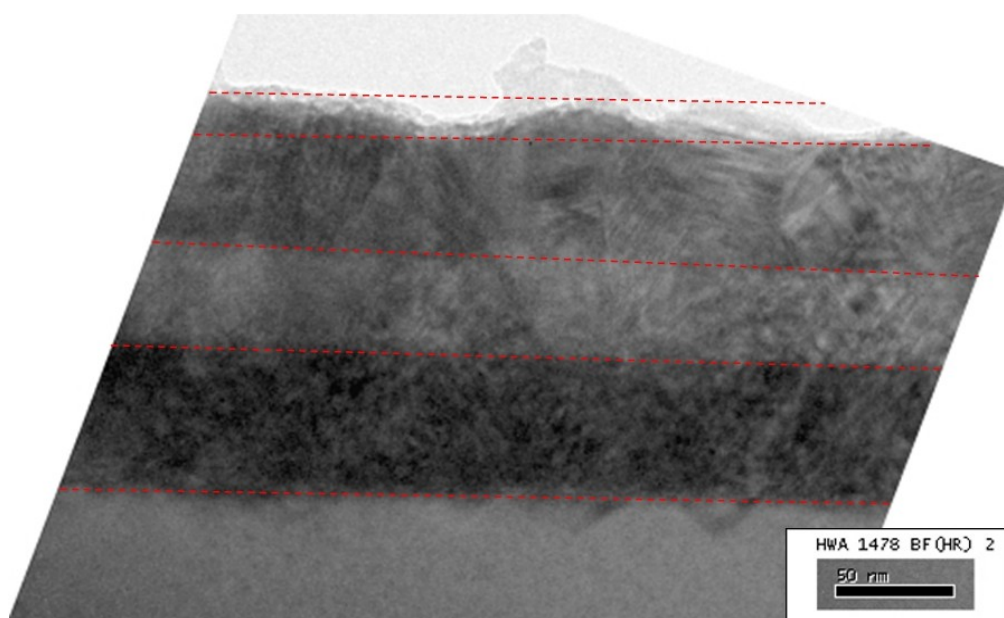


Fig. 6.29. Cross sectional TEM image of HWA1478. Red dotted lines have been added to improve clarity of layer boundaries and show where the layer thicknesses were measured from.

The expected thickness values in table 6.16 are based on measurements

presented in L. David's thesis [6.97], comprising XRI measurements made of a series of MnS samples. These appeared highly accurate but a number of the samples were subsequently investigated using TEM at Philipps-Universität Marburg (see figure 6.29) and different thicknesses found, see table 6.17.

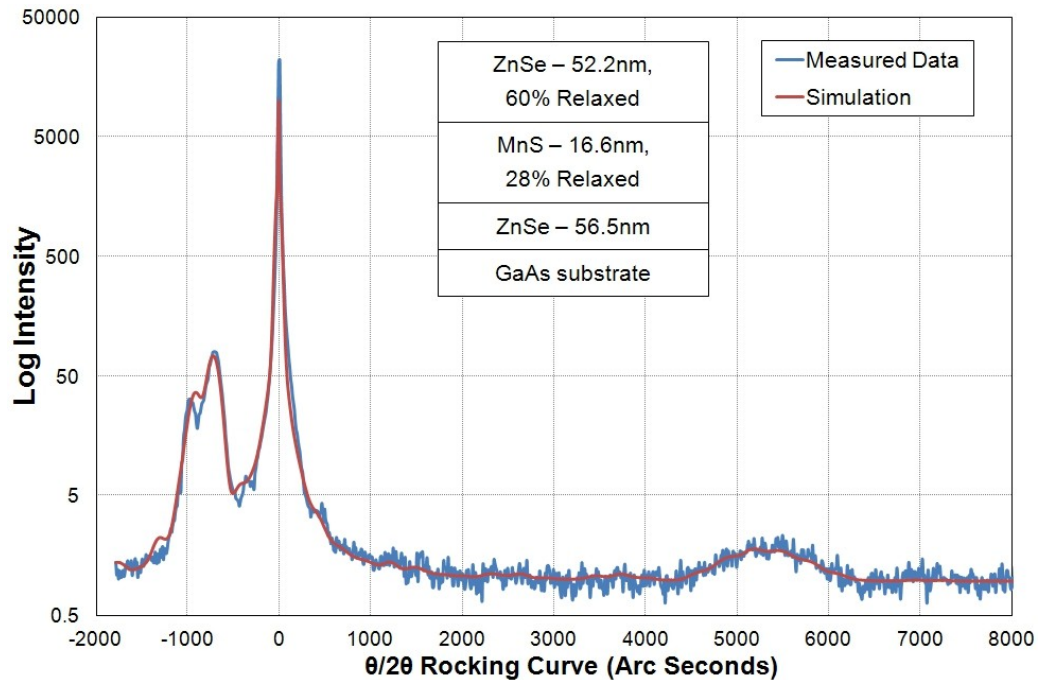


Fig. 6.30. Measured and simulated XRI/XRD data for HWA1476. Modelled structure is inset. The blue curve is the measured data and the red a simulation based on the inset structure.

All the MnS samples were then measured again using HRXRD and a more detailed analysis made of their model. The majority of the samples were intended as XRI sample, but those with larger thicknesses produce an MnS XRD peak making their characterisation much easier. An example is shown in figure 6.30 for HWA1476. When modelling these samples the only unknown parameter is relaxation, which reduces the intensity of the XRD peak compared to a strained layer, so the MnS thickness values in table 6.17 must have an associated error. Comparing the thicknesses in table 6.16 and 6.17 a number (such as 1476 and 1478) show large differences in the MnS thickness and growth rate, which was unexpected.

# HWA	Growth Time (s)	TEM		XRI				
		MnS (nm)	$G_R$ (Å/s)	MnS (nm)	Relaxation (%)	$G_R$ (Å/s)	GOF	
							004	115
1423	390	-	-	86	100	2.21	0.14	-
1476	100	-	-	16.6	28	1.66	0.06	0.13
1478	150	36.9	2.46	34.8	33	2.32	0.10	-
1500	200	-	-	34	34	1.70	0.08	0.17
1616	47	2.2	0.47	2.1	0	0.45	0.09	-
1710	60	-	-	8.4	46	1.40	0.18	-

Table 6.17. MnS sample TEM and XRI/XRD characterisation results.

To investigate this, the growth rate was plotted against the manganese cell temperature and flux, shown in figure 6.31. If the  $G_R$  determined for HWA1710 is ignored (the red data points in the two graphs) a strong linear trend is observed with cell temperature while no such trend can be seen for the measured flux. This suggests that the measurement of the manganese flux using an ion gauge may not be reliable. The data point for HWA1710 may not fit this trend as the X-ray scans for this sample are very poor.

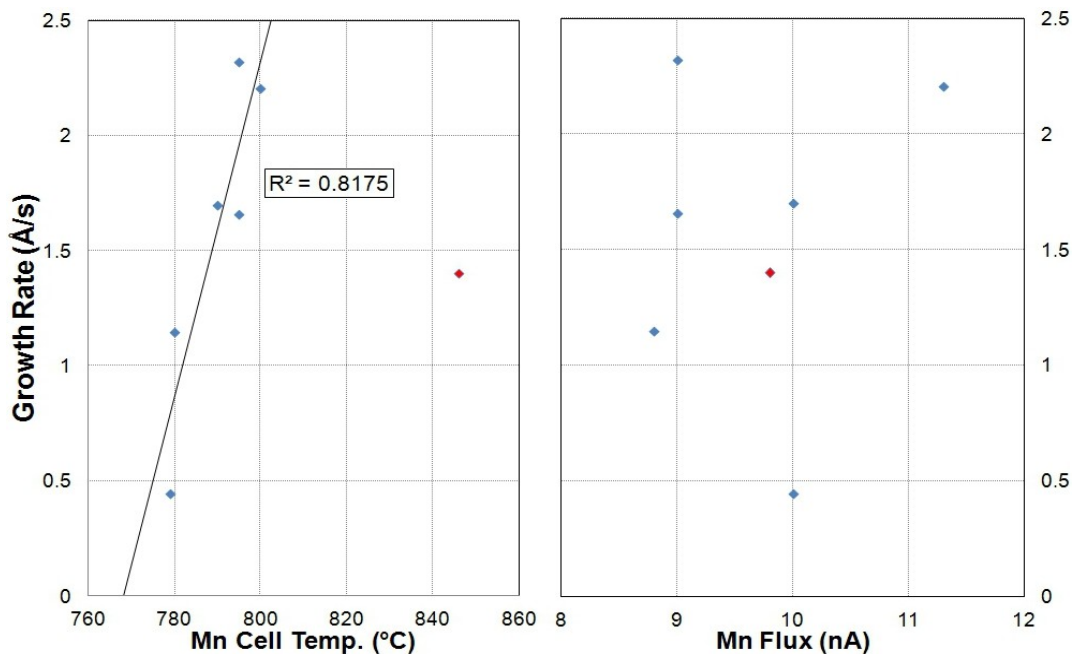


Fig. 6.31. MnS growth rate vs. Mn cell temperature and measured flux.

The MnS layer in HWA1710 also shows anomalous relaxation when compared to the relaxations of the other samples and suggests the MnS layer thickness should actually be between 34 and 86nm. If this is the case then the  $G_R$



observed for HWA1710 would be increased to 6-10Å/s which would fit with the linear trend shown in fig. 6.31. This may also explain the poor x-ray data for this sample, as that high a growth rate is likely to result in poor epitaxy.

Cauchy modelling was used to generate a dispersion relation for the below bandgap behaviour of the MnS layer, <3.5eV, generated by modelling a series of the samples between 1.55-3.10eV (400-800nm). The generated dispersion relation and a fit to the measured data of HWA1478 made using it are shown in figure 6.32. Table 6.18 shows the structural parameters generated by the modelling. The growth rate predicted by SE, TEM and X-ray for most of the samples are very similar, which suggests the dispersion relation generated is close to the true dispersion of MnS.

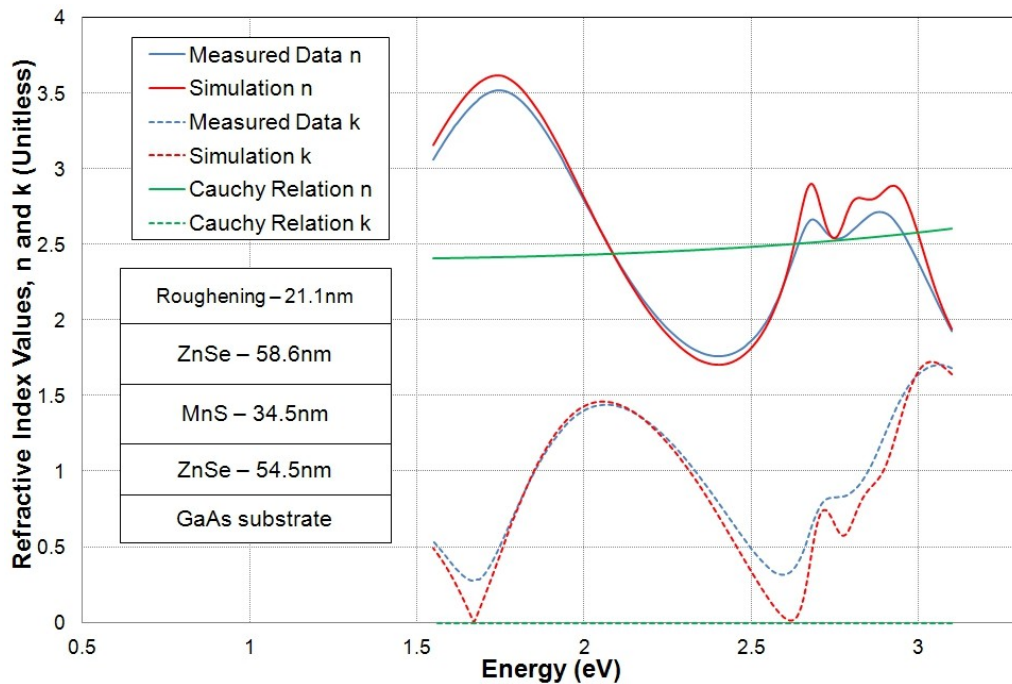


Fig. 6.32. Measured and modelled below band-gap SE data for HWA1478.

Attempts to extend the dispersion relation to the above bandgap region were not successful as all the generated relations were either unrealistic or showed noise similar to that in fig 6.27. However if a larger number of samples were investigated and multi-sample techniques used, it should be possible to generate an accurate relation over the entire energy range available.



#HWA	Growth Rates (Å/s)						
	MSE	SE		TEM		X-ray	
		ZnSe	MnS	ZnSe	MnS	ZnSe	MnS
1423	43.628	0.89	2.33	-	-	1.12	2.21
1476	23.644	0.49	3.28	-	-	0.64	1.66
1478	23.98	0.52	2.30	0.48	2.46	0.30	2.32
1500	38.22	0.62	3.23	-	-	0.79	1.70
1616	12.67	0.58	0.50	0.64	0.48	0.53	0.45
1710	10.48	0.45	3.20	-	-	0.59	1.40
1790	42.35	1.42	0.84	-	-	-	-
1838	28.73	0.33	0.80	-	-	-	-

Table 6.18. Growth rate predicted by SE, TEM and X-ray analysis of MnS containing samples. Entry for HWA1423 is highlighted as the MnS thickness was set for this simulation.

#### 6.4.7. Cadmium Selenide, CdSe

As was discussed in section 6.2.2., CdSe can only be grown in the ZB phase as thin layers on GaAs, which makes SE measurements more complicated. However as ZB-ZnCdSe QWs are regularly produced by the MBE group it would be useful to use SE to characterise them and this requires the dispersion of ZB-CdSe. This has been measured before [6.98], but the measurements were made of CdSe grown on a ZnTe buffer layer and therefore under far less strain than if grown directly on ZnSe/GaAs.

Two CdSe samples were investigated as described in table 6.19. They are both XRI structures, which introduces additional problem for SE as the thin CdSe layer is a QW and will be under significant strain due to the large lattice mismatch (~7% for CdSe on GaAs), and these will both affect its band structure and dispersion [6.99, 6.100]. However these were the only samples available

	ZnSe	CdSe		ZnSe
HWC	Thickness (nm)	ALE cycles	Thickness (nm)	Thickness (nm)
260	120	6	0.9	60
270	96	8	1.2	48

Table. 6.19. Growth time and expected thickness for CdSe samples

The CdSe sample thicknesses are based on the assumption that each ALE cycle deposits 0.5ML of CdSe, which represents the maximum possible deposition rate [6.101, 6.102]. However it is likely the rate is close to this, as a further sample (HWC262) was grown under identical conditions but using twice the cadmium flux and showed near identical emission to HWC270 - 2.34 vs. 2.33eV and 1.91 vs. 1.90eV, QW and QD emission for HWC262 and 270 respectively.

Both samples were grown using our standard QD process (MBE growth of a ZnSe cap and buffer at ~240°C, CdSe by ALE at 240°C and then annealed at 290°C). HWC260 shows only a single emission peak consistent with a QW, while HWC270 shows emission from both a QW and a low density of QDs.

# HWC	QW Emission		QD Emission			QW Thickness (nm)	QD Thickness (nm)
	Energy (eV)	FWHM (meV)	Energy (eV)	FWHM (meV)	Rel. Intensity		
260	2.472	42	-	-	-	0.79±0.1	-
270	2.335	40	1.920	400	0.6%	1.12±0.11	3.30±0.20

Table 6.20. Emission details for CdSe samples and modelled layer thicknesses.

The details of the PL emission from the samples are shown in table 6.20. Modelling this emission suggests that there has been minimal intermixing in these samples, as the QD emission seen in HWC270 would need >3.7nm (~7ML) high dots if they contained even 5% Zn. The QWs in 260 and 270 must also contain less than 20 and 13% Zinc if their widths are less than the maximum thicknesses for a 6 and 8 ALE cycle well respectively.

As previously explained, the inherent structural disorder introduced by the formation of QDs means these samples are not typically X-rayed. However HWC270 was and figure 6.33 shows the 004 scan obtained, with the structure used for its modelling inset. A GOF of 0.097 and 0.095 were obtained for the 004 and 115 reflections respectively using this structure. The modelling software had been allowed to choose any zinc content for the CdSe layer, but consistently chose pure CdSe. The thickness of 1.07nm is a good match to the value obtained by the PL emission modelling, although this thickness would

require a CdSe layer with 3-4% zinc.

It is surprising that the X-ray spectrum from the sample has such well resolved fringes, considering the  $\sim 2\text{nm}$  (200%) variations in CdSe layer thickness required to model the QD emission and the non-uniform strain introduced into the surrounding ZnSe layer. However the low intensity of the QD emission suggests the dots must have a very low density and this may explain their limited influence on the X-ray spectrum.

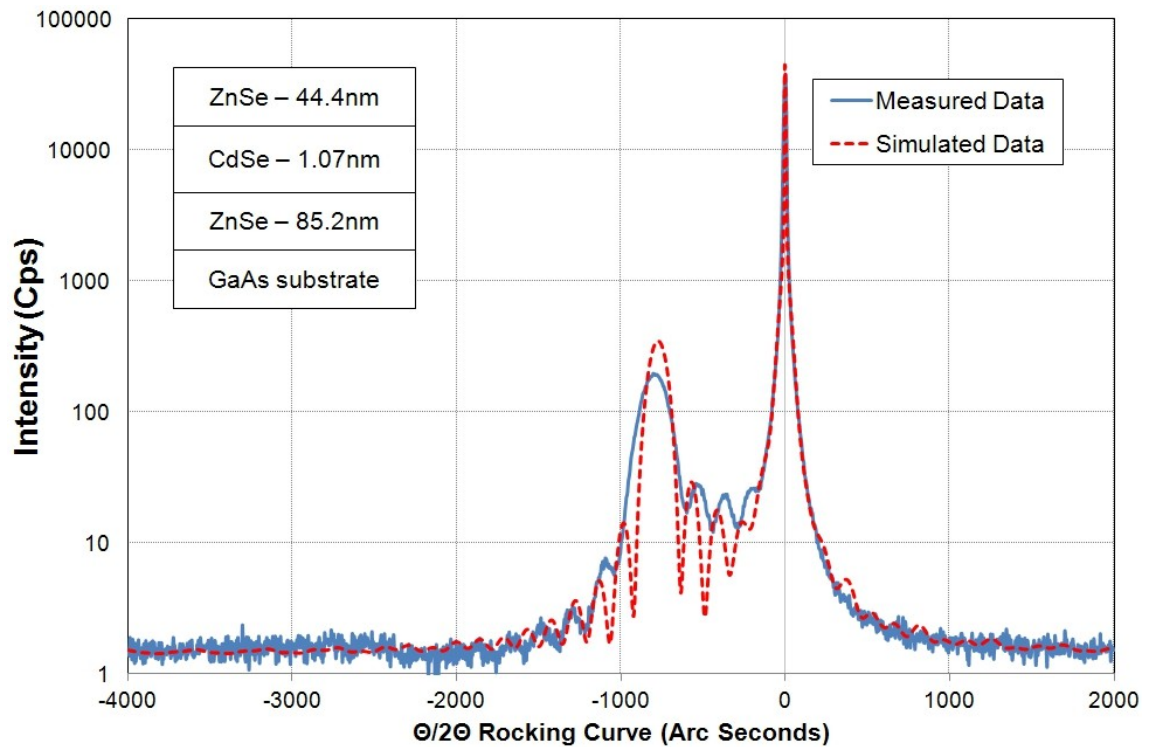


Fig. 6.33. XRI modelling of HWC270 a CdSe QW/QD sample. The blue curve is the measured data and the red dashed curve a simulation based on the inset structure.

The SE spectra obtained from HWC260 and 270 were both modelled with a 4 layer model comprising a surface roughening BEMA layer, ZnSe layers (using the dispersion derived in section 6.4.1) and a CdSe layer - using the dispersion values taken from Kim et al. [6.98]. The model produces ZnSe thicknesses for both HWC260 and 270 that are within 3.5% of the expected values (see table 8.21). However the CdSe thicknesses show a greater deviation and are  $\sim 34\%$  thicker on average. Table 6.21 also shows the details of the fits achieved using the ordinary (O) and extra-ordinary (E) axis dispersion curves for WZ-CdSe taken from Palik [6.8].

# HWC	Palik (E)		Palik (O)		Kim et al.	
	CdSe Thickness (nm)	MSE	CdSe Thickness (nm)	MSE	CdSe Thickness (nm)	MSE
260	1.49	14.7	1.53	14.9	1.56	14.68
270	1.36	9.50	1.30	9.75	1.40	9.48

Table 6.21. SE fitting data for HWC260 &270.

The reason for the difference in thicknesses between XRI/PL and SE is not immediately obvious. One option could be the QW effect discussed in this sections introduction, as this would cause the CdSe layers in HWC 260 and 270 to have different bandgaps and therefore dispersions. To investigate this further, the Kim model was chosen as the basis for new dispersion models for each sample. These models were produced in an identical way to the ZnSe model in section 6.4.1.

Figure 6.34 shows the result of this modelling along with Kim et al. CdSe dispersion relations for comparison. The structures used were identical to those previously in table 6.19 (60 & 120nm ZnSe layers for HWC260, 50 & 100nm for 270, all  $\pm 3.5\%$ ) except with the CdSe thickness set to 0.9/1.1nm for HWC260/270. The new curves show slight improvements in the fits, with an MSE of 13.8 and 9.5 being achieved for HWC260 and 270.

The new curves are quite different to the original Kim data with significantly enhanced peaks, especially around the  $E_2$  critical point. There is no obvious trend in oscillator energy, as many oscillators shift to a higher energy in HWC270 but decrease in HWC260. However there is a clear increase in the intensity of the oscillators as the width of the CdSe layer is decreased. This would support the CdSe thickness discrepancy being caused by the QW effect.

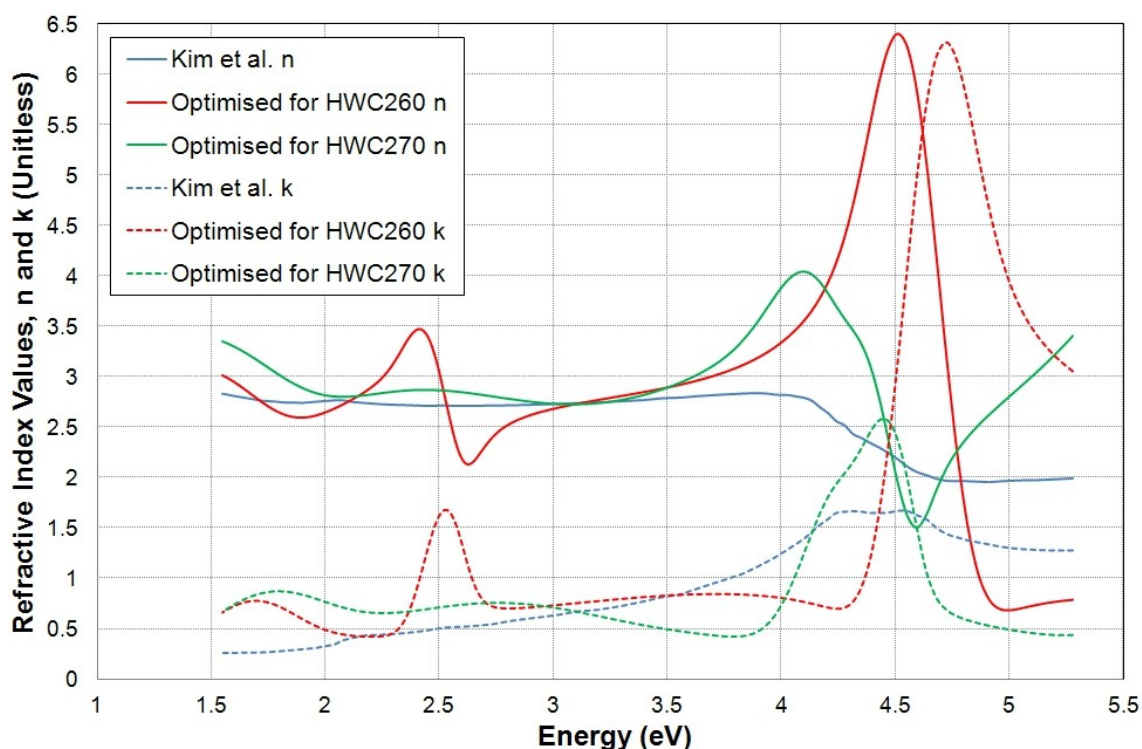


Fig. 6.34. Refractive index values for the Kim et al. CdSe data and 2 dispersion relations based upon it generated by the modelling of samples HWC260 and 270.

#### 6.4.8. Zinc Cadmium Selenide, ZnCdSe

Four ZnCdSe samples were investigated using SE, three ZnSe/ZnCdSe XRI samples, HWC 250-252, and one that contained a single thick layer of ZnCdSe, HWC138. The three XRI samples were discussed and characterised earlier in section 6.2.3.1. The layer thicknesses for all four samples are listed in table 6.22 along with the energy of their PL emission.

# HWC	Thicknesses (nm)			Cd %	GOF		PL energy (eV)
	ZnSe 1	ZnCdSe	ZnSe 2		004	115	
138	9.4	302.8	-	23	0.11	-	-
250	52.5	8.3	48.3	7.3	0.11	0.13	2.707
251	51.9	9.5	48.3	9.6	0.10	0.10	2.676
252	51.4	9.9	48.5	10.8	0.12	0.13	2.636

Table 6.22. ZnCdSe X-ray and PL characterisation details. PL peaks were measured at 77K.

HWC138 comprises a thick ZnCdSe layer (expected to be ~650nm thick) grown on top of a ZnSe layer. The ZnCdSe layer was found to be fully relaxed (as expected) and therefore the thickness produced by XRI is unlikely to be

accurate. No PL measurements have been made of HWC138, so unfortunately the composition (Cd %) cannot be checked against the emission energy.

The bandgap of the three QW samples will again be different to the bulk material with the same composition. However, as was explained previously, it would be useful to be able to use SE to structurally characterise ZnCdSe QW samples so it is worthwhile trying these samples to determine its suitability.

The simplest way to model a ZnCdSe layer would be to use a BEMA composed of ZnSe and CdSe, as below the bandgap of both end compounds the dispersion should change smoothly as a function of composition. However above the bandgap this model would work less well, as more complex effects will occur such as the exciton peak energy shifts and band anti-crossing etc. This is particularly relevant here, as the bandgap of CdSe is  $1.65 \pm 0.05$  eV at 300K meaning that almost the entire range measured (1.55-5.3 eV) is above its bandgap and it is unlikely a BEMA will accurately model the dispersion of the ZnCdSe layers in these samples.

# HWC	Thickness (nm)				Cd%	MSE
	roughness	ZnSe	ZnCdSe	ZnSe		
138	5.3	-	656.1	25.8	6.3	68.1
250	4.0	44.1	67.8	0.0	2.7	10.0
251	5.0	33.0	78.9	0.0	3.1	9.9
252	5.0	44.0	25.4	46.8	4.5	10.8
Sum	19.3	121.0	828.1	72.6	16.6	98.8

Table 6.23. Model structural parameters for the ZnCdSe sample SE data with a ZnSe/CdSe BEMA.

Table 6.23 reports the results of using a ZnSe/CdSe BEMA to model the four samples, it shows that although the BEMA models the thicknesses of HWC138 and the ZnSe thickness of 252 reasonably accurately, it produces values that are very different to those expected for all the other thicknesses and Cd percentages. These differences are caused by the low contrast between the ZnCdSe and ZnSe layers, as HWC138 and 252 have cadmium contents >10% whilst HWC250 and 251 are not.

Using point inversion models for HWC250-252 based on the thicknesses in table 6.23 produces three distinct dispersion relations but the curves are again very noisy. As there are only three samples available, with different compositions, it is impossible to smooth these curves and produce accurate dispersion curves. However the Tauc plots of these models have transitions at 2.58, 2.54 and 2.51eV for HWC250-252 respectively, which are shifted from the PL peaks by 5, 16 and 26meV respectively.

Modelling HWC138 using a MO model based on ZnSe and the thicknesses in table 6.23 results in a good fit (not shown) but a cadmium content of 15.5%. The Tauc plot from this model shows a transition at 2.465eV, which represent a cadmium content of  $\sim 14 \pm 1\%$ . These composition figures are very different to that produced by the XRI modelling, but this could be due to the layer not being fully relaxed but instead having a  $\sim 15\%$  cadmium content and being  $\sim 50\text{-}60\%$  relaxed. However without a PL measurement to prove the layer composition it is impossible to prove this is the reason for the different composition figures.

#### **6.4.9. Zinc Magnesium Sulphur Selenide, ZnMgSSe**

Nine ZnMgSSe (QA) samples were investigated using SE. These samples are divided between the ZnSe and MgS rich, stable regions of the ZnMgSSe compositional space and are modelled separately. The four ZnSe rich samples (HWC225-228) will be analysed first, based on the ZnSe model produced in section 6.4.1. The MgS rich samples will then be modelled on the basis of the MgS work reported in section 6.4.3.

As was demonstrated in chapter 5, the growth of ZnMgSSe alloys potentially allows both the lattice constant and bandgap to be tuned over a very wide range and this is also true for the refractive index. The range of possible values is bounded by ZnSe at the high end and MgS on the low end (see fig 6.35). MgSe and ZnS have intermediate values and it should (at least below bandgap) be possible to model any QA dispersion data using either the ZnSe or MgS

dispersion curves produced previously. Above bandgap the dispersion of all four compounds will be different and this will affect the form of dispersion. However as all the QA produced at HWU have compositions close to ZnSe or MgS it should still be possible to model the dispersion of the QA throughout the entire energy range using the dispersion relation for MgS or ZnSe.

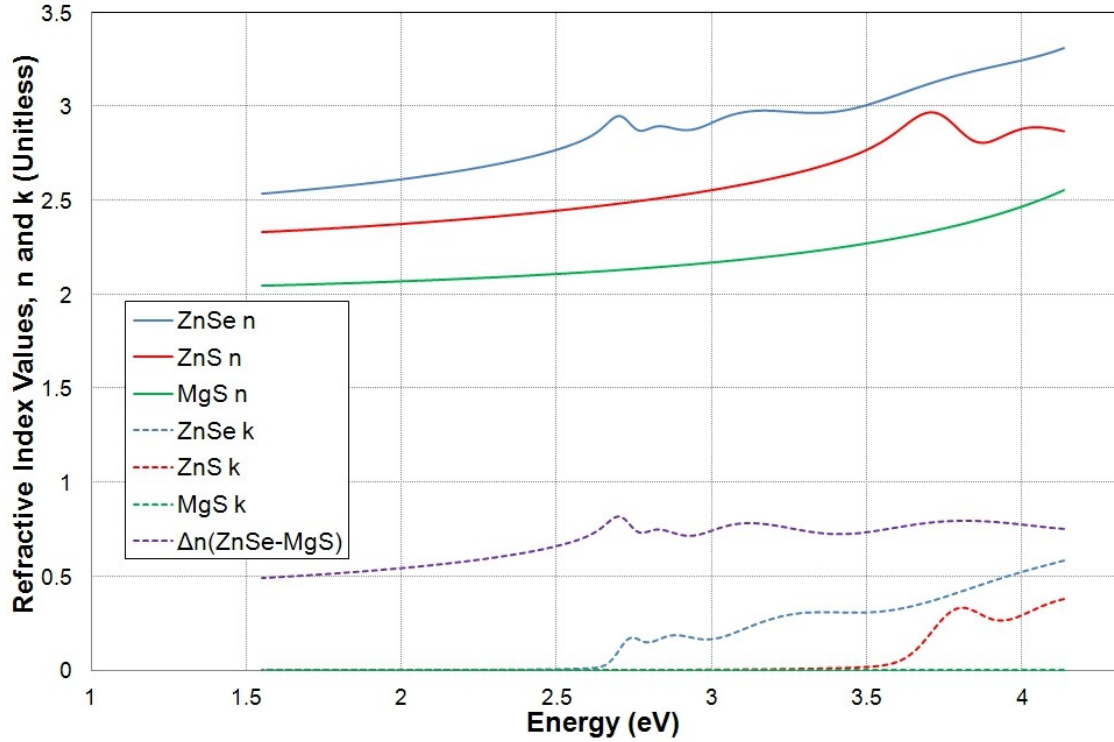


Fig. 6.35. Refractive index dispersion curves for ZnSe, ZnS and MgS. All the curves are based on the work presented in sections 6.4.1., 6.4.3. and 6.4.8. Refractive index difference,  $\Delta n$ , between ZnSe and MgS is also shown as this will be of importance in section 6.5.

#### 6.4.9.1. ZnSe rich ZnMgSSe

The structural characterisation of HWC225-228 was described in chapter 3 and will not be repeated here. All four samples are ZnMgSSe/ZnSe/GaAs structures. The layer thicknesses determined by both X-ray/PL characterisation and SE for the 4 samples are shown in table 6.24 along with X-ray GOF and SE MSE figures. A Cauchy relation based on ZnSe was used to model the QA layer in the region 1.55-2.75eV (450-800nm).



# HWC	X-ray/PL Characterisation			SE Characterisation			
	Thickness (nm)		GOF	Thickness (nm)			MSE
	QA	ZnSe		Roughness	QA	ZnSe	
225	74.4	37.4	0.127	4.76	89.36	20.9	4.76
226	375.9	24.9	0.105	6.06	376.9	25.3	16.55
227	268.1	20	0.094	7.1	264.1	27	5.327
228	130.4	22.9	0.098	17.4	136.9	20.7	4.165

Table 6.24. Structural data for low MgS QA samples from X-ray/PL and SE characterisation.

The SE modelling was straightforward as the initial Cauchy model parameters are based on ZnSe. The ZnSe buffer layer was initially chosen as 50nm and the QA thickness chosen to produce the correct number of n and k oscillations to match the measured data. The modelling software then refined the data to produce the thicknesses shown in table 6.24. The only drawback with this SE characterisation is that it doesn't generate any compositional information. Compositional information might be obtained by also considering the alloy's above bandgap dispersion and comparing it to those of ZnSe, ZnS, MgSe and MgS. However this will still not be as effective as using XRD/PL.

# HWC	Thickness (nm)			E0 (eV)	MSE	PL Emission (eV)
	Roughness	QA	ZnSe			
225	5.11	88.4	20.9	2.903	4.855	2.874
226	6.08	379.4	24.2	2.904	6.887	2.896
227	6.99	264.2	24.2	2.944	12.495	2.968
228	15.97	137.2	20.5	2.916	15.105	2.928

Table 6.25. Structural details generated by the MO modelling of HWC225-228. E0 transition from modelling and PL emission energies are also reported.

To model the entire measured range it is again necessary to use a more complex model. As HWC225-228 are all ZnSe rich QAs, their dispersion is close to ZnSe, and the easiest solution is to use the MO model developed for ZnSe in section 6.4.1. and then allow it to vary. The results are shown in table 6.25. The models typically had 5 or 6 oscillators at various energies. HWC225 for example has oscillator energies of 2.903, 3.330, 4.900, 5.384 and 9.123eV. The oscillator at 2.903eV represents E0, the bandgap of the alloy layer.

The dispersion relations for the QA layers all follow the expected trend with the refractive index decreasing as the bandgap of the alloy increases. The measured and modelled data for HWC225 and the MO modelled dispersion of the QA layer and ZnSe for comparison are shown in figure 6.36.

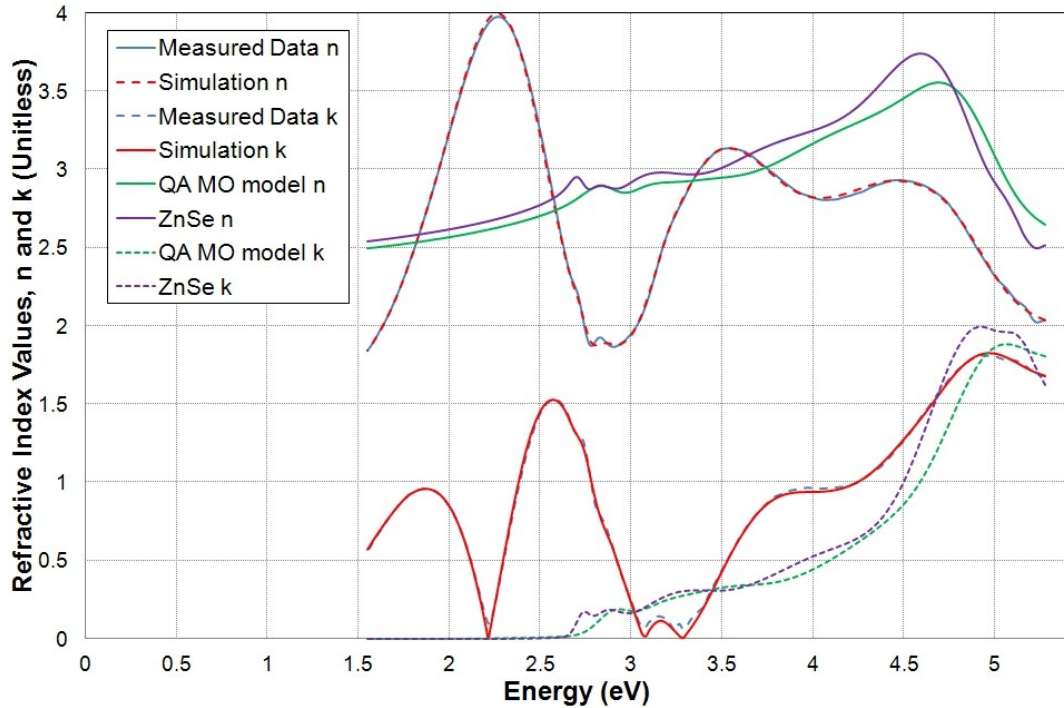


Fig. 6.36. Measured and modelled SE data for HWC225. The MO generated dispersion curves for the QA layer and ZnSe dispersion curves, for comparison, are also shown.

#### 6.4.9.2. MgS rich ZnMgSSe

Four MgS rich QA XRI/XRD samples taken from the three sets of QA samples discussed and characterised in chapter 5, were investigated using SE. The layer thicknesses determined by X-ray and SE analysis are shown in table 6.26. The main purpose of this section is to measure the refractive index of the QA samples so that their use in DBR structures can be evaluated. As such the modelling focuses on the below bandgap region, which enables simple Cauchy relations to be used for the samples.

The initial thickness values used for the SE modelling were taken from the X-ray analysis and the Cauchy parameters from the MgS work in section 6.5.3., but all the values were allowed to vary over a large range. The modelling covered the region 1.55-4.13eV, as the bandgap of all the alloys was expected to be greater than 4.13eV.

# HWC	X-ray Characterisation					SE Characterisation				
	Thickness (nm)			GOF		Thickness (nm)				MSE
	ZnSe	QA	ZnSe	004	115	Roughness	ZnSe	QA	ZnSe	
167	51.4	15.8	50.6	0.118	0.080	6.71	54.1	10.9	59.4	13.5
298	48.0	4.9	48.6	0.116	0.118	4.62	48.0	3.0	52.4	11.8
302	42.2	8.9	43.0	0.105	0.063	3.62	41.3	7.9	46.1	15.4
340	53.2	8.7	60.0	0.101	0.108	4.12	59.0	8.5	57.0	12.6

Table 6.26. X-ray and SE characterisation details for the high MgS fraction QA samples. The values the show a large (>10%) difference between x-ray and SE are highlighted in red.

Figure 6.37 shows the dispersion of the QA samples, ZnSe and MgS. All the QA curves fall between the ZnSe and MgS, as expected. As the samples are known to have compositions in the range  $x=0.85\pm0.10$ ,  $y=0.67\pm0.04$  (see Chapter 5), the form of the dispersion is realistic. The increase in the refractive index at higher energy suggests that the samples are approaching their bandgap.

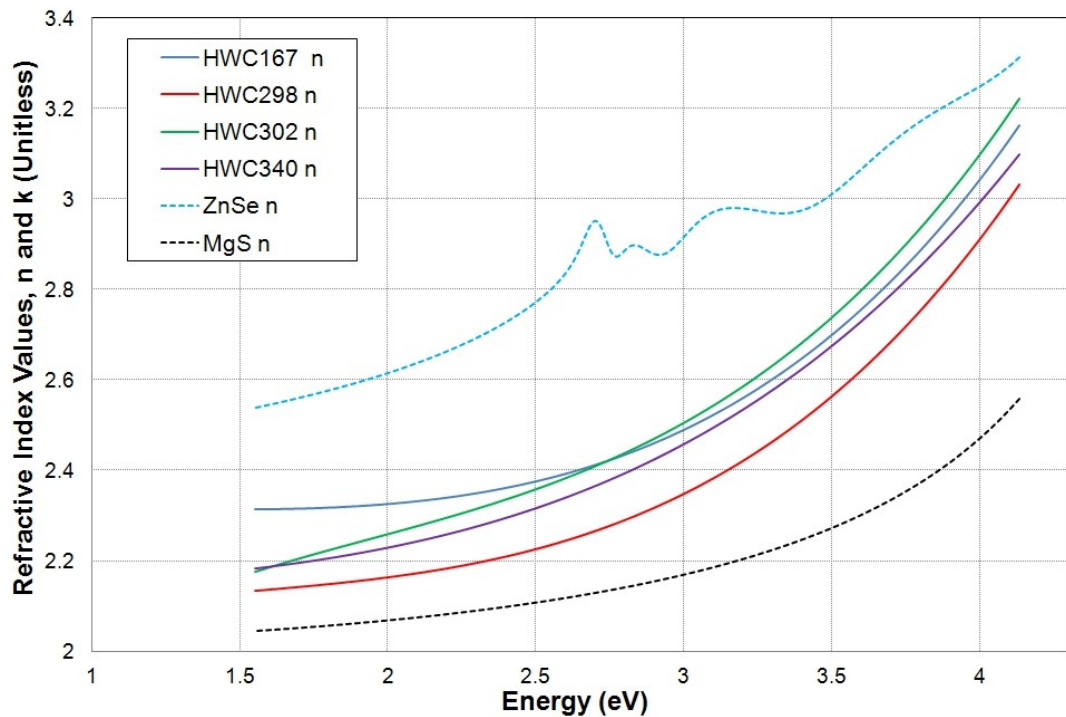


Fig. 6.37. Refractive index dispersion relations for the High MgS fraction QA samples, ZnSe and MgS.

To model the entire measured energy range an SEO model was used and the models generated are shown in figure 6.38. All four refractive index curves are realistic although HWC298 and 340 are higher than expected. The absorption curves are not as sharp as expected for a semiconductor, but this is caused by the SEO modelling rather than being a particular feature of the QA dispersion. All the ZnSe thicknesses are similar to those from the Cauchy modelling, but

there are differences in the QA thicknesses. In particular HWC302 has a predicted QA thickness of 4.97nm which is roughly 50% the thickness expected and comparable to 298, which is was grown for half the time.

Attempts to produce more accurate models for the QA samples were unsuccessful. Adding additional oscillators to the SEO model in order to convert it to a MO model, resulted in unrealistic dispersion curves and the use of PI again produced very noisy dispersion curves. Therefore further analysis of the alloys dispersion cannot be performed at present.

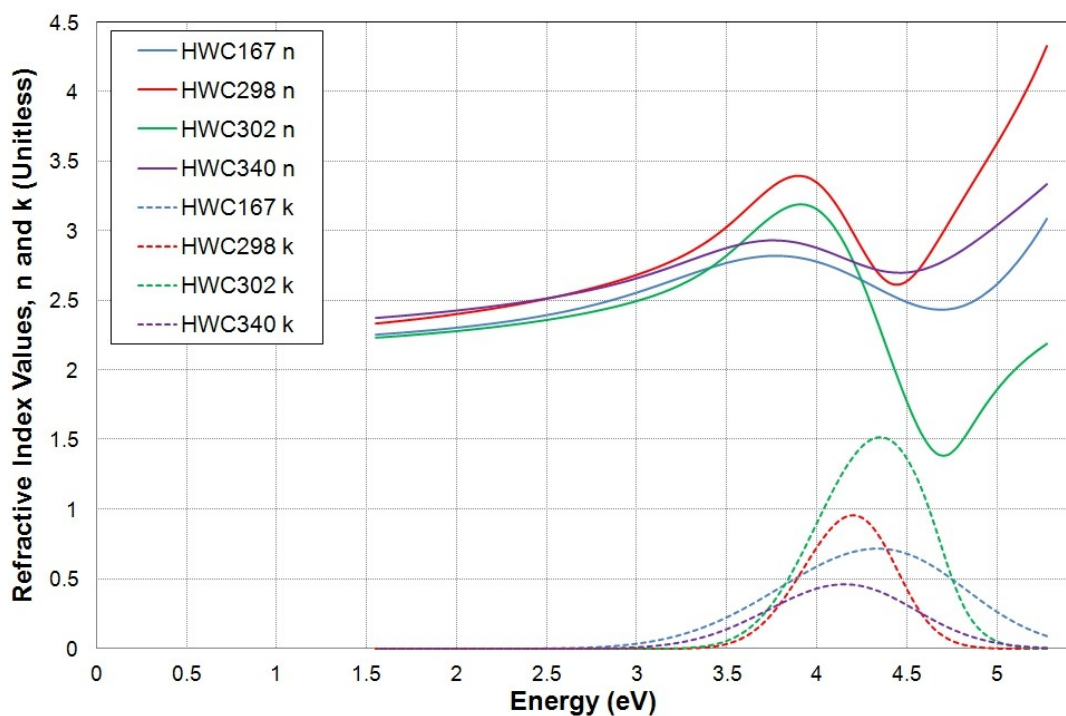


Fig. 6.38. SEO modelled dispersion curves (n and k) for the 4 QA samples.

## 6.5 Distributed Bragg Reflector (DBR)

As mentioned in the introduction, making effective DBRs with II-VI materials is challenging. In this section DBR designs based on the refractive index measurements made previously are evaluated to show that although the range of materials available in II-VI epitaxy severely limits the production of a high quality DBR, it is possible.

The growth of a DBR requires pairs of high and low index materials which must

be grown together without introducing sufficient strain energy for relaxation, as this introduces dislocations which will increase the optical losses in the DBR and any structures grown on them. At HWU the obvious pair of materials to produce a DBR are ZnSe and MgS, as these are both closely lattice matched to GaAs and possess high and low refractive indices ( $\sim 2.7$  vs.  $2.1$  at  $500\text{nm}$ ). However in section 6.5.1. it is shown that their lattice mismatches are such that ZnSe/MgS DBRs will relax

There are a number of ways to resolve this but all require that ZnSe, MgS or both are replaced with either a ternary or quaternary alloy. For a number of reasons, the solution chosen here (and described in section 6.5.2.) is to replace MgS with an MgS rich QA.

#### **6.5.1. MgS/ZnSe DBR**

Figure 6.28 shows the MgS refractive index measured by SE. At  $500\text{nm}$  it is  $2.055$  and a  $\lambda/4$  thick layer is therefore  $60.8\text{nm}$  thick. Figure 6.19 shows the dispersion of ZnSe and at  $500\text{nm}$  the refractive index is  $2.763$  and a  $\lambda/4$  thick layer is  $45.2\text{nm}$  thick. The Fresnel reflection at each interface between the 2 layers is  $2.16\%$ . Figure 6.39 shows the reflectivity from a ZnSe/MgS DBR stack and the total reflectivity of a DBR grown on GaAs with either a  $\lambda/2$  or  $\lambda/4$  thick ZnSe buffer layer [6.46] (which is necessary as the growth of ZB-MgS directly onto GaAs is not possible [6.103]).

To achieve an overall reflectivity of  $99\%$  (easily available from a cheap commercial DBR) requires 8 pairs of  $\lambda/4$  thick ZnSe and MgS layers and for a  $99.9\%$  reflectivity (the typical reflectivity of a laser high reflector) requires 12 pairs. Figure 6.39 also shows that at high reflectivities ( $>95\%$ ) the presence of either a  $\lambda/2$  or  $\lambda/4$  thick buffer layer has limited effect on the structures overall reflectivity.

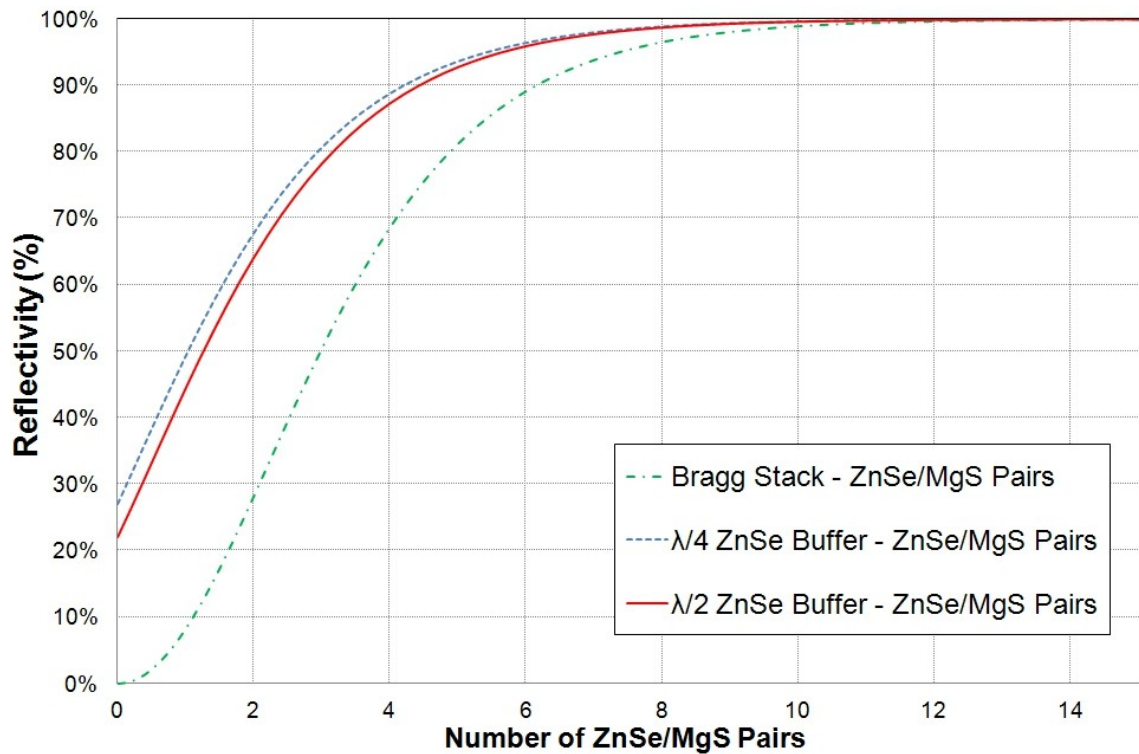


Fig. 6.39 DBR reflectivity vs. the number of ZnSe/MgS quarter wavelength pairs.

Figure 6.40 shows the strain-thickness product for a DBR composed of eight pairs of MgS and ZnSe with a  $\lambda/2$  buffer layer grown on GaAs. After two pairs the structures strain-thickness product exceeds the critical strain-thickness value. Subsequently the structure will begin to relax and by the 8<sup>th</sup> MgS/ZnSe pair it is likely the structure is almost totally relaxed. This will both generate high dislocations densities and cause surface roughening and possibly make the growth of ZB-MgS impossible. MgS/ZnSe based DBRS are therefore limited to ~3 pairs before the strain become too high, a maximum reflectivity of 80%.

It is possible to increase the maximum to 4 pairs before relaxation occurs by increasing the ZnSe layers thickness from  $\lambda/4$  to  $3\lambda/4$ . However the ZnSe layers would be 135.6nm thick and with a strain-thickness product for each layer of -0.377, close to the relaxation limit for an individual layer.

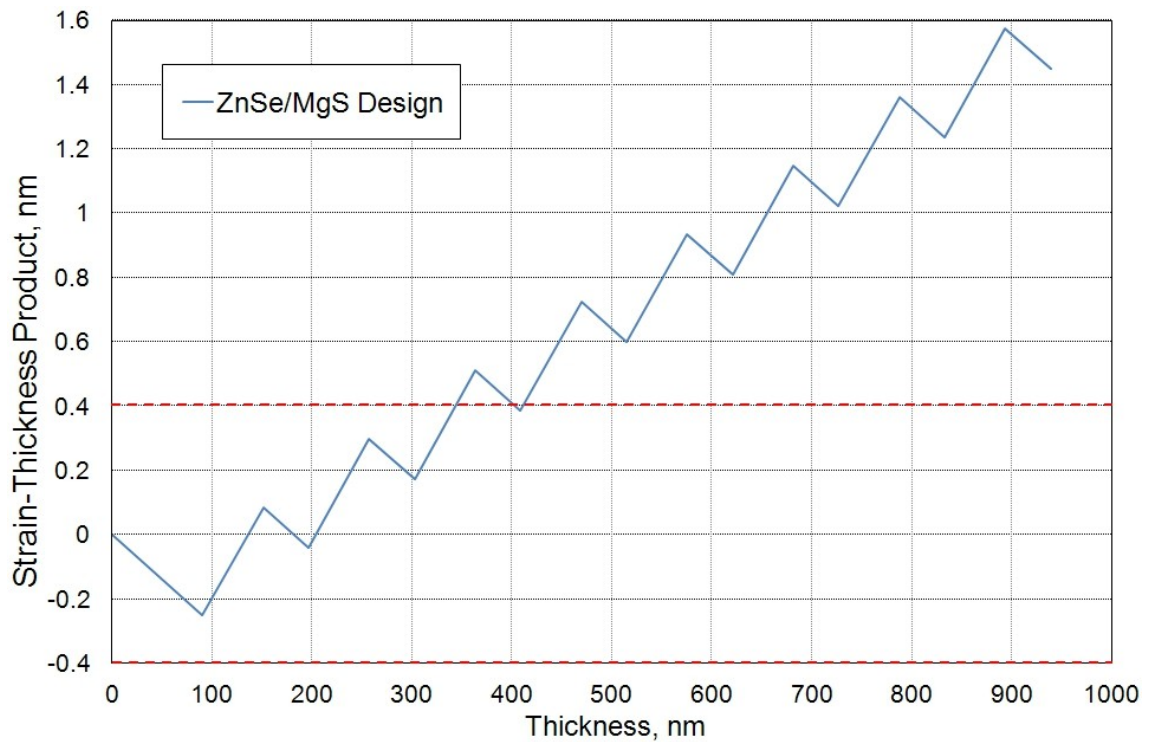


Fig. 6.40. ZnSe/MgS DBR design strain-thickness product vs. thickness plot. Red dotted lines show the  $\pm 0.4$  critical strain-thickness boundary.

### 6.5.2. QA/ZnSe DBR

Figure 6.37 and 6.38 show the dispersion of the MgS rich QA determined by Cauchy and SEO modelling. Averaging the values of all the alloys at 500nm produces a refractive index of  $2.38 \pm 0.1$ . All of the alloys produced are stable in air, so it should be possible to produce an alloy with a desired lattice constant and a refractive index of  $\sim 2.28$ . A  $\lambda/4$  thick layer would therefore be 54.8nm thick. This results in a reduced Fresnel reflection at each interface of 0.92% (vs. 2.16% achieved with the MgS/ZnSe pairs), but it is possible to achieve a similar total reflectivity by introducing additional pairs, as can be seen from fig. 6.41.

To achieve a reflectivity of 99%, 12 pairs of  $\lambda/4$  thick, QA/ZnSe layers are necessary. Each ZnSe layer has a strain-thickness product of  $-0.126\text{nm}$ . To symmetrise this each QA layer needs a product of  $+0.126\text{nm}$  and as the QA layers are 54.8nm thick, a lattice constant of  $5.6416\text{\AA}$ .



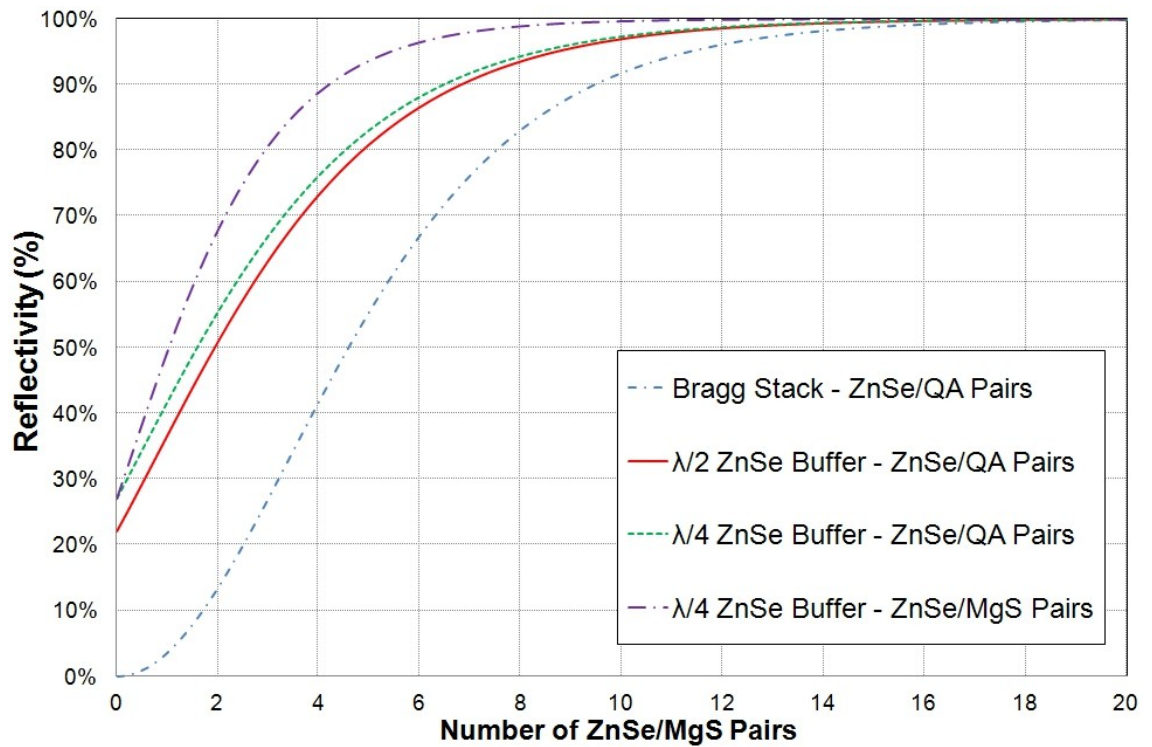


Fig. 6.41. DBR reflectivity vs. number of ZnSe/QA pairs.

Figure 6.42 shows the strain-thickness product vs. thickness plot for a DBR with 12 pairs of ZnSe/QA layers. If the QA mismatch stays constant it is possible to grow a very large number of QA pairs without the structure relaxing. However as was discussed in chapter 5, it is extremely difficult to accurately control the composition of a QA during growths and as the growth of the DBR shown in figure 6.42 would at take 3-5hrs it is likely the composition would change. This means it is important to determine what range of compositions would allow the desired structure (12 pairs of ZnSe/QA layers) to be grown. This is demonstrated in figure 6.42. Changes in composition will also change the QA layers  $n$ , but these changes will be much smaller than the change in strain.

The green lines in figure 6.42 represent the maximum and minimum QA lattice constants possible that still allow 12 pairs of layers to be grown. They are 5.6371Å and 5.6424Å, so any alloy with a lattice constant inside this range will allow 12 pairs to be grown before the structure exceeds the critical strain-thickness value. This range of lattice constants is approximately a  $\pm 1.2\%$  variation in either  $x$  or  $y$ . Although this is quite a small range, with care the composition of the alloy can be kept within it, as it represents a 1-2 degrees change in cell temperatures.



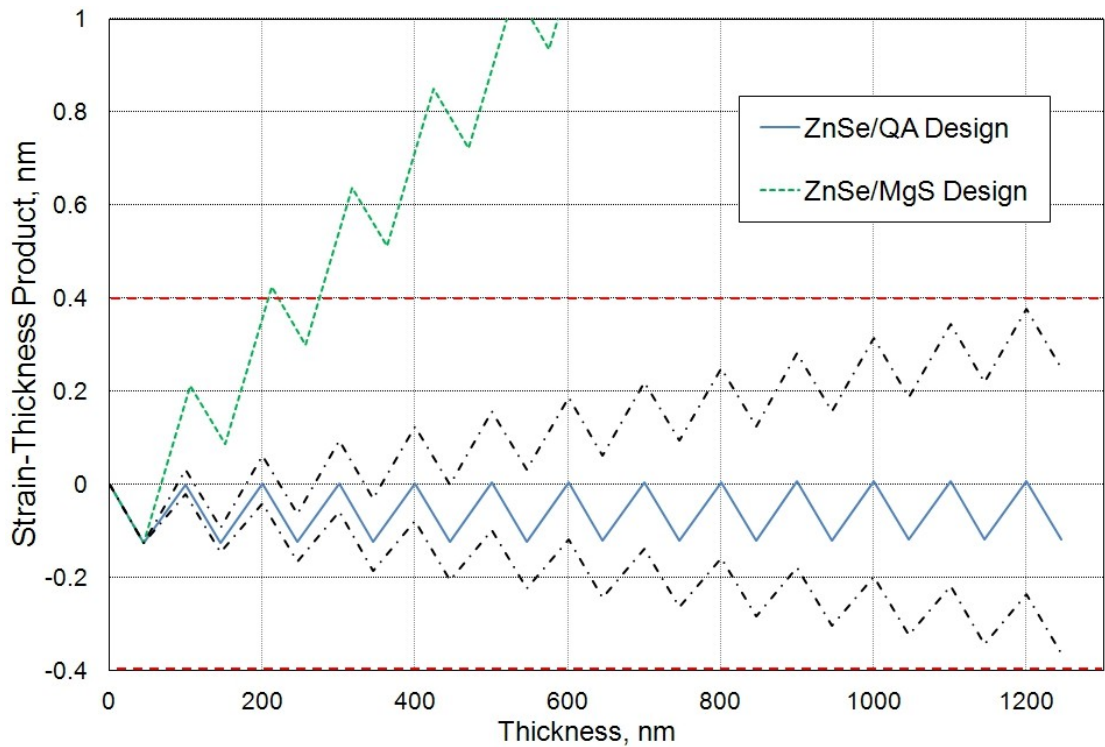


Fig. 6.42. ZnSe/QA DBR design strain-thickness product vs. thickness. Green line shows the MgS/ZnSe design for comparison. Black dashed lines show the minimum and maximum QA composition/mismatches to allow the full 12 pairs to be grown without relaxation.

A more significant problem would be the reproducibility of the QA composition between growths as the cells empty. However without attempting to grow trial DBR structures it is impossible to determine whether or not the regular production of the effective DBRs is possible.

## 6.6. Conclusions

This chapter reports a large number of measurements to characterise the optical properties of the various materials that the MBE group at HWU produces. As such it will be easiest to conclude and suggest further work (where applicable) for each section independently.

### 6.6.1. ZnSe PL/Bandgap Measurement

The PL emission from thin (~50nm) fully strained and thick (~1450nm) fully relaxed ZnSe samples was measured. The thin strained layer PL emission at 77K was dominated by the heavy hole emission at 2.795eV (equivalent to

2.673eV at 300K/2.810eV at 4K) and showed both band to band emission and LO phonon replicas of the exciton peaks. The relaxed layer PL spectrum was dominated by emission from a neutral donor bound exciton at 2.789eV at 77K. However free exciton, band-to-band and exciton LO phonon replicas were also seen. Measurements from both the thick and thin layers allow the exciton binding energy to be determined as  $18.1 \pm 0.3$  eV and the LO phonon energy as  $31.7 \pm 0.3$  meV and these both match values from the literature closely [6.55, 6.60, 6.61, 6.63-6.65].

Transmission measurements were made at 300K of a 50nm thick layer of ZnSe deposited on glass. This showed two transitions at 2.560 and 2.651eV. The 2.651eV is due to the band-edge of ZnSe. However the 2.560eV emission has not been identified. The ZnSe band-edge showed a Stokes shift of 32.2meV which is extremely close to the LO phonon energy measured from the PL, suggesting that the deposited layer was of a very high quality,

#### **6.6.2. CdSe PL**

Samples containing thin CdSe layers deposited on MgS (to avoid intermixing) were measured at 77K and showed both QW and QD emissions. By modelling the QW emission a bulk (but strained) layer bandgap for ZB-CdSe of  $1.65 \pm 0.05$  eV at 300K was determined.

#### **6.6.3. ZnCdSe PL and Bowing Parameter**

The PL emission from ZnCdSe QW and thick layers samples was measured and combined with the PL data for ZnSe and CdSe to give a bowing parameter for the ZnCdSe ternary alloy of  $0.37 \pm 0.05$  eV. This figure is consistent with the range of figures commonly published in the literature (0.3-0.5eV) but is one of the few attempts to measure samples across the entire compositional range. It should therefore be more accurate than those reported previously.

#### **6.6.4. Reflectometry**

The use of XRD and reflectometry was reviewed and XRD found to be inaccurate when used to determine the thickness of relaxed layers. Combining the relaxation (lattice constant) data from by XRD with the thickness information from reflectometry gave the relaxation vs. thickness graph for ZnSe. This was modelled using the Dunstan geometrical model [6.77] and showed a hyperbolic dependency with a critical thickness of ~150nm and a residual strain of -0.07%.

#### **6.6.5. Spectroscopic Ellipsometry**

A large number of samples were investigated using SE, so again it will be easiest to conclude about each set individually. However some comments can be made about the types of structure that are best for the investigation of the dispersion of these materials. Below bandgap, both XRI and AFM structures give useful refractive index data. However above bandgap, the dispersion is more complicated and the behaviour of a central layer in XRI structures is often masked by its cladding. Although this does not mean that XRI samples cannot be used for SE characterisation, it does suggest that in future samples with a thin (<10nm) capping layer would be better with the capping material chosen so its dispersion does not overlap that of the material underneath.

##### **6.6.5.1. ZnSe**

A large number of ZnSe OG samples were investigated and behaved like those reported in the literature [6.21-6.26]. However after analysis, including looking at samples with a ZnSe layer buried under other materials, it was found that the majority of the reported dispersion curves for ZnSe appear to under-estimate the effect of the native oxide layer/surface roughening. An improved ZnSe dispersion curve was produced and this showed an improved fit to all the SE data measured for ZnSe containing samples when compared to those taken from the literature.

##### **6.6.5.2. ZnSe Native Oxide Layer**

The oxide layer formed on ZnSe was investigated by modelling and chemical etching and annealing, and found to be consistent with the reported composition of ZnO, SeO<sub>2</sub> and elemental selenium. The amount of selenium decreased slowly with time, consistent with the oxidation to SeO<sub>2</sub>. Attempts to accurately model the oxide layer using the dispersion relations for ZnO and amorphous selenium produced results only marginally better than a surface roughening layer alone, this is most likely due to the lack of a dispersion curve for SeO<sub>2</sub>.

#### 6.6.5.3. ZnS

A single sample consisting of a thick layer of ZnS grown on GaP was analysed. It was modelled well by the published ZnS dispersion relations [6.86] but produced a far higher growth rate than expected, 3Å/s. An improved MO model was produced for the ZnS layer but insufficient samples were available to accurately determine whether this represents a better model of the ZnS dispersion or not.

#### 6.6.5.4. ZnSSe

The X-ray modelling of ZnSSe samples showed that the layers were relaxed, with a graded composition. The SE data from the samples could be well modelled by a BEMA consisting of ZnS and ZnSe across the entire range. SE modelling worked extremely well for these samples as they were uncapped and the majority of the measured energy range was below their bandgap.

#### 6.6.5.5. MgS

A number of dispersion curves were generated for MgS. Of these the one generated by averaging the point inversion models for a series of AFM samples produced a realistic dispersion curve for the region 1.55-5.28eV. This dispersion curve showed a transition at  $5.20 \pm 0.02$  eV. Repeating with a more accurate ZnSe oxide model produced a nearly identical result but with a band-edge of  $5.15 \pm 0.02$  eV. Combining both gives a bandgap for MgS of  $5.17 \pm 0.05$  eV.

#### 6.6.5.6. MnS

MnS samples again produced high quality data. The below bandgap region was modelled using a Cauchy model and when constrained to realistic values of  $n$  and  $k$  produced extremely useful information about the MnS layer thickness. This, in combination with XRI/XRD and TEM, allowed the growth rate of these samples to be re-evaluated and this was found to be correlated to the manganese cell temperature more strongly than to the measured flux, suggesting that the measurement of the manganese flux using an ion gauge is more complicated than was previously thought.

#### 6.6.5.7. CdSe

ZnSe/CdSe XRI samples were measured and modelled to produce highly realistic dispersion curves for the CdSe layer. QD emission was seen in the samples PL but this did not cause problems with the SE measurements.

#### 6.6.5.8. ZnCdSe

ZnCdSe samples were investigated and produced high quality data. Attempts to model this data with a BEMA based on ZnSe and CdSe, so that compositional data could be extracted were unsuccessful. However the data could be accurately modelled using a MO model based on ZnSe and showed transitions at roughly the energy of the PL emission from the samples.

#### 6.6.5.9. ZnMgSSe

MgS and ZnSe rich QA samples were investigated. The ZnSe rich samples were all uncapped thick layers and were efficiently modelled using MO models based on ZnSe. This allowed their band edge to be determined accurately but did not produce any compositional data. The MgS rich samples were predominantly XRI structures and were modelled using Cauchy relations below

the bandgap and SEO model above bandgap. Both models produced realistic dispersion data and the transitions seen in SEO models were as expected for the composition of the QA.

#### **6.6.6. DBR**

Two DBR designs were discussed based on ZnSe/MgS and ZnSe/QA. The ZnSe/MgS design was simulated to be 99% reflectivity with 8 pairs of layers but is too strained causing it to relax, which should degrade its optical quality. The ZnSe/QA design needs 12 pairs of layers to produce 99% reflectivity, and is feasible if the QA composition can be calibrated and kept within a  $\pm 1.2\%$  compositional window in terms of x and y.

## 7. $\mu$ -PL Characterisation of CdSe Quantum Dots Grown on an MgS rich ZnMgSSe Barrier

This chapter reports the work undertaken to optically characterise a series of samples containing CdSe quantum dots grown on MgS rich ZnMgSSe barriers. The characterisation comprises both 77K ensemble PL and 4K  $\mu$ -PL measurements performed using the PL and confocal PL microscope setups described in the experimental techniques chapter.

The ensemble PL shows that the dots grown on the QA have similar emission spectra to those grown on either ZnSe or MgS barriers. The 4K  $\mu$ -PL spectra showed a large number of sharp peaks which all experienced jitter (spectral diffusion) on a timescale of  $<25\text{ms}$ . By looking at the correlation of the variation of the peaks energies and intensities they can be assigned to individual dots and the number of dots within the resolved spot of the microscope determined. This was found to be consistent with a QD density of  $4\pm1\times10^{10}\text{ cm}^{-2}$ .

A number of power-scaling measurements were also made and used to identify the various emission lines (exciton, biexciton etc.). These suggest a biexciton binding energy,  $E_B^{\text{xx}}$ ,  $24.5\pm1.5\text{ meV}$  and a trion (charged exciton) binding energy,  $E_B^{\text{cx}}$ , of  $23\pm3\text{meV}$ . They also provide information about the process that drives the jitter present in the dots emission. The possible mechanisms behind this jitter are also discussed and compared with the experimental data.

Finally the work will be concluded in section 8.6 and suggestions for further work suggested.

## 7.1. Introduction

Self-assembled quantum dots (SAQD) have been a highly active area of semiconductor research for a number of years due to their interesting physical properties and the prospect of dramatic device performance improvements through their use [7.1, 7.2]. With II-VI semiconductors there are a number of material combinations that will result in the formation of SAQD – for example CdSe on ZnSe, CdS on ZnSe, CdS on ZnSSe or ZnTe on ZnSe [7.3-7.5]. Of these, the growth of CdSe on ZnSe is the most highly developed due to the material combinations major advantage of utilising widely available GaAs wafers.

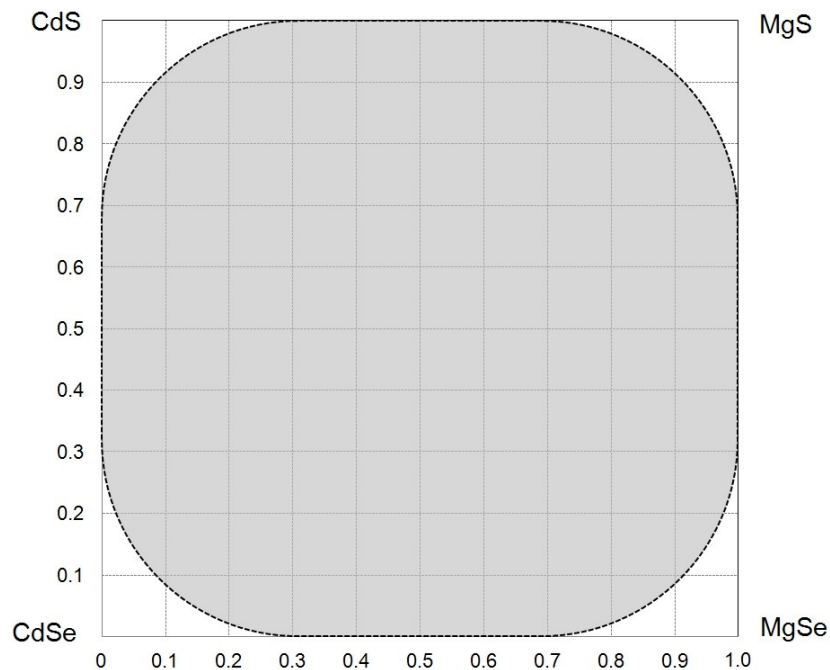


Fig. 7.1. Schematic of the CdMgSSe composition space, showing the large spinodal decomposition region (the grey shaded region). Compared to the ZnMgSSe composition space diagram in chapter 5, fig. 5.2, the spinodal decomposition region is much larger here.

The MBE group at HWU have previously investigated the CdSe/ZnSe system and CdSe QDs grown on MgS [7.3, 7.6]. The dots grown on MgS have been found to behave in a similar manner to those grown on ZnSe. This was unexpected, as it was anticipated that the emission from individual dots would be substantially sharper due to the reduction in intermixing arising from the large immiscibility region of the CdMgSSe compositional space, see fig. 7.1, and the increased confinement provided by the MgS barriers [7.6].



As already explained in this thesis, we have developed an ELO technique that utilises MgS as a sacrificial layer and a series of ZnMgSSe alloys (QA) to act as a replacement barrier in ELO structures [7.7]. As part of this development work a series of CdSe QD samples were grown with QA barriers both to allow the evaluation of their behaviour, and to ensure that it was possible to integrate CdSe QDs into future ELO structures. Part of the motivation in developing this material system is to eventually integrate CdSe dots into micro-cavities to allow their optical behaviour to be fully investigated as a step toward creating a possible room temperature polariton source [7.8].

Previously other groups have grown CdSe QDs on ZnMgSSe [7.9]. However the alloys used were all in the ZnSe rich region of ZnMgSSe and therefore the results presented here are the first for CdSe QDs grown on an MgS rich ZnMgSSe alloy. As such a comparison between these dots and those grown previously on ZnSe and MgS will be presented in an attempt to both further understand the broad emission lines seen from the dots grown on MgS and to try to understand the evolution of the interaction between the CdSe layer and the barrier material as a function of barrier composition.

## 7.2. Growth

The samples described in this chapter were all grown using our standard growth procedure. All the layers, except the QDs, were grown by conventional MBE at 250°C. The QDs were grown by atomic layer epitaxy (ALE) again at 250°C using 8 second deposition cycles of Cd and Se with a 2 second pause between cycles, and were then annealed for 4 minutes at 310°C to thermally activate the dot formation process [7.10].

The structure of the samples is shown in figure 7.2 and the specific growth conditions are detailed in table 7.1. The QA used in the growth of these samples was designed to be the same composition as samples HWC 167, 178 and 180 previously characterized as having a composition  $\text{Zn}_{1-x}\text{Mg}_x\text{S}_y\text{Se}_{1-y}$  with

$x=0.82\pm0.07$  and  $y=0.87\pm0.05$  and a bandgap of 4.2eV at 300K (4.35eV at 4K). None of the samples are capped with ZnSe, as this ZnMgSSe alloy has been found to resist oxidation sufficiently to protect them [chapter 4, 7.11, 7.12].

QA ~ 10-15nm
CdSe – 7/9/11 cycles
QA ~ 10-15nm
ZnSe – 36nm
GaAs Substrate

Fig. 7.2. Schematic of the structure of QA QD samples.

All of the samples were monitored with RHEED throughout the growth. The ZnSe buffer layer for all the samples showed a strong and streaky 2x1 pattern, as expected. During the growth of the first ZnMgSSe barrier layer both a c(2x2) and a 2x1 RHEED pattern was observed. This is typical during the growth of this material [7.13].

The CdSe dot layers initially showed a weak 2x1 pattern which converted into a series of spots during thermal activation. The final upper ZnMgSSe barrier showed a spotty pattern initially, but after a short time (~30 seconds) both faint c(2x2) and 2x1 RHEED patterns were again seen. By the end of the QA layer growth the RHEED pattern had strengthened and become streakier.

# HWC	Zn:Se Ratio	Cd:Se Ratio	QA Barrier Thickness (nm)	ALE Cycles
223	0.67	0.38	10	11
224	0.70	0.39	15	9
236	0.40	0.36	10	7

Table 7.1. Growth conditions and structure of the QA QD samples.

### 7.3. Ensemble PL Characterisation

Ensemble PL measurements were made of the first two samples (HWC223 and 224) using our original PL setup (Argon ion laser and PMT detector). The spectra obtained are shown in figure 7.3 and show a broad peak centred at

~2.5eV from the CdSe QDs which is similar to the emission from dots grown on ZnSe or MgS barriers [7.14-7.16]. There is also a smaller peak at ~2.79eV arising from emission from the ZnSe buffer layer.

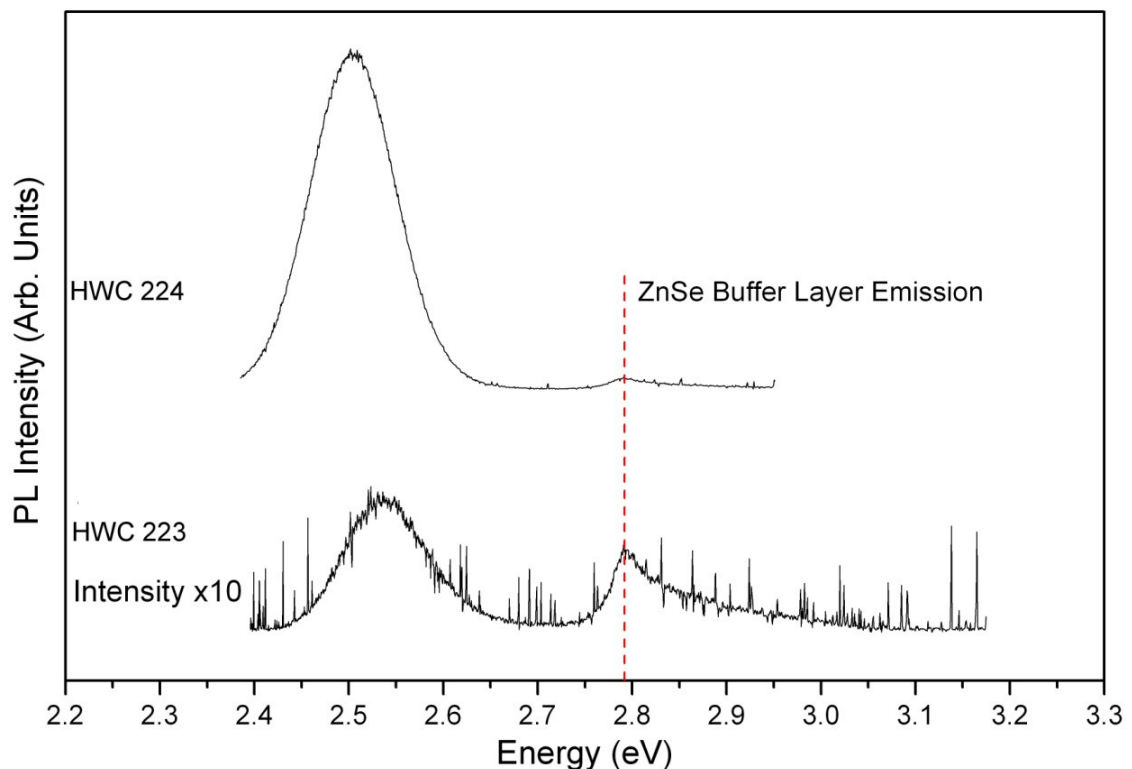


Fig. 7.3. Ensemble 77K PL measurements of CdSe/ZnMgSSe QD samples. Red dotted line shows position of ZnSe emission at 77K. The low intensity of the emission from HWC223 is the source of the noise.

HWC236 was investigated using the  $\mu$ -PL confocal microscope system at 77K, see fig.7.4. The  $\mu$ -PL system has a much higher resolution (imaging a spot ~300nm in diameter compared to the ensemble PL systems ~1 $\mu$ m spot [7.17]) and will therefore excite a much smaller number of dots. The dot densities in these samples are high (a figure of  $\sim 4 \times 10^{10}$  per  $\text{cm}^2$  is obtained later). In addition, at 77K the emission peaks are found to be much broader than that seen at 4K, due to the thermalisation of carriers from the highly localised QD states [7.18]. As a result the measured spectra form an ensemble spectrum similar to those from the normal PL system.

None of the samples show an obvious wetting layer (WL). However the long tail on the high energy side of the ZnSe buffer layer peak in HWC223's spectrum

could represent emission from a WL. Alternatively, the WL may be thin enough that it emits at a higher energy than measured see fig. 6.11 in chapter 6

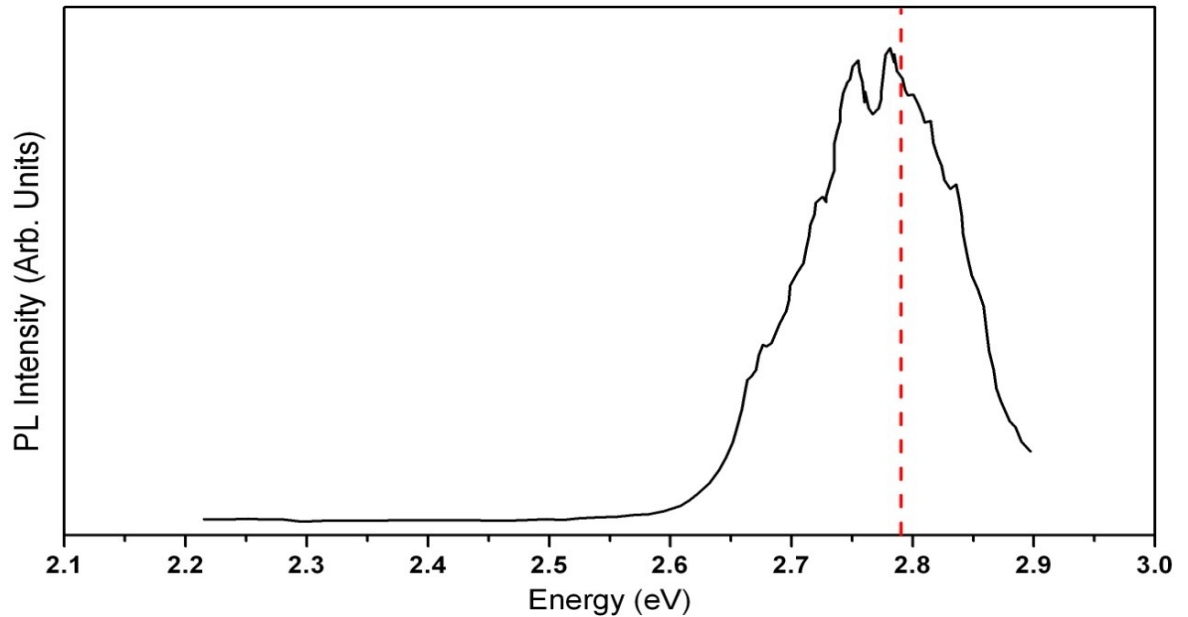


Fig. 7.4. 77K ensemble PL from HWC236 taken using the confocal microscope setup. The red line shows the position of the ZnSe peak at 77K,  $\sim 2.79$  eV.

The intensity of the PL emission from these samples is significantly lower than that typically observed for CdSe quantum dots samples with ZnSe barriers, by a factor of approximately 500. This is due in part to the reduction in absorption cross section caused by changing from ZnSe to QA barriers, as the MgS rich ZnMgSSe alloy has a bandgap  $\sim 4.2$  eV at 300K (estimated to be  $\sim 4.3$  eV at 77K) which is far larger than the incident photon energy. As a result it will be transparent at the pump wavelength (351 or 405nm) and hence only the CdSe containing layer (and the buffer and substrate) will absorb incident photons.

The absorption of the 0.5-1.5nm thick CdSe layer can be estimated using the extinction coefficient values of CdSe and gives a value of between 0.5-1.5% depending on the layer thickness [7.19, 7.20]. There will also be a small additional effect due to the absorption of the light re-emitted by the ZnSe layer below, however this is likely to contribute at most an additional 0.5% to the absorption.

In comparison the 100nm combined thickness of the ZnSe barriers in a typical QD sample would absorb ~60% of the pump light. Some of this will of course be lost to the GaAs substrate rather than the CdSe QDs but even assuming only 75nm (the top barrier and half of the lower barrier) provide carriers, it would still be an increase of 50-100 times in the absorbed flux.

No samples with MgS barriers were measured under the same conditions, so it is impossible to determine their relative emission intensity. However an estimate can be made from spectra taken previously under similar conditions. In this case a sample with MgS barriers and 3.5 ML of CdSe produced an emission intensity approximately 7 times greater than the samples with QA barriers, as shown in figure 7.5. This is far closer to the intensity expected, considering the reduction in the absorption experienced by moving from ZnSe to MgS barriers. And suggests that there must be an additional factor causing the reduction in emission intensity from the samples studied here.

Comparing the PL spectra from HWC 223, 224 and 236 to CdSe QDs with MgS barriers grown at HWU, fig. 7.5, we can see that the dot emission in the new samples is at a higher energy compared to QDs in HWA1352, 1346 & 1357. This suggests that the dots in the new samples may be smaller than those in fig. 7.5.

As HWC223, 224 and 236 had 11, 9 and 7 CdSe ALE cycles respectively they can contain a maximum of 5.5, 4.5 and 3.5 mono-layers (ML) of CdSe. However it seems unlikely that 0.5 ML has been deposited per cycle, as looking at fig. 7.5 and assuming similar behaviour for dots grown on QA, it would suggest these samples have between 2 and 4ML. This may also possibly explain the lack of an observed emission from a WL (assuming one is present), as a CdSe layer <3ML would have a bandgap of >3eV, outside the energy range measured.

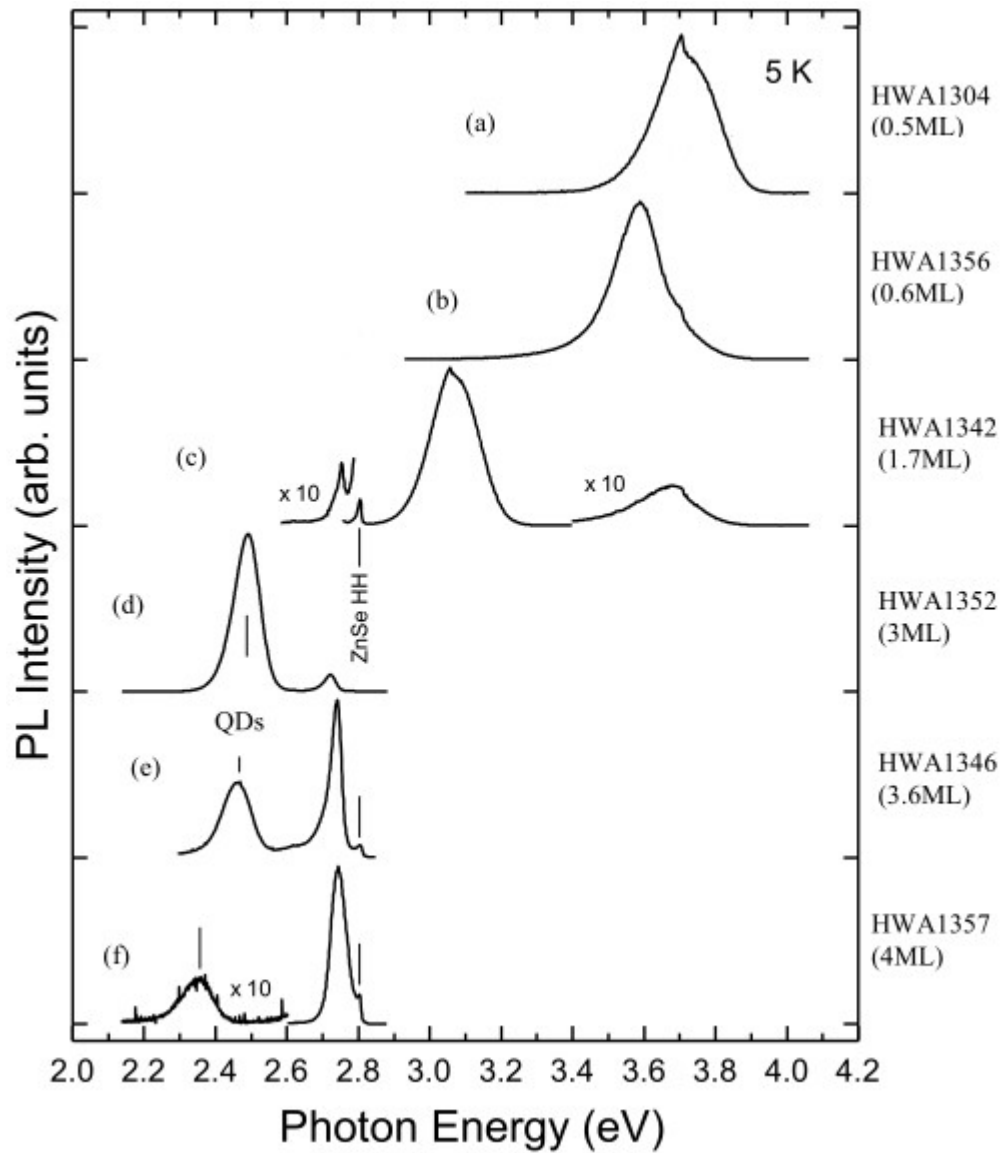


Fig. 7.5. Photoluminescence spectra for a series of CdSe/MgS samples, taken from ref. [7.15], demonstrating the variation of the emission with increasing Cd deposition.

#### 7.4. $\mu$ -PL Characterisation

$\mu$ -PL measurements were obtained from HWC223, 224 and 236 at 4K using the confocal microscope system [7.17]. For the majority of the measurements made, the excitation intensity was the maximum available,  $1.4 \text{ MWcm}^{-2}$ , to compensate for the low emission intensity of the samples.

Figures 7.6 and 7.7 show the  $\mu$ -PL spectra for each of the samples. These were obtained by averaging the emission of the samples over 30s, again to compensate for the low emission intensity. All of the samples show a series of

closely spaced, relatively narrow features ( $\sim 2\text{-}5\text{meV}$ ) characteristic of emission from highly confined states, which is typically of the emission from QDs.

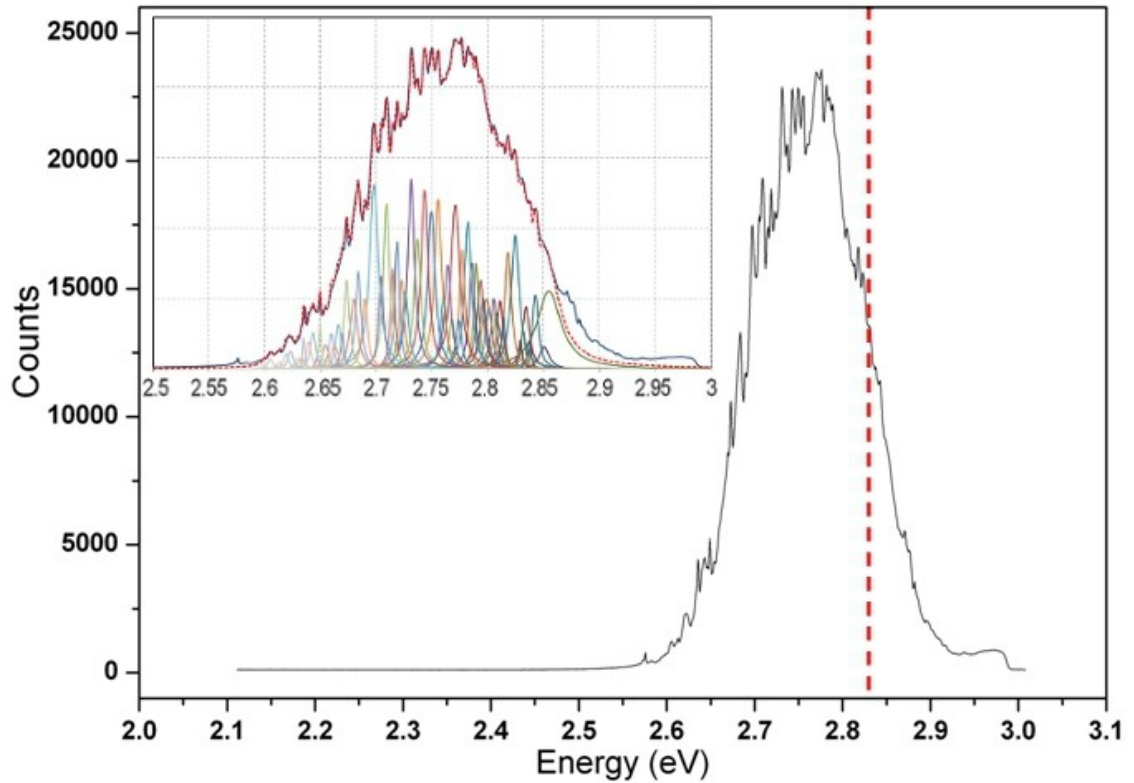


Fig. 7.6. 4K  $\mu$ -PL spectra from HWC236. The red dotted line indicates the ZnSe bandgap at 4K. The inset shows a portion of the measured PL spectra being fitted with Lorentzians to illustrate the number of emission lines present.

The spectrum shown for HWC236 is taken at the same location as that in fig. 7.4. It clearly shows that reducing the samples temperature from 77K to 4K result in dramatically sharper emission peaks. The emission is still centred at  $\sim 2.75\text{eV}$  close to emission of the ZnSe buffer layer ( $2.83\text{eV}$ ) and consists of a very large number of sharp emission lines ( $\sim 80$  emission lines between 2.5 and 2.9 eV, see inset in fig. 7.6). This made it impossible to find any individual emission lines that were well enough resolved to make single dot measurements. For this reason the majority of the work in the remainder of the chapter focussed on HWC 223 and 224.

HWC 223 and 224 also show a large number of sharp features but these are now centred at  $\sim 2.5\text{ eV}$  and are spaced further apart, which is more typical of CdSe QD dot emission. An additional smaller feature is again seen at  $\sim 2.8\text{eV}$  representing the emission from the ZnSe buffer layer.

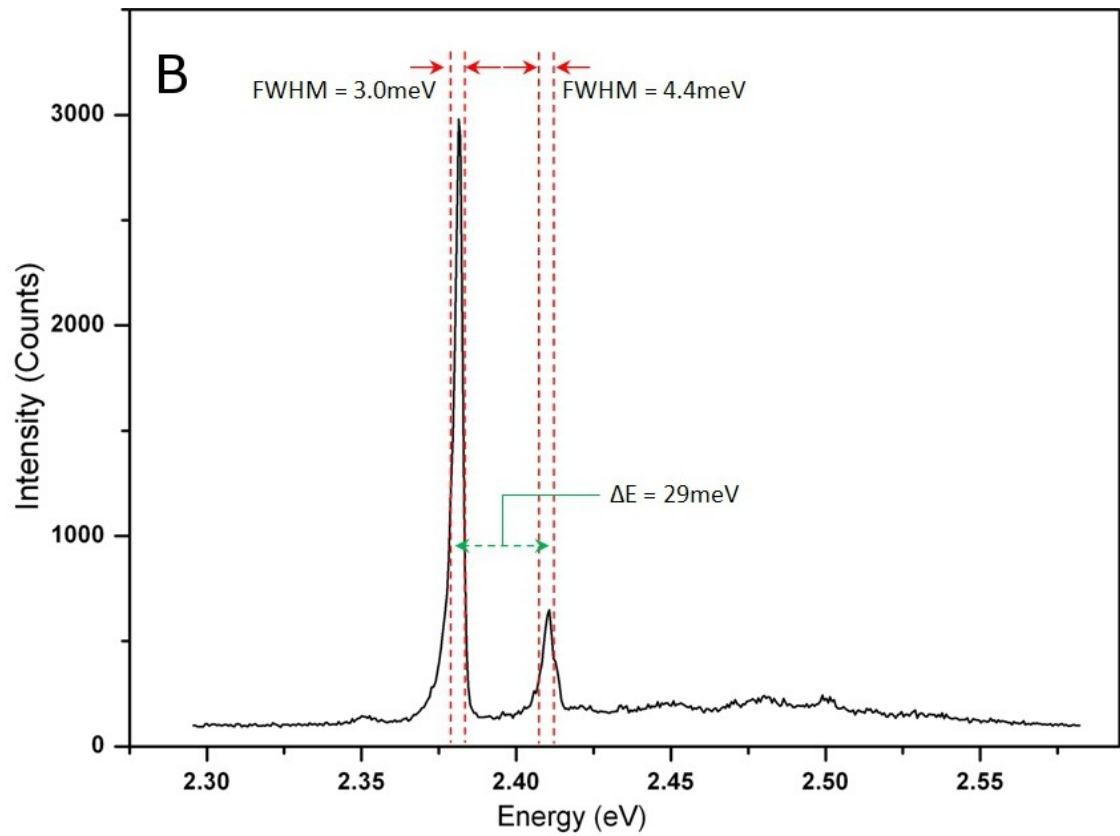
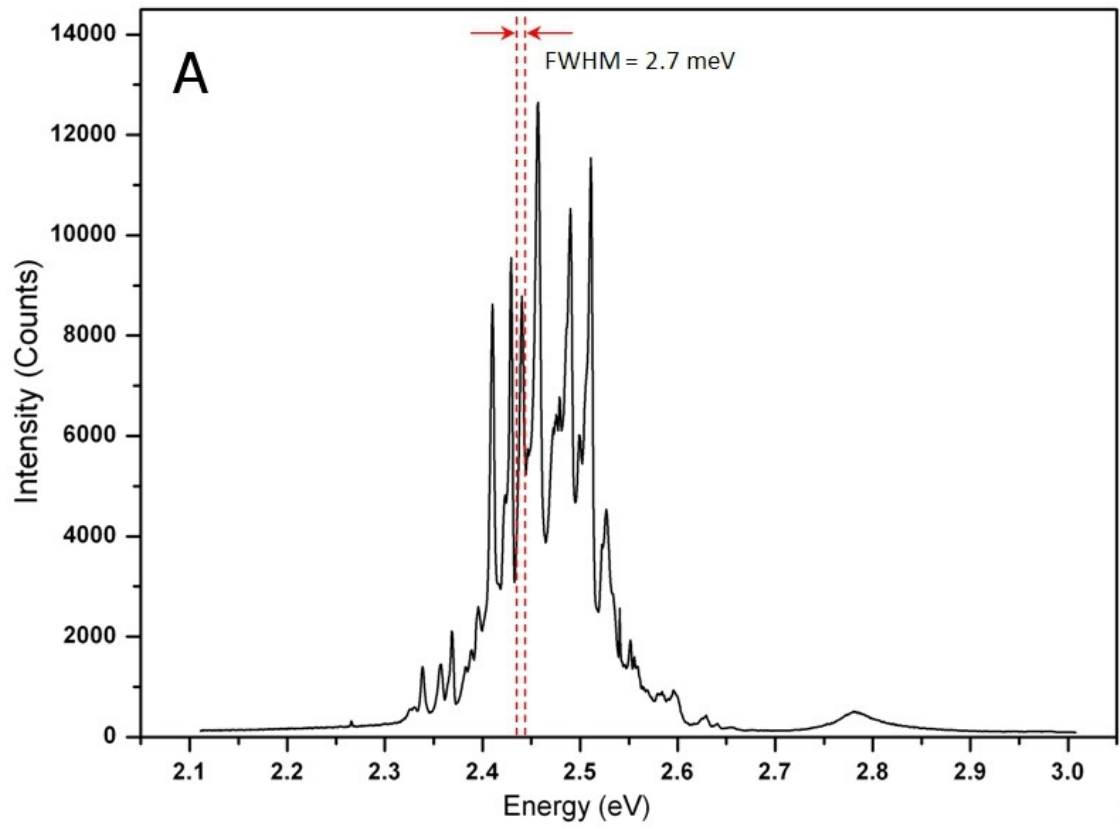


Fig. 7.7.  $\mu$ -PL spectra for HWC223 (A) and 224 (B) sample at 4K. FWHM and peak separations have been shown where possible.



By translating the sample using sub-nm positioning stages, it is possible to find spatially isolated individual dots that are sufficiently separated from the main ensemble to investigate their behaviour. An example of this can be seen in figure 7.7(B). The sharpest individually identifiable features from these samples were found to have FWHM in the region of  $3 \pm 0.35$  meV, which although sharp in comparison to QW emission is still very broad for a QD emission, which are typically found to be of the order of 50-500 $\mu$ eV – less than the resolution of the spectrometer used to measure them [7.21, 7.22].

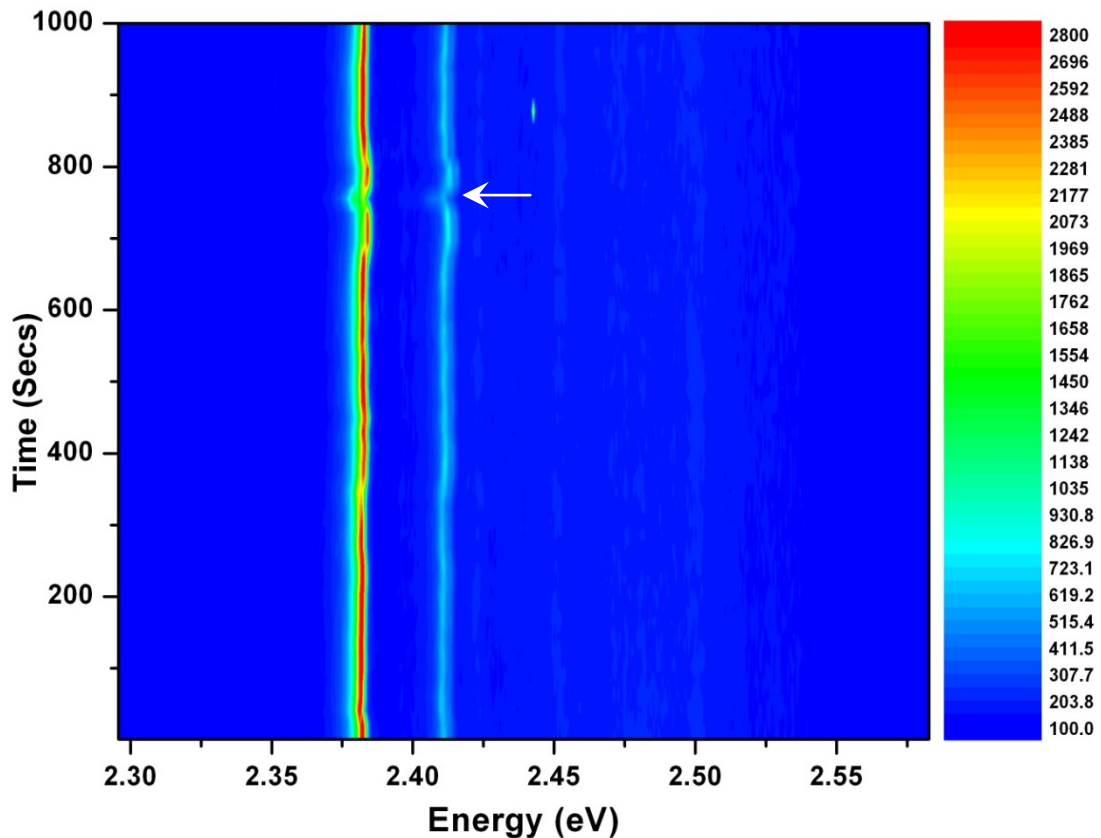


Fig. 7.8. 4K  $\mu$ -PL spectra of HWC224 intensity and energy as a function of time. The white arrow shows a point where the emission drops such that it is not well resolved against the background.

Figure 7.8 shows the temporal evolution of the spectra shown fig. 7.7(B). Over a period of time both the intensity and peak emission energy of the dot fluctuate. It should be noted that although it appears in the figure that the emission intensity periodically falls to almost zero (at around  $t=750$ s for example, as indicated by the white arrow) this is not actually the case. Instead the intensity has just dropped to a level where it is not well resolved from the background in this colour map. However for a small number of the spectra obtained some of the emission lines were seen to disappear or switch off for periods of up to a few seconds, an example of this is shown in figure 7.16.

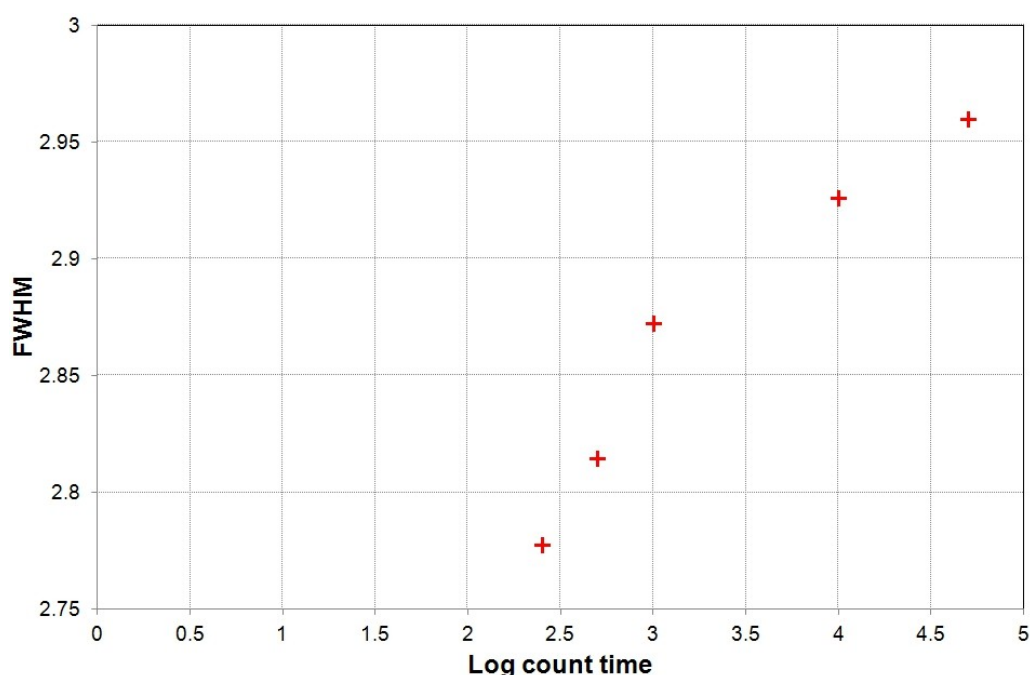


Fig. 7.9. The FWHM of the single emission peak centred at 2.38eV in fig. 8.7(B) vs. log count time.

It is also apparent from the figure that the large FWHM of the lines obtained in the integrated traces arises from the fluctuations in the peak position [7.23, 7.24]. This is still true even when the most intense features are imaged at the temporal resolution of CCD detector used (25ms), as even on these short time scales the intensity and emission energy of the features is seen to fluctuate. Figure 7.9 shows the variation of the FWHM of a single emission peak with count time. There is an increase in the FWHM with increased count time as would be expected if jitter is responsible for the large FWHM seen in these samples. The very short timescale of the jitter is evident from the figure, as the rate of change of the FWHM is very small on the timescales investigated. The range of count times measured is too small to be able to accurately predict a minimum FWHM for the emission from these dots.

Attempts to use a single-photon avalanche diode (SPAD) with a much better temporal resolution (<50ns) to investigate the timescale of the fluctuations and the decay of the emission peaks further was unsuccessful. This was due to the jitter in the samples being sufficiently large that the emission would periodically move outside of the narrow energy region the SPAD had been setup to detect. All attempts to use the detector over a wider energy range resulted in too low a signal to noise ratio to extract meaningful data.

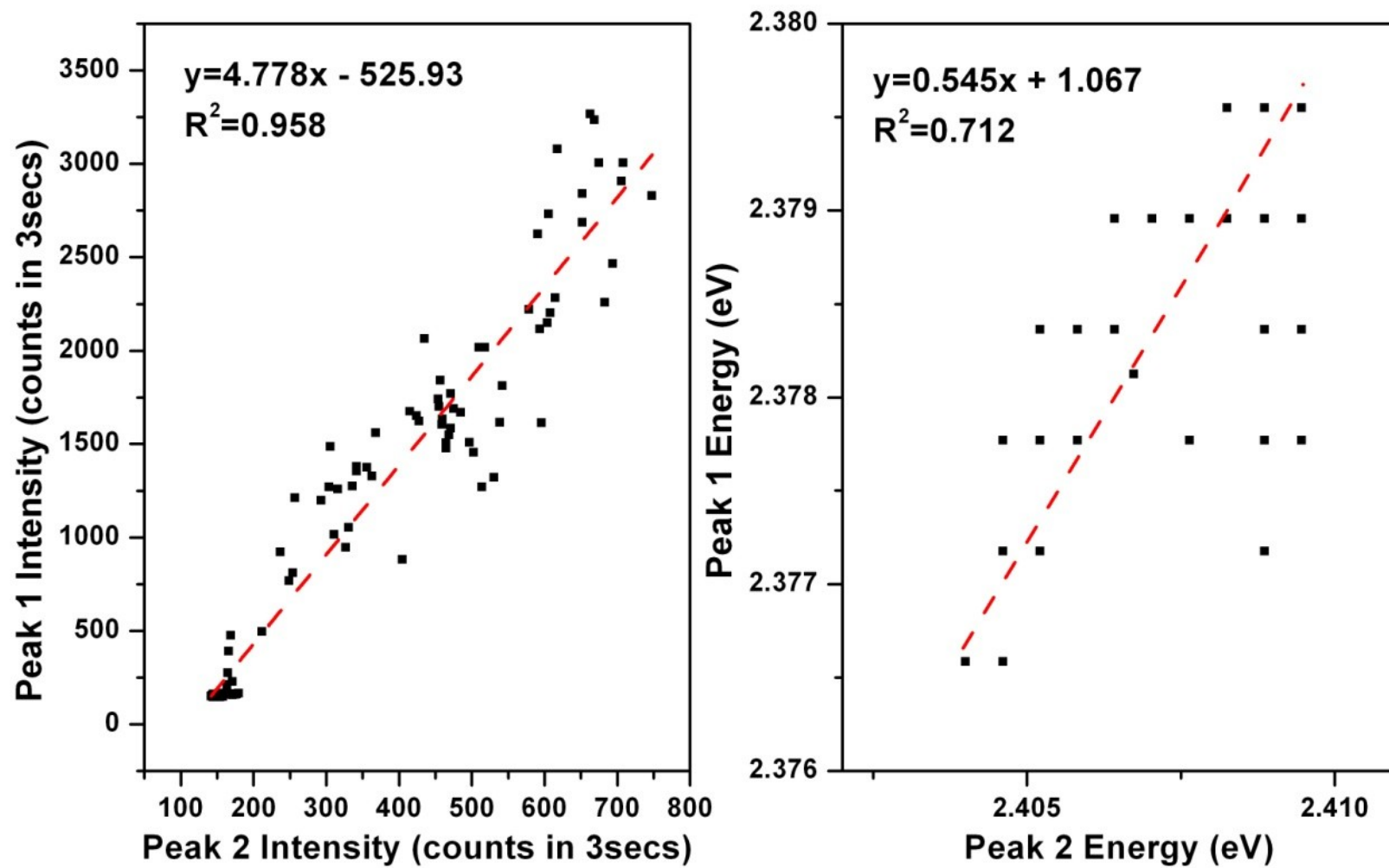


Fig. 7.10. Correlation between the intensities and energies of the two peaks in fig. 8.8. The red dashed lines are least squares fits to the data points, the equation and  $R^2$  values of the lines are also shown.

The fluctuations in intensity and energy of the 2 emission features in figure 7.7(B) (roughly centered at 2.38 and 2.41 eV) are highly correlated, with  $R^2$  values of 0.958 and 0.712 to a linear fit respectively, see fig. 8.10, indicating that they arise from the same dot. This behavior has previously been observed in ZnSe/CdSe QD emission [7.25, 7.26]. The 29 meV separation between the emission lines suggests (as will be explained later) that they arise from the exciton and biexciton emission from the same dot.

Fig. 7.11 shows the temporal evolution of a representative spectra observed for HWC224 and contains fifteen well resolved peaks. Examination of the energies and intensities of these peaks show that of these fifteen, six of them (three pairs, indicated by the colored arrows) show a strong correlation ( $>0.7$ ). Therefore, this spectrum contains a maximum of twelve distinguishable dots. If this analysis is repeated over several spectra from both samples, it shows the results are consistent with a dot density of  $4 \pm 1 \times 10^{10}$  dots  $\text{cm}^{-2}$ , which is similar to the densities seen with CdSe dots grown on ZnSe and MgS [7.14-7.16].

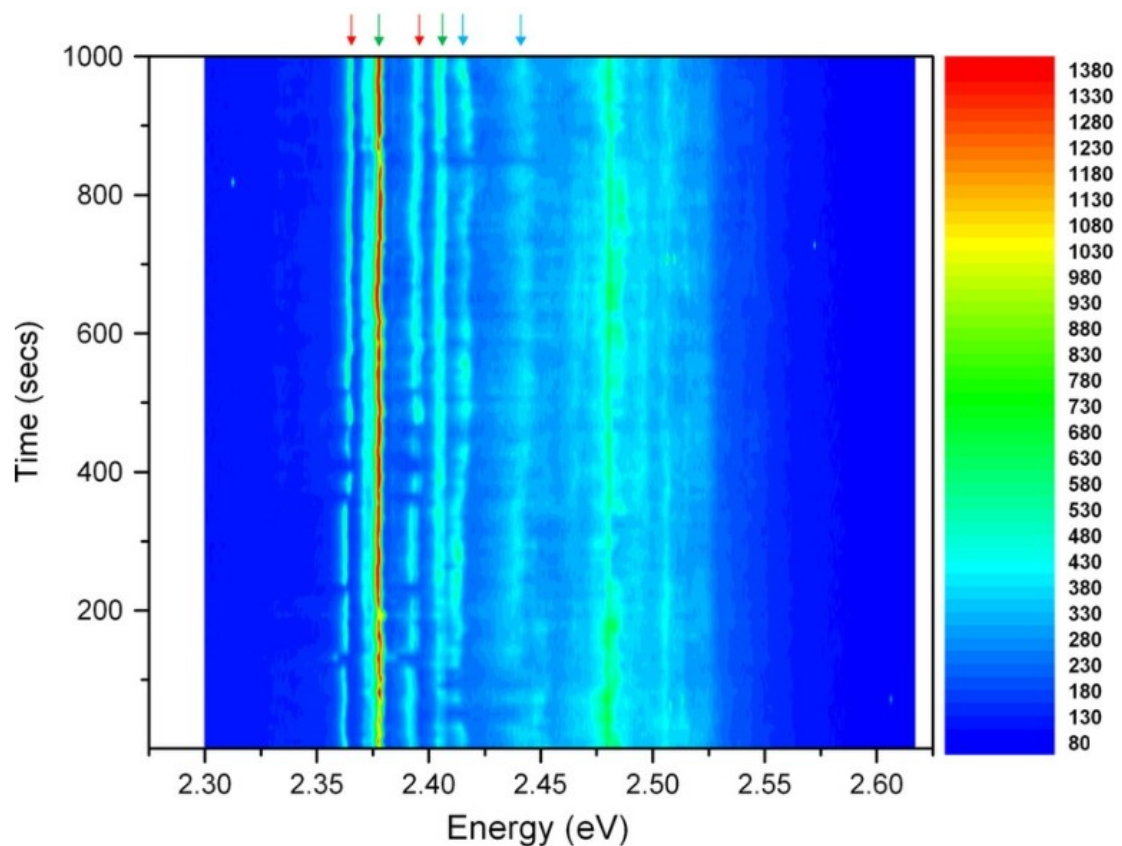


Fig. 7.11. Time evolution of a representative spectrum at 4K. The colour map shows the variation of the PL intensity and energy with time.

The 3 pairs of spectral lines in fig. 7.11 which are highly correlated in terms of both energy and intensity all share common features: the peaks are separated by  $\sim 26 \pm 2$  meV and the lower energy peak shows a larger emission intensity. No power scaling or polarization dependence measurements were performed for this spectrum, which makes determining the origin of the transitions impossible. However by looking at power scaling measurements made of other spectra from the same sample an attempt at identification can be made.

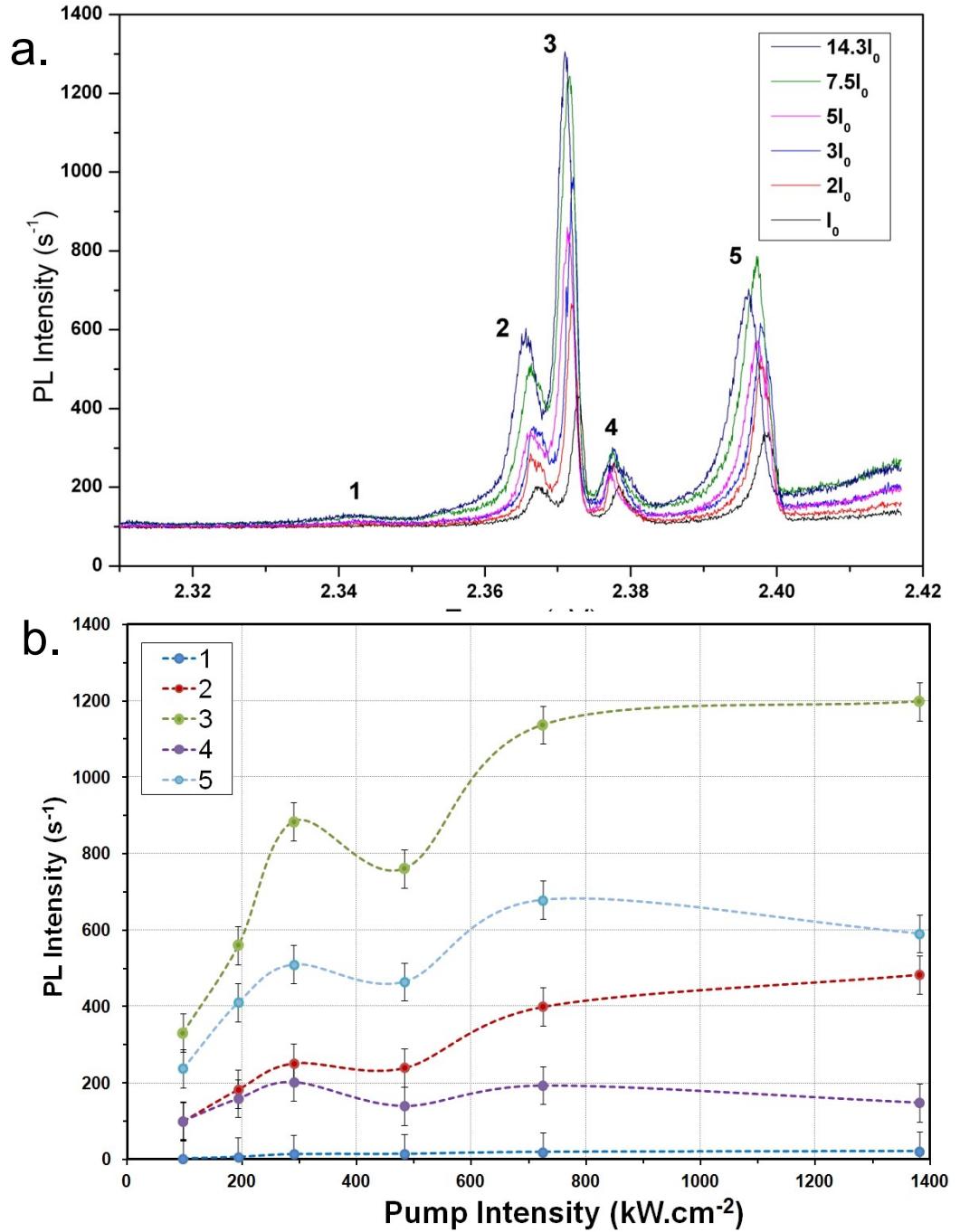


Fig. 7.12.  $\mu$ -PL spectrum (a) and power scaling (b) for 5 emission lines from HWC224.

Figure 7.12 shows a series of 6 spectra taken at another position on sample HWC224 at varying pump power intensities -  $I_0$ ,  $2I_0$ ,  $3I_0$ ,  $5I_0$ ,  $7.5I_0$ ,  $14.3I_0$ , where  $I_0=30\mu\text{W}$ . The final measurement at  $14.3I_0$  is the full pump power available, which is  $0.43\text{mW}$  (or an average intensity of  $\sim 1\text{MW}/\text{cm}^2$ , giving an electric field of  $32\text{kVcm}^{-1}$ ). All 5 emission lines show power dependences that roll-over at high pump power, which is indicative of some sort of saturation or loss mechanism at high pump power.

The apparent oscillation in the plots also appears to be a genuine feature, as all attempts to explain it experimentally proved unsuccessful. The cause of the oscillation is hard to determine as the only report of a similar feature found in the literature is explained as Rabi oscillations under pulsed excitation [7.27, 7.28], which may not be comparable to this work.

$$I_{\text{emission}} \propto I_{\text{pump}}^k \quad (1)$$

Equation 1 shows the relation between pump and emission intensities, where  $k$  is the power dependence co-efficient. By plotting  $\log I_{\text{emission}}$  vs.  $\log I_{\text{pump}}$  for the measurements, the coefficient  $k$  can be determined for each line, see figure 7.13. Excitons typically have a linear power dependence and hence  $k \approx 1$ , whereas biexcitons scale superlinearly with  $k > 1$  [7.24, 7.29-7.34]. Plotting the power dependence of the 5 features in fig. 7.12 over the whole power range results in power dependence exponents of between 0.1-0.6, which are far lower than would be expected for excitonic transitions. However by considering only low power the linear region the values in table 7.2 are obtained. This suggests that emission lines 2-5 are excitonic while line 1 is biexcitonic in nature.

Except for line 4, all the emission energies have a strong negative correlation with the pump power, coefficients of -0.84 to -0.98. Once this effect has been removed by linearising the data, it is then possible to look at the correlation of the lines with one another, see table 7.2. This shows that lines 1 and 2 are strongly negatively correlated (-0.86) with one another, whilst lines 3, 4 and 5 are positively correlated with each other with high coefficients  $> 0.9$ .



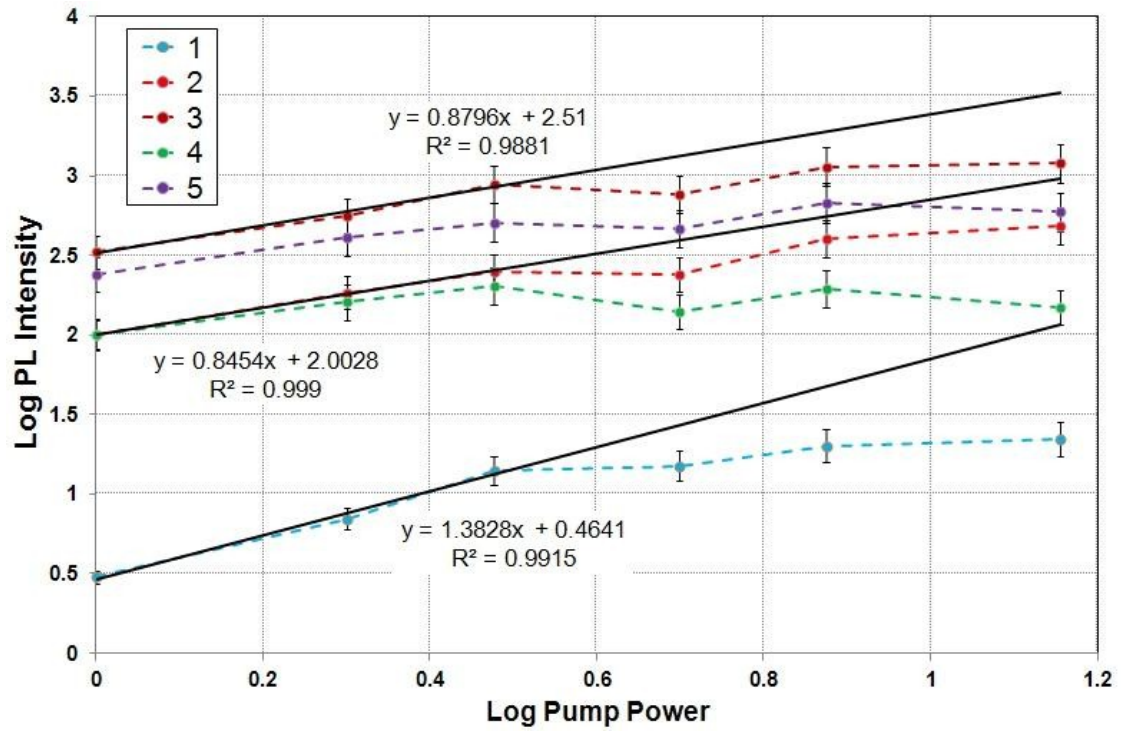


Fig. 7.13. Logarithmic power scaling plot for a HWC 224 spectra. Three linear fits (black lines) have been performed on the first 3 points to show representative scaling coefficients.

Some of the other emission line pairs show relatively strong correlations ( lines 2 and 5 for instance), but as the sample size is very small and even after the removal of the power dependence there may still be a some residual additional correlation, these pairs have been ignored. In the case of lines 2 and 5, the overlap of emission line 2 with 3 (and possibly 4) may also enhance the apparent relatively strong correlation.

	Power Dependence Coefficient, k	Correlation coefficients					Energy Separation (meV)				
		1	2	3	4	5	1	2	3	4	5
1	1.38	1.00	-0.86	-0.18	0.00	-0.49	0	23	28	34	54
2	0.85	-	1.00	0.60	0.44	0.78	-	0	5	10	31
3	0.88	-	-	1.00	0.99	0.94	-	-	0	6	26
4	0.64	-	-	-	1.00	0.90	-	-	-	0	21
5	0.70	-	-	-	-	1.00	-	-	-	-	0

Table 7.2. Power dependence, correlation and energy difference between emission lines or HWC 224. The two groups of correlated lines have been shaded for easy of identification.

Combining the correlation data with the information already gathered from the power scaling plots it appears that line 2 and 1 are the exciton and biexciton emission respectively from the same dot. Lines 3, 4 and 5 are all from a

different dot and as they have a linear power dependence, it suggests that they are all excitonic in nature. Therefore Line 3 or 4 is identified as the negative trion (charged exciton,  $X^-$ ) of line 5 [7.26, 7.34]. The small energy separation between lines 3 and 4 is harder to explain but could suggest that the dot has an asymmetric profile and therefore has two emission modes [7.18]. However polarization dependent micro-PL or time resolved correlation measurements would be needed to identify lines 3-5 unambiguously [7.24, 7.26].

The strongly negative correlation the intensities of line 1 and 2 is somewhat unexpected as other groups looking at the emission of CdSe/ZnSe QDs have typically found a positive correlation between exciton and biexciton emission [7.26, 7.34]. However Kaniber et al [7.35] found that in a strong electric field (5-20 kVcm<sup>-1</sup>) the exciton and biexciton emission from InGaAs dots grown on GaAs experienced opposing energy shifts (positive and negative for the biexciton and exciton respectively). They believe this is due to the repulsive interactions between the pairs of electrons and holes in the biexciton not being compensated for by the e-h interaction. However as the biexcitons in these dots appear to be in an anti-binding regime, as they emits at a higher energy than the exciton, this may or may not be applicable to the dots studied here.

Kaniber et al also found sub-linear ( $k < 1$ ) power dependence coefficients for the emission lines they looked at. They attribute this to the strong electric field ( $> 4.5$  kVcm<sup>-1</sup>) causing carrier ionization in the WL resulting in the QDs capturing individual electrons or holes rather than excitons [7.35]. As the CdSe/QA samples investigated here will be experiencing a field of 8-32 kVcm<sup>-1</sup> it is possible that emission line 3 is actually the bi-exciton emission from the same dot emitting lines 4 (trion) and 5 (exciton).

If this is the case, then the coefficients of lines 1 and 2 (1.38 and 0.85) might suggest that they also come from a biexciton and multi-exciton complex (a composite of  $> 2$  e-h pairs) respectively. However as a charged biexciton or



multi-exciton need to have an electron or hole in the p-level, and so typically emit at a higher energy than the exciton, this does not seem likely.

It is more likely that as the pump spot will have a Gaussian shape, the dot producing lines 1 and 2 may be situated further away from the centre of the beam than the dot producing lines 3- 5 and hence will experience a lower pump intensity. In turn this will result in it capturing a lower flux of excitons than the second dot and therefore having a more linear power dependence.

However without further measurements it is impossible to determine absolutely which transition each line represents. But from the data available approximate values of  $24.5 \pm 1.5$  and  $23.5 \pm 2.5$  meV can be determined for the biexciton and trion binding energies respectively. These values are close to those reported for CdSe dots grown on MgS or ZnSe [7.6, 7.14, 7.24, 7.26, 7.36].

For the 3 pairs of correlated emission lines in figure 7.11, it is still not possible to say exactly what transitions comprise each pair, as they are all around 26 meV. However, from the power scaling data obtained, it suggests that the 2 pairs with larger energy separations (26 and 28 meV) are exciton and biexciton pairs and the other pair (indicated by the blue arrows and with a separation of ~23 meV) is an exciton and either a trion or biexciton.

#### **7.4.1. Comparison of $\mu$ -PL Results with ZnSe/CdSe and MgS/CdSe Samples**

Figure 7.14 shows the temporal evolution of the emission from a ZnSe/CdSe QD sample (HWA1555). Comparing it to figures 7.8 and 7.10, the main difference is the lack of fluctuations in the emission lines energies or intensities during the 100s measured. Small variations may be present but they will be less than the energy resolution of the system (0.7 meV).

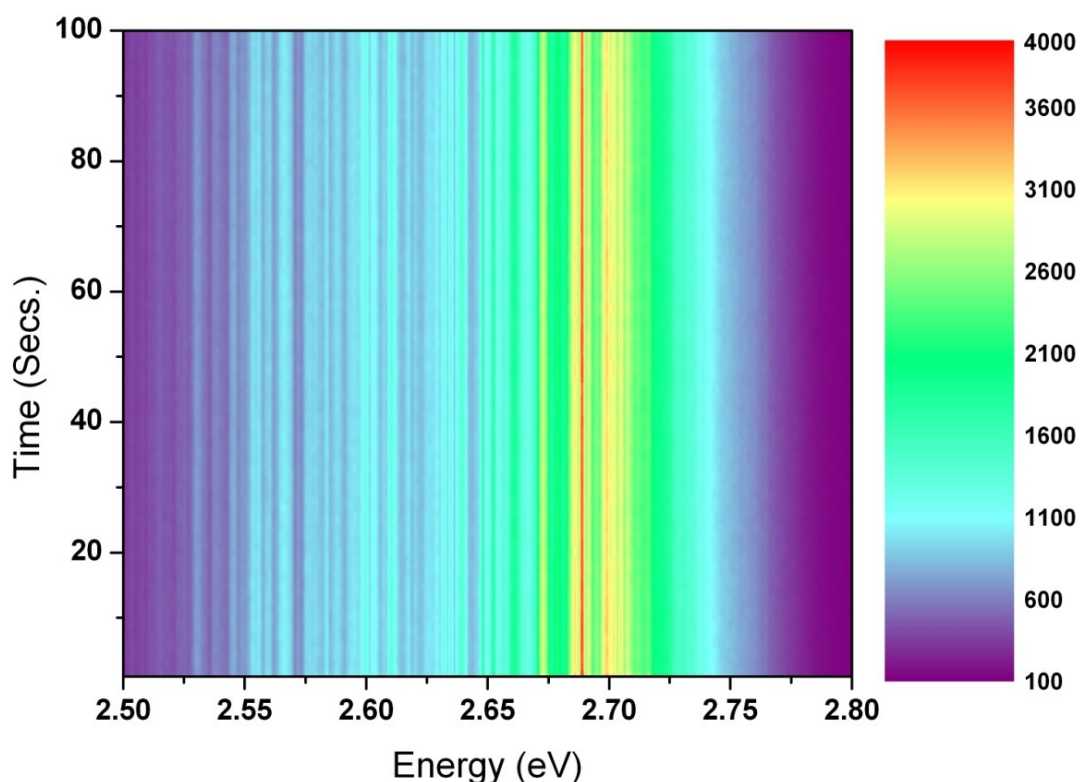


Fig. 7.14. Temporal evolution of the emission spectra from HWA1555 ZnSe/CdSe QD sample. Again the colour map shows the variation of PL intensity and energy with time.

Unfortunately no samples with MgS barriers have been investigated under comparable conditions, so it is impossible to produce a colour map diagram to show how their QD emissions vary with time. However from the analysis of their jitter (see section 7.5) it is likely that the plot would look a lot like those produced by the samples with QA barriers.

### 7.5. Jitter/Blinking

Emission jitter is seen in virtually every material system where single emitters are measured and is related to the phenomenon of blinking [7.25, 7.33, 7.37-7.44]. Jitter is a relatively well defined effect, the '*stochastic variation of the peak energy*' of emitters with time [7.33], whereas the exact definition of blinking seems to be less clear; principally there seems to be disagreement as to what constitutes a drop in intensity sufficient for it to be consider a 'blink'.

Some groups observe the intensity of the emission from QD (either self-assembled or colloidal) completely disappear while others just see a significant

drop, typically to a level of <30% the original value. Some groups interpret this >70% drop in intensity of the emitter as an off state whilst others refer to it as a 'grey' state [7.45, 7.46]. However they all seem to behave in a similar way with a power law governing the frequency of their on and off states [7.37-7.46].

During the  $\mu$ -PL measurements of CdSe QDs grown on QA barriers significant emission energy and intensity jitter was seen. Fluctuations in both the energy and intensity of QD emission have previously been observed for CdSe dots grown on both ZnSe and MgS barriers [7.26, 7.15] and in the case of the samples grown on ZnSe it has been demonstrated that these fluctuations arise from the Quantum Confined Stark Effect (QCSE) produced by fluctuating charge close to the dots, which is shown schematically in figure 7.15. The charges are thought to be located either at the sample surface [7.23], at a dislocation originating from a stacking fault [7.47] or in the WL due to potential fluctuations [7.48].

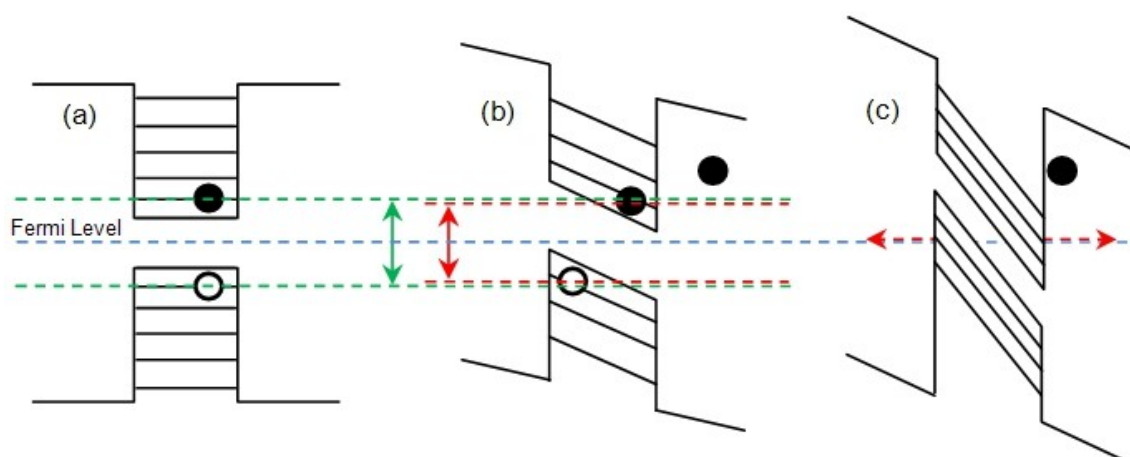


Fig. 7.15. Schematic representation of QCSE, b) shows reduction in bandgap due to the presence of an electric charge close to the QD. C) shows the presence of a charge extremely close to the QD, the reduction of the offsets is such that charge carrier tunneling from the QD is more likely than emission.

A variety of different blinking events were also observed for the samples investigated here. These ranged from drops in intensity of 40-50% for long periods (~10's of seconds) to others with a near 100% loss of intensity. However the total number of distinct events (ones that resulted in a 70% or greater drop in intensity for a period of 100ms or more) was quite small and they seemed to occur fairly randomly. This made any systematic investigation of their origin impossible.

Figure 7.16 shows an example of one of the more noticeable blinking events recorded for sample HWC224. The figure shows the change in intensity of two correlated lines over time. At two points during the 100 seconds (between 50-57 and 75-78 seconds) their emission intensity is seen to drop to <30% indicating that the dot has entered a grey or off state. This can be more clearly seen in the normalised intensity plot shown underneath the spectra. The two lines in the figure show a correlation in terms of emission energy and intensity of 0.78 and are separated by 27meV, which is consistent with an exciton and biexciton pair.

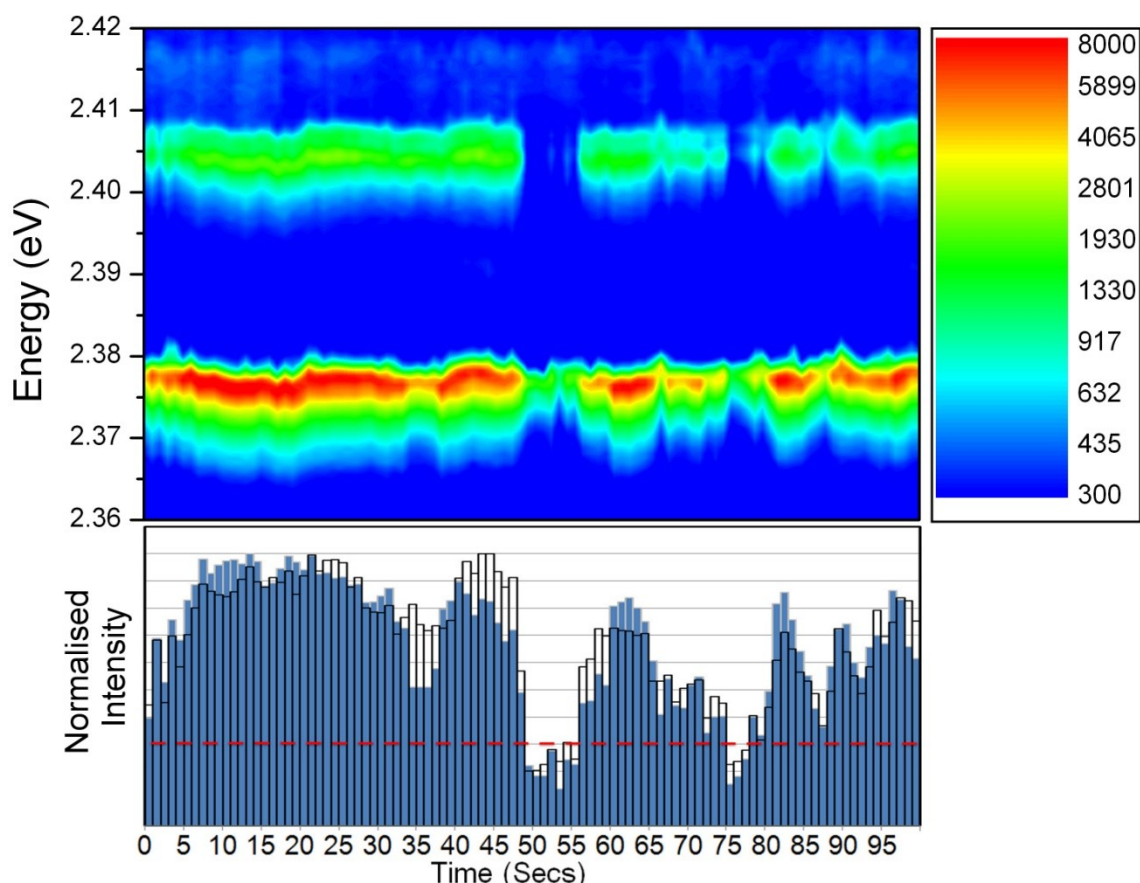


Fig. 7.16. Time dependence of the intensity of the emission lines from a dot on HWC 224 over a 100s period (top) and the normalized intensity from the two dots (bottom). Between 50-57 and 75-78 seconds the intensity of both lines drops below 30% indicative of a grey or off state.

A number of theories have been proposed to describe the blinking and many of these also explain the jitter seen. The first model was proposed by Efros and Rosen in 1997 [7.49], they suggest that the blinking is caused by QD becoming ionized either through thermalisation or Auger auto-ionisation of an exciton under photoexcitation, ejecting the electron from the dot to a surrounding acceptor-like state. This would cause any further excitons captured by the dot to

undergo non-radiative Auger recombination due to the much faster non-radiative relaxation time. This model is shown schematically in fig. 7.17.

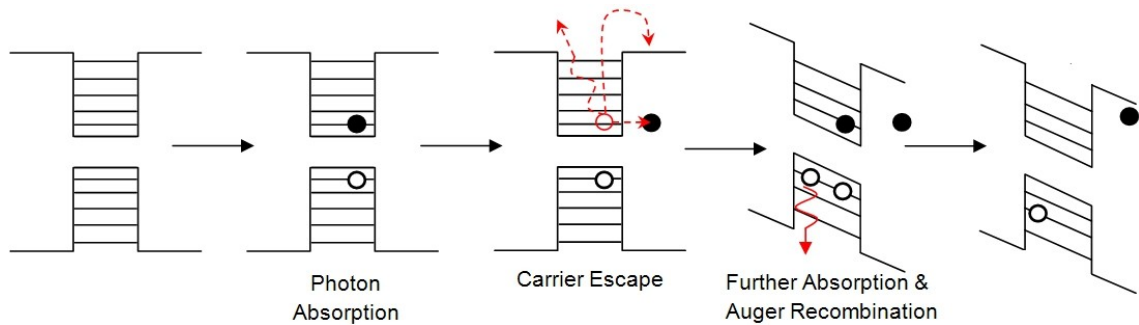


Fig. 7.17. Schematic showing the model proposed by Eros and Rosen. The tunneling, Auger auto-ionisation and thermalisation of an electron out of the QD has also been shown as a possible route to charged exciton formation.

This process on its own would not cause emission jitter in the affected dot, as the presence of the charge in the dot will simply quench its emission, but the presence of a nearby trapped electron could be sufficient to produce an electric field in the surrounding dots and cause them to experience jitter. However this would require the charge to fluctuate or move as otherwise it would only produce a static electric field.

A significant fault with the Eros and Rosen model is that it predicts characteristic on/off rates and hence an exponential distribution of on and off times, which is not seen in the measured data [7.38]. A number of attempts have been made to modify the original model so that it does produce the correct distribution. These include the introduction of multiple trap states outside the dot, the ejected electron resonantly tunneling away from the dot or spacial diffusion of the electron [7.43, 7.50-7.54]. All of these also improve the model's ability to explain the jitter seen in the data, as they allow the ejected electrons position to fluctuate to produce the varying electric field required.

The other possibility is that rather than a charge being generated in the QD directly, instead a charge is created either in the WL (where the pump photons are absorbed) or at the surface of the samples. As there are a large number of trap states in both of these locations (due to disorder in the WL and dangling bonds etc. at the surface) the likelihood of either the electron or hole generated

when a photon is absorbed being trapped is relatively high. This would leave the other charged particle free to diffuse until it encounters another electron or hole and recombines.

The advantage of this model is that it produces free charges that are capable of producing the jitter seen without quenching the emission from the dots, which is closer to the observed behaviour here. It could also generate a significant reduction in the emission intensity through QCSE when the free charge gets very close to a QD. Whether or not a charge located near the dot would be sufficient to produce a true dark state like those seen in other materials, where a dot emits no photons for a period of time, is harder to predict, as this would require the induced band bending to be so large that the Fermi level intersects both the electron and hole ground states, as depicted in figure 7.15(C).

Certainly in the case of self-assembled QDs and surface charges this would not be possible as the thick ( $>10\text{nm}$ ) barriers will not allow the charge to get close enough to the dot. But for colloidal QDs it is more likely as they have a much larger surface to volume ratio and far thinner barriers (typically  $<5\text{nm}$ ), bringing any surface charges much closer to the dot.

In the case of the dots studied here, the presence of charged exciton (trion) emission from the dots shows two things. First, Auger recombination cannot be the only cause of the blinking seen in the dots, and second, there must be (by definition) free charges present in the QDs. Whether these charges are due to the escape of the other component of an e-h pair or the intrinsic n-type doping seen in CdSe layers is however unclear.

Comparing the spectra obtained from samples with the 3 different barrier materials, ZnSe, MgS and ZnMgSSe, we find that all of them show jitter in the emission energy of QDs. With ZnSe barriers the magnitude of the energy jitter can be as low as  $0.2 \pm 0.15\text{meV}$  and is so small that in many cases its

measurement is limited by the resolution of the spectrometer (with 1 pixel representing  $\sim 0.09\text{meV}$  at  $500\text{nm}$ ).

Samples with MgS and QA barriers have larger energy jitters of  $0.7\pm 0.4\text{meV}$  and  $1.4\pm 1.7\text{meV}$  respectively. However with the small number of samples examined so far it is impossible to determine if this difference is due to the barrier material.

For HWC223 and 236, the magnitude of the energy jitter varies but averaging a large number of readings gives  $3\pm 4\text{meV}$  and  $1\pm 0.8\text{meV}$  respectively. Assuming the dots in these samples are roughly similar in size and polarizability to CdSe dots grown on ZnSe [7.55], which should be a reasonable assumption, the fluctuations observed can arise from QCSE caused by a single charges located  $\sim 10\text{nm}$  from the dot, compatible with the charge being located at the surface.

The jitter for HWC224 is smaller than 223 and 236,  $0.4\pm 0.2\text{meV}$ , with the average of all 3 results being the value reported earlier for QA samples. HWC 223 and 236 have thinner top barrier/capping layers than HWC224,  $10\text{nm}$  compared to  $15\text{nm}$ , which is compatible with the QCSE from surface charges.

The amount of CdSe deposited is increased from 7 MEE cycles in HWC236 to 11 cycles in 223, likely resulting in a higher dislocation density in the dots or WL in HWC223 than in HWC236. If the charges responsible for the QCSE are trapped in the WL then the variation in the energy jitter would scale with the CdSe thickness, but this does not seem to be the case.

By comparing a number of other samples with ZnSe, MgS and QA barriers a trend is seen, see fig. 7.18. As the capping layer/top barrier thickness is increased the jitter present in the samples is reduced. Figure 7.18 seems to show a roughly inverse square law relationship between the thickness and jitter

(shown by the red line in the figure), as would be expected if the cause of the jitter is charges located at the surface of the samples. However as the graph was produced using data from only 7 samples (3 with QA barriers, 2 with MgS and 2 with ZnSe) and is based on only 6 points with quite large error bounds, any attempt to deduce a relationship can only be a guess.

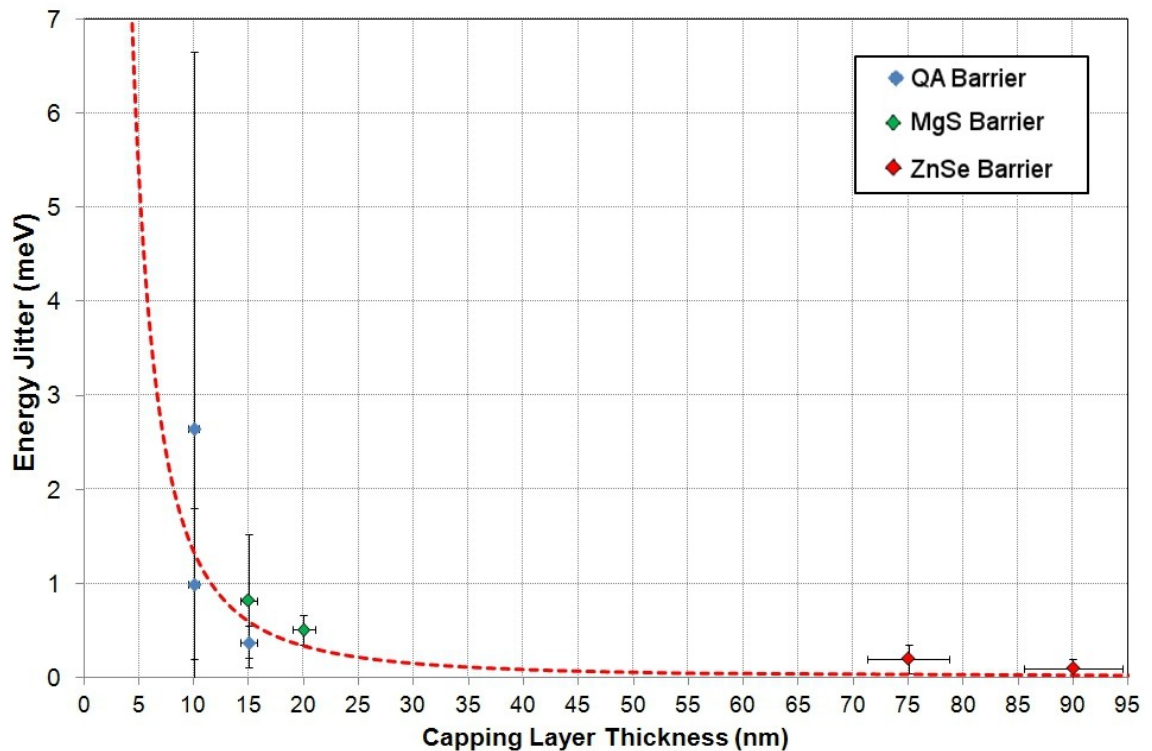


Fig. 7.18, Variation of emission energy jitter with capping layer/top barrier thickness. The red dashed line was generated using an inverse square law using arbitrary constants as a guide to the eye.

The dielectric permittivity of the barrier material has been found to have an effect on the blinking behavior of the some QDs [7.51] and so it is worth considering the effect of the relative dielectric constant of the barriers as well as their thicknesses. As the relative permittivity (dielectric constant) of a material represents how much the electrical field inside it will be reduced in comparison to a vacuum it is easiest to include its influence by using the product of dielectric constant and thickness, this is shown in figure 7.19. Values for an additional ZnSe/CdSe sample and an InAs/AlAs/GaAs sample have been added to the graph with the data, taken from values reported in references [7.26] and [7.29]. The relative permittivity figures used were calculated from the refractive index of the material at the emission wavelength of the QDs.



The data again seems to fit relatively well to an inverse square law. The error bound on the CdSe/ZnSe sample from Patton et al unfortunately has to have large error bounds on its thickness as it is quoted as only 25-50nm in the paper. If the dielectric constant of the barrier material is of significant importance to the jitter (and blinking) in the samples then this might explain the differences between the samples with QA barriers, as a ~5-10% increase in both x and y composition values would be enough to change the refractive index by ~0.05 and the dielectric constant by ~0.25. This would increase the dielectric thickness product equivalent to a thickness increase of 4% and hence split the two points with dielectric thickness products of ~51nm.

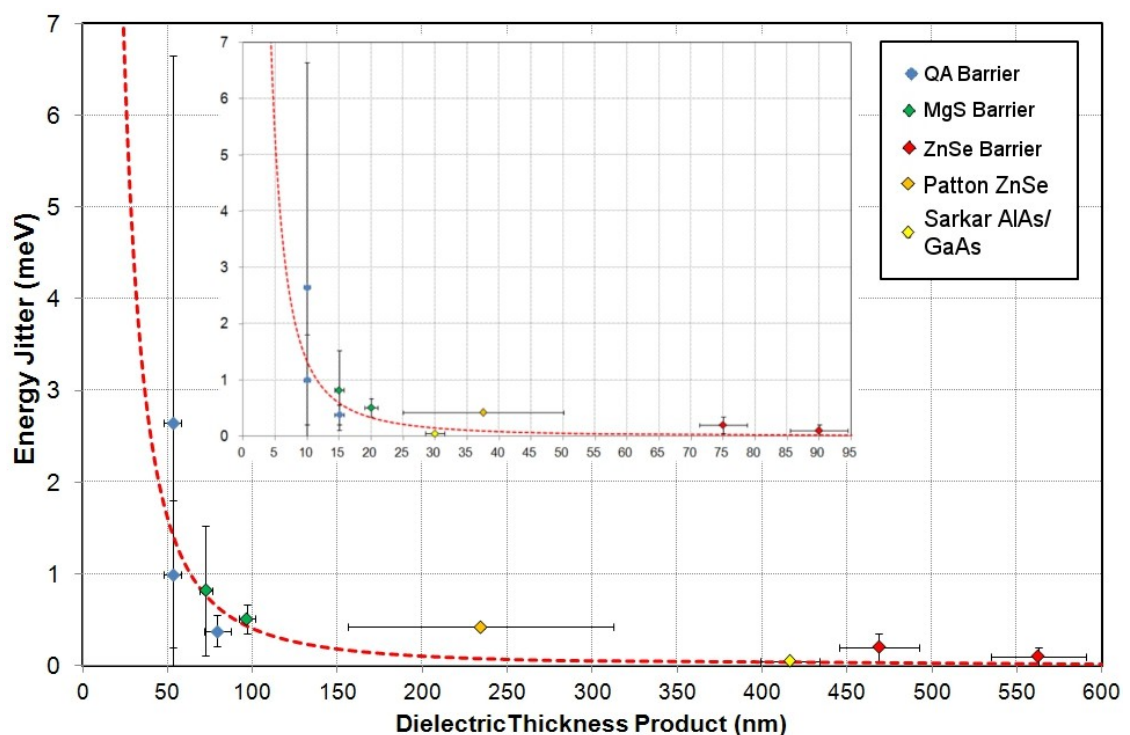


Fig. 7.19. Magnitude of the energy jitter vs. the dielectric thickness product for a number of samples. Inset is the jitter data plotted against the thickness. Again the red dashed line was generated using an inverse square law using the same arbitrary constants as a guide to the eye.

Mahler et al have investigated the influence of the barrier layer (shell) thickness on the blinking behavior of colloidal QDs [7.56]. They found that the blinking behavior depends strongly on the shell thickness of their dots with those with the thickest barrier showing blinking on a <30ms level only.

In further work on colloidal QDs, Galland et al. found that there were 2 different blinking mechanisms present in their sample [7.57]. They propose that the first mechanism is an Auger type process, while the other is due to the influence of a

charge state close to the dot. This may explain the result found by Mahler et al, as the fast Auger blinking may still be present even in the thick shelled samples.

Interestingly Wang et al report that they do not see any blinking behavior in the ZnCdSe/CdSe colloidal QDs they are working with. They believe this is due to the dots having a graded ZnCdSe shell which removes the abrupt step in the dots band structure and suppresses any Auger processes [7.58].

As the Auger recombination rate is inversely proportional to the volume of the QD [7.59] and self-assembled QDs have a much larger volume than colloidal ones, by a ratio of at least 3:1, any Auger processes present in the dots investigated here will be less significant than in colloidal dots. However it is still possible that Auger recombination will occur.

QCSE produced by a fluctuating electric field also reduces the energy of the emission line together with the emission intensity. Consequently, there should be a strong correlation between these two effects produced by the fluctuating electric field, as has been previously observed for ZnSe/CdSe dots [7.47, 7.55, 7.60]. However, the weaker emission from the ZnMgSSe/CdSe samples means that although both energy and intensity fluctuations have been identified for all the dots examined so far, presently any statistical correlation between the two quantities for an individual emission line has not been seen.

If the quantities are indeed correlated, then the inability to resolve them signifies that the fluctuations are occurring on timescales shorter than the smallest integration time used in these experiments (25ms). This is in agreement with the measured temporal variation data, see fig. 7.9, as even at 25ms resolution jitter is still present at a similar level to longer timescale measurements. The persistence of the jitter across a wide range of timescales is also in agreement with the work undertaken to determine the blinking mechanism, where the frequency of blinking events behaves similarly [7.33, 7.35, 7.38-7.46, 7.49].

## 7.6. Conclusions

The behavior of CdSe QDs grown on an MgS-rich ZnMgSSe QA barrier have been investigated. Ensemble PL measurements showed that the dots grown on QA appear similar to those grown on either ZnSe or MgS barriers with the usual emission profile. The emission energy of the ensemble suggests that the dots are smaller than those produced by depositing 3.6ML of CdSe on MgS.

4K  $\mu$ -PL measurements of the dots produced peaks made up of a large number of individual emission lines each with FWHM of  $3\pm0.35$ meV. The temporal measurements of the individual lines showed significant jitter of their energy and intensity on a  $<25$ ms timescale resulting in the larger than anticipated FWHM seen. The FWHM was found to be a weak function of the count time used suggesting a very fast underlying jitter mechanism. By looking at the correlation of the variation of the peak energies and intensities these lines are assigned to individual dots and hence the number of distinguishable dots within the resolved spot of the microscope system determined. This represents a dot density for the sample of  $4\pm1\times10^{10}$  cm<sup>-2</sup>, which is similar to the density measured for CdSe QDs grown on either ZnSe or MgS barriers.

Power scaling measurements made with spectra from HWC224 showed that the intensity initially increases approximately linearly ( $k=0.75\pm0.15$ ) before rolling over. This along with the lower than expected emission energy when compared to samples with ZnSe and MgS barriers suggests that there is a strong non-radiative process at work.

By considering the power scaling co-efficient of the emission lines and their correlation it is possible to measure binding energies for the biexciton,  $E_B^{xx}$ , and trion,  $E_B^{cx}$ , of  $24.5\pm1.5$  meV and  $23\pm3$ meV respectively. Using these values the various pairs of correlated emission lines seen can be identified depending on whether their separation is greater or less than 24.5meV.

Emission intensity jitter was observed to produce intensity decreases of more than 70% for a small number of the spectra obtained. These dramatic decreases are consistent with the blinking seen in other single emitter work. The various models suggested to explain the related phenomena of blinking and jitter were discussed and their predictions compared to measured data. By looking at the variation of the energy jitter with barrier thickness and relative dielectric permittivity,  $\epsilon_r$ , a roughly inverse square law relationship was found. This suggests that charges located at the surface of the QD samples may be one of the sources of the observed jitter in these samples.

## 8. Final Conclusions and Suggestions for Future Work

In the previous five chapters (chapters 3-7) a range of different experimental results were reported. Each chapter ended with both a conclusion and suggestions for future work, so these will not be repeated here, instead this section will briefly summarise each experimental chapter and then detail a few suggestions for further work that fall outside the areas covered in the preceding chapter.

### 8.1. Chapter 3 – Spin Current Detector

This chapter explained the growth and characterisation of structures grown for the ESP groups at Philipps-Universität Marburg. Details of the PL and XRD characterisation of these structures along with a series of ZnSe rich QA samples were presented. All of the samples were shown to have been produced as per their designs and to produce intense and well resolved PL emission. However when the samples were sent to Marburg they found that the samples were unsuitable for use due to issues with their original design. A new design based around ELO is proposed in the future work section to solve these design issues.

The failure of these samples also very clearly demonstrates one of the main problems faced by a semiconductor epitaxy groups when collaborating with others, the need to fully understand the way the samples are to be used and to explain the exact properties of the materials used in their growth.

### 8.2. Chapter 4 – Epitaxial Lift-Off

This chapter shows demonstrated the use of ELO to lift material grown on both GaAs and InP substrates utilising either an MgS or MgSe sacrificial layer. It also showed that when performed under ideal conditions the lifted material will be

identical, in terms of both physical and optoelectronic properties, to the as-grown material. The additional cracking often seen in the material lifted using an MgS layer was investigated and shown to be due either to the etching process or rough handling of the material after it has been etched.

The failure of recent samples with MgS and MgSe to produce successful ELO was investigated and a model of the samples microstructure was presented to explain this behaviour based on the sacrificial layers being very rough with columns of cladding material through them. This model accurately describes the behaviour seen in a number of examples. However no measurements have been made to prove the existence of the pillars in the sacrificial layers at present. A range of future work topics were proposed to both further investigate the mechanisms behind ELO, to investigate the proposed microstructure model and to extend the process to samples with an MgTe sacrificial layer.

### 8.3. Chapter 5 – Development of a Lattice Matched, MgS rich QA

This chapter detailed all of the work undertaken to develop a lattice matched, wide bandgap, etch resistant quaternary alloy. A number of PL, XRI and XRD results were presented as part of this development and the reliability of the XRI technique itself investigated, with the outcome being that for a number of material systems (those where the thickness and lattice constant of the central layer are completely unknown) the XRI technique is not completely reliable.

The bandgaps of two of the alloys produced were determined as  $4.19 \pm 0.05\text{eV}$  and  $3.8 \pm 0.1\text{eV}$ , and these shown to allow the bandgap of MgS to be determined as  $4.55 \pm 0.35\text{eV}$ . The work also demonstrated the effect that varying some of the flux ratios has on the composition, showing that varying the selenium flux has a larger effect than varying the zinc. This also shows that it may be hard to grow thick layers of lattice matched alloy consistently as even small (2-5%) changes in the fluxes seemed to have a significant effect on the composition of the resultant alloy.

## 8.4. Chapter 6 – Optical Characterisation of II-VI Compounds and DBR Development

This chapter reported a large number of measurements made to optically characterise a number of the materials that the MBE group at HWU produces. PL measurements were made of a number of ZnCdSe based samples and these combined with results reposted elsewhere in this thesis used to determine a more accurate bowing parameter for ZnCdSe as  $0.37 \pm 0.05 \text{ eV}$ . PL measurements of ZnSe samples allowed the LO phonon and exciton binding energy to be determined as  $31.7 \pm 0.3 \text{ meV}$  and  $18.1 \pm 0.3 \text{ eV}$  respectively. Transmission measurements made at 300K of a 50nm thick ZnSe layer deposited on glass showed a Stokes shift of 32.2meV from the PL emission which is extremely close to the LO phonon energy measured from the PL, suggesting that the deposited layer is of a very high quality.

Reflectometry and XRD were used to show that the relaxation of ZnSe with increasing thickness is most closely modelled by the Dunstan geometrical model [8.1] and therefore shows a hyperbolic dependency with a critical thickness of ~150nm and a residual strain of -0.07%.

A large number of samples were also investigated using SE. Much of this investigation was of XRI samples where the layer of interest was sandwiched between ZnSe and as this is a new technique it was investigated thoroughly. The outcome of this investigation showed that below bandgap it produces good results but the masking of the features of the central layer by the ZnSe dispersion meant that the results were fairly unreliable above bandgap.

New dispersion curves were presented for ZnSe, ZnS, MgS, MnS and CdSe and in the case of MnS the curve presented is believed to be first reported data for the ZB phase. The oxide layer present on ZnSe was also investigated and found to be similar to that reported in the literature [8.2-8.4]. SE proved particularly good for characterising ZnS, MnS and ZnSSe as it provides a fast

and effective way to determine their thickness and composition in the case of ZnSSe. It also demonstrated that there appears to be an issue with the measurement of the flux from a manganese cell using an ion gauge and allowed the failure of ZnS/CrS XRI samples to be determined – the ZnS was growing five times faster than expected and therefore had fully relaxed. For these reasons SE appears to be a highly useful structural characterisation tool that should be further developed in the future.

## 8.5. Chapter 7 - $\mu$ -PL Characterisation of CdSe Quantum Dots Grown on QA Barrier

This chapter described the  $\mu$ -PL characterisation of a series of samples containing CdSe QDs grown on an MgS-rich QA barrier. Ensemble PL measurements showed that the dots appear similar to those grown on either ZnSe or MgS barriers and that the dots are smaller than those produced by depositing 3.6ML of CdSe on MgS.  $\mu$ -PL measurements showed a large number of individual emission lines each with FWHM of  $3 \pm 0.35$  meV. Temporal measurements of these individual lines showed significant energy and intensity jitter on a  $< 25$  ms timescale resulting in the larger than anticipated FWHM seen. The FWHM was found to be a weak function of the count time used suggesting a very fast underlying jitter mechanism. By looking at the correlation of the variation of the peak energies and intensities these lines are assigned to individual dots a dot density of  $4 \pm 1 \times 10^{10} \text{ cm}^{-2}$  determined.

Power scaling measurements made with spectra from HWC224 showed that the intensity initially increases approximately linearly ( $k=0.75 \pm 0.15$ ) before saturating, which suggests that there is a strong nonradiative process at work. By considering the power scaling co-efficient of the emission lines and their correlation it is possible to measure binding energies for the biexciton,  $E_B^{xx}$  and trion,  $E_B^{cx}$ , of  $24.5 \pm 1.5$  meV and  $23 \pm 3$  meV respectively.

Emission intensity jitter was observed to produce intensity decreases of more than 70% for a small number of the spectra obtained. These dramatic



decreases are consistent with the blinking seen in other single emitter work. By looking at the variation of the energy jitter with barrier thickness and relative dielectric permittivity,  $\epsilon_r$ , a roughly inverse square law relationship was found. This suggests that charges located at the surface of the QD samples may be one of the sources of the observed jitter in these samples.

## 8.6. Suggestions for Future Work

As each section of this thesis has covered fairly un-related work, future work will be proposed for each chapter individually.

### **Chapter 3. Spin Current Detector**

The main pieces of future work would be to grow new SCD samples based on a new design so as to solve the issues with the GaAs substrate and the difficulties in collecting emitted light due to the samples low thickness. There are a number of ways to address the issues with the SCD design but a lot of these are likely to have significant drawbacks, such as needing to etch away the GaAs substrate. However one option for solving both these issues would be to use the epitaxial lift-off (ELO) process pioneered for II-VI semiconductors by the MBE group at HWU and described in chapter 4.

The ELO process works by introducing a thin (5-10nm thick) sacrificial MgS layer into a structure and then etch it away after growth. This allows the layers above to then be transferred to a new substrate. As this new substrate can be selected without concern for its suitability for II-VI growth, it can therefore be chosen so it is suitable for the application the structure is to be used for. So in the case of the SCD it could be deposited on a material that is transparent at the pump wavelength, such as glass or fused silica. As MgS is used for the sacrificial layer it cannot also be used as a barrier material, so it would be necessary to use a suitable replacement barrier material. As will be explained in chapter 5, the MBE group has found that a QA with 15-20% zinc is both etch resistant and provides identical barrier behaviour to MgS.

The replacement of the MgS barriers in the SCD design would also allow the samples to be grown much thicker, as a composition that is lattice matched to GaAs could be used (this will also be discussed in chapter 5). This in turn would make collecting the emitted light from the samples easier as a much lower NA lens (or possibly a directly coupled optical fibre) could be used.

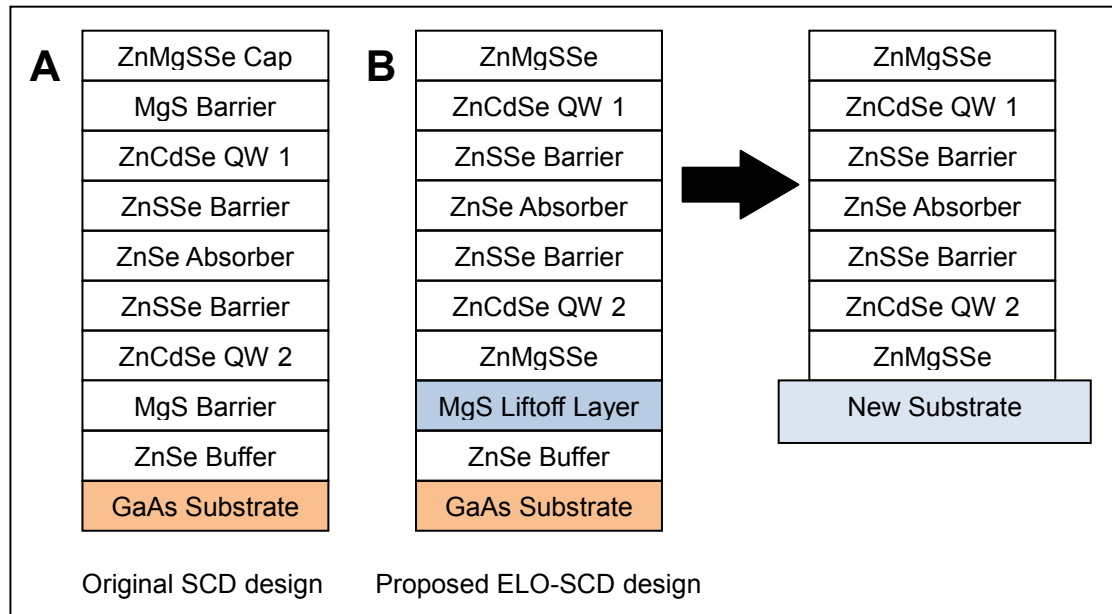


Fig. 8.1. Original (A) and proposed (B) spin current detector designs. The proposed structure after lift-off is also shown.

The original SCD1 design and a possible replacement are shown in figure 8.1. The changes are very small with only one extra QA layer being needed, due to the need to cap the original design with a QA layer to protect the MgS barrier.

The thickness of both the individual layers and the whole SCD structure are limited by the amount of strain energy they introduce due to their mismatch to GaAs, -0.28% and 0.56% for ZnSe and MgS respectively. From previous work it has been found that the maximum thickness of ZnSe that can be grown before relaxation occurs is ~150nm [8.5]. This represents a strain-thickness product of -0.4nm and it is assumed that this figure will be similar for II-VI layers (and samples) that have a positive mismatch. Hence any layer (or sample) whose strain-thickness product exceeds  $\pm 0.4\text{nm}$  will relax.

This is the reason that the ZnSe layer in the original SCD design was less than

100nm thick and limits the thickness of the other layers. This is shown schematically in figure 8.2, where the strain-thickness product for a series of SCD designs is shown. As one layer with a positive mismatch will can compensate for another layer with a negative mismatch, by summing the strain-thickness products for each layer, it is possible to determine at what point a multi-layer sample will begin to relax.

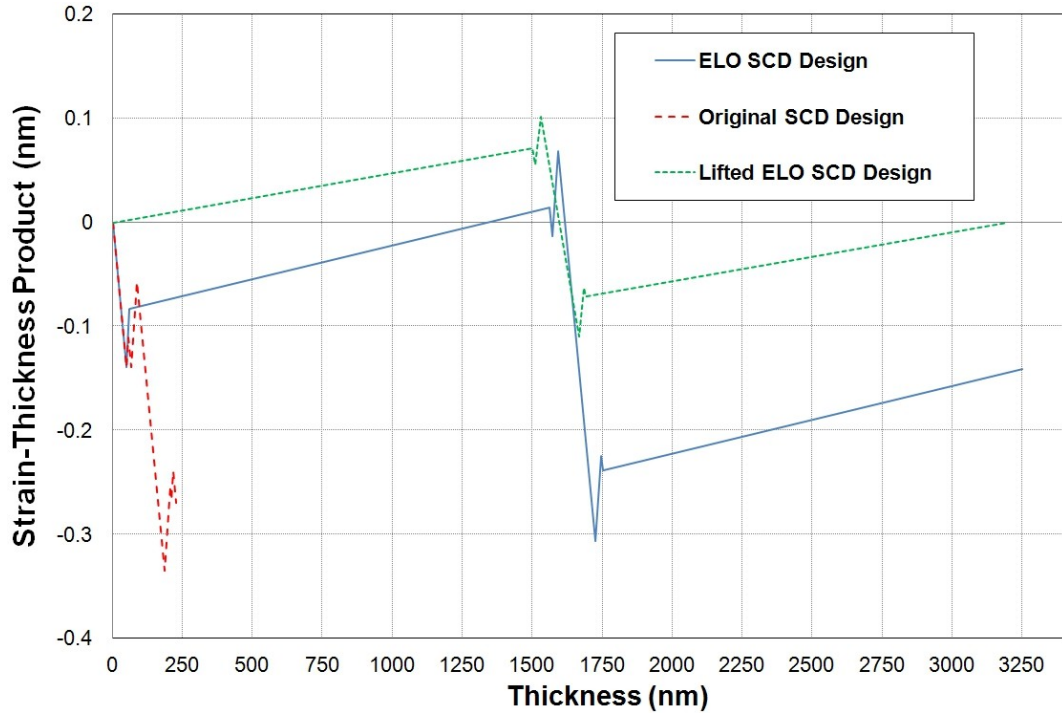


Fig 8.2. Strain-Thickness plot for a series of SCD designs.

In the case of the original SCD design the limiting factor is the absorption region thickness. It would be possible to increase the samples thickness to around 500nm by increasing the thickness of the MgS and ZnSSe barriers but this is likely to affect the structures optical performance. By replacing the MgS with QA barriers the thickness could theoretically be infinitely increased with the only limiting factor being the growth time (which would limit the thickness to ~6 $\mu$ m).

After growth the structures can be deposited onto a range of new substrates, but by depositing it onto a plano-convex lens it should be possible to increase the intensity of the 800nm light in the sample and therefore increase the two-photon absorption. The collection intensity could also be improved if a cleaved optical fibre with a carefully chosen core and cladding diameter was position close to the sample with a drop of index matching fluid placed between them, as

this should result in very effective coupling from the sample.

## Chapter 4. Epitaxial liftoff

There is much additional work that could be undertaken in this area to further develop the ELO process. One of the first possibilities would be to investigate the use of an MgTe sacrificial layer to extend the process to CdTe/ZnCdTe structures grown on InSb (or other substrates).

It would also be very interesting to continue the work to determine if the presence of pillars in the sacrificial layer can be detected. To achieve this two possible routes are suggested. The first would be to produce a structure with two N-doped ZnSe layers separated by an MgS layer. If there are pillars of ZnSe in the MgS then this would result in current flowing through the device and a much lower resistance. This could be compared to an identical structure but with an MgS layer grown under more optimised conditions.

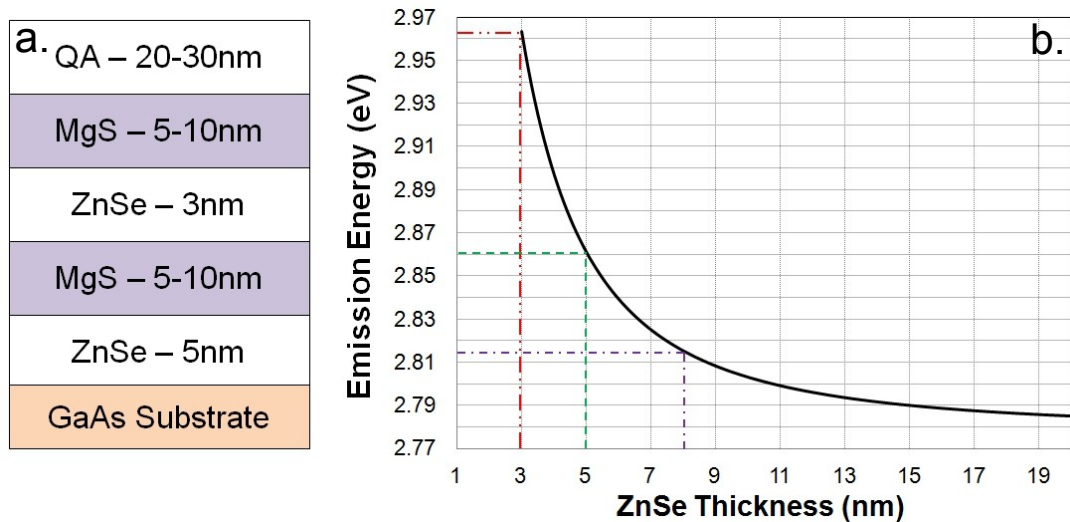


Fig. 8.3. (a) Proposed ZnSe/MgS QW structure and (b) ZnSe/MgS QW emission energy vs. thickness.

The second method to test for ZnSe pillars in the MgS layer would be to grow a ZnSe/MgS QW structure like that shown in figure 8.3(a). If there are pillars in the MgS, then during PL measurements at 77K some of the excitons generated will decay in the confined QW, some in the buffer layer and some in the pillar, and all of these will experience differing potentials so will emit at different energies. The only problem is ensuring that the emission energies are

sufficiently separated to be resolved. However by using a very thin buffer layer 5-10nm and a thin QW it should be possible to achieve this. The predicted energies of the three emissions are shown in fig. 8.3(b).

### MgS Based Samples

There is still considerable work to be done to optimise the original MgS process in terms of improving the percentage of lifted samples that are successfully deposited, as well as to investigate ways of improving the process, such as increasing the maximum area that can be lifted by using a different support mechanism. A flexible polymer film would be a sensible starting point as this has successfully been used with the III-V lift-off process [8.6].

### MgSe Based Samples

All of the samples produced for this work so far have either suffered from some sort of structural issues and therefore produced low quality deposited material, or have failed to lift. Therefore any further work would ideally begin with the growth of new structures. In particular 3-4 XRI samples should be grown with MgSe layer thickness varied from ~3–10nm but with lattice matched ZnCdSe. Using these structures it should then be possible to repeat the investigation contained in this chapter but hopefully produce higher quality deposited material. It would also be very interesting to compare successfully lifted MgSe samples with MgS ones lifted under similar conditions to see if there are any fundamental differences in the two processes. This has obviously not been possible so far due to the difficulties experienced with the MgSe based samples.

## **Chapter 5. Quaternary Alloy**

Information on the composition from other techniques that do not rely on X-ray diffraction would be useful, such as XPS. The XPS analysis of the samples which will be undertaken at St. Andrews University should produce

compositions with a reasonable degree of accuracy ( $\pm 1-2\%$ ) and allow the location of the alloy in the ZnMgSSe compositional space to be determined. As there are also bandgap figures for two of the samples it should also allow further restrict the range of allowed bandgaps for MgS. This is a priority as the uncertainty in its bandgap, as was demonstrated, is the largest source of uncertainty in determining the composition of QA.

It may also be possible to determine a bandgap for MgS directly by growing a structure that will allow its bandgap to be measured by a transmission measurement. The structure of the sample is shown in figure 8.4 and it contains two MgS layers. One layer (the lower one) is designed to act as a normal sacrificial layer, whilst the other is designed to be sufficiently thin that it does not lift. The QA layers around it then protect it from oxidation while its transmission is measured.

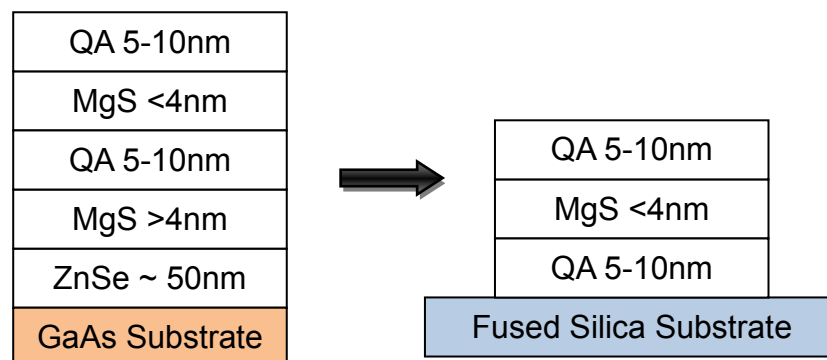


Fig. 8.4. Schematic of proposed MgS bandgap measurement sample.

The key to making this measurement possible is obtaining the correct composition and thicknesses for the QA. In this structure the composition does not necessarily need to be lattice matched but instead needs to be as wide bandgap as possible, but not more than 200-300meV below that of MgS, while at the same time remaining etch resistant. The thickness must also be carefully chosen to be thick enough to protect the MgS but thin enough that it does not absorb too much of the light incident on the sample, as otherwise the measurement will be of the QA and not the MgS.

Even if this can be achieved it will still be a difficult measurement to perform, as

trying to detect the absorption from 3-4nm of MgS sandwiched between two layers of QA 5-10nm thick will be difficult. However by comparing the transmission with that from a QA layer with the same composition and thickness as the two individual layers it should be possible to extract the bandgap of the MgS. I have already attempted to grow two samples based on this design but they both suffer from the same problem as the third series samples and will not etch.

If thick layers of a lattice match alloy are required, this work should be continued with the growth of another series of ELO XRD with QA thicknesses of 20-50nm and fluxes that are as near to those from the original series as possible. This will ensure that the lattice constant is close enough to GaAs that they will not relax. These samples should then be fully characterised so that the next set of samples can be designed to have a composition with a smaller mismatch.

After a lattice matched composition has been achieved, layers more than 100nm can be grown and x-ray measurements made to see if the layers have relaxed or show any signs of composition drift. Another approach would be to grow a super-lattice of multiple 50-100nm thick QA and ZnSe layers to determine the samples quality through the presence of additional XRD superlattice peaks. This second structure would also have the additional advantage that if properly designed (with ZnSe layers ~53nm thick and QA layers ~59nm thick) it will act as a distributed Bragg reflector (DBR) at a chosen wavelength (532nm for instance). This can then be used as another way to characterise the sample, as any change in the thickness or composition should produce a change in the reflectivity.

To improve the repeatability of the samples composition the standard Knudsen cell used for the selenium should be replaced with a sumo cell. These cells have a higher temperature and flux stability both inter and intra-growth, and should therefore reduce any changes in the flux that may effect the composition.

## Chapter 6. Optical Characterisation

As this chapter also covered a wide range of topics each area of future work will be presented in its own section.

### ZnCdSe PL and Bowing Parameter

To further improve this figure additional ZnCdSe samples should be investigated using PL. As bandgap figures were able to be determined for thin CdSe layers grown on GaAs, it should also be possible to measure a wider range of compositions grown on GaAs or InP.

### Spectroscopic Ellipsometry

Additional work to further develop SE as a characterisation tool would be the next area worth investigating. Looking at materials and samples that have already been thoroughly characterised using other techniques (PL, XRD, TEM, AFM etc.) would be of particular use as these would obviously allow the validity of the information produced by SE to be tested.

### ZnSe Native Oxide Layer

The use of a characterisation technique that is sensitive to surface composition would be an interesting extension of this work. The composition could be determined both over time and ideally during and after various etching or annealing of ZnSe samples had been performed. This would allow a greater understand of the oxide to be obtained.

### ZnS

Looking at further samples would be the obvious extension to this work as it should allow the reported dispersion curves for ZnS to be tested and a new model developed, if needed. Again looking at samples with other techniques that are sensitive to surface composition would be useful as it should allow better modelling of the surface oxide layer. It would also be highly useful to



attempt to obtain *in vacuo* dispersion data, which would probably be most easily achieved by collaborating with a group that possesses an *in situ* SE system.

## MgS

The MgS work should be continued as it is able to provide a lot of information about this material that would not otherwise be available. By looking at a large number of MgS samples grown under optimised conditions with thin ZnSe capping layers and then averaging their measured dispersion should allow a much more accurate dispersion relation to be determined.

## MnS

Again looking at a large number of additional samples should allow the work present here to be improved and expanded upon. As MnS does not appear to suffer from the oxidation that affects MgS it should be possible to work with samples that consist of a thick layer of uncapped MnS, but it would also be interesting to work with capped samples to both see how this effects the measured dispersion and to further investigate the dispersion of ZnSe,

## DBR

The obvious extension to the work presented here would be to attempt to grow the various designs present in this thesis and then measure their performance. As the reflectivity of the structures can be tailored to have specific values at different wavelengths and these are highly dependent on the dispersion of the materials that make up the DBR, in producing a series of DBRs it would allow the validity of the dispersion relations measure in this chapter to be determined.

## **Chapter 7. Micro-PL characterisation of CdSe QDs**

A large amount of work still needs to be undertaken to fully develop and investigate the growth of CdSe QDs on either MgS or ZnMgSSe barriers. For applications in optical spectroscopy this work would centre on eliminating the jitter seen in these samples to produce much sharper emission peaks.

The first step toward this would be to fully investigate the possibility that charges located at the surface are the cause of the jitter. There are 2 obvious approaches to investigate this, the first is to grow a series of identical samples with barriers of increasing thickness and see how this affects the jitter. The barriers can either be homogenous, or made up of a thin MgS or QA barrier with a thicker ZnSe layer grown on top, as either should move the surface charges away from the dot. Both options are shown schematically in fig. 8.5.

The second strategy would be to take the samples already studied and attempt to passivate any surface states present. This has already been attempted in other materials by using sulphur containing chemicals as sulphur atoms will bond with any dangling bonds on the surface [7.61]. As selenium dioxide has been found to be a strong oxidising agent [7.62], it would also be worth removing any that is present on the surface, as this should leave behind a metal oxide rich surface with a lower number of surface states. It is possible to achieve this simply by heating a sample that has been exposed to the atmosphere for a period of time in a vacuum chamber as this will allow the  $\text{SeO}_2$  to desorb.

Another key area for further investigating is the low emission intensity of these samples. An interesting approach to attempting to increase the carrier concentration without changing the CdSe layer would be to either to thin the lower barrier so it is only a few nanometres thick, or to grow an additional ZnSe layer a few nanometres below the CdSe layer, see fig. 8.5. The thicker ZnSe layer will absorb a large proportion of the photons transmitted through the CdSe layer and if the barrier thickness between the layer and the CdSe is carefully controlled, it should then be possible for excitons to tunnel into the QDs.

Increasing the emission intensity will also allow the pump intensity to be reduced, and in turn this would allow the effect of the electric field induced by the pump beam to be investigated. This could be investigated by placing contacts on the top and bottom of the sample so that a variable electric field can

be created whilst pumping at constant intensity.

A	ZnSe/QA/MgS ~ 10-100nm	B	QA/MgS ~ 10-	C	ZnSe/QA/MgS ~ 0-100nm
	QA/MgS ~ 10-		CdSe QDs		QA/MgS ~ 10-
	CdSe QDs		QA/MgS ~ 2-5nm		CdSe QDs
	QA/MgS ~ 10-		ZnSe ~ 10-20nm		QA/MgS ~ 2-5nm
	ZnSe – 36nm		QA/MgS ~ 10-		ZnSe – 36nm
	GaAs Substrate		ZnSe – 36nm		GaAs Substrate
			GaAs Substrate		

Fig. 8.5. Schematic of proposed future work samples. A) Thick top barrier/capping layer, B) enhanced QA/ZnSe QD sample, and C) standard sample with thinned lower barrier.

Another area that warrants further investigation would be the growth of further QD samples with QA barriers to fully investigate the variation of emission energy, intensity and FWHM with CdSe thicknesses. This further work would provide additional information about any similarities or differences between the QA barriers and MgS or ZnSe ones and would be a first step towards work to control the dot size, distribution and emission profile [8.7].

### Further Suggestions for future work

In addition to the future work suggested throughout this thesis two further ideas seem like they might produce interesting results. The first is to look at the intra-bandgap transitions of QD and QWs, as with the very large band offsets in our samples (estimated to be as much as 1.8eV for CdSe and MgS [8.8]) it should be possible to see emission and absorption at wavelengths that are otherwise un-accessible for the MBE group at HWU.

The second (and final) suggestion would be to look at producing lead sulphide or selenide (PbS/PbSe) QDs as although these are immiscible in II-VI compounds they have been shown to produce dots when grown on ZB barriers [8.9, 8.10]. PbS and PbSe are also very narrow bandgap (~0.37/0.27eV respectively) so would again provide a route to more interesting emission and absorption ranges that maybe of technological or commercial interest [8.11-8.17].

## 9. References

- [1.1] A.Y. Cho and J.R. Arthur, Prog. Solid State Chem. **10** (1975) p.157
- [1.2] A.Y. Cho, M.B. Panish, I. Hayashi, IOP Conf. Series **9** (1970) p.18
- [1.3] M.A. Herman and H. Sitter, "Molecular Beam Epitaxy", Springer (1996)
- [1.4] L. Torrison, J. Tolle, I.S.T. Tsong, and J. Kouvetakis, Thin Solid Films **434** (2003) p.106
- [1.5] A. Balocchi, A. Curran, T.C.M. Graham, C. Bradford, K.A. Prior, and R.J. Warburton, Appl. Phys. Lett. **86** (2005) 011915
  
- [2.1] A.Y. Cho, Thin Solid Films **100** (1983) p.291
- [2.2] J. Massies and J.P. Contour, J. Appl. Phys. **58** (1985) p.806
- [2.3] M.J. Chester and T. Jach, Phys. Rev. B **48** (1993) p.17262
- [2.4] M. Rei Vilar, J. El Beghdadi, F. Debontridder R. Artzi, R. Naaman, A.M. Ferraria, and A.M. Botelho do Rego, Surf. Interface Anal. **37** (2005) p.673
- [2.5] K.A. Prior, G.J. Davies, and R. Heckingbottom, J. Cryst. Growth **66** (1984) p.55
- [2.6] H. Morota and S. Adachi, J. Appl. Phys. **105** (2009) 043508
- [2.7] A. Guillén-Cervantes, Z. Rivera-Alvarez, M. López-López, E. López-Luna, and I. Hernández-Calderón, Thin Solid Films **373** (2000) p.159
- [2.8] A. Colli, E. Pelucchi, A. Franciosi, Appl. Phys. Lett. **83** (2003) p.81
- [2.9] W.C. Hughes, J.C. Boney, M.A.L. Johnson, J.W. Cook, Jr., and J.F. Schetzina, J. Cryst. Growth **175** (1997) p.546
- [2.10] J. Qiu, D.R. Menke, M. Kobayashi, R.L. Gunshor, D. Li, Y. Nakamura, and N. Otsuka, Appl. Phys. Lett. **58** (1991) p.2788
- [2.11] A. Stroppa and M. Peressi, Phys. Rev. B **72** (2005) 245304
- [2.12] A. Garcia and J.E. Northrup, Appl. Phys. Lett. **65** (1994) p.708
- [2.13] B.A. Joyce, J.H. Neave, P.J. Dobson, P.K. Larsen, Phys. Rev. B **29** (1984) p.814
- [2.14] J. Qiu, Q.D. Qian, R. L. Gunshor, M. Kobayashi, D. R. Menk, D. Li, and N. Otsuka, Appl. Phys. Lett. **56** (1990) p.
- [2.15] T.T. Hashizume, Q.-K. Xue, A. Ichimiya, and T. Sakurai, Phys. Rev. B **51** (1995) p.4200

- [2.16] A. Ohtake, T. Hanada, T. Yasuda, K. Arai, and T. Yao, Phys. Rev. B **60** (1999) p.8326
- [2.17] J.M. DePuydt, H. Cheng, J.E. Potts, T.L. Smith, and S.K. Mohapatra, J. Appl. Phys. **62** (1987) p.4756
- [2.18] A. Garcia, J. Vacuum Sci. and Tech. B **12** (1994) p.2678
- [2.19] C. Bradford, C.B. O'Donnell, B. Urbaszek, A. Balocchi, C. Morhain, K.A. Prior, and B.C. Cavenett, Appl. Phys. Lett. **76** (2000) p.3929
- [2.20] M. Funato, K. Omae, Y. Kawakami, Sg. Fujita, C. Bradford, A. Balocchi, K.A. Prior, and B.C. Cavenett, Phys. Rev. B **73** (2006) 245308
- [2.21] C. Bradford, C.B. O'Donnell, B. Urbaszek, A. Balocchi, C. Morhain, K.A. Prior, and B.C. Cavenett, J. Cryst. Growth **227** (2001) p.634
- [2.22] J. Luyo-Alvarado, M. Melendez-Lira, M. Lopez-Lopez, I. Hernandez-Calderon, M.E. Constantino, H. Navarro-Contreras, M.A. Vidal, Y. Takagi, K. Samonji, H. & Yonezu, J. Appl. Phys. **84** (1998) p.1551
- [2.23] R.T. Senger and K.K. Bajaj, Phys. Stat. Sol. (b) **241** (2004) p.1896
- [2.24] K. Yoshino, H. Mikami, K. Imai, M. Yoneta, and T. Ikari, Physica B **302** (2001) p.299
- [2.25] C.L. Mitsas and D.I. Siapkas, Appl. Optics **34** (1995) p.1678
- [2.26] S. Adachi, J. Appl. Phys. **66** (1989) p.6030
- [2.27] I.A. Davidson, R.T. Moug, F. Izdebski, C. Bradford, and K.A. Prior, Phys. Stat. Sol. (b) **247** (2010) p.1396
- [2.28] K. Pinaridi, U. Jain, S.C. Jain, H.E. Maes, R. Van Overstraeten, and M. Willander, J. Appl. Phys. **83** (1998) p.4724
- [2.29] J. Petruzzello, B.L. Greenberg, and R. Dalby, J. Appl. Phys. **63** (1988) p.2299
- [2.30] K.A. Prior, X. Tang, C. O'Donnell, C. Bradford, L. David, B.C. Cavenett, J. Cryst. Growth **251** (2003) p.565
- [2.31] A. Authier, Int. Union of Crystallography (2001) - '*Dynamical theory of x-ray diffraction*'
- [2.32] V. Holy, Springer (1999) - '*High-Resolution X-Ray Scattering from Thin Films and Multilayers*'
- [2.33] M.C. Tamargo, Taylor and Francis (2002) - '*II-VI semiconductor materials and their applications*'
- [2.34] B. Patton, W. Langbein, U. Woggon, Phys. Rev. B **68** (2003) 125316

- [2.35] R. Seguin, S. Rodt, A. Strittmatter, L. Reißmann, T. Bartel, A. Hoffmann, D. Bimberg, E. Hahn, and D. Gerthsen, *Appl. Phys. Lett.* **84** (2004) p.4023
- [2.36] J.A. Tuchman, S. Kim, Z. Sui, I.P. Herman, *Phys. Rev. B* **46** (1992) p.13371
- [2.37] Y.P. Varshni, *Physica* **34** (1967) p.149
- [2.38] U. Lunz, C. Schumacher, J. Nurnberger, K. Schull, A. Gerhard, U. Schussler, B. Jobst, W. Faschinger, G. Landwehr, *Semicond. Sci. Tech.* **12** (1997) p.970
- [2.39] K.A. Serrels, E. Ramsay, P.A. Dalgarno, B.D. Gerardot, J.A. O'Connor, R.H. Hadfield, R.J. Warburton and D.T. Reid, *J. Nanophotonics* **2** (2008) 021854
- [2.40] R.K. Ahrenkiel, *JOSA* **61** (1971) p.1651
- [2.41] K. Kato, F. Akinaga, T. Kamai, M. Wada, *J. Cryst. Growth* **138** (1994) p.373
- [2.42] R. Dahmani, L. Salamanca-Riba, N.V. Nguyen, D. Chandler-Horowitz, B.T. Jonker, *J. Appl. Phys.* **76** (1994) p.514
- [2.43] S. Adachi and T. Taguchi, *Phys. Rev. B* **43** (1991) p.9569
- [2.44] S. Adachi, *Phys. Rev. B* **43** (1991) p.12316
- [2.45] Y.D. Kim, Y.D. Ko, S.G. Choi, S.D. Yoo, D.E. Aspnes, and B.T. Jonker, *J. Korean Physical Soc.* **31** (1997) p.L553
- [2.46] G.E. Jellison, *Thin Solid Films* **233** (1993) p.416
- [2.47] H. Fujiwara, Wiley (2007) -'Spectroscopic Ellipsometry: Principles and Applications'
- [2.48] J. Li and S.-T. Wu, *J. Appl. Phys.* **95** (2004) p.896
- [2.49] W. Sellmeier, *Annalen der Physik und Chemie* **219** (1871) p.272
- [2.50] G.E. Jellison and F.A. Modine, *Appl. Phys. Lett.* **69** (1996) p.371
- [2.51] G.E. Jellison and F.A. Modine, *Appl. Phys. Lett.* **69** (1996) p.2137
- [2.52] A.S. Ferlauto, G.M. Ferreira, J.M. Pearce, C.R. Wronski, R.W. Collins, X. Deng, and G. Ganguly, *J. Appl. Phys.* **92** (2002) p.2424
- [2.53] P. Drude, *Annalen der Physik* **306** (1900) p.566
- [2.54] A.R. Forouhi and I. Bloomer, *Phys. Rev. B* **34** (1986) p.7018
- [2.55] W.A. McGahan, T. Makovicka, J. Hale, and J.A. Woollam, *Thin Solid Films* **253** (1994) p.57
- [2.56] C.C. Kim and S. Sivananthan, *Phys. Rev. B* **53** (1996) p.1475

- [2.57] D. Franta, I. Ohlídal, P. Klapetek, A. Montaigne-Ramil, A. Bonanni, D. Stifter, and H. Sitter, J. Appl. Phys. **92** (2002) p.1873
- [2.58] H. Wemple and M. DiDomenico, Phys. Rev. B **3** (1971) p.1338
- [2.59] D.E. Aspnes, J.B. Theeten, and F. Hottier, Phys. Rev. B **20** (1979) p.3292
  
- [3.1] J. Bardeen and W.H. Brattain, Phys. Rev. **74** (1948) p.230
- [3.2] Semiconductor Industry Association (SIA) Global Sales Report 2012
- [3.3] G.E. Moore, Electronics **38** (1965) p.4
- [3.4] W. Arden, M. Brillouët, P. Cogez, M. Graef, B. Huizing, R. Mahnkopf, ITRS (2010) - “More-than-Moore” White Paper
- [3.5] S.A. Wolf, D.D. Awschalom, R.A. Buhrman, J.M. Daughton, S. von Molnar, M.L. Roukes, A.Y. Chtchelkanova, D.M. Treger, Science **294** (2001) p.1488
- [3.6] I. Zutic, J. Fabian, and S. Das Sarma, Rev. Mod. Phys. **76** (2004) p.323
- [3.7] D.D. Awschalom and M.E. Flatté, Nature Physics **3** (2007) p.153
- [3.8] D.D. Awschalom, R.J. Epstein, and R. Hanson, Scientific American **297** (2007) p.84
- [3.9] P. Asshoff, A. Merz, H. Kalt, and M. Hetterich, Appl. Phys. Lett. **98** (2011) 112106
- [3.10] W.H. Lau, J.T. Olesberg, and M.E. Flatté, Phys. Rev. B **64** (2001) 161301
- [3.11] ITRS 2007 Edition
- [3.12] G. Prinz, Science **282** (1998) p.1660
- [3.13] P. Ball, Nature **404** (2000) p.918
- [3.14] R. Jansen, Nature Materials **11** (2012) p.400
- [3.15] S.A. Wolf, Science **294** (2001) p.1488
- [3.16] M. Tanaka, J. Crystal Growth **201** (1999) p.660
- [3.17] G. Prinz and K. Hathaway, Phys. Today **48** (1995) p.24
- [3.18] R. Fiederling, M. Keim, G. Reuscher, W. Ossau, G. Schmidt, A. Waag and L.W. Molenkamp, Nature **402** (1999) p.787
- [3.19] M. Demper, L. Chen, C. Bradford, K.A. Prior, W. Heimbrod, Solid State Comm. **150** (2010) p.1092
- [3.20] W. Heimbrod, L. Chen, H.-A. Krug von Nidda, A. Loidl, P.J. Klar, L. David, and K.A. Prior, J. Korean Phys. Soc., **53** (2008) p.2852

- [3.21] L. David, C. Bradford, X. Tang, T.C.M. Graham, K.A. Prior, B.C. Cavenett, J. Crystal Growth **251** (2003) p.591
- [3.22] L. David and K.A. Prior, Phys. Stat. Sol. (b) **243** (2006) p.778
- [3.23] E. Hazrati, S.J. Hashemifar, and H. Akbarzadeh, J. Appl. Phys. 104 (2008) p.113719
- [3.24] B.T. Jonker, Y.D. Park, B.R. Bennett, H.D. Cheong, G. Kioseoglou, and A. Petrou, Phys. Rev. B **62** (2000) p.8180
- [3.25] J. Hübner, W.W. Rühle, M. Klude, D. Hommel, R.D.R. Bhat, J.E. Sipe, and H.M. van Driel, Phys. Rev. Lett. **90** (2003) 216601
- [3.26] S. M. Shibli, M. C. Tamargo, B. J. Skromme, S. A. Schwarz, C. L. Schwartz, R. E. Nahory, and R. J. Martin, J. Vacuum Sci. and Tech. B **8** (1991) p.187
- [3.27] C. D. Lee, B. K. Kim, J. W. Kim, S. K. Chang, and S. H. Suh, J. Appl. Phys. **76** (1994) p.928
  
- [4.1] A. Balocchi, A. Curran, T.C.M. Graham, C. Bradford, K.A. Prior, and R.J. Warburton, Appl. Phys. Lett. **86** (2005) 011915
- [4.2] A. Curran, R. Barbour, J.K. Morrod, K.A. Prior, A.K. Kar and R.J. Warburton, J. Korean Phys. Soc. **53** (2008) p.3007
- [4.3] A. Curran, S. Brown, R.J. Warburton and K.A. Prior, Phys. Stats. Sol. (b) **247** (2010) p.1399
- [4.4] L.M. Liu, G. Lindauer, W.B. Alexander, and P.H. Holloway. J. Vacuum Sci. and Tech. B **13** (1995) p.2238
- [4.5] M. Rei Vilar, J. El Beghdadi, F. Debontridder R. Artzi, R. Naaman, A.M. Ferraria, and A.M. Botelho do Rego, Surf. Interface Anal. **37** (2005) p.673
- [4.6] S. Pinel, J. Tasselli, J.P. Bailbé, A. Marty, P. Puech and D. Estève, J. Micromech. Microeng. **8** (1998) p.338
- [4.7] F. Dross, J. Robbelein, B. Vandevelde, E. Van Kerschaver, I. Gordon, G. Beaucarne and J. Poortmans, Applied Physics A **89** (2007) p.149
- [4.8] W.S. Wong, A.B. Wengrow, Y. Cho, A. Salleo, N.J. Quitoriano, N.W. Cheung, and T. Sands, J. Electronic Materials **28** (1999) p.1409
- [4.9] M. Konagai, M. Sugimoto and K. Takahashi, J. Cryst. Growth **45** (1978) p.277



- [4.10] E. Yablonowitch, T. Gmitter, J.P. Harbison, R. Bhat, Appl. Phys. Lett. **51** (1987) p.2222
- [4.11] E. Yablonovitch, D.M. Hwang, T.J. Gmitter, L.T. Forez and J.P. Harbison, Appl. Phys. Lett. **56** (1990) p.2419
- [4.12] E. Yablonovitch, T. Sands, D.M. Hwang, I. Schnitzer, T.J. Gmitter, S.K. Shastry, D.S. Hill, and J.C.C. Fan, Appl. Phys. Lett. **59** (1991) p.3159
- [4.13] E. Yablonovitch, T.J. Gmitter, J.P. Harbison and R. Bhat, IEEE Photo. Technol. Lett. **1** (1989) p.41
- [4.14] I. Pollentier, P. Demeester, A. Ackaert, L. Buydens, P. van Daele, R. Baets, Electron. Lett. **26** (1990) p.193
- [4.15] C. van Hoof, W. De Raedt, M. van Rossum, G. Borghs, Electron. Lett. **25** (1989) p.136
- [4.16] J. F. Klem, E. D. Jones, D. R. Jones, D. R. Myers, and J. A. Lott, J. Appl. Phys. **66** (1989) p.459
- [4.17] M.M.A.J. Voncken, J.J. Schermer, G. Maduro, G.J. Bauhuis, P. Mulder, P.K. Larsen, Mat. Sci. and Engineering B **95** (2002) p.242
- [4.18] J.J. Schermer, P. Mulder, G.J. Bauhuis, M.M.A.J. Voncken, J.V. Deelen, E. Haverkamp, & P.K. Larsen, Phys. Stat. Sol. (a) **202** (2005) p.501
- [4.19] W Chang, C.P Kao, G.A Pike, J.A Slone, E Yablonovitch, Solar Energy Mat. and Solar Cells **58** (1999) p.141
- [4.20] E. Yablonovitch final technical report ELO solar cells
- [4.21] C. Bradford, C.B. O'Donnell, B. Urbaszek, A. Balocchi, C. Morhain, K.A. Prior, and B.C. Cavenett, Appl. Phys. Lett. **76** (2000) p.3929
- [4.22] M. Funato, K. Omae, Y. Kawakami, Sg. Fujita, C. Bradford, A. Balocchi, K.A. Prior, and B.C. Cavenett, Phys. Rev. B **73** (2006) 245308
- [4.23] C. Bradford, C.B. O'Donnell, B. Urbaszek, A. Balocchi, C. Morhain, K.A. Prior, and B.C. Cavenett, J. Cryst. Growth **227** (2001) p.634
- [4.24] K. Prior, personal communication
- [4.25] A. Gusso and G. J. Delben, J. Phys. D, Appl. Phys. **41** (2008) 175405
- [4.26] R. Taylor, HWU BSc Student Project Report 2009
- [4.27] Apezion Wax Datasheet
- [4.28] S.Y. Wang, J. Simpson, K.A. Prior, and B.C. Cavenett, J. Appl. Phys. **72** (1992) p.5311
- [4.29] J.D. Wu, Y.S. Huang, B.S. Li, A. Shen, M.C. Tamargo, and K.K. Tiong, J. Appl. Phys. **108** (2010) 123105

- [4.30] S.P. Guo, L. Zeng, and M.C. Tamargo, Appl. Phys. Lett. **78** (2001) p.1
- [4.31] K.A. Prior, X. Tang, C. O'Donnell, C. Bradford, L. David, B.C. Cavenett, J. Cryst. Growth **251** (2003) p.565
- [4.32] C. D. Lee, B. K. Kim, J. W. Kim, S. K. Chang, and S. H. Suh, J. Appl. Phys. **76** (1994) p.928
- [4.33] F. Séby, M. Potin-Gautier, E. Giffaut, G. Borge, and O.F.X. Donard, Chemical Geology **171** (2001) p.173
- [4.34] R.T. Moug, C. Bradford, F. Izdebski, I. Davidson, A. Curran, K.A. Prior and R.J. Warburton, Microelectronics Journal **40** (2009) 530
- [4.35] R.T. Moug, C. Bradford, K.A. Prior, J. Cryst. Growth **301** (2007) p.289
  
- [5.1] A. Curran, S. Brown, R.J. Warburton and K.A. Prior, Phys. Stats. Sol. (b) **247** (2010) p.1399
- [5.2] G. Horsburgh, K.A. Prior, W. Meridith, I. Galbraith, B.C. Cavenett, G. Lacey, A.G. Cullis, C.R. Whitehouse, P. Parbrook, P. Möck and K. Mizuno, Appl. Phys. Lett. **72** (1998) p.3148
- [5.3] B. Urbaszek, C.M. Townsley, X. Tang, C. Morhain, A. Balocchi, K.A. Prior, R.J. Nicholas, B.C. Cavenett, Phys. Rev. B **64** (2001) 155321
- [5.4] V.S. Sorokin, S.V. Sorokin, V.A. Kaygorodov, S.V. Ivanov, J. Cryst. Growth **214** (2000) p.130
- [5.5] R.T. Moug, C. Bradford, F. Izdebski, I. Davidson, A. Curran, R.J. Warburton, K.A. Prior, A. Aouni, F.M. Morales, S.I. Molina, J. Crystal Growth **311** (2009) p.2099
- [5.6] I.A. Davidson , R.T. Moug, F. Izdebski, C. Bradford, and K.A. Prior, Phys. Stat. Sol. (b) **247** (2010) p.1396
- [5.7] U. Lunz, C. Schumacher, J. Nurnberger, K. Schull, A. Gerhard, U. Schussler, B. Jobst, W. Faschinger, G. Landwehr, Semicond. Sci. Tech. **12** (1997) p.970
- [5.8] S. Yamaguchi, Y. Kawakami, S. Fujita, S. Fujita, Y. Yamada, T. Mishina, and Y. Masumoto, Phys. Rev. B **54** (1996) p.2629
- [5.9] Z. Charifi, H. Baaziz, N. Bouarissa, Physica B **337** (2003) p.363
- [5.10] J. Gutowski, N. Presser, G. Kudlek, Phys. Stat. Sol. (a) **120** (1990) p.11
- [5.11] B. Rockwell, H.R. Chandrasekhar, M. Chandrasekhar, A.K. Ramdas, M. Kobayashi, and R.L. Gunshor, Phys. Rev. B **44** (1991) p.11307

- [5.12] J. Riley, D. Wolfram, D. Westwood, A. Evans, J. Cryst. Growth **160** (1996) p.193
- [5.13] C. Bradford, C.B. O'Donnell, B. Urbaszek, C. Morhain, A. Balocchi, K.A. Prior, and B.C. Cavenett, Phys. Rev. B **64** (2001) 195309
- [5.14] T. Taguchi, Y. Kawakami and Y. Yamada, Physica B **191** (1993) p.23
- [5.15] X. Fang, T. Zhai, U.K. Gautam, L. Li, L. Wu, Y. Bando, D. Golberg, Progress in Materials Science **56** (2011) p.175
- [5.16] R.A. Rosenberg, G.K. Shenoy, F. Heigl, S.-T. Lee, P.-S.G. Kim, X.-T. Zhou, and T.K. Sham, Appl. Phys. Lett. **86** (2005) 263115
- [5.17] S. Ozaki and S. Adachi, J. Appl. Phys. **75** (1994) p.7470
- [5.18] H. Okuyama, Y. Kishita, A. Ishibashi, Phys. Rev. B **57** (1998) p.2257
- [5.19] C. Bradford, C.B. O'Donnell, B. Urbaszek, A. Balocchi, C. Morhain, K.A. Prior, and B.C. Cavenett, Appl. Phys. Lett. **76** (2000) p.3929
- [5.20] P. Pouloupoulos, S. Baskoutas, V. Karoutsos, M. Angelakeris and N.K. Flevaris, J. Phys.: Conf. Ser. **10** (2005) p.259
- [5.21] A. Chergui, J. Valenta, J. Moniatte, P. Gilliot, J.B. Grun, T. Cloitre and R.L. Aulombard, Semicond.Sci.Technol. **11** (1996) p.952
- [5.22] T. Tawara, H. Yoshida, T. Yogo, S. Tanaka, I. Suemune, J. Cryst. Growth **214** (2000) p.1019
- [5.23] H. Okuyama , Y. Kishita, A. Ishibashi, Phys. Rev. B **57** (1998) p.4
- [5.24] El Haj Hassan, F.A. Bleybel, A. Hijazi, A. Alaeddine, B. Beydoun and M. Zoaeter, Mater. Lett. **61** (2007) p.1178
- [5.25] R. Pandey, J.E. Jaffe, A.B. Kunz, Phys. Rev. B **43** (1991) p.11
  
- [6.1] N.M. Ravindra, P. Ganapathy, J. Choi, Infrared Phys. and Tech. **50** (2007) p.21
- [6.2] P.J.L. Herve, L.K.J. Vandamme, Infrared Phys. and Tech. **35** (1994) p.609
- [6.3] T.S. Moss, Phys. stat. sol. (b) **131** (1985) p.415
- [6.4] S. Zollner, J. Appl. Phys. **90** (2001) p.515
- [6.5] S. Adachi, J. Appl. Phys. **66** (1989) p.6030
- [6.6] D.E. Aspnes and A.A. Studna, Phys. Rev. B **27** (1983) p.985
- [6.7] M. Wassermeier, J. Behrend, J.-T. Zettler, K. Stahrenberg, K.H. Ploog, Appl. Surf. Sci. **107** (1996) p.48

- [6.8] E.D. Palik, Academic Press (1998) - 'Handbook of optical constants of solids (3rd edition)'
- [6.9] T. Taguchi, Y. Kawakami and Y. Yamada, *Physica B* **191** (1993) p.23
- [6.10] U. Lunz, C. Schumacher, J. Nurnberger, K. Schull, A. Gerhard, U. Schussler, B. Jobst, W. Faschinger, G. Landwehr, *Semicond. Sci. Tech.* **12** (1997) p.970
- [6.11] R.A. Rosenberg, G.K. Shenoy, F. Heigl, S.-T. Lee, P.-S.G. Kim, X.-T. Zhou, and T.K. Sham, *Appl. Phys. Lett.* **86** (2005) 263115
- [6.12] H. Okuyama, Y. Kishita, A. Ishibashi, *Phys. Rev. B* **57** (1998) p.2257
- [6.13] A. Chergui, J. Valenta, J. Moniatte, P. Gilliot, J.B. Grun, T. Cloitre and R.L. Aulombard, *Semicond.Sci.Technol.* **11** (1996) p.952
- [6.14] P. Hlubina, J. Lunacek, D. Ciprian, and R. Chlebus, *Appl. Phys. B* **92** (2008) p.203
- [6.15] F.C. Peiris, S. Lee, U. Bindley, and J.K. Furdyna, *J. Appl. Phys.* **84** (1998) p.5194
- [6.16] K. Betzler, A. Gröne, N. Schmidt, and P. Voigt, *Rev. Sci. Instrum.* **59** (1988) p.652
- [6.17] M.H. Chiu, J.Y. Lee, D.C. Su, *Appl. Optics* **38** (1999) p.4047
- [6.18] I.M. Dharmadasa, C.J. Blomfield, R. Coratger, F. Ajustron, J. Beauvillain, J. Simpson, K.A. Prior and B.C. Cavanett, *Mat. Sci. and Tech.* **12** (1996) p.86
- [6.19] O. Fursenko, J. Bauer, A. Goryachko, D. Bolze, P. Zaumseil, D. Krüger, D. Wolansky, E. Bugiel, B. Tillack, *Thin Solid Films* **450** (2004) p.248
- [6.20] T. Trepk, M. Zorn, J.-T. Zettler, M. Klein, W. Richter, *Thin Solid Films* **313** (1998) p.496
- [6.21] K. Kato, F. Akinaga, T. Kamai, M. Wada, *J. Cryst. Growth* **138** (1994) p.373
- [6.22] R. Dahmani, L. Salamanca-Riba, N.V. Nguyen, D. Chandler-Horowitz, B.T. Jonker, *J. Appl. Phys.* **76** (1994) p.514
- [6.23] S. Adachi and T. Taguchi, *Phys. Rev. B* **43** (1991) p.9569
- [6.24] S. Adachi, *Phys. Rev. B* **43** (1991) p.12316
- [6.25] Y.D. Kim, Y.D. Ko, S.G. Choi, S.D. Yoo, D.E. Aspnes, and B.T. Jonker, *J. Korean Physical Soc.* **31** (1997) p.L553
- [6.26] M.S. Koo, T.J. Kim, M.S. Lee, M.S. Oh, Y.D. Kim, S.D. Yoo, D.E. Aspnes, and B.T. Jonker, *Appl. Phys. Lett.* **77** (2000) p.3364

- [6.27] B. Jobst, PhD Thesis (1996) Würzburg University
- [6.28] D. Franta, I. Ohlídal, P. Klapetek, A. Montaigne-Ramil, A. Bonanni, D. Stifter, and H. Sitter, *J. Appl. Phys.* **92** (2002) p.1873
- [6.29] M. Schmidt, P. Bornmann and I. Wilhelm, *Angewandte Chemie International Edition in English* (1963) p.691
- [6.30] G.R. Waitkins and C.W. Clark, *Chem. Rev.* **36** (1945) p.250
- [6.31] X.B. Zhang and S.K. Hark, *Appl. Phys. Lett.* **74** (1999) p.3857
- [6.32] A. Kita, M. Ozawa, D.D. Gutleben, *Appl. Surf. Sci.* **100** (1996) p.652
- [6.33] J.B. Smathers, E. Kneeder, B.R. Benett, B.T. Jonker, *Appl. Phys. Lett.* **72** (1998) p.1238
- [6.34] I.M. Dharmadasa, C.J. Blomfield, G.E. Gregory, B.C. Cavanett, K.A. Prior and J. Simpson, *Surf. And Interface Anal.* **21** (1994) p.718
- [6.35] R. Coratger, C. Girardin, J. Beauvillain, I.M. Dharmadasa, A.P. Samanthilake, J.E.F. Frost, K.A. Prior, B.C. Cavenett, *J. Appl. Phys.* **81** (1997) p.7870
- [6.36] Y. Koide, K. Hashimoto, H. Ishikawa, K. Tsukui, T. Oku, N. Teraguchi, Y. Tomomura, A. Suzuki, and M. Murakami, *J. Cryst. Growth* **159** (1996) p.709
- [6.37] R.B. Finkelman and M.E. Mrose, *American Mineralogist* **62** (1977) p.316
- [6.38] R.F. Brebrick, *J. Phase Equilibria* **21** (2000) p.235
- [6.39] T. Innami, T. Miyazaki and S. Adachi, *J. Appl. Phys.* **86** (1999) p.1382
- [6.40] S. Zollner, *Appl. Phys. Lett.* **63** (1993) p.2523
- [6.41] H. Yoshikawa and S. Adachi, *Jpn. J. Appl. Phys.* **36** (1997) p.6237
- [6.42] J.M. Khoshman and M.E. Kordesch, *Thin Solid Films* **515** (2007) p.7393
- [6.43] L.T. Brownmiller, *American Mineralogist* **12** (1927) p.43
- [6.44] E.F. Schubert, J.K. Kim, and J.-Q. Xi., *Phys. Stat. Sol. (b)* **244** (2007) p.3002
- [6.45] M. Linnik and A. Christou, *Mat. Sci. and Eng. B* **80** (2001) p.245
- [6.46] C.B. Fu, C.S. Yang, M.C. Kuo, Y.J. Lai, J. Lee, J.L. Shen, W.C. Chou, and S. Jeng, *Chin. J. Phys.* **41** (2003) p. 535
- [6.47] A. Salokatve, K. Rakennus, P. Uusimaa, M. Pessa, T. Aherne, J.P. Doran, J. O'Gorman, and J. Hegarty, *Appl. Phys. Lett.* **67** (1995) p.407
- [6.48] P. Uusimaa, K. Rakennus, A. Salokatve, M. Pessa, T. Aherne, J.P. Doran, J. O'Gorman, J. Hegarty, *Appl. Phys. Lett.* **67** (1995) p.2197

- [6.49] T. Tawara, I. Suemune, S. Tanaka, J. Cryst. Growth **214** (2000) p.1019
- [6.50] C. Kruse, H. Lohmeyer, K. Sebald, J. Gutowski, D. Hommel, J. Wiersig, and F. Jahnke, Appl. Phys. Lett. **92** (2008) 031101
- [6.51] W. Pacuski, C. Kruse, S. Figge, and D. Hommel, Appl. Phys. Lett. **94** (2009) 191108
- [6.52] A. Sweiti, F. Medina, L. Martinez and A. Lopez-Rivera, Semicond. Sci. Tech. **23** (2008) 035019
- [6.53] D. Mourad, G. Czycholl, C. Kruse, S. Klembt, R. Retzlaff, D. Hommel, M. Gartner, M. Anastasescu, Phys. Rev. B **82** (2010) 165204
- [6.54] U. Lunz, J. Kuhn, F. Goschenhofer, U. Schüssler, S. Einfeldt, C.R. Becker, and G. Landwehr, J. Appl. Phys. **80** (1996) p.6861
- [6.55] A. Chergui, J. Valenta, J.L. Loison, M. Robino, I. Pelant, J.B. Grun, R. Levy, O. Briot and R.L. Aulombard, Semicond. Sci. Tech. **9** (1994) p.2073
- [6.56] X. Wang, D. Huang, C. Sheng, and G. Yu, J. Appl. Phys. **90** (2001) p.6114
- [6.57] J. Gutowski, Semicond. Sci. Tech. **6** (1991) p.A51
- [6.58] G. Kudlek, N. Presser, J. Gutowski, K. Hingerl, H. Sitter, S.M. Durbin, D.R. Menke, M. Kobayashi, and R.L. Gunshor, J. Appl. Phys. **68** (1990) p.5630
- [6.59] J. Luyo-Alvarado, M. Melendez-Lira, M. Lopez-Lopez, I. Hernandez-Calderon, M.E. Constantino, H. Navarro-Contreras, M.A. Vidal, Y. Takagi, K. Samonji, H. & Yonezu, J. Appl. Phys. **84** (1998) p.1551
- [6.60] R. Tommasi, M. Lepore, M.C. Netti, I.M. Catalano, and I. Suemune, Phys. Rev. B **49** (1994) p.14367
- [6.61] J.A. Tuchman, S. Kim, Z. Sui, I.P. Herman, Phys. Rev. B **46** (1992) p.13371
- [6.62] R. Pässler, J. Appl. Phys. **86** (2003) p.4403
- [6.63] I. Kuskovsky, C. Tian, C. Sudbrack, G.F. Neumark, S.P. Guo, M.C. Tamargo, J. Crystal Growth **214** (2000) p.335
- [6.64] L.C. Calhoun and R.M. Park, J. Appl. Phys. **85** (1999) p.490
- [6.65] K. Yoshino, H. Mikami, K. Imai, M. Yoneta, and T. Ikari, Physica B **302** (2001) p.299
- [6.66] F. Gindele, U. Woggon, W. Langbein, J.M. Hvam, K. Leonardi, D. Hommel, and H. Selke, Phys. Rev. B **60** (1999) p.8773

- [6.67] E.D. Sim, J.H. Song, K.S. Baek and S.K. Chang, J. Korean Phys. Soc. **52** (2008) p.631
- [6.68] M.E. Constantino, H. Navarro-Contreras, M.A. Vidal, B. Salazar-Hernandez, A. Lastras-Martinez, I. Hernandez-Calderon and M. Lopez-Lopez, J. Phys. D **32** (1999) p.1293
- [6.69] N. Samarth, H. Luo, J.K. Furdyna, S.B. Qadri, Y.R. Lee, A.K. Ramdas, and N. Otsuka, Appl. Phys. Lett. **54** (1989) p.2680
- [6.70] W. Shan, J.J. Song, H. Luo, and J.K. Furdyna, Phys. Rev. B **50** (1994) p.8012
- [6.71] M. Funato, K. Omae, Y. Kawakami, Sg. Fujita, C. Bradford, A. Balocchi, K.A. Prior, and B.C. Cavenett, Phys. Rev. B **73** (2006) 245308
- [6.72] S. Birner, S. Hackenbuchner, M. Sabathil, G. Zandler, J.A. Majewski, T. Andlauer, T. Zibold, R. Morschl, A. Trellakis, and P. Vogl, Acta Physica Polonica A **110** (2006) p.111
- [6.73] H. Mathieu, P. Lafebvre, and P. Christol, Phys. Rev. B **46** (1992) p.4092
- [6.74] QWtrans program written by B. Urbaszek and M. Funato
- [6.75] G.. Horsburgh, K.A. Prior, W. Meridith, I. Galbraith, B.C. Cavenett, G. Lacey, A.G. Cullis, C.R. Whitehouse, P. Parbrook, P. Möck and K. Mizuno, Appl. Phys. Lett. **72** (1998) p.3148
- [6.76] A.G. Kontos, E. Anastassakis, N. Chrysanthakopoulos, M. Calamiotou and U. Pohl, J. Appl. Phys. **86** (1999) p.412
- [6.77] D. Dunstan, S. Young, and R. Dixon, J. Appl. Phys. **70** (1991) p.3038
- [6.78] V.H. Etgens, B. Capelle, L. Carbonell, and M. Eddrief, Appl. Phys. Lett. **75** (1999) p.2108
- [6.79] K. Pinardi, U. Jain, S.C. Jain, H.E. Maes, R. Van Overstraeten, and M. Willander, J. Appl. Phys. **83** (1998) p.4724
- [6.80] C.D. Lee, B.K. Kim, J.W. Kim, S.K. Chang, and S.H. Suh, J. Appl. Phys. **76** (1994) p.928
- [6.81] K. Mohammed, D.A. Cammack, R. Dalby, P. Newbury, B.L. Greenberg, J. Petruzzello, and R.N. Bhargava, Appl. Phys. Lett. **50** (1987) p.37
- [6.82] C.C. Kim and S. Sivananthan, Phys. Rev. B **53** (1996) p.1475
- [6.83] L. Rolland, C. Vallée, M.-C. Peignon, C. Cardinaud, Appl. Surf. Sci. **164** (2000) p.147
- [6.84] Y.D. Kim, S.L. Cooper, M.V. Klein, and B.T. Jonker, Appl. Phys. Lett. **62** (1993) p.2387

- [6.85] T.J. Kim, M.S. Koo, M.S. Lee, Y.D. Kim, D.E. Aspnes and B.T. Jonker, J. Korean Phys. Soc. **39** (2001) p.S372
- [6.86] T. Tsuchiya, S. Ozaki and S. Adachi, J. Phys.:Codens. Mater. **15** (2003) p.3717
- [6.87] U. Lunz, B. Jobst, S. Einfeldt, C.R. Becker, D. Hommel, G. Landwehr, J. Appl. Phys. **77** (1995) p.5377
- [6.88] M. Rabah, B. Abbar, Y. Al-Douri, B. Bouhafs, B. Sahraoui, Mat. Sci. and Engineering **B100** (2003) p.163
- [6.89] T. Tawara, H. Yoshida, T. Yogo, S. Tanaka, I. Suemune , J. Cryst. Growth **221** (2000) p.699
- [6.90] R. Schmidt-Grund, A. Carstens, B. Rheinländer, D. Spemann, H. Hochmut, G. Zimmermann, M. Lorenz, M. Grundmann, C.M. Herzinger, and M. Schubert, J. Appl. Phys. **99** (2006) 123701
- [6.91] T. Tawara, H. Yoshida, T. Yogo, S. Tanaka, I. Suemune, J. Cryst. Growth **214** (2000) p.1019
- [6.92] H. Okuyama, Y. Kishita, A. Ishibashi, Phys. Rev.B **57** (1998) p.4
- [6.93] El Haj Hassan, F.A. Bleybel, A. Hijazi, A. Alaeddine, B. Beydoun and M. Zoaeter, Mater. Lett. **61** (2007) p.1178
- [6.94] R. Pandey, J.E. Jaffe, A.B. Kunz, Phys. Rev. B **43** (1991) p.11
- [6.95] B.J. Wood and R.G.J. Strens, Mineralogical Magazine **43** (1979) p.509
- [6.96] L. David PhD Thesis (2006) Heriot-Watt Uni.
- [6.97] T. Tawara, H. Yoshida, T. Yogo, S. Tanaka, I. Suemune, J. Korean Phys. Soc. **50** (2007) p.367
- [6.98] C.M. Herzinger, P.G. Snyder, B. Johs, and J.A. Woollam, J. Appl. Phys. **77** (1995) p.4677
- [6.99] F.C. Peiris, S. Lee, U. Bindley, and J.K. Furdyna, J. Appl. Phys. **86** (1999) p.918
- [6.100] T. Yao, Z.Q. Zhu, K. Uesugi, S. Kamiyama, M. Fujimoto, J. Vac. Sci. Technol. A **8** (1990) p.997
- [6.101] Z. Zhu, M. Hagino, K. Uesugi, S. Kamiyama, M. Fujimoto and T. Yao, Jpn. J. Appl. Phys. **28** (1989) p. 1659
- [6.102] Y.H. Lai, W.-Y. Cheung, S.-K. Lok, G.K.L. Wong, S.-K. Ho, K.-W. Tam and I.-K. Sou, AIP Advances **2** (2012) 012149
- [7.1] A. Mews and J. Zhao, Nature Photonics **1** (2007) p.683



- [7.2] R.B. Laghumavarapu, M. El-Emawy, N. Nuntawong, A. Moscho, L.F. Lester, and D.L. Huffaker, Appl. Phys. Lett. **91** (2007) 243115
- [7.3] T.C.M. Graham X. Tang, K.A. Prior, B.C. Cavenett, and R.J. Warburton, J. Crystal Growth **278** (2005) p.743
- [7.4] K. Kitamura, H. Umeya, A. Jia, M. Shimotomai, Y. Kato, M. Kobayashi, A. Yoshikawa, K. Takahashi, J. Crystal Growth **214** (2000) p.680
- [7.5] M.C Kuo, C.S Yang, P.Y Tseng, J Lee, J.L Shen, W.C Chou, Y.T Shih, C.T Ku, M.C Lee, W.K Chen, J. Crystal Growth **242** (2002) p.533
- [7.6] C. Bradford, B. Urbaszek, M. Funato, A. Balocchi, T.C.M. Graham, E.J. McGhee, R.J. Warburton, K.A. Prior, B. Cavenett, J. Crystal Growth **251** (2003) p.581
- [7.7] A. Balocchi , A. Curran, T.C.M. Graham, C. Bradford, K.A. Prior, and R.J. Warburton, Appl. Phys. Lett. **86** (2005) 011915
- [7.8] A. Curran J.K. Morrod, K.A. Prior, A.K. Kar and R.J. Warburton, Semicond. Sci. Technol. **22** (2007 ) p.1189
- [7.9] I.L. Krestnikov, N.N. Ledentsov, A. Hoffmann, and D. Bimberg, Phys. Stats. Sol. (a) **183** (2001) p.207
- [7.10] C. Bradford, C.B. O'Donnell, B. Urbaszek, A. Balocchi, C. Morhain, K.A. Prior, and B.C. Cavenett, Appl. Phys. Lett. **76** (2000) p.3929
- [7.11] R.T. Moug, C. Bradford, F. Izdebski, I. Davidson, A. Curran, K.A. Prior and R.J. Warburton, Microelectronics Journal **40** (2009) 530
- [7.12] I.A. Davidson , R.T. Moug, F. Izdebski, C. Bradford, and K.A. Prior, Phys. Stat. Sol. (b) **247** (2010) p.1396
- [7.13] R.T. Moug, C. Bradford,D. Thuau, A. Curran, R.J. Warburton and K.A. Prior, J.Korean Physical Society **53** (2008) p.3004
- [7.14] T. Makino, R. André, J.-M. Gérard, R. Romestain, Le Si Dang, M. Bartels, K. Lischka, and D. Schikora, Appl. Phys. Lett. **82** (2003) p.2227
- [7.15] M. Funato, A. Balocchi, C. Bradford, K.A. Prior, and B.C. Cavenett, Appl. Phys. Lett. **80** (2002) p.443
- [7.16] B. Urbaszek , C. Bradford , M. Funato , T.C.M. Graham , E.J. McGhee , R.J. Warburton , K.A. Prior , B.C. Cavenett, IOP Conference Series **171** (2002) p.154
- [7.17] R.J. Warburton, C. Schäflein, D. Haft, F. Bickel, A. Lorke, K. Karrai, J.M. Garcia, W. Schoenfeld & P.M. Petroff, Nature **405** (2000) p.926

- [7.18] S. Lee, J.C. Kim, H. Rho, C.S. Kim, L.M. Smith, H.E. Jackson, J.K.. Furdyna, and M. Dobrowolska, Phys. Rev. B **61** (2000) p.R2405
- [7.19] T.J. Kim, S.Y. Lee, A.J. Choi and Y.D. Kim, J. Korean Physical Society **50** (2007) p.806
- [7.20] T.H. Ghong, Y.W. Jung, J.J. Yoon, Y.D. Kim, H.J. Kim and Y.C. Chang, J. Korean Physical Society **53** (2008) p.367
- [7.21] H. Zajicek, P. Juza, E. Abramof, O. Pankratov, H. Sitter, M. Helm, G. Brunthaler, W. Faschinger, and K. Lischka, Appl. Phys. Lett. **62** (1993) p.717
- [7.22] R. Arians, T. Kümmell, G. Bacher, A. Gust, C. Kruse, and D. Hommel, Appl. Phys. Lett. **90** (2007) 101114
- [7.23] V. Türck, S. Rodt, R. Heitz, M. Strassburg, U.W. Pohl, D. Bimberg, Physica E **13** (2002) p.269
- [7.24] G. Sallen, A. Tribu, T. Aichele, R. André, L. Besombes, C. Bougerol, S. Tatarenko, K. Kheng, and J. Ph. Poizat, Phys. Rev. **80** (2009) 085310
- [7.25] J. Seufert, R. Weigand, G. Bacher, T. Kümmell, A. Forchel, K. Leonardi, and D. Hommel, Appl. Phys. Lett. **76** (2000) p.1872
- [7.26] B. Patton, W. Langbein, U. Woggon, Phys. Rev. B **68** (2003) 125316
- [7.27] K. Goshima, K. Komori, T. Sugaya, Jap. J. Appl. Phys. **46** (2007) p.2626
- [7.28] Q.Q. Wang, A. Muller, P. Bianucci, E. Rossi, Q.K. Xue, T. Takagahara, C. Piermarocchi, A.H. MacDonald, and C.K. Shih, Phys. Rev. B **72** (2005) 035306
- [7.29] D. Sarkar, H.P. van der Meulen, J.M. Calleja, J.M. Becker, R.J. Haug, and K. Pierz, J. Appl. Phys. **100** (2006) 023109
- [7.30] M. Grundmann and D. Bimberg, Phys. Rev B **55** (1997) p.9740
- [7.31] I.A. Akimov, A. Hundt, T. Flissikowski, P. Kratzert and F. Henneberger, Physica E **17** (2003) p.31
- [7.32] H.D. Sun, T. Makino, Y. Segawa, M. Kawasaki, A. Ohtomo, K. Tamura, and H. Koinuma , Appl. Phys. Lett. **78** (2001) p.3385
- [7.33] R. Seguin, S. Rodt, A. Strittmatter, L. Reißmann, T. Bartel, A. Hoffmann, D. Bimberg, E. Hahn, and D. Gerthsen, Appl. Phys. Lett. **84** (2004) p.4023
- [7.34] I.A. Akimov, A. Hundt, T. Flissikowski, F. Henneberger, Appl. Phys. Lett. **81** (2002) p.4730

- [7.35] M. Kaniber, M.F. Huck, K. Müller, E.C. Clark, F. Troiani, M. Bichler, H.J. Krenner and J.J. Finley, *Nanotechnology* **22** (2011) 325202
- [7.36] R.T. Senger and K.K. Bajaj, *Phys. Rev. B* **68** (2003) 205314
- [7.37] J. Valenta, R. Juhasz and J. Linnros, *Appl. Phys. Lett.* **80** (2002) p.1070
- [7.38] K. Matsuda, T. Inoue, Y. Murakami, S. Maruyama, and Y. Kanemitsu, *Phys. Rev. B* **77** (2008) 193405
- [7.39] P. Frantsuzov, M. Kuno, B. Jánko and R.A. Marcus, *Nature Physics* **4** (2008) p.519
- [7.40] R.R.G. Neuhauser, K.T. Shimizu, W.K. Woo, S.A. Empedocles, and M.G. Bawendi, *Phys. Rev. Lett.* **85** (2000) p.3301
- [7.41] H.D. Robinson and B.B. Goldsberg, *Phys. Rev. B* **61** (2000) p.R5086
- [7.42] G. Sallen, A. Tribu, T. Aichele, R. André, L. Besombes, C. Bougerol, M. Richard, S. Tatarenko, K. Kheng, and J.Ph. Poizat, *Nature Photonics* **4** (2010) p.698
- [7.43] P.A. Frantsuzov and R.A. Marcus, *Phys. Rev. B* **72** (2005) 155321
- [7.44] M. Califano, A. Franceschetti, and A. Zunger, *Phys. Rev. B* **75** (2007) 115401
- [7.45] D.-H. Lee, C.-T. Yuan, M. Tachiya, and J. Tang, *Appl. Phys. Lett.* **95** (2009) 163101
- [7.46] M. Ye and P.C. Searson, *Phys. Rev. B* **84** (2011) 125317
- [7.47] J. Seufert, M. Obert, M. Scheibner, N.A. Gippius, G. Bacher, A. Forchel, T. Passow, K. Leonardi, and D. Hommel, *Appl. Phys. Lett.* **79** (2001) p.1033
- [7.48] H.D. Robinson and B.B. Goldsberg, *Physica E* **6** (2000) p.444
- [7.49] A.L. Efros and M. Rosen, *Phys. Rev. Lett.* **78** (1997) p.1110
- [7.50] R. Verbeck, A. M. van Oijen, and M. Orrit, *Phys. Rev. B* **66** (2002) 233202
- [7.51] F. Cichos, C. von Borczyskowski, and M. Orrit, *Curr. Op. Coll. Int. Sci.* **12** (2007) p.272
- [7.52] K.T. Shimizu, W.K. Woo, B.R. Fisher, H.J. Eisler, and M.G. Bawendi, *Phys. Rev. B* **63** (2001) 205316
- [7.53] G. Margolin and E. Barkai, *Phys. Re. Lett.* **94** (2005) 080601
- [7.54] M. Kuno, D.P. Fromm, H.F. Hamann, A. Gallagher, and D.J. Nesbitt, *J. Chem Phys.* **115** (2001) p.1028

- [7.55] T. Makino, R. Andre, J.M. Gerard, R. Romestain, L.S. Dang, M. Bartels, K. Lischka and D. Schikora, Solid State Comms. **130** (2004) p.63
- [7.56] B. Mahler, P. Spinicelli, S. Buil, X. Quelin, J.P. Hermier, B. Dubertret, Nature Materials **7** (2008) p.659
- [7.57] C. Galland, Y. Ghosh, A. Steinbrück, M. Sykora, J.A. Hollingsworth V.A. Klimov, H. Htoon, Nature **479** (2011) p.203
- [7.58] X. Wang, X. Ren, K. Kahen, M.A. Hahn, M. Rajeswaran, S. Maccagnano-Zacher, J. Silcox, G.E. Cragg, A.L. Efros and T.D. Krauss, Nature **459** (2009) p.686
- [7.59] V.I. Klimov, J. Phys. Chem B **110** (2006) p.16827
- [7.60] B. Urbaszek, C. Morhain, C. Bradford, C.B. O'Donnell, S.A. Telfer, X. Tang, A. Balocchi, K.A. Prior, B.C. Cavenett, C.M. Townsley and R.J. Nicholas, Phys. Condens. Matter **13** (2001) p.2317
- [7.61] É. O'Connor, B. Brennan, V. Djara, K. Cherkaoui, S. Monaghan, S.B. Newcom3, R. Contreras, M. Milojevic, G. Hughes, M.E. Pemble, R.M. Wallace, and P.K. Hurley, J. Appl. Phys. **109** (2011) 024101
- [7.62] G.R. Waitkins and C.W. Clark, Chem. Rev. **36** (1945) p.235
  
- [8.1] D. Dunstan, S. Young, and R. Dixon, J. Appl. Phys. **70** (1991) p.3038
- [8.2] S. Adachi and T. Taguchi, Phys. Rev. B **43** (1991) p.9569
- [8.3] D. Franta, I. Ohlídal, P. Klapetek, A. Moutaigne-Ramil, A. Bonanni, D. Stifter, and H. Sitter, J. Appl. Phys. **92** (2002) p.1873
- [8.4] C.C. Kim and S. Sivananthan, Phys. Rev. B **53** (1996) p.1475
- [8.5] C. Bradford, C.B. O'Donnell, B.Urbaszek, C.Morhain, A. Balocchi, K.A. Prior, and B.C. Cavenett, Phys. Rev. B **64** (2001) 195309
- [8.6] J.J. Schermer, P. Mulder, G.J. Bauhuis, M.M.A.J. Voncken, J.V. Deelen, E. Haverkamp, & P.K. Larsen, Phys. Stat. Sol. (a) **202** (2005) p.501
- [8.7] T.C.M. Graham X. Tang, K.A. Prior, B.C. Cavenett, and R.J. Warburton, J. Crystal Growth **278** (2005) p.743
- [8.8] M. Funato, K. Omae, Y. Kawakami, Sg. Fujita, C. Bradford, A. Balocchi, K.A. Prior, and B.C. Cavenett, Phys. Rev. B **73** (2006) 245308
- [8.9] A.B. Preobrajenski, K. Barucki, and T. Chassé, PRL **85** (2000) p.4337
- [8.10] W. Heiss, E. Kaufmann, M. Böberl, T. Schwarzl, G. Springholz, G. Hesser, F. Schäffler, K. Koike, H. Harada, M. Yano, R. Leitsmann, L.E. Ramos, F. Bechstedt, Physica E **35** (2006) p.241

- [8.11] A. Svane, N.E. Christensen, M. Cardona, A.N. Chantis, M. van Schilfgaarde, and T.Kotani, Phys. Rev. B **81** (2010) 245120
- [8.12] J.M. Harbold and F.W. Wise, Phys. Rev. B **76** (2007) 125304
- [8.13] M. Eibelhuber, T. Schwarzl, G. Springholz, and W. Heiss, Appl. Phys. Lett. **94** (2009) 021118
- [8.14] M. Boberl, W. Heiss, T. Schwarzl, K. Wiesauer, and G. Springholz, Appl. Phys. Lett. **82** (2003) p.4065
- [8.15] B. Ullrich, X.Y. Xiao, and G.J. Brown, J. Appl. Phys. 108 (2010) 013525
- [8.16] J.J. Peterson and T.D. Krauss, Nano Lett. **6** (2006) p.510
- [8.17] N. Koguchi and S. Takahashi, Appl. Phys. Lett. **58** (1991) p.799